# Advancing Upconversion Emissions for Biomedical Imaging

Liu, Haichun

2014

# Advancing upconversion emissions for biomedical imaging

Haichun Liu

Doctoral Thesis
2014


Lund University

Advancing upconversion emissions for biomedical imaging


Printed in Sweden by Media-Tryck, Lund, 2014

Division of Atomic Physics
Department of Physics
Faculty of Engineering, LTH
Lund University
P.O. Box 118
SE–221 00 Lund
Sweden

http://www.atomic.physics.lu.se

ISSN 0281-2762
Lund Reports on Atomic Physics, LRAP-484

ISBN: 978-91-7473-880-3

*To my father*

# Abstract

During the past decade, upconverting nanoparticles (UCNPs) doped with rare earth ions have become an important class of fluorescence contrast agents for molecular imaging, due to their unique properties. Their property of anti-Stokes luminescence, with both the excitation and emission wavelengths close to the optimal for biomedical imaging, has been extensively explored in various biomedical applications. The work described in this thesis is mainly concerned with the investigation of other unique properties of UCNPs, including nonlinearity and saturation, to improve fluorescence diffuse imaging and tomography. The aim of this work was also to develop a suitable method of characterizing the power-density-dependent quantum yield of UCNPs, and to optimize the excitation scheme in order to facilitate their use in deep tissues.

Upconversion emission has a nonlinear dependence on the excitation intensity. This nonlinearity was exploited to improve the image reconstruction quality in fluorescence diffuse optical tomography, by increasing the orthogonal information density through simultaneous multibeam excitation. It is also demonstrated that the use of nonlinear UCNPs as contrast agents in fluorescence tomography can breach the current limit on spatial resolution encountered when using linear fluorophores. UCNPs can emit multiple emission bands with large differences in tissue attenuation under excitation of near-infrared light. Such multispectral information was used to create a regularization map to guide fluorescence diffuse optical tomography, which yielded significantly better axial resolution in the reconstructed images than using standard Tikhonov regularization.

The quantum yield of upconversion emission increases with excitation intensity and gradually reaches a plateau. In this work, an initial model was developed to describe the quantum yield of two-photon upconversion emission as a function of the excitation intensity, based on rate equation analysis. A balancing power density was identified, which characterizes the excitation-intensity dependence of the quantum yield. At such a power density, the quantum yield reaches half the maximum attainable value, occurring at very

high excitation intensities when UCNPs are saturated. Pulsed excitation is proposed as a superior mode of excitation to continuous wave excitation, due to the potential of achieving higher intrinsic quantum yields from UNCPs without increasing the average excitation power. This will fundamentally increase the applicability of UCNPs in deep tissues.

# Popular science description

Have you ever thought about what healthcare could be like in the future, or in other words, how medical treatment will develop? As non-invasive diagnostics and treatment are the ultimate goal of many scientists and engineers, fluorescence-based biomedical techniques could be expected to occupy an important place in future medical techniques. Imagine how wonderful it would be, if you could just illuminate the body with light, allowing lesions in deep tissues to be located and cured. Such a scenario has only seemed possible in the movies until now, but will in all probability be possible in the future.

Fluorescence-based techniques, such as fluorescence imaging and photodynamic therapy, have shown great promise in various biomedical applications. The physical basis of such techniques is the fluorescent properties of different molecules that either constitute the building blocks of living organisms or are externally introduced luminescent biomarkers. If the molecules embedded in tissues are regarded as microscopic lamps, they could be switched on remotely by laser radiation, and then emit fluorescent light with a molecule-dependent color, or wavelength. Lesions such as tumors have different molecular compositions from healthy tissue, sometimes containing disease-related biomolecules. These microscopic lamps could be used to visualize the lesion by the detection of fluorescent light of different wavelengths.

In techniques based on fluorescence, the introduction of exogenous luminescent molecules or phosphors is often necessary to improve the visualization of the lesion, as endogenous molecules generally exhibit poorer spectroscopic characteristics, making the distinction between diseased tissue and healthy tissue difficult. Another advantage of introducing external luminescent biomarkers is that they could be used as drug carriers, as the fluorescent light that they emit could be used to control the release of drugs. These luminescent biomarkers must be surface modified and functionalized, for example, by coating with specific antibodies, so that they target the lesion. Common luminescent biomarkers include fluorescent dyes and semiconductor quantum dots.

Upconverting nanoparticles (UCNPs) composed of rare earth ions doped in an inorganic host material are an emerging group of luminescent biomarkers with excellent spectroscopic and physicochemical properties. Such "nanolamps" can be lit up, or excited, by near-infrared light, and will then emit visible or near-infrared light with a wavelength shorter than the excitation wavelength. Since the fluorescent light originating from the labeled biological tissues, called autofluorescence, usually has a longer wavelength than the excitation light, the unique spectroscopic properties of UCNPs can be used to avoid the overlap of the fluorescence spectra of the biomarkers with the autofluorescence. This would enable autofluorescence-free optical imaging with very high sensitivity and contrast. In addition, research has shown that UCNP-mediated fluorescence imaging has much higher spatial resolution than that possible with conventional luminescent biomarkers such as fluorescent dyes, thanks to the nonlinear power dependence of UCNPs. Besides their use as fluorescent contrast agents, UCNPs can also be incorporated into photo-responsive compounds that contain bio-functional molecules, and the ultraviolet or visible emission induced by near-infrared excitation can be used to control the release of those biomolecules.

Upconverting nanoparticles have been used in numerous preclinical biomedical applications, including microscopy, diffuse imaging and tomography, photodynamic therapy and photoactivation. However, the low luminescence quantum efficiency of UCNPs, especially at the low excitation fluence rate that is typical in deep biological tissues, prevent their successful application in clinical settings. A large part of the work presented in this thesis has been devoted to developing a convenient method to characterize the quantum efficiency of UCNPs, with strong dependence on the excitation intensity, in a reproducible way, and exploring ways of using UCNPs in deep tissues by adjusting the fashion in which the excitation light is delivered.

# List of Publications

This thesis is based on the following papers, which will be referred to in the text by their Roman numerals.

I **Drug quantification in turbid media by fluorescence imaging combined with light-absorption correction using white Monte Carlo simulation**
H. Xie, H. Liu, P. Svenmarker, J. Axelsson, C. T. Xu, S. Gräfe, J. H. Lundeman, H. P. H. Cheng, S. Svanberg, N. Bendsoe, P. E. Andersen, K. Svanberg, S. Andersson-Engels.
*Journal of Biomedical Optics* **16(6)**, 066002-1 - 066002-11 (2011).

II **Synthesis of $NaYF_4$:$Yb^{3+}$, $Er^{3+}$ upconverting nanocrystals in a capillary-based continuous microfluidic reaction system**
H. Liu, O. Jakobsson, C. T. Xu, H. Xie, T. Laurell, S. Andersson-Engels.
*Proc. of SPIE* **7909**, 790917-1 - 790917-6 (2011).

III **Upconverting nanoparticles for pre-clinical diffuse optical imaging, microscopy and sensing: Current trends and future challenges**
C. T. Xu, Q. Zhan, H. Liu, G. Somesfalean, J. Qian, S. He, S. Andersson-Engels.
*Laser & Photonics Reviews* **7(5)**, 663-697 (2013).

IV **Balancing power density based quantum yield characterization of upconverting nanoparticles for arbitrary excitation intensities**
H. Liu, C. T. Xu, D. Lindgren, H. Xie, D. Thomas, C. Gundlach, S. Andersson-Engels.
*Nanoscale* **5**, 4770-4775 (2013).

V **Deep tissue optical imaging of upconverting nanoparticles enabled by exploiting higher intrinsic quantum yield through use of millisecond single pulse excitation with high peak power**
H. Liu, C. T. Xu, G. Dumlupinar, O. B. Jensen, P. E. Andersen, S. Andersson-Engels.
*Nanoscale* **5**, 10034-10040 (2013).

VI **Autofluorescence insensitive imaging using upconverting nanoparticles in scattering media**
C. T. Xu, N. Svensson, J. Axelsson, P. Svenmarker, G. Somesfalean, G. Chen, H. Liang, H. Liu, Z. Zhang, S. Andersson-Engels.
*Applied Physics Letters* **93(17)**, 171103-1 - 171103-3 (2008).

VII **High-resolution fluorescence diffuse optical tomography developed with nonlinear upconverting nanoparticles**
C. T. Xu, P. Svenmarker, H. Liu, X. Wu, M. E. Messing, L. R. Wallenberg, S. Andersson-Engels.
*ACS Nano* **6(6)**, 4788-4795 (2012).

VIII **Multibeam fluorescence diffuse optical tomography using upconverting nanoparticles**
H. Liu, C. T. Xu, S. Andersson-Engels.
*Optics Letters* **35(5)**, 718-720 (2010).

IX **Multispectral guided fluorescence diffuse optical tomography using upconverting nanoparticles**
P. Svenmarker, C. T. Xu, H. Liu, X. Wu, S. Andersson-Engels.
(2013) *Accepted for publication by Applied Physics Letters.*

Related publications not included in this thesis:

**Upconversion emission tuning from green to red in $Yb^{3+}/Ho^{3+}$-codoped $NaYF_4$ nanocrystals by tridoping with $Ce^{3+}$ ions**
G. Chen, H. Liu, G. Somesfalean, H. Liang, Z. Zhang.
*Nanotechnology* **20**, 385704 (6pp) (2009).

**Near vacuum ultraviolet luminescence of $Gd^{3+}$ and $Er^{3+}$ ions generated by super saturation upconversion processes**
G. Chen, H. Liang, H. Liu, G. Somesfalean, Z. Zhang.
*Optics Express* **17(19)**, 16366-16371 (2009).

**Anomalous power dependence of upconversion emissions in $Gd_2O_3$:$Er^{3+}$ nanocrystals under diode laser excitation of 970 nm**
G. Chen, H. Liang, H. Liu, G. Somesfalean, Z. Zhang.
*Journal of Applied Physics* **105**, 114315-1 - 114315-5 (2009).

# Abbreviations

| | |
|---|---|
| CT | computed tomography |
| CW | continuous wave |
| ED | electric dipole |
| ESA | excited state absorption |
| ETU | energy transfer upconversion |
| FDOT | fluorescence diffuse optical tomography |
| MC | Monte Carlo |
| MPE | maximum permissible exposure |
| MRI | magnetic resonance imaging |
| NIR | near-infrared |
| QY | quantum yield |
| RE | rare earth |
| RTE | radiative transport equation |
| TTA | triplet-triplet annihilation |
| UCNP | upconverting nanoparticle |

# Contents

## Papers

Chapter 1

# Introduction

Molecular imaging is a rapidly developing biomedical research discipline, the aim of which is the early detection of diseases *via* visual representation, characterization, and quantification of physiology and molecular signaling at the cellular and subcellular levels within intact living organisms [1, 2]. It has now become an indispensable tool, particularly in cancer research, clinical trials and medical practice. Among these techniques, fluorescence imaging has become one of the most commonly used modalities, due to its ability to visualize, for example, gene delivery [3], angiogenesis [4], and apoptosis [5, 6], together with its simplicity and cost-effectiveness.

In fluorescence molecular imaging, contrast agents are of essential importance, as they are the final reporters of the biological processes being probed. These can be either natural chromophores in the body, or externally introduced fluorophores with the desired spectroscopic properties. The latter are particularly widely employed, as they provide a large degree of freedom in tuning the fluorescence pathways in the way people expect. The most commonly investigated and applied exogenous contrast agents include fluorescent dyes (e.g. indocyanine green and Cy5.5) [6, 7], fluorescent proteins [4, 8, 9], and semiconductor quantum dots [10–17]. Despite considerable success, the use of these fluorophores is limited in fluorescence molecular imaging techniques by problems associated with tissue autofluorescence, poor spatial resolution and limited light penetration, making it difficult to image deeply located regions with high sensitivity [18]. Furthermore, photobleaching of traditionally used organic fluorophores limits the possibility of the repeated imaging required in longitudinal studies.

An emerging group of contrast agents - upconverting nanoparticles (UCNPs) have the potential to overcome the limitations discussed above due to their unique properties. UCNPs are nanosized inorganic crystals, doped with certain trivalent rare earth (RE) ions that act as sensitizers and activators [19]. The most no-

table sensitizer-activator pairs include $Yb^{3+}/Er^{3+}$, $Yb^{3+}/Tm^{3+}$ and $Yb^{3+}/Ho^{3+}$. $Yb^{3+}/Tm^{3+}$-codoped UCNPs can be excited by laser light of about 980 nm, and emit light at 800 nm. Both these wavelengths are close to the optimal for *in vivo* imaging in biological tissues, ensuring adequate imaging depths. In addition, imaging with UCNPs is background-free, without influence from tissue autofluorescence, due to the large anti-Stokes shift of the upconverted photoluminescence signal [20, 21], making it possible to detect very weak signals. Today, functional UCNPs with designed optical and physicochemical properties have become an important group of fluorescent contrast agents especially for preclinical studies in diffuse optical imaging, microscopy and bioassays [22, 23]. Although the quasi-optimal luminescent pathway and anti-Stokes shifted property have been studied and applied extensively, the potential advantage of the nonlinearity of UCNPs has been less exploited in fluorescence molecular imaging. As demonstrated by Svenmarker et al. [24], UCNP imaging provides improved spatial resolution in the recorded images, due to the nonlinear relation between the emitted signal and excitation power. Furthermore, few studies have been carried out on the optimization of the excitation scheme for UCNPs. Since the discovery of upconversion phenomena, continuous wave (CW) light sources have been used for pumping upconverting materials. However, the study in this thesis shows that pulsed excitation constitutes a superior excitation approach for UCNPs in biomedical applications.

The work described in this thesis has contributed to the characterization of the nonlinearity and the induced power-density-dependent quantum yield of UCNPs, and exploits such properties to achieve better-quality fluorescence imaging with high spatial resolution. The optimization of the excitation scheme for UCNPs is discussed, with regard to fluorescence[1] imaging in deep tissues. This chapter provides a brief introduction to these two central points. In addition, an outline and the aims of the work presented in this thesis are presented.

## 1.1 Nonlinearity and quantum yield characterization of upconverting nanoparticles

Upconversion emission is generated by accumulating the energy of more than one excitation photon *via* sequential energy transfer between dopant ions, and thus the emission intensity exhibits a nonlinear dependence on the excitation power. This is of benefit in

[1] Strictly speaking, upconversion emission should be named using a more general term - *luminescence*. However, in order to stress the similarities to conventional fluorescence imaging, the term *fluorescence* is adopted for UCNP imaging and tomography throughout this thesis.

both fluorescence imaging and tomography, providing higher spatial resolution than conventional linear fluorescent contrast agents such as dyes and quantum dots. In addition, the nonlinear fluorophores being probed in fluorescence diffuse optical tomography (FDOT) using UCNPs as contrast agents could make different excitation beams "interfere" with each other, thus providing additional information useful for image reconstruction. Such additional information is contained in the difference between the fluorescence images collected when using the individual excitation beams and that obtained with simultaneous, multiple excitation beams.

In contrast to other multi-photon processes, which are instantaneous, such as second-harmonic generation and two-photon fluorescence, the upconversion process is relatively slow, as it involves real intermediate energy states. These intermediate levels may become saturated at high excitation intensities, leading to a less steep excitation-power-density dependence of the fluorescence intensity. Due to the nonlinearity of UCNPs, exhibiting saturation, their quantum yield, which is defined as the ratio between the number of excitation photons and the number of emission photons, increases with excitation intensity, finally approaching a constant value [25]. Characterization of such a dependence on the excitation intensity of upconversion emission is important in guiding the practical use of UCNPs in biomedical applications. In addition, it could potentially provide standard indices for characterizing UCNPs with respect to energy conversion, whereas at present, local references are employed in different labs.

## 1.2 Excitation scheme optimization of upconverting nanoparticles

A major limitation of the use of UCNPs in biological applications is their relatively low quantum yield, especially under low excitation intensities. This limitation is particularly severe when UCNPs are used in deep tissues, as the excitation light is significantly attenuated due to tissue absorption and scattering. Besides fundamentally improving the luminescence efficiency of UCNPs by means of material engineering, the low light limit, and thus small applicable depth, of UCNP imaging could be partly overcome by employing pulsed excitation.

Similar to two-photon fluorescence microscopy, pulsed excitation would provide high photon density during the pulse, thus enabling a high quantum yield of upconversion emission, while the average power (responsible for tissue heating) remains moderate. In this way, the upconversion signal could be enhanced without raising concerns regarding side effects and laser safety. The pulsed laser excitation has the potential to fundamentally broaden the applicability of UCNPs in deep tissue regions relying on diffuse

light excitation. Until now, the advantages of pulsed excitation have generally been ignored in the literature, although numerous studies have been conducted using pulsed laser sources for pumping upconverting materials, e.g., femtosecond pulses [26–28] and microsecond pulses [29, 30]. Gainer et al., for example, investigated the use of pulsed excitation to control the color of upconversion emission by varying the repetition rate of the excitation laser [29, 31].

## 1.3 Aims and outline of this thesis

The general aims of the work presented in this thesis were:

(i) to improve the overall quality of fluorescence imaging and tomography of fluorescent agents for biomedical applications,

(ii) to develop standard indices for characterizing the quantum yield of UCNPs, and

(iii) to facilitate the use of UCNPs in deep tissues.

The general outline of the thesis is as follows.

**Chapter 2** describes the light-tissue interactions when light propagates through biological media, including scattering, absorption and luminescence. In addition, an overview of the physical models used to describe light propagation in turbid media is provided, including the radiative transport equation, the diffusion approximation, and Monte Carlo simulations. In Paper **I**, time-resolved white Monte Carlo simulation was used to correct for the influence of tissue absorption in fluorescence imaging, with the aim of achieving quantitative evaluation of the photosensitizer.

**Chapter 3** provides an overview of UCNPs. The property of luminescence, including upconversion processes of rare earth ions doped in solids, is described. The material engineering of UCNPs, from their synthesis, to surface modification and functionalization, is discussed. Microfluidic synthesis of UCNPs is proposed in Paper **II**. Finally, the assessment of toxicity and biomedical applications of UCNPs are discussed. In Paper **III**, a review of the current state of the art of UCNPs and their applications in diffuse imaging, microscopy and bioassays is given.

**Chapter 4** focuses on the quantum yield characterization and excitation scheme optimization of UCNPs. A two-parameter method for quantum yield characterization of UCNPs is discussed, based on the existence of the balancing power density, which reflects the dependence of quantum yield on the excitation intensity (Paper **IV**). The advantages of pulsed excitation over

CW excitation are demonstrated experimentally in Paper **V**, together with numerical simulations considering the excitation dynamics of upconversion emissions. It is shown that the use of pulsed excitation, including strong single-pulse excitation, can increase the applicability of UCNPs in deep tissues by employing higher intrinsic quantum yield.

**Chapter 5** presents FDOT in scattering media using UCNPs as contrast agents. In Paper **VI**, it is demonstrated that autofluorescence-free imaging can be achieved using UCNPs. The nonlinearity of UCNPs proved to be a useful property for FDOT. In Paper **VII**, this property is exploited to breach the present resolution limit in fluorescence tomography. In Paper **VIII**, the nonlinearity is exploited to increase the orthogonal information density for image reconstructions. In addition, multicolor upconversion emissions were used to guide FDOT, as described in Paper **IX**.

Chapter 2

# Light-tissue interactions and photon migration theory

Photonics-based techniques have been attracting increasing interest in clinical diagnosis and therapy, largely because they are non-invasive and cost-effective. A good understanding of how light interacts with biological tissues is the basis for the success of such techniques. This chapter starts with a discussion of the underlying physics of basic light-tissue interactions, including light scattering, light absorption and luminescence. This is followed by the introduction and discussion of the most commonly used models for describing light propagation in tissues, which are necessary for quantitative and controllable optical diagnosis and therapy.

## 2.1 Light-tissue interactions

### 2.1.1 Tissue scattering

Light is scattered, i.e., being forced to deviate from a straight trajectory to travel in all directions, when it encounters inhomogeneities in the medium through which it is propagating. From a classical electromagnetic point of view, the inhomogeneity, usually called the scatterer, consists of a collection of elementary charges, while the light beam is an oscillating electromagnetic wave. The charges will be excited by the incident wave causing them to oscillate, and thereby radiate secondary electromagnetic waves. The superposition of the secondary waves gives the total scattered field. Scattering can be either elastic, for example, Rayleigh [32] and Mie scattering [33], or inelastic, such as Raman [34] and Brillouin scattering [35, 36], depending on whether the energy, and thus the wavelength is conserved in the scattering process. Theoretically, calculating the scattered field by superposing all the sec-

ondary waves is impracticable, due to the extremely large number of elementary charges forming the scatterers. Depending on the number density of the scatterers, two different regimes exist, i.e. single scattering and multiple scattering, and different calculation approaches can be applied.

**Single-particle scattering**

In the modern theory of electromagnetic scattering by a single small particle, the large collection of charges forming the particle is treated as a macroscopic body with a specific refractive index distribution, and the scattered field is computed by solving the Maxwell's equations for the macroscopic electromagnetic field subject to appropriate boundary conditions. The size and shape of the particle are of fundamental importance in determining the scattered field, as they influence the phase differences, and thus the superposition of the secondary waves. Rayleigh treated the scattering problem involving scatterers much smaller than the wavelength of incident light in 1871 [32, 37], and was the first to explain the blue color of the sky. Mie investigated scattering by spherical particles of different sizes using Maxwell's theory in 1908 [33].

Generally, scattering by a single particle can be characterized by two parameters: the integral scattering cross-section, $\sigma_{\text{sca}}$ [cm$^2$], and the scattering phase function, $p(\hat{\mathbf{s}}', \hat{\mathbf{s}})$, where $\hat{\mathbf{s}}'$ and $\hat{\mathbf{s}}$ denote the directions of propagation of the incident wave and the scattered wave, respectively. $\sigma_{\text{sca}}$ describes the strength or probability of scattering. For Rayleigh scattering, $\sigma_{\text{sca}}$ depends on the wavelength, $\lambda$ [nm], according to:

$$\sigma_{\text{sca}}^{\text{Ray}} \propto \lambda^{-4}. \tag{2.1}$$

As for Mie scattering, the wavelength dependence of the scattering cross-section can be also approximated by a power law:

$$\sigma_{\text{sca}}^{\text{Mie}} \propto a\lambda^{-\text{b}}. \tag{2.2}$$

Here, the coefficient $a$ is related to the number density of the scatterers, and $b$ to the size of the scatterer.

The scattering phase function, $p(\hat{\mathbf{s}}', \hat{\mathbf{s}})$, describes the normalized angular distribution of the power of the scattered field, fulfilling the expression:

$$\int_{4\pi} p(\hat{\mathbf{s}}', \hat{\mathbf{s}}) \mathrm{d}\omega' = 1. \tag{2.3}$$

The phase function is usually assumed to depend only on the deflection angle $\theta$, and not on the azimuthal angle $\phi$, yielding:

$$p(\hat{\mathbf{s}}', \hat{\mathbf{s}}) \approx p(\hat{\mathbf{s}}' \cdot \hat{\mathbf{s}}) = p(\cos\theta). \tag{2.4}$$

In the case of Rayleigh scattering, the phase function is isotropic, while for Mie scattering, it typically exhibits dominant forward scattering, as shown in Figure 2.1. The exact shape of Mie scattering phase function depends on the size and refractive index of the spherical scatterer. The multiple side lobes in the phase function are due to interference effects. In addition, the phase function is also dependent on the wavelength, as can be seen in the same figure.

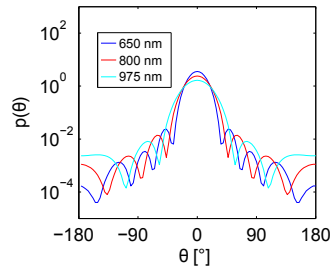


**Figure 2.1.** *Mie scattering phase functions for dielectric spherical scatterers with a diameter of 1 μm and refractive index of 1.5, at three different wavelengths. Data from the Mie calculator [38].*

### Multiple scattering

For a collection of scatterers, each scatterer will contribute to the final scattered light field. If the number density of scatterers, $N_{\text{sca}}$ [cm$^{-3}$], is small, the contribution of each scatterer can be regarded as linearly independent, and thus the scattering property of the medium can be characterized by a scattering coefficient, $\mu_{\text{s}}$ [cm$^{-1}$]:

$$\mu_{\text{s}} = N_{\text{sca}}\sigma_{\text{sca}}, \tag{2.5}$$

which describes the scattering probability per unit length.

In a turbid medium such as tissue, where scatterers with different sizes, shapes, refractive indices and orientation are densely packed, and sometimes also moving randomly, the treatment of multiple scattering is not trivial in the framework of electromagnetic wave propagation. Therefore, a statistic description of the scattering medium is generally employed instead. In this case, the scattering material is described using an average scattering coefficient ($\mu_{\text{s}}$), together with an average angular distribution function, i.e., the scattering phase function ($p(\cos\theta)$). $\mu_{\text{s}}$ is still the probability of scattering per unit length, and its reciprocal, usually called the mean free path, characterizes the average distance between two adjacent scattering events. The so-called Henyey-Greenstein phase function is commonly adopted to describe the angular distribution of the scattered light by tissues [39–41], and has the form:

$$p(\cos\theta) = \frac{1}{4\pi}\frac{1-g^2}{(1+g^2-2g\cos\theta)^{3/2}}. \tag{2.6}$$

Here, $g$ is the anisotropy factor, defined as the average of the cosine of the scattering angle, which characterizes the directionality of the scattered light. The Henyey-Greenstein phase function for different anisotropy factors is illustrated in Figure 2.2.

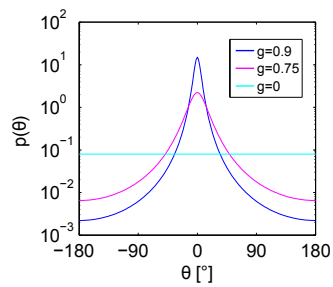


**Figure 2.2.** *Henyey-Greenstein scattering phase function for $g = 0.9$, $g = 0.75$, and $g = 0$. Biological tissues usually exhibit forward scattering, typically with $g > 0.8$.*

The so-called reduced scattering coefficient, $\mu_{\text{s}}'$ [cm$^{-1}$], is usually introduced to describe light scattering solely, which is defined by:

$$\mu_{\text{s}}' = (1-g)\mu_{\text{s}}, \tag{2.7}$$

The wavelength dependence of the scattering parameters of scattering media is related to the sizes of the scatterers. Generally, the scattering coefficient and the phase function exhibit a complex

dependence on the wavelength. However, the reduced scattering coefficient can be well approximated as a function of wavelength by a power law, in a similar way to that specified in Equation (2.2) [42, 43]. Alternatively, the reduced scattering coefficient can be described as a sum of the Mie-scattering and Rayleigh-scattering contributions with different weights [44], i.e.:

$$\mu_{\mathrm{s}}' = a' \left[ f_{\mathrm{Ray}} \lambda^{-4} + (1 - f_{\mathrm{Ray}}) \lambda^{-b_{\mathrm{Mie}}} \right], \tag{2.8}$$

where $a'$ is a scaling factor, $f_{\mathrm{Ray}}$ is the fraction of Rayleigh scattering, $(1 - f_{\mathrm{Ray}})$ is the fraction of Mie scattering, and $b_{\mathrm{Mie}}$ is the scattering power of Mie scattering.

### 2.1.2 Tissue absorption

In addition to scattering, another important process may occur when light encounters an object, i.e., absorption. Light absorption can be well described using quantum mechanics. In such a framework, the object, consisting of a collection of atoms or molecules, can be quantized into discrete energy states, and the light can be quantized as photons with energies characterized by the frequency of the electromagnetic wave. When the energy of the photon matches the energy difference between two different energy states of the object, there is a probability of light absorption.

Absorption by a single absorber can be described by the absorption cross-section, $\sigma_{\mathrm{abs}}$ [$\mathrm{cm}^2$]. A medium is normally composed of numerous absorbers. Hence, the absorption properties of the medium can be described by the absorption coefficient, $\mu_{\mathrm{a}}$ [$\mathrm{cm}^{-1}$], taking into account the contributions of all the absorbers:

$$\mu_{\mathrm{a}} = N_{\mathrm{abs}} \sigma_{\mathrm{abs}}, \tag{2.9}$$

where $N_{\mathrm{abs}}$ [$\mathrm{cm}^{-3}$] denotes the number density of the absorbers. The absorption coefficient describes the absorption probability per unit optical path length. Absorption causes energy loss of the incident beam. In Equation (2.9), the absorbers are considered to be identical, and thus have the same absorption cross-section. Tissues contains many different absorbers (or chromophores), including oxygenated ($\mathrm{HbO_2}$) and deoxygenated hemoglobin (Hb) [45, 46], water [47, 48], lipids [49] and melanin [50–52]. The absorption coefficient of the medium is thus the sum of the contributions from all the absorbing chromophores, with their different absorption properties. For convenience, the absorption coefficient is usually described using the concentrations $C_i$ [M], and extinction coefficients $\varepsilon_i$ [$\mathrm{cm}^{-1}\mathrm{M}^{-1}$], of different chromophores [44], instead of using number densities and absorption cross-sections, yielding:

$$\mu_{\mathrm{a}} = \sum_i C_i \varepsilon_i. \tag{2.10}$$

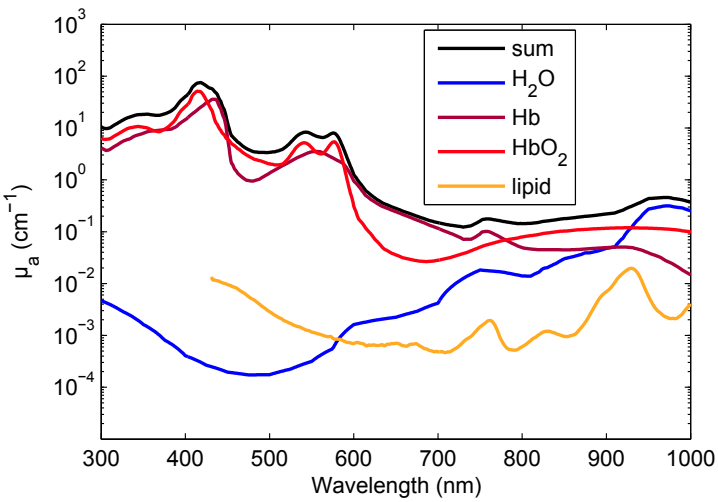


**Figure 2.3.** *Absorption coefficients for the main absorbing chromophores in biological tissues and the corresponding synthetic absorption coefficient. The absorption coefficients were calculated using 70 % water [53], 3 % blood volume fraction with 60 % oxygen saturation [54], and 15 % lipids [55].*

Figure 2.3 shows the absorption spectra of a few chromophores found in tissue. Tissue has a relatively low light absorption in the spectral range of 600-1000 nm, and thus light of these wavelength can propagate to depths of millimeters to centimeters. This spectral range is called the tissue optical window.

Absorption causes energy loss of the incident beam, and the loss of light intensity after traveling an infinitesimal distance, $\mathrm{d}L$, can be described as:

$$\mathrm{d}I = -\mu_{\mathrm{a}} I \mathrm{d}L. \tag{2.11}$$

This leads to the famous Beer-Lambert law, describing the transmitted light intensity after traveling through a homogeneous non-scattering, but absorbing medium [56]:

$$I = I_0 \exp(-\mu_{\mathrm{a}} d), \tag{2.12}$$

where $I$ [Wcm$^{-2}$] is the transmitted intensity, $I_0$ [Wcm$^{-2}$] is the incident intensity, and $d$ [cm] is the thickness of the medium. In highly scattering media such as biological tissue, the Beer-Lambert law can be applied with modifications accounting for the distribution of the optical path lengths [57, 58]. A modified Beer-Lambert law was used in Paper **I**.

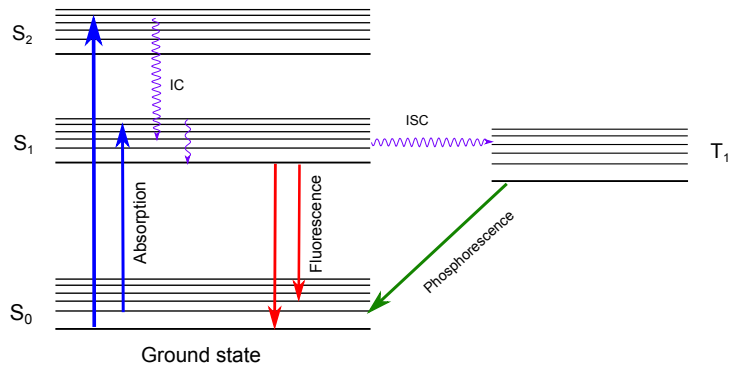


**Figure 2.4.** *Schematic Jablonski diagram depicting the luminescence process. $S_n$ (n=0, 1, 2) denote singlet states, and $T_1$ is a triplet state. IC–internal conversion. ISC–intersystem crossing.*

### 2.1.3 Luminescence

After the energy of the light has been absorbed by the chromophores, one portion of the absorbed energy is generally dissipated nonradiatively within the chromophores through the medium, finally resulting in heat. The other portion of the absorbed energy is emitted as light or luminescence. This luminescence may be named differently depending on the mechanisms involved, sometimes even for the same chromophore. For instance, the transition between singlet states in molecules yields fluorescence, which has a lifetime typically on the order of nanoseconds. The transition between an excited triplet state and a lower-lying singlet state generates phosphorescence, with much longer lifetimes than fluorescence due to the violation of the transition selection rule. A Jablonski diagram illustrating the processes of light absorption and luminescence is shown in Figure 2.4. A chromophore that can generate luminescence upon excitation is usually called as a fluorophore.

Compared with light absorption and scattering, luminescence can provide structural and functional information on tissues with much higher spatial resolution, sometimes even at the single molecule level. Hence, the luminescence from endogenous and exogenous fluorophores is used extensively in various biomedical applications based on optical techniques. Endogenous fluorophores that exist naturally in biological tissues include reduced nicotinamide-adenine dinucleotide and reduced nicotinamide-adenine dinucleotide phosphate [59, 60], flavin adenine dinucleotide [61], collagen and elastin [62, 63], lipopigments [61, 64], amino acids and porphyrins. Exogenous fluorophores

are introduced into living organisms using biotechniques, and include, for example, fluorescent dyes [7, 65], fluorescent proteins [4, 9, 66, 67] and semiconductor quantum dots [68, 69]. In the present work, RE-ion-doped inorganic UCNPs were mainly utilized as exogenous luminescent biomarkers in various biomedical applications, including fluorescence diffuse optical imaging and FDOT. The UCNPs will be introduced in detail in Chapter 3, and their optical properties and applications are presented in Chapters 4 and 5.

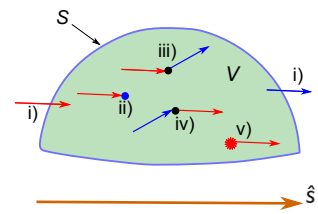


**Figure 2.5.** *Events considered in the derivation of the RTE. i) Photon transfer across the boundary. ii) Photon loss due to absorption. iii) Photon loss due to scattering. iv) Photon scattering in the* $\hat{\mathbf{s}}$ *direction from all other directions. v) Photons generated by the source.*

## 2.2 Radiative transport theory

A central issue in tissue optics is the modeling of the propagation of light in a medium with known absorption and scattering properties. This is the prerequisite for quantitative light diagnostics and therapy. As discussed previously, due to the generally high scattering of light in tissue, light propagation modeling by solving Maxwell's equation is impracticable from an electromagnetic wave point of view. Instead, radiative transport theory is employed, in which light is treated as a flow of neutral particles, ignoring its wave properties. This concept was borrowed from studies within the field of radiation transfer [70–72], neutron transport [73], and the diffusion of charged particles [74]. Early works include those by Longini et al. [75], Reynolds et al. [76], and Ishimaru et al. [77].

Transport theory depends on an important quantity, namely the photon distribution function, $N(\mathbf{r}, \hat{\mathbf{s}}, t)$ $[\mathrm{m}^{-3}\mathrm{sr}^{-1}]$, which defines the number of photons per unit volume per steradian traveling in direction $\hat{\mathbf{s}}$ at a given position, $\mathbf{r}$, and time, $t$. The radiative transport equation (RTE) is constructed heuristically by considering the conservation of energy or photons in any direction, $\hat{\mathbf{s}}$, inside a small volume, $V$, with boundary, $S$, taking into account the effects of tissue absorption and scattering, and the photon source, as illustrated in Figure 2.5. This yields:

$$\int_V \frac{\partial N}{\partial t}\mathrm{d}V = \underbrace{-\int_S cN\hat{\mathbf{s}}\cdot\hat{\mathbf{n}}\mathrm{d}A}_{\text{i)}} \underbrace{-\int_V c\mu_\mathrm{a}N\mathrm{d}V}_{\text{ii)}} \underbrace{-\int_V c\mu_\mathrm{s}N\mathrm{d}V}_{\text{iii)}} + \underbrace{\int_V c\mu_\mathrm{s}\int_{4\pi} p(\hat{\mathbf{s}}', \hat{\mathbf{s}})N(\hat{\mathbf{s}}')\mathrm{d}\omega'\mathrm{d}V}_{\text{iv)}} + \underbrace{\int_V q\mathrm{d}V}_{\text{v)}}, \quad (2.13)$$

where $c$ $[\mathrm{ms}^{-1}]$ is the speed of light in the medium, and $q(\mathbf{r}, \hat{\mathbf{s}}, t)$ $[\mathrm{m}^3\mathrm{s}^{-1}\mathrm{sr}^{-1}]$ is a source term defining the production of photons per unit volume, per steradian at time $t$ and position $\mathbf{r}$. Arguments for different quantities are omitted for brevity unless considered neces-

sary. The terms on the right-hand side describe the contributions of:

**i)** photon transfer across the boundary,

**ii)** photons loss due to absorption,

**iii)** photons loss due to scattering from direction $\hat{\mathbf{s}}$ to other directions,

**iv)** photons scattering in the $\hat{\mathbf{s}}$ direction from all other directions, and

**v)** photons generated by the source.

Applying Gauss's divergence theorem to term i)[1] and dropping all volume integrations, gives the RTE valid for an arbitrary volume:

$$\frac{\partial N}{\partial t} = -c\hat{\mathbf{s}} \cdot \nabla N - c(\mu_\mathrm{a} + \mu_\mathrm{s})N + c\mu_\mathrm{s} \int_{4\pi} p(\hat{\mathbf{s}}', \hat{\mathbf{s}})N(\hat{\mathbf{s}}')\mathrm{d}\omega' + q. \tag{2.14}$$

Another quantity, $L(\mathbf{r}, \hat{\mathbf{s}}, t)$ [$\mathrm{Wm^{-2}sr^{-1}}$], called the radiance, is often of interest, and describes the radiant power flow along $\hat{\mathbf{s}}$ through unit area at position $\mathbf{r}$ and time $t$. It is related to the photon distribution function by [78]:

$$L = Nhvc, \tag{2.15}$$

where $h$ [$\mathrm{m^2kgs^{-1}}$] is Planck's constant, and $\nu$ [$\mathrm{s^{-1}}$] the frequency of the light. The transport equation can then be expressed using the radiance as:

$$\frac{1}{c}\frac{\partial L}{\partial t} = -\hat{\mathbf{s}} \cdot \nabla L - (\mu_\mathrm{a} + \mu_\mathrm{s})L + \mu_\mathrm{s} \int_{4\pi} p(\hat{\mathbf{s}}', \hat{\mathbf{s}})L(\hat{\mathbf{s}}')\mathrm{d}\omega' + hvq. \tag{2.16}$$

The RTE is analytically solvable only in very simple cases such as one-dimensional geometries [79]. In most cases, the RTE is solved using numerical methods, or is simplified based on certain approximations so that simple analytical solutions may be found. Such techniques include the spherical harmonics method [80, 81] and the diffusion approximation [80], the simplified spherical harmonics method [82–86], the discrete ordinates method [87], and Monte Carlo (MC) simulations [88, 89]. In this thesis, the diffusion approximation and MC simulations were mainly used, and they will be introduced in the following sections.

[1] Here, Gauss's divergence theorem is used, i.e., $\int_A \mathbf{F} \cdot \mathbf{n}\mathrm{d}A = \nabla \cdot \mathbf{F}\mathrm{d}V$. Note that $\nabla \cdot (N\hat{\mathbf{s}}) = \nabla N \cdot \hat{\mathbf{s}} + N\nabla \cdot \hat{\mathbf{s}} = \nabla N \cdot \hat{\mathbf{s}}$, as $\hat{\mathbf{s}}$ is fixed.

## 2.3 Diffusion theory

The diffusion approximation is one of the most commonly used methods to solve the RTE [73, 77, 80]. The basic idea is to expand the radiance, the source term, and the phase function into infinite series of spherical harmonics, and the series is truncated to include only the first-order terms[2] [92]. In this case, the radiance can be expressed by the sum of an isotropic part and a gradient part:

$$L(\mathbf{r}, \hat{\mathbf{s}}, t) \approx \frac{1}{4\pi}\Phi(\mathbf{r}, t) + \frac{3}{4\pi}\mathbf{J}(\mathbf{r}, t) \cdot \hat{\mathbf{s}}, \tag{2.17}$$

where $\Phi(\mathbf{r}, t)$ [$\mathrm{Wm}^{-2}$] is the fluence rate, and $\mathbf{J}(\mathbf{r}, t)$ [$\mathrm{Wm}^{-2}$] is the flux, fulfilling the expression:

$$\Phi(\mathbf{r}, t) = \int_{4\pi} L(\mathbf{r}, \hat{\mathbf{s}}, t)\mathrm{d}\omega, \tag{2.18}$$

and

$$\mathbf{J}(\mathbf{r}, t) = \int_{4\pi} L(\mathbf{r}, \hat{\mathbf{s}}, t)\hat{\mathbf{s}}\mathrm{d}\omega, \tag{2.19}$$

respectively. In addition, the source is assumed to be isotropic, i.e.:

$$hvq = \frac{1}{4\pi}q_0(\mathbf{r}, t). \tag{2.20}$$

Inserting Equations (2.17) and (2.20) into the RTE, i.e., Equation (2.16), results in two coupled equations:

$$\left(\frac{1}{c}\frac{\partial}{\partial t} + \mu_\mathrm{a}\right)\Phi + \nabla\mathbf{J} = q_0, \tag{2.21}$$

$$\left(\frac{1}{c}\frac{\partial}{\partial t} + \mu_\mathrm{a} + \mu_\mathrm{s}'\right)\mathbf{J} + \frac{1}{3}\nabla\Phi = 0. \tag{2.22}$$

One more assumption is needed to give the diffusion equation, i.e., that the temporal change in the flux is negligible, $\partial\mathbf{J}/\partial t = 0$, yielding Fick's first law of diffusion:

$$\mathbf{J} = -\frac{1}{3(\mu_\mathrm{a} + \mu_\mathrm{s}')}\nabla\Phi = -D\nabla\Phi, \tag{2.23}$$

where $D$ [m] is the diffusion coefficient. The diffusion equation can be obtained by inserting Equation (2.23) into Equation (2.21):

$$\frac{1}{c}\frac{\partial\Phi(\mathbf{r}, t)}{\partial t} - \nabla D(\mathbf{r})\nabla\Phi(\mathbf{r}, t) + \mu_\mathrm{a}(\mathbf{r})\Phi(\mathbf{r}, t) = q_0(\mathbf{r}, t). \tag{2.24}$$

Accordingly, the steady-state diffusion equation is given by:

$$-\nabla D(\mathbf{r})\nabla\Phi(\mathbf{r}) + \mu_\mathrm{a}(\mathbf{r})\Phi(\mathbf{r}) = q_0(\mathbf{r}). \tag{2.25}$$

[2] The diffusion equation can be derived in different ways, e.g., using random walk theory, as described by Alerstam [90, 91]

In deriving this diffusion equation, two assumptions were made: that the temporal change of the flux is negligible, and that the source is isotropic. The first assumption is acceptable if the requirement $\omega \ll c\mu_s'$ is fulfilled [93–98], where $\omega$ is the modulation angular frequency in frequency-domain techniques, and is related to time *via* the Fourier transform. For steady-state problems, $\omega = 0$. The second assumption is valid far from the source for strongly scattering media, as the directed source may be treated as an isotropic source at a depth of $1/\mu_s'$ [99]. In addition, scattering must dominate over absorption, i.e., $\mu_s' \gg \mu_a$, in order for the diffusion assumption to be valid [97], rooted in the difficulties in describing strong gradients of the first order truncation. In cases where these assumptions are not valid, other techniques such as the spherical harmonics method or MC simulation should be used instead.

The diffusion equation can be extended to model the fluorescence problem. In this case, the fluorophores inside the medium are treated as point light sources, and the strengths are described by the product of the local excitation fluence rates and the fluorescent yield of the fluorophores. The equation for modeling fluorescent light becomes [100, 101]:

$$-\nabla D_m(\mathbf{r})\nabla\Phi_m(\mathbf{r}) + \mu_{am}(\mathbf{r})\Phi_m(\mathbf{r}) = \Phi_x(\mathbf{r})\eta\mu_{af}(\mathbf{r}). \qquad (2.26)$$

Here, m and x denote emission and excitation, respectively, $\eta$ [-] is the quantum yield of the fluorophores at the emission wavelength, and $\mu_{af}$ [$\mathrm{cm}^{-1}$] is the absorption coefficient of the fluorophores at the excitation wavelength. The fluence rate of excitation light, $\Phi_x(\mathbf{r})$, is calculated using Equation (2.25).

### Boundary conditions

Boundary conditions are a general prerequisite for obtaining unique solutions when solving differential equations. For the RTE or diffusion equations dealing with the radiance, the boundary conditions mainly concern the reflection of light at the boundary, if the refractive indices inside ($n$) and outside the medium ($n_0$) are mismatched.

Considering the reflection of the total radiance on the boundary yields the modified Robin-type boundary condition [80, 102]:

$$\Phi(\mathbf{r},t) + 2AD\nabla\Phi(\mathbf{r},t)\cdot\hat{\mathbf{n}} = 0, \qquad (2.27)$$

Here, $\hat{\mathbf{n}}$ is the outward normal direction of the boundary; parameter $A$ takes into account the refractive index mismatch at the boundary, and as a result of Fresnel's law [103], is given by:

$$A = \frac{2/(1-R_0) - 1 + |\cos\theta_c|^3}{1 - |\cos\theta_c|^2}, \qquad (2.28)$$

where

$$R_0 = \frac{(n-n_0)^2}{(n+n_0)^2}, \tag{2.29}$$

and

$$\theta_c = \arcsin\left(\frac{n_0}{n}\right). \tag{2.30}$$

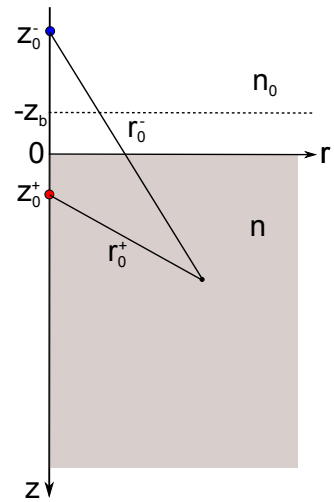


**Figure 2.6.** *A homogeneous medium with a semi-infinite geometry.*

### Analytical solutions

For some simple geometries, there are analytical solutions to the diffusion equation. For a homogeneous infinite medium, with a point source expressed as $q_0(\mathbf{r},t) = P_0\delta(\mathbf{r})\delta(t)$, where $P_0$ [W] is the power of the source, the solution is [104]:

$$\Phi(r,t) = cP_0(\frac{1}{4\pi Dct})^{3/2}\exp(-\frac{r^2}{4\pi Dct} - \mu_{\mathrm{a}}ct). \tag{2.31}$$

The solution for the steady-state diffusion equation with a source term $q_0(\mathbf{r}) = P_0\delta(\mathbf{r})$ can be described by [105, 106]:

$$\Phi(r) = \frac{P_0}{4\pi D}\frac{\exp(-\mu_{\mathrm{eff}}r)}{r}, \tag{2.32}$$

where the effective attenuation coefficient, $\mu_{\mathrm{eff}}$ [$\mathrm{m}^{-1}$], is defined by:

$$\mu_{\mathrm{eff}} = \sqrt{\frac{\mu_{\mathrm{a}}}{D}}. \tag{2.33}$$

For semi-infinite or slab geometries, the analytical solutions can be obtained through the use of mirrored sources. In these cases, the so-called extrapolated boundary condition is employed, i.e., the virtual boundaries, placed away from the real medium boundaries by a distance $z_b = 2AD$, are considered to have a fluence rate of zero [105]. In a semi-infinite geometry, as illustrated in Figure 2.6, the real source is placed at a depth $z_0^+ = 1/\mu_{\mathrm{s}}'$, and thus a mirrored, negative source with the same power is placed at $z_0^- = -2z_b - z_0^+$. The resulting fluence rate inside the medium is given by the sum of the contributions of these two sources:

$$\Phi(r) = \frac{P_0}{4\pi D}\left[\frac{\exp(-\mu_{\mathrm{eff}}r_0^+)}{r_0^+} - \frac{\exp(-\mu_{\mathrm{eff}}r_0^-)}{r_0^-}\right], \tag{2.34}$$

where $r_0^{+,-} = \sqrt{r^2 + (z - z_0^{+,-})^2}$.

In an infinite slab geometry as shown in Figure 2.7, the extrapolated boundary condition must be fulfilled at both interfaces, and the z-positions of the resulting positive and negative sources can

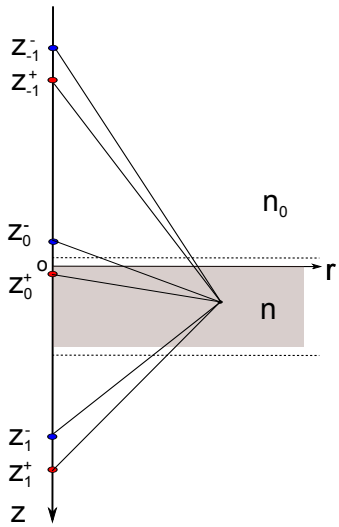


**Figure 2.7.** *A homogeneous medium with a slab geometry.*

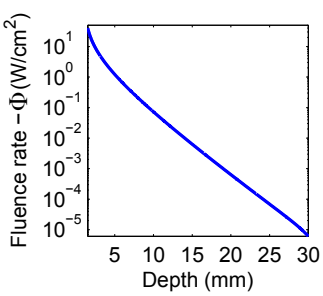


**Figure 2.8.** *Calculated fluence rate for a 3 cm thick slab with optical parameters of* $\mu_s' = 10$ cm$^{-1}$ *and* $\mu_a = 0.5$ cm$^{-1}$. *The incident power was set to* $P_0 = 1$ W.

thus be derived from [104, 107, 108]:

$$z_m^+ = 2m(d + 2z_b) + z_0^+, \tag{2.35}$$

$$z_m^- = 2m(d + 2z_b) - 2z_b - z_0^+, \tag{2.36}$$

$$m = 0, \pm1, \pm2, \pm3, \ldots, \tag{2.37}$$

giving the fluence rate inside the medium expressed as:

$$\Phi(r) = \frac{P_0}{4\pi D} \sum_{m=-\infty}^{m=+\infty} \left[ \frac{\exp(-\mu_{\text{eff}} r_m^+)}{r_m^+} - \frac{\exp(-\mu_{\text{eff}} r_m^-)}{r_m^-} \right], \tag{2.38}$$

where $r_m^{+,-} = \sqrt{r^2 + (z - z_m^{+,-})^2}$.

The inclusion of mirrored sources of the first few orders is usually sufficient to provide good accuracy. Figure 2.8 presents the fluence rate as a function of depth in a homogeneous slab, calculated using Equation (2.38) with $m = 0$ and $\pm1$.

## 2.4 Monte Carlo simulations

Monte Carlo simulation is a numerical problem-solving technique based on probability theory and mathematical statistics. It relates the problem to certain probabilistic models, and provides an approximate solution by performing multiple simulations using random variables. Turning to transport of light in turbid media, MC method can provide an accurate solution to the RTE, as it is subject to the same approximation as the equation being solved. Thus, MC method is considered the gold standard for solving the RTE. The MC method can handle any geometry. The solution provided by MC method is generally noisy, and the accuracy is dependent on the number of "particle" packages used in the simulations.

In the MC simulation of light propagation in a scattering medium, the problem-solving process is based on the following scheme. A virtual particle with an initial weight, is launched into the medium and travels in a stepwise manner. Its weight, position and direction of motion are influenced, and accordingly updated, by the interactions between the particle and the medium, including absorption, scattering, internal reflection and transmission [89]. All these interactions are treated from the perspective of probability theory. This process is repeated for all the particles, and the final light distribution is given by the contributions of all simulated particles. A flowchart depicting the main components of MC simulation is shown in Figure 2.9. The main limitation of MC method is the long computational time due to the large number of particle packages that is needed in order to get an accurate solution. Recently, graphics-processing-unit-accelerated MC simulations, based on the concept of parallel computing, have been

developed, which can reduce the computational time by a factor of $10^3$ [109, 110]. The simulation of light-tissue interactions in MC method will be discussed in the following.

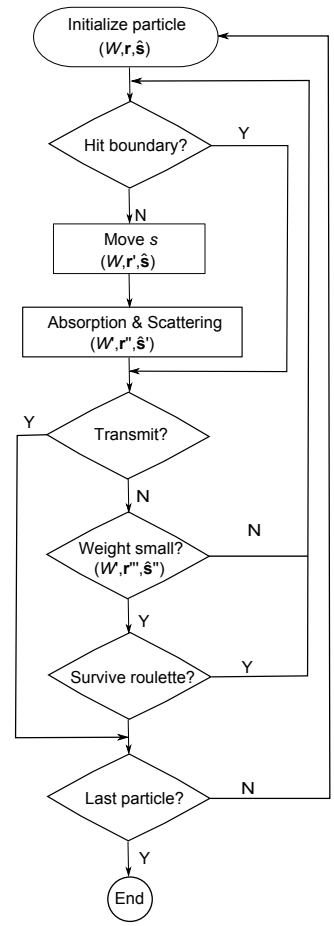


**Figure 2.9.** *Monte Carlo simulation flowchart. $W$, $\mathbf{r}$ and $\hat{\mathbf{s}}$ are the weight, position, and direction of travel of the particle, respectively.*

### 2.4.1 Simulation of light-tissue interactions

#### The simulation of absorption

Absorption is considered to have the effect of reducing the particle weight at each interaction event by an amount [89]:

$$\Delta W = \frac{\mu_\mathrm{a}}{\mu_\mathrm{t}} W, \tag{2.39}$$

where $W$ is the particle's current weight, and $\mu_\mathrm{t}$ is the total interaction coefficient, equal $\mu_\mathrm{a} + \mu_\mathrm{s}$. This fraction of weight will be deposited in the local grid element. The particle with the new weight, i.e., $W - \Delta W$, will undergo scattering.

Photon absorption is also involved in the probability density function in the sampling of the step size, $s$, for particle motion [111], i.e.:

$$\mathrm{p}(s) = \mu_\mathrm{t} \exp(-\mu_\mathrm{t} s), \tag{2.40}$$

originating from the Beer-Lambert law for light propagation.

A pseudo-random number, $\xi$, uniformly distributed over the interval [0, 1] is generated. A non-uniformly distributed variable, $\chi$, can generally be obtained by one-to-one mapping between $\xi$ and $\chi$. The mapping function is defined by the equality of the cumulative probabilities for these two variables:

$$F_\chi(\chi_1) = F_\xi(\xi_1). \tag{2.41}$$

For the step size obeying the probability density function stated in Equation (2.40), it thus can be mapped by:

$$s = -\frac{\ln(1-\xi)}{\mu_\mathrm{t}}, \tag{2.42}$$

which is equivalent with:

$$s = -\frac{\ln(\xi)}{\mu_\mathrm{t}}, \tag{2.43}$$

as $\xi$ is uniformly distributed over [0, 1].

The weight of the particle will decrease step by step, but never reach zero. As a particle with a minuscule weight yields very little information, it must be terminated, but without violating energy conservation. A technique called roulette is used for this. This technique gives a particle whose weight falls below a specified minimum one chance in $m$ of surviving with a weight $mW$, otherwise, it is terminated.

**The simulation of scattering**

Photon scattering exerts an influence on the step size in a similar way to absorption, as described in Equation (2.43). Scattering will also change the direction of the particle's motion. Here, the normalized scattering phase function is reinterpreted as a probability density function. The azimuthal angle is uniformly distributed in $(0, 2\pi]$, and thus sampled by:

$$\phi = 2\pi\xi. \tag{2.44}$$

The Henyey-Greenstein distribution, specified in Equation (2.6), is commonly used to determine the deflection angle. By applying Equation (2.41), the cosine of the deflection angle can be sampled using the uniform random number $\xi$:

$$\cos\theta = \begin{cases} \frac{1}{2g}\left[1+g^2-\left(\frac{1-g^2}{1-g+2g\xi}\right)^2\right], & \text{if g>0} \\ 2\xi - 1, & \text{if g=0} \end{cases} \tag{2.45}$$

**The simulation of reflection and transmission**

When the particle hits the boundary of the medium, internal reflection and transmission occur. The reflection probability is determined by the Fresnel reflection coefficient $R(\theta)$:

$$R(\theta_i) = \frac{1}{2}\left[\frac{\sin^2(\theta_i-\theta_t)}{\sin^2(\theta_i+\theta_t)} + \frac{\tan^2(\theta_i-\theta_t)}{\tan^2(\theta_i+\theta_t)}\right], \tag{2.46}$$

where $\theta_i$ is the incident angle, and $\theta_t$ is the transmission angle, given by Snell's law:

$$n_i \sin\theta_i = n_t \sin\theta_t. \tag{2.47}$$

Here, $n_i$ and $n_t$ are the refractive indices of the medium from which the particle is incident and transmitted. A uniformly distributed random number, $\xi$, is used to decide whether the particle is reflected or transmitted. If $\xi < R(\theta_i)$, the particle is reflected, otherwise, it is transmitted.

### 2.4.2 Time-resolved, fluorescence, and white Monte Carlo simulations

Time-resolved MC simulation can be implemented by recording the step size information for each movement, as the traveling time is related to the step size by the velocity of the particle.

Monte Carlo simulations can be adapted to deal with fluorescence problems. Basically, the propagation of the excitation light is first simulated, and fluorescence photons can then be generated with a certain probability and time delay, followed by the modeling

of fluorescence photon propagation. Such a standard method for fluorescence MC simulations can be accelerated using the reverse emission procedure and convolution technique [112], as in Paper **I**.

In an appropriate geometry, a single MC simulation with zero absorption may be rescaled and attenuated to accommodate any combination of scattering and absorption [109]. Such an approach is referred to as white MC simulation. This method is particularly useful in infinite and semi-infinite media.

Chapter 3

# Upconverting nanoparticles

Exogenous luminescent biomarkers are often introduced to enhance fluorescence imaging and tomography. UCNPs, composed of RE ions doped into an inorganic host material, are an emerging group of biomarkers with excellent spectroscopic and physicochemical properties. In this chapter, the spectroscopic properties of RE ions are first discussed. Then, the upconversion mechanisms, based on the interactions between dopant ions, are introduced. Finally, the material engineering and biomedical applications of UCNPs are reviewed.

## 3.1 Rare-earth luminescence

### 3.1.1 Spectroscopic properties of rare earths in solids

#### Energy level structure

The RE elements include 15 lanthanides together with scandium and yttrium. Scandium and yttrium are considered RE elements since they exhibit similar chemical properties and tend to occur in the same ore deposits as the lanthanides. Trivalent yttrium ions are optically inert due to the lack of 4f electrons, and their compounds are usually used as the host for luminescent materials. Trivalent scandium ions are often used as host ions [113], except in few studies [114]. In the following, RE elements refer mainly to the lanthanides.

The electronic configuration of lanthanides can be described as $1s^2 2s^2 2p^6 3s^2 3p^6 3d^{10} 4s^2 4p^6 4d^{10} \mathbf{4f}^{\boldsymbol{N}} 5s^2 5p^6 \mathbf{5d}^{\boldsymbol{M}} 6s^2$, where $N$ and $M$ are natural numbers, specifying the number of 4f and 5d electrons, respectively, with different values for different lanthanides, as listed in Table 3.1. Trivalent lanthanide ions, formed when the two 6s electrons and one 4f or 5d electron are delocalized (see Ta-

**Table 3.1.** *Electronic configurations of lanthanide atoms and trivalent ions.*

| Element | RE | $RE^{3+}$ |
|---|---|---|
| La | $4f^0 5d^1 6s^2$ | $4f^0$ |
| Ce | $4f^1 5d^1 6s^2$ | $4f^1$ |
| Pr | $4f^3 5d^0 6s^2$ | $4f^2$ |
| Nd | $4f^4 5d^0 6s^2$ | $4f^3$ |
| Pm | $4f^5 5d^0 6s^2$ | $4f^4$ |
| Sm | $4f^6 5d^0 6s^2$ | $4f^5$ |
| Eu | $4f^7 5d^0 6s^2$ | $4f^6$ |
| Gd | $4f^7 5d^1 6s^2$ | $4f^7$ |
| Tb | $4f^9 5d^0 6s^2$ | $4f^8$ |
| Dy | $4f^{10} 5d^0 6s^2$ | $4f^9$ |
| Ho | $4f^{11} 5d^0 6s^2$ | $4f^{10}$ |
| Er | $4f^{12} 5d^0 6s^2$ | $4f^{11}$ |
| Tm | $4f^{13} 5d^0 6s^2$ | $4f^{12}$ |
| Yb | $4f^{14} 5d^0 6s^2$ | $4f^{13}$ |
| Lu | $4f^{14} 5d^1 6s^2$ | $4f^{14}$ |

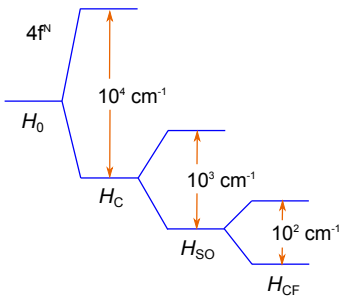


**Figure 3.1.** *A schematic illustration of energy level splitting of $RE^{3+}$ ions in solids.*

ble 3.1), have been extensively used to activate luminescent and photonic materials. The majority of applications involve electronic transitions between states within a $4f^N$ configuration in trivalent RE ions doped in solids.

The electronic energy level structure of trivalent RE ions is established primarily using quantum theory. For free ions, the primary terms of the Hamilton for an $N$-electron system are commonly described by:

$$H = H_0 + H_C + H_{SO}, \tag{3.1}$$

where $H_0$ includes the kinetic energies of electrons and the Coulomb interactions between the nucleus and electrons, $H_C$ represents the inter-electron Coulomb repulsion, and $H_{SO}$ describes the spin-orbit interactions. In calculations of energy levels, the central field approximation and Hartree-Fock method are used to handle the Coulomb interactions [115, 116]. As the Coulomb electrostatic interactions and spin-orbit interactions have the same order of magnitude, the intermediate coupling scheme of momentum summation is involved for trivalent RE ions. Despite this, the symbol $^{2S+1}L_J$ is used to denote the energy states of RE ions, where $L$, $S$, and $J$ denote the total orbital momentum, the total spin momentum, and the total angular momentum, respectively. When doped in solids, the solid-state effects, known as the crystal-field interaction ($H_{CF}$), cause further energy level splitting. In theory, the crystal-field interactions are treated as a perturbation. Figure 3.1 presents schematically the energy levels of $RE^{3+}$ in crystals. Other mechanisms, including ion-ion interactions, hyperfine splitting, and ion-ligand hyperfine splitting, generate energy level splitting on even smaller scales. Electrons in the 4f shell have localized states, exhibiting weak coupling to ligand electrons and lattice vibrations due to shielding by 5s and 5p electrons.

The energy level structure of RE ions is usually called a Dieke chart, and was first created for trivalent ions in a $LaCl_3$ crystal [118], as shown in Figure 3.2. The chart was later extended by Carnall et al. to include ions in $LaF_3$ [119]. Energy levels of $RE^{3+}$ ions can vary by approximately 1% in different matrices [120].

### Transition intensities

In free $RE^{3+}$ ions, electric dipole (ED) transitions between states of 4f configurations are forbidden, as 4f states have definite parity. In a solid, states with different parities are mixed by the crystal field, making the forbidden 4f-4f transitions slightly allowed [121].

Completely reliable *ab initio* calculations of the oscillator strengths for ED transitions of $RE^{3+}$ ions are not possible at present. Instead, a parameterization scheme is used, making use of the concept of effective operators. In practice, an effective dipole

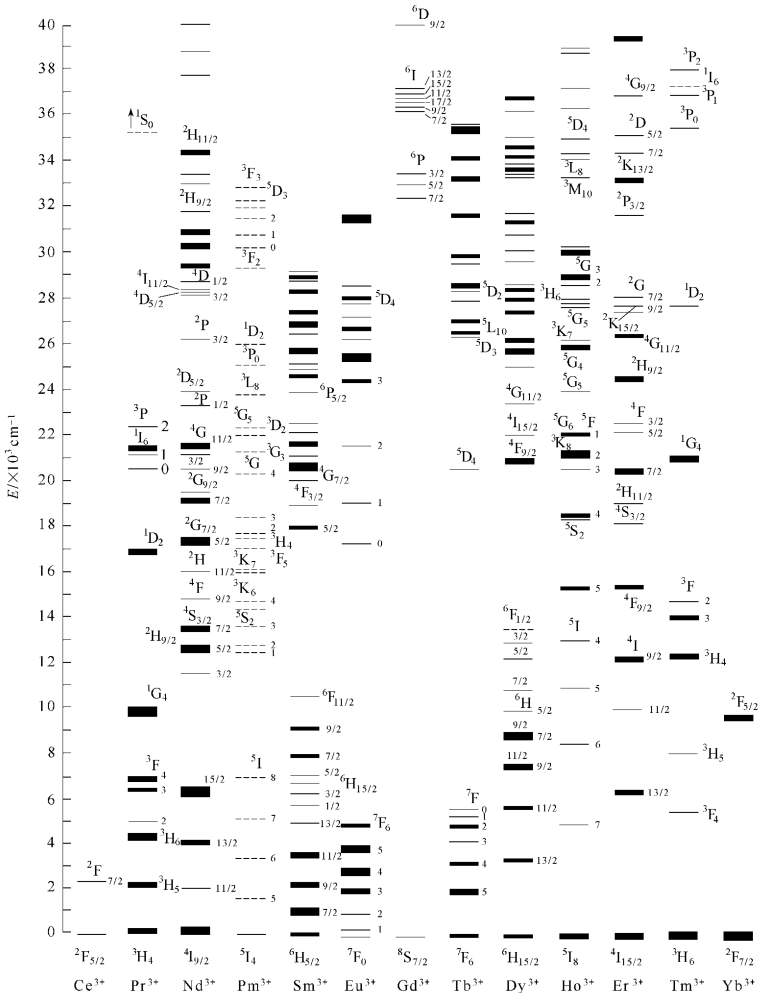


**Figure 3.2.** *The lower 4f levels of trivalent RE ions in a $LaCl_3$ crystal. Reproduced from [117]*

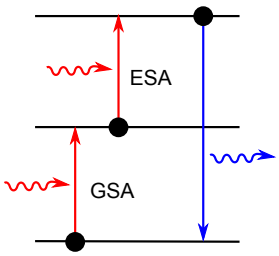


**Figure 3.3.** *Schematic diagram of the excited state absorption (ESA) upconversion process, following ground state absorption (GSA).*

moment operator ($D_{\text{eff}}$), expanded in tensor operator space, is employed in order to connect 4f states, i.e. [122–124]:

$$D_{\text{eff}} = D^{(1)} + D^{(1)} \sum_{\beta \notin M} \frac{|\ \beta >< \beta\ |\ V}{E_0 - E_\beta^{(0)}} + V \sum_{\beta \notin M} \frac{|\ \beta >< \beta\ |}{E_0 - E_\beta^{(0)}} D^{(1)} + \ldots \tag{3.2}$$

Here, $D^{(1)}$ is the ED operator, $|\ \beta >$ are excited states of the RE ions or ligand, and $M$ is the model space. The potential $V$ is the sum of the crystal field, Coulomb interaction and spin-orbit interaction. At first order in $V$, only the odd parity part of the crystal-field potential can connect the 4f configurations of $RE^{3+}$ ions. The parameters in the expansion are determined by fitting with experimental data.

Early work by Judd and Ofelt yielded the Judd-Ofelt theory [125, 126], which has been extensively used in areas such as laser and phosphor design for calculating the total intensities of transitions between $J$-multiplets [127]. The key accomplishment of the Judd-Ofelt theory is that the ED transition strength can be expanded as the sum of three even-ranked tensors, with certain assumptions, and the standard parameters are usually denoted $\Omega_\lambda$ ($\lambda = 2, 4, 6$). However, the Judd-Ofelt theory should be applied with care, as it is based on a poor approximation even for room temperature conditions, i.e., that there is equal occupations of the states of the ground multiplets [128].

The symmetry and strength of the crystal field play an important role in the splitting of ${}^{2S+1}L_J$ levels and radiative decay rates between 4f-levels. The local crystal field around RE ions can be tailored by ion doping, leading to altered transition intensities [129, 130].

### 3.1.2 Upconversion mechanisms

When $RE^{3+}$ ions are incorporated into solids, upconversion emission with anti-Stokes shift can occur in the absence of direct multiphoton processes, through the accumulation of excitation energy. Upconversion is complicated in practice, but several basic mechanisms contribute to upconversion emission, including direct photoexcitation and energy transfer between ions. These will be discussed in the following.

#### Excited state absorption

The first identified upconversion mechanism is excited state absorption (ESA), following ground state absorption, as illustrated in Figure 3.3. In 1959, Bloembergen proposed that infrared photons could be detected and counted through sequential absorption within the levels of a given ion in a solid [131]. This can be re-

garded as the origin of the whole field of upconversion in ion-doped systems. ESA is a weak process.

### Energy transfer upconversion

Energy transfer upconversion (ETU) is a far more efficient upconversion process than ESA, and was first proposed by Auzel [132, 133] and by Ovsyankin et al. [134] independently in 1966. The process is illustrated in Figure 3.4. In a microscopic view, the ETU process is achieved by nonradiative energy transfer between two neighboring ions. Such energy transfer can take place not only between excited- and ground-state ions (e.g., ETU1 in Figure 3.4), but also between excited ions (e.g., ETU2 in Figure 3.4) [132, 133]. In addition, the participating ions are not limited to ions of the same type [132, 134]. The energy transfer process between the same type of ions that results in the population of an intermediate level is known as cross relaxation. In the field of upconversion emission, the energy donor and accepter involved in the ETU process are usually termed the sensitizer and activator, respectively.

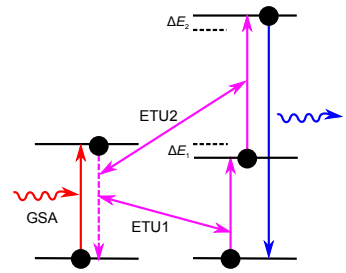


**Figure 3.4.** *Schematic diagram of the energy transfer upconversion process. $\Delta E_{1,2}$ denote the energy mismatches. GSA–ground state absorption.*

The mutual interactions between the two ions are Coulomb interactions of the van der Waals type. Förster first treated such interactions theoretically using quantum mechanical theory, considering the dipole-dipole interaction [135]. Later, this theory was extended by Dexter to include higher multipole and exchange interactions [136]. Generally, the probability of energy transfer for electric multipolar interactions can be expressed as [136, 137]:

$$p_{\mathrm{SA}} = \frac{1}{\tau_{\mathrm{s}}} \left( \frac{R_0}{R} \right)^s , \tag{3.3}$$

where $\tau_{\mathrm{s}}$ [s] is the actual lifetime of the excited state of the sensitizer including the contribution of multiphonon radiative decay, $R$ [m] is the distance between the two ions, while $R_0$ [m] is the critical transfer distance for which energy transfer and spontaneous deactivation of the sensitizer have equal probability, and $s$ is a positive integer associated with the index of the multipolar interaction, with $s = 6$ for dipole-dipole interactions, $s = 8$ for dipole-quadrupole interactions, and $s = 10$ for quadrupole-quadrupole interactions. However, this form of power law is less applicable when calculating the energy transfer probability, because the critical distance cannot be easily obtained theoretically. Another calculation technique was developed by Kushida [138] for multipolar interactions, applying Racah's tensorial methods. Pouradier and Auzel treated magnetostatic and exchange interactions in a similar fashion [139].

In many cases, the ETU process is non-resonant, as illustrated in Figure 3.4, where phonons play a critical role to account for the energy mismatches. Actually, energy transfer with energy mismatch as high as several thousand inverse centimeters can take

place, with the assistance of multi-phonons [140, 141]. Unawareness of this once led to the misinterpretation of upconversion emission from a $Yb^{3+}/Tm^{3+}$ pair as being due to cooperative sensitization [142]. The phonon-assisted energy transfer probability depends exponentially on the energy mismatch $\Delta E$ [143]:

$$p_{\text{phonon}}(\Delta E) = p_{\text{phonon}}(0)\exp(-\beta\Delta E), \tag{3.4}$$

where $p_{\text{phonon}}(0)$ is the energy transfer probability when the zero phonon lines overlap, and $\beta$ is a constant determined by the characteristics of the host lattice and the electron-phonon interaction.

A tremendous number of ions are assembled in a macroscopic system, even in a very local region. In such cases, the energy transfer between ions is very complicated. Basically, three types of energy transfer can occur: sensitizer-sensitizer, activator-activator, and sensitizer-activator transfer. The first two represent excitation migration or energy diffusion through the crystal. In order to obtain an association with experimental data acquired from real macroscopic samples, a statistical analysis of the energy transfer between many ions is needed, taking into account all three types of energy transfer. Average transfer probabilities can be calculated using certain assumptions regarding the concentrations of the doping ions and their spatial distributions [136, 137, 144, 145]. Excitation migration could be a limiting step, or not, depending on the sensitizer concentration, leading to different decay behavior of the luminescence [145]. The case of high sensitizer concentration, when the migration rate is faster than spontaneous sensitizer decay or sensitizer-activator energy transfer, is called the fast migration case. In such a case, the energy transfer probability is proportional to the activator concentration, but not depending on the sensitizer concentration [145]. Otherwise, the probability is also dependent on the sensitizer concentration. Rate equations dealing with the populations of ions in given states can also be used for the macroscopic system, especially in the fast migration case [19]. The validity of this has been discussed from first principles by Grant [146].

Excitation migration is of essential importance in upconversion emission, as it allows energy transfer over a long distance in a stepwise manner. This makes the pumping of activators possible, even if they are located far away from the sensitizer ions excited directly by photons. Such a feature opens up the possibility of designing new efficient upconverting nanomaterials with core-shell structure, in which the sensitizers and activators are isolated in different layers to suppress concentration quenching[1] [147–149].

[1] High doping levels of dopant ions lead to deleterious energy transfer among activator ions or back energy transfer from activator ions to sensitizer ions, resulting in quenching of upconversion emission.

### Cooperative upconversion

Another upconversion mechanism consists of cooperative processes, including cooperative sensitization (Figure 3.5) [150, 151] and cooperative luminescence (Figure 3.6) [152], which are about 3-5 orders of magnitude less effective than ETU [19]. The cooperative processes involve cooperative pair states, and are thus likely to take place within clusters, and must only be considered practically when ETU cannot take place [143]. Examples of such cases are when the real single-ion levels allowing energy transfer do not exist, and when the concentration is too low to allow efficient transfer. Apart from the detection of RE ion clusters [153], very few applications of cooperative processes exist.

The synergistic effect of all the upconversion mechanisms discussed above and the basic ground state absorption process can lead to complex upconversion phenomena, such as the photon avalanche effect [154–158] and the looping upconversion processes [159, 160].

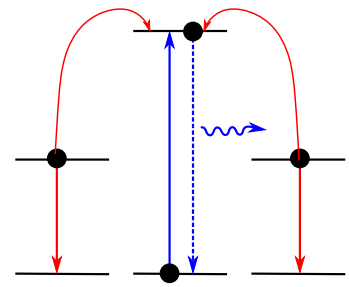

**Figure 3.5.** *Schematic diagram of cooperative sensitization.*

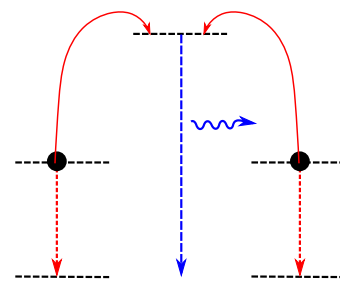

**Figure 3.6.** *Schematic diagram of cooperative luminescence.*

## 3.1.3 Efficient upconversion systems

An upconversion system generally consists of three components: an inorganic host, sensitizer ions and activator ions. These must be carefully chosen in order to achieve efficient upconversion emission. Among the numerous applications of upconverting materials, such as in display [161] and upconversion lasers [157], this thesis focuses mainly on UCNPs for biomedical applications. The selection of the components of the upconversion systems discussed below is primarily based on this purpose.

### Host materials

The host material is required to have good lattice matching with the dopant ions. Inorganic compounds containing $RE^{3+}$, alkaline earth and some transition metal ions (e.g., $Zr^{4+}$, $Ti^{4+}$ and $Mn^{2+}$) are thus suitable host candidates. The cations of the host materials are generally chosen so as to be optically inert in the spectral range of interest, in order to suppress luminescence due to the host ions. $Sc^{3+}$, $Y^{3+}$, $Gd^{3+}$, $La^{3+}$ and $Lu^{3+}$ are commonly used as host ions, but not other $RE^{3+}$ ions.

As discussed in Subsection 3.1.1, the crystal field of the host lattice has an important influence on the optical properties of a given ion, as it determines the spectral positions and splitting of certain optical transitions. In addition, the uneven components of the crystal field, present when a RE ion occupies a crystallographic site without inversion symmetry, are able to relax the parity selection rule by mixing a small amount of opposite-parity wave functions into the 4f wave functions [162]. Thus, a host lattice with low symmetry is usually preferable [163]. Although

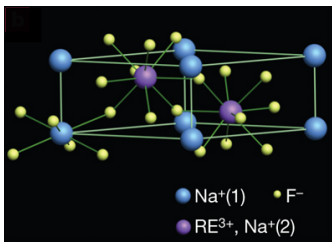


**Figure 3.7.** *Schematic presentation of hexagonal phase $NaYF_4$. Reproduced from [182].*

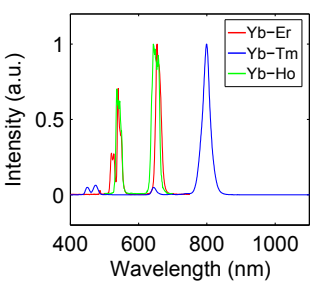


**Figure 3.8.** *Typical photoluminescence spectra of different sensitizer-activator pairs. The spectra are normalized to the maximum.*

phonon assistance is needed in ETU, ideal host materials should have low lattice phonon energies in order to minimize nonradiative energy loss and ensure long lifetimes of the intermediate states [164]. Other considerations for host materials include chemical stability, the interionic distance between the sensitizer and activator in the host lattice, and the bio-compatibility of the materials.

Fluorides, having low phonon energies ($\sim$350 $cm^{-1}$) and high chemical stability, are widely used as the host materials for UCNPs. In particular, hexagonal-$NaYF_4$-based UCNPs shown in Figure 3.7 have been found to be among the most efficient [165, 166], and have been investigated and applied extensively in various biomedical applications [22, 23, 167, 168]. However, recent studies have shown that better candidates exist. $CaF_2$ has been proposed to be a better host material than $NaYF_4$ [169], as the $CaF_2$ lattice promotes the formation of ion clusters when doped with lanthanide ions, facilitating ETU due to an effective reduction in the interionic distance [170, 171]. In addition, $CaF_2$ is more biocompatible, as calcium is a common endogenous component and a lattice substituent of calcified tissues [172, 173]. $NaLuF_4$-based UCNPs have also been found to exhibit higher luminescence intensity than their Y-based counterparts [174–179]. Several explanations have been proposed. The ionic radius of $Lu^{3+}$ (0.85 Å) is much closer to that of $Yb^{3+}$ (0.86 Å) than $Y^{3+}$ (0.89 Å), and the $Lu^{3+}$-based host is thus expected to be more stable when doped with a high concentration of $Yb^{3+}$ ions [180]. The valence band could also play a role by relaxing the parity selection rule by mixing the 4f state with the 5d states [181]. In addition, the lifetimes of the energy levels of the activator ions have been found to be prolonged, indicating the suppression of nonradiative processes [175] .

### Sensitizer-activator combination

In singly doped nanoparticles, two parameters effecting the upconversion processes must be balanced, i.e., the activator ion concentration and the inter-ion distance. Although high doping levels can facilitate the absorption of pump energy, this would lead to deleterious cross relaxation due to the decreased distance between the ions, eventually resulting in upconversion emission quenching.

The choice of a sensitizer-activator pair is based on efficient energy transfer between them. As stated by Auzel [19], “As is often in science, the most efficient systems are the ones discovered at first, here the Yb-Er and the Yb-Tm systems.” The Yb-Ho pair has also been found to be efficient, but has been less extensively investigated, probably due to emission band overlap with the Yb-Er pair. The emission bands of these upconversion systems are shown in Figure 3.8. Good sensitizer-activator pairs such as these have the following characteristics.

(i) The sensitizer ions have a simple energy level structure, matching commercially available and cost-effective laser sources. For instance, $Yb^{3+}$ ions have a simple two-level structure that matches laser sources of around 980 nm.

(ii) The sensitizer ions have relatively long-lived excited levels.

(iii) The sensitizer ions have a large absorption cross-section. The absorption cross-section of $Yb^{3+}$ ions at 975 nm is on the order of $10^{-20}$ $cm^2$, which is significantly larger than those of other RE ions at the same wavelength.

(iv) The activator ions have a ladder-like energy level structure with long-lived intermediate energy states, and the energy gaps match those of the sensitizer ions well.

(v) The activator ions have luminescence channels that fulfill the demands of specific applications, e.g., the 800 nm emission of $Tm^{3+}$ ions for biomedical imaging in deep tissues.

In such codoped materials, the concentration of the activator is relatively low, usually less than 2 mol%, while that of the sensitizer is often high, e.g., ∼20 mol% for $Yb^{3+}$ ions in fluoride nanoparticles.

Interactions between different types of ions can be introduced in order to tune the excitation and emission pathways. Typically, different activator ions are incorporated into the same nanoparticles to achieve multicolor emission bands, aiming at multiplexing encoding in optical imaging [183], or white light generation in displays [184]. $Ce^{3+}$ ions can be introduced into the Yb-Ho system to adjust the upconversion emission from green to red [185], and tri-doping of $Nd^{3+}$ ions in the Yb-Tm system can significantly enhance the blue upconversion emission band of $Tm^{3+}$ ions [186].

## 3.2 Material engineering of upconverting nanoparticles

During the past decade, considerable effort has been devoted to material engineering of UCNPs, in order to address the issues of size and morphology, efficiency, and the bioapplicability of UCNPs, of interest for biomedical applications. Tremendous progress has been made.

### 3.2.1 Size and morphology control

Size and morphology are two major concerns when using nanoparticles as exogenous contrast agents in living organisms [187, 188]. Different sizes are required, depending on the applications. In order to trace biological activity on the subcellular level, particles are generally required in the range of 4-10 nm, comparable to most

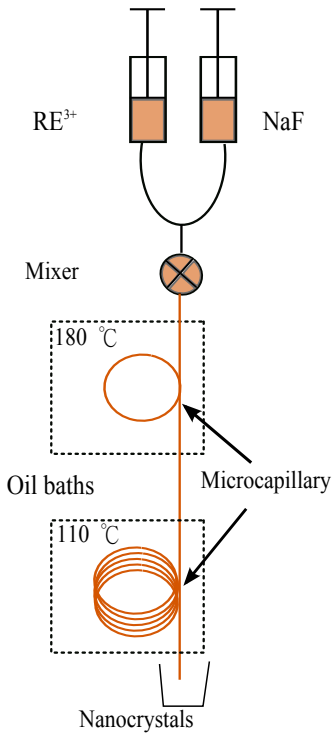


**Figure 3.9.** *Schematic description of the microfluidic synthesis of upconverting nanoparticles.*

membrane and globular proteins [189]. The morphology (or shape) of nanoparticles is also of importance due to its effect on cellular intake and metabolism [190–192]. Nanoparticles must often be monodispersible for successful biomedical applications. In addition, the hexagonal phase is preferred for $NaREF_4$-based UCNPs, as these provide about one order of magnitude higher emission efficiency than their cubic counterparts [165, 166, 193]. All these issues can be addressed by using appropriate synthesis methods.

Many synthesis methods have been developed over the past decade for the fabrication of high-quality $NaREF_4$ UCNPs, with the desired size and size distribution, as well as monodispersity [194–196]. Two routes are the most widely used: the trifluoroacetate route [197, 198] and the oleate route [199]. Fluoride UCNPs ranging from sub-10 nm to a few hundred nanometers can now be produced [175, 200, 201]. Different shapes, e.g., nanopolyhedra, nanorods, nanoplates, and nanospheres, can also be achieved by tuning reaction parameters such as the Na/RE ratio, the solvent composition, and the reaction temperature and time [197].

Generally, the synthesis of UCNPs, from the preparation of reaction precursors to the final nanoparticles, is very time consuming [202]. This is a considerable problem, especially when optimizing reaction parameters. Parallel synthesis has been employed, providing rapid screening for optimization of synthesis parameters [203]. Methods employing other types of heat sources, such as microwave synthesis [204], which enables rapid energy transfer, are promising to significantly shorten the reaction time.

Microfluidic synthesis (Figure 3.9), presented in Paper **II**, offers new possibilities including real-time reaction monitoring and scale-up *via* continuous synthesis.

### 3.2.2 Luminescence enhancement

UCNPs suffer from low emission efficiency, which is a major barrier to their practical applications in biomedical areas. A great deal of effort has been devoted to enhancing the upconversion emission. Considering a single UCNP, the emitted power of upconversion emission, $P_{\mathrm{em}}$ [W], can be expressed by the following equation:

$$P_{\mathrm{em}} = \alpha N_{\mathrm{s}} V \sigma_{\mathrm{abs}} I_{\mathrm{ex}} \eta, \tag{3.5}$$

where $N_{\mathrm{s}}$ [$\mathrm{cm}^{-3}$] is the concentration of sensitizer ions, $V$ [$\mathrm{cm}^3$] is the volume of the nanoparticle, $\sigma_{\mathrm{abs}}$ [$\mathrm{cm}^2$] is the absorption cross-section of the sensitizer ion at the excitation wavelength, $I_{\mathrm{ex}}$ [$\mathrm{Wcm}^{-2}$] is the excitation intensity, $\eta$ [-] is the quantum yield, and $\alpha$ [-] is a constant compensating for the energy difference between the excitation photon and emission photon, i.e., $\alpha = \nu_{\mathrm{em}}/\nu_{\mathrm{ex}}$, where $\nu_{\mathrm{em,ex}}$ [$\mathrm{s}^{-1}$] denote the frequency of the emission and excitation photon, respectively. Many emission enhancement proce-

dures have been developed by manipulating relevant parameters, as described below.

### Manipulating the light absorption

Although the intrinsic absorption cross-section of the sensitizer ion, $\sigma_{\text{abs}}$, is expected to be constant for a specific host material, the absorption of the excitation light can be increased by attaching optical antennas, such as dye molecules with large absorption cross-section, taking advantage of the subsequent efficient energy transfer between the antennas and the nanoparticles [205]. Broadband excitation of upconversion emission can be achieved simultaneously.

Increasing the doping level of sensitizer ions will increase the absorption of excitation light, which will lead to enhanced upconversion emission [206, 207]. On the other hand, it will also influence the quantum efficiency of the upconversion system by affecting the energy transfer between the dopant ions. For instance, too high a sensitizer concentration has been reported to result in upconversion emission quenching in some systems [208]. It should be noted that a large amount of sensitizer ions can be incorporated into a shielding layer to increase the absorption efficiency of the excitation energy while suppress emission quenching, caused by high concentration of sensitizer ions [209–211].

### Manipulating the excitation intensity

The excitation intensity can be increased by increasing the pump power. For the conventional CW excitation of UCNPs, this is trivial, but is generally restricted especially in *in vivo* studies due to laser safety concerns. Pulsed excitation, as proposed in Paper **V**, was found to be optimal in this case, as a higher intrinsic quantum yield of upconversion emission could be employed due to the high peak power, while the thermal effect of the excitation light is suppressed. The advantages of pulsed excitation will be discussed in detail in Chapter 4. Another approach to increase the excitation level is through the use of the surface plasmonic effect of noble metal nanostructures to enhance the local excitation intensity at the UCNPs [30, 212–219]. This technique is unfortunately very demanding, because many parameters must be precisely controlled, such as the geometry and the distance between the upconverting nanomaterials and the metal nanostructure, otherwise, upconversion emission quenching could dominate [212]. This topic is discussed in more detail in Paper **III**.

### Manipulating the intrinsic quantum yield

The quantum yield of an upconversion emission band is the result of the synergic effect of multiple factors involved in the upcon-

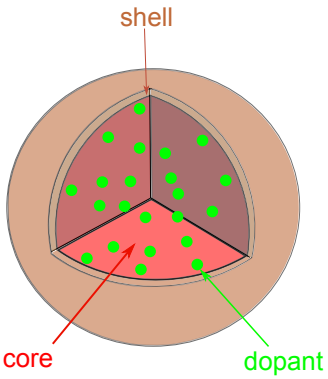


**Figure 3.10.** *Schematic description of the core-shell structure.*

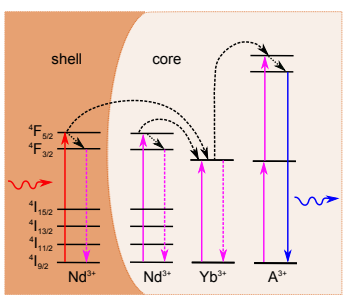


**Figure 3.11.** *Energy transfer mechanisms of $Nd^{3+}$-$Yb^{3+}$ cosensitized upconversion emission in a core-shell structured UCNP under 800* nm *excitation.*

version process, such as the host lattice, doping level and energy dissipation on the nanoparticle surface, as well as the excitation intensity. Several approaches for upconversion emission enhancement have been developed by considering these factors. Typical methods include the use of ion doping, e.g., lanthanide and transition ions, to promote the formation of the hexagonal phase of $NaREF_4$ nanoparticles [182, 220, 221], and alkali ions to adjust the local environment of dopant ions [129, 130, 222, 223]. Another important concept for the enhancement of upconversion emission is the adoption of a core-shell structure (Figure 3.10). A shielding layer on the surface of the UCNPs can reduce crystal defects and protect the optically active ions from coupling with the vibrational modes of, for example, -OH or $-NH_2$ groups in the solvent, thereby reducing the nonradiative energy losses [224, 225]. The shell can be either inert or active [172, 209, 210, 226, 227]. In addition, the concentration quenching threshold of upconversion emission can be also exceeded *via* spatial separation of dopant ions [147, 228–230].

### 3.2.3 Excitation and emission wavelength optimization

When designing new UCNPs for biomedical applications, the optical properties of tissues discussed in Chapter 2 are of major importance. Ideal UCNPs for such applications should have excitation and emission bands located in the tissue optical window, in order to achieve maximum penetration depth. Strictly speaking, the 975 nm excited UCNPs are less optimal, because the excitation wavelength overlaps an absorption peak of water (as shown in Figure 2.3), which constitutes a major part of most tissues. Zhan et al. suggested the use of 915 nm excitation [231]. The problem of overheating can be partly alleviated, but this wavelength is associated with decreased emission efficiency.

The energy transfer properties between $RE^{3+}$ ions provide opportunities for tuning the luminescence pathway. A novel upconversion emission pathway was recently achieved by cascade sensitization through introducing $Nd^{3+}$ ions as co-sensitizers [232], where ∼800 nm light was used as excitation. Bright upconversion emission with efficiency comparable to that under 975 nm excitation can be obtained by using a core-shell structure with $Nd^{3+}$ ions in the shell and the emitting ions in the core [148, 149], as illustrated in Figure 3.11. Compared with the most promising upconversion system for biological applications discovered previously, i.e., $Yb^{3+}/Tm^{3+}$-codoped fluoride nanoparticles with excitation and emission wavelengths of 975 nm and 800 nm, respectively [21], the major emission bands (green and red) of such new types of nanoparticles are less optimal. However, the optimization of the excitation wavelength will still provide significant signal gain,

in particular when UCNPs are used in deep tissues, due to the nonlinearity of upconversion emission.

The emission wavelength from the same activator ions can also be tuned by introducing other ions into the upconversion system [185, 233], or by adjusting the doping concentrations [183, 234]. Optimization of the emission wavelength to the near-infrared (NIR) range will remain a subject of interest in the future.

### 3.2.4 Biocompatibility

As with other exogenous nanosized biomarkers, UCNPs must also be biocompatible, and in some applications they are required to target cells or molecules. The techniques involved are mainly hydrophilic processes and surface functionalization, as discussed below.

#### Hydrophilic processing

The need for hydrophilic processing for UCNPs arises from the need to use hydrophobic surfactant (e.g., oleic acid) in nanoparticle production. Although several one-pot synthesis methods have been developed for fabricating hydrophilic UCNPs [235–239], it is still difficult to obtain UCNPs with a quality as high as those synthesized using oil-phase methods. A multitude of strategies are available for achieving water dispersibility, including ligand exchange [198, 231, 240–243], ligand oxidation [240, 244, 245], ligand attraction [246], surface silanization [247–250] and cross-linked polymer coating [251]. This topic is reviewed in Paper **III**, and other recent reviews [23, 163].

#### Surface functionalization

After hydrophilic processing, further treatment is necessary in order to make the UCNPs capable of interacting with the proteins and molecules involved in cellular and organ functions. The functional groups (e.g., carboxyl, amino, and thiol) or the strongly charged surface obtained after hydrophilic processing provide the basis for conjugation with various biological or polymeric molecules. Several well-developed bio-conjugation methods with biomolecules (e.g., folic acid, peptide, protein, and DNA) exist, which can allow UCNPs targeting specific cell lines to be made [23, 238, 238, 244, 252–258]. Such methods mainly make use of physical electrostatic adsorption or chemical covalent binding.

### 3.2.5 Multi-functionalization

Molecular imaging based on luminescent contrast agents has high sensitivity, but is often associated with poor spatial resolution due to the high scattering of biological tissues. Thus, it is generally

beneficial to combine the optical imaging modality with other bioimaging modalities that have higher spatial resolution but lower sensitivity, such as X-ray computed tomography (CT) and magnetic resonance imaging (MRI). In many cases, it is thus favorable to have a contrast agent that can be used for multiple modalities [259]. For UCNP-based imaging, multimodality imaging can be enabled by modifying the chemical composition of the nanoparticles. The high atomic number of the RE elements can lead to effective attenuation of X-rays. Thus, the use of UCNPs for X-ray CT imaging has recently been proposed [260–263]. Ytterbium (Yb) and lutetium (Lu) have received most attention due to their high atomic numbers. The UCNPs can be modified to provide contrast in MRI by incorporating $Gd^{3+}$ ions or a $Gd^{3+}$ complex into the crystal host or in a core-shell structure [264–266]. Another approach for achieving MRI contrast is through the use of iron oxide nanomaterials [255, 267–270].

Doping or coating UCNPs with radioisotopes or agents can endow them with radioactivity contrast for nuclear imaging, e.g., positron emission tomography [271–274] and single-photon emission computed tomography [179, 275, 276]. Nuclear imaging has a sensitivity comparable to that of fluorescence molecular imaging. However, nuclear imaging and fluorescence imaging can still provide independent and complementary information, as the data acquisition for these two modalities has a different time window.

## 3.3 Biomedical applications

In recent years, UCNPs have been extensively used in diverse biomedical areas, as well as other areas, due to their properties of being autofluorescence-free (Paper **VI**, [277, 278]) and photostable [266], and having large anti-Stokes shifts [19], narrow emission bands, non-blinking behavior [279], deep detection ability and high spatial resolution [24]. Areas of application include cell microscopy and optical thermometry [280], small animal imaging [281], FDOT [282], bioassays [283] and photoactivation of biomolecules in deep tissues [284–286]. Other areas of application include photovoltaics [287–291] and photocatalysis [292–295]. The toxicity of nanomaterials is of considerable concern in biomedical applications, and, therefore, results on the toxicity of UCNPs are summarized below.

### 3.3.1 Toxicity assessment

The possible toxicity of nanosized materials must be thoroughly investigated before they can be used in biomedical applications. The toxic effects of nanomaterials are due to their physicochemical properties, including size [296], shape [297], surface charge [243, 298], surface modification [299], chemical composition [300],

metal impurities [301], agglomeration and dispersion [302], degradation [303], and the formation of a "protein corona"[2] [304, 305]. The toxicity of UCNPs has been less systematically investigated than that of quantum dots and metal nanomaterials, due to their relatively short history of existence. This topic has, however, attracted great interest.

The *in vitro* cytotoxicity of UCNPs with different surface modifications has been investigated in many studies, on a large number of both human and animal cell lines [20, 238, 253, 272, 306, 307]. It was found that the cytotoxicity was very low, generally with cell viability remaining above 80%, provided the nanoparticle concentration was kept below 100 $\mu$g/ml [248].

Studies on the long-term effects of UCNPs on small animals have recently started to appear. Zhang's group investigated the biodistribution and clearance of polyethyleneimine-coated $NaYF_4$:Yb,Er nanoparticles in female Wistar rats following an intravenous injection [20]. They found that the nanoparticles were accumulated in the lungs immediately after injection, but the amount of nanoparticles was significantly reduced in all tissues 24 h post-injection; the highest concentration being found in the spleen. After 7 days, the nanoparticles were undetectable in the rats. This group also studied the biocompatibility of silica-coated $NaYF_4$:Yb,Er nanoparticles using the same rat model, and found accumulation in the lungs and the heart [248], and that clearance time was significantly less than 7 days. The study by Li's group on polyacrylic-acid-coated $NaYF_4$:Yb,Tm nanoparticles in athymic nude mice showed the UCNPs to be mainly accumulated in the spleen and liver, with a clearance time longer than 7 days [308]. The same group recently studied the time-dependent biodistribution of poly(ethylene glycol)-coated $NaYF_4$:Yb,Er labeled with a radioisotope ($^{153}$Sm) using single-photon emission computed tomography imaging and $\gamma$-counter analysis [309], and found that they had a long retention time in the blood, and were partly eliminated through urinary excretion *in vivo*.

In addition to small animal studies, the toxicity of UCNPs has also been assessed in other models. Yan's group recently investigated the toxicity of polyethyleneimine-coated $NaYF_4$:Yb,Tm nanoparticles in the roundworm Caenorhabditis elegans [310], and found that feeding them 100 $\mu$g UCNPs had no obvious toxic effect based on observations on the growth and procreation. In a study by Wang et al., on zebrafish embryos, they reported that concentrations of silica-coated $LaF_3$:Yb,Er nanoparticles under 100 $\mu$g/ml had no obvious toxic effects, but concentrations above 200 $\mu$g/ml led to chronic toxicity, which resulted in delayed hatching and embryonic and larval development, and malformation [311].

[2] A corona formed by adsorbed proteins surrounding a nanoparticle in physiological environment.

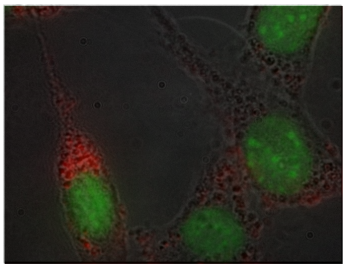

**Figure 3.12.** In vitro *microscopy imaging of mouse stem cells incubated in a suspension containing $NaYF_4$:Yb,Tm UCNPs and stained with fluorescent dyes. Red and green are the luminescence from the UCNPs and dyes, respectively. The figure is pseudo-color encoded.*

### 3.3.2 Promising applications

Numerous applications of UCNPs have been proposed during the past few years, of which the most successful and promising are microscopy, bioassays, deep tissue imaging (including UCNP-based multimodality imaging), and photoactivation of biomolecules.

#### Microscopy, bioassays and deep tissue imaging

*In vitro* microscopic imaging of cells using UCNPs (Figure 3.12) has been extensively demonstrated. The imaging may be non-specific [21, 243, 312, 313] or specific [238, 253, 314–316], depending on the surface modification and functionalization of the nanoparticles. However, the long lifetime of upconversion emission appears to be a limiting factor for laser scanning microscopy, as this imposes restrictions on the scanning speed and real-time monitoring [317].

The autofluorescence-free property of UCNPs and their relatively narrow emission bands and large anti-Stokes shifts suggest that these particles will exhibit unique advantages in the field of bioanalytical chemistry, in bioassays based on Förster resonance energy transfer [254, 283, 318–322], or other types of bioassays [323–326]. Various assays, including immunoassays [258, 318, 327], enzyme activity assays [320], and protein and DNA hybridization assays [321, 328–331], have already been successfully performed using UCNP-based techniques.

Deep tissue imaging is another potentially important application for UCNPs, thanks to the large penetration depths for both the excitation and emission wavelengths. This will be discussed further in Chapter 5.

Further details on the above applications can be found in Paper **III**, which presents a review of the use of UCNPs for preclinical diffuse optical imaging, microscopy and sensing.

#### Photoactivation

The controlled activation or release of biomolecules is of essential importance in many biological applications. Controlling the activity of biomolecules by light has attracted increasing interest in recent years. As light can be readily tuned, both temporally and spatially, photoactivation of biomolecules can provide on-demand drug delivery. One major drawback of this process is that photoresponsive compounds mostly respond to UV or visible radiation, which has small penetration depths in biological tissue and induce undesirable photochemical reactions. The photon upconversion ability of UCNPs makes them excellent nanotransducers, which can absorb NIR light and emit UV light locally that is needed for the photoactivation of biomolecules.

In 2008, Zhou et al. demonstrated an upconversion luminescence switch using intermolecular energy transfer, employing a diarylethene derivative and $LaF_3$:Yb,Ho nanoparticles loaded in a poly(methyl methacrylate) film [332]. Since then, UCNP-based photoactivation has gained a considerable amount of interest. The group led by Branda achieved reversible ring-closing and ring-opening reactions of dithienylethene photoswitches using NIR light together with $NaYF_4$:Yb,Tm and $NaYF_4$:Yb,Er nanoparticles [285, 333, 334], as well as NIR-light-triggered release of a carboxylic acid from "caged" compounds[3] [286]. Zhao's group reported NIR-triggered release of caged nitric oxide using UCNPs, facilitating the therapeutic delivery of nitric oxide to physiological targets [335]. Zhang's group recently demonstrated the photorelease of small interfering RNA and plasmid DNA from caged compounds in tissue phantoms with thicknesses up to 4 mm [284]. Xing's group also reported the controlled photorelease of small interfering RNA [336], and a system for the controlled uncaging of D-luciferin and bioluminescence imaging based on D-luciferin-conjugated UCNPs [337]. Other interesting progress in this field can be found in recent publications [338–342].

It is worth mentioning that the low quantum yield of UCNPs is still a major limiting factor for applications such as these, especially when used in deep tissue, where the excitation fluence rate is low. The use of such photoactivation systems in deep tissues could be greatly facilitated by the adoption of pulsed excitation, which will be discussed in detail in Chapter 4.

[3] Caged compounds are light-sensitive probes that functionally encapsulate biomolecules in an inactive form.

Chapter 4

# Quantum yield characterization and excitation scheme optimization for upconverting nanoparticles

The quantum yield (QY) of UCNPs is a critical parameter for their use in biomedical applications. The QY of UCNPs is dependent on the excitation intensity in a complex manner. This is due to the nonlinear nature of upconversion emission achieved by sequential energy transfer between sensitizer and activator ions, as well as due to the saturation of intermediate energy levels involved in the upconversion processes. With advances in material engineering of UCNPs, the saturation of upconversion emissions can occur even at the moderate excitation intensities required in biological applications. Thus, characterization of the QY of UCNPs for the entire excitation intensity regime is of essential importance for the optimal use of UCNPs. This chapter deals with the QY characterization of UCNPs. In addition, excitation scheme optimization for UCNPs is explored, based on the investigation of the nonlinearity of UCNPs with the property of gradual saturation.

## 4.1 Quantum yield characterization

The characterization of the QY of UCNPs, accounting for the excitation power density dependence, is of paramount importance, both for materials development and practical applications. There is currently no standard for characterizing and presenting the luminescence efficiency of UCNPs. Each group uses their own local references, and compares the relative brightness of different sam-

ples. Although the QY has been measured in some studies, these measurements were mostly performed at a specific excitation intensity [172, 175, 193, 200], usually in the saturating excitation intensity range. The lack of a standard characterization method of the QY makes it difficult to compare the luminescence efficiency of UCNPs from different labs. For biomedical applications, especially in clinical studies, the dose of biomarkers is an important parameter that must be carefully controlled in order to guarantee good signal quality while avoiding overuse. The lack of QY data at different fluence rates, as would be the case at various depths in biological tissues, makes it impossible to estimate the correct dose.

### 4.1.1 Definition of the quantum yield

The QY is usually defined in percent, as the ratio between the number of emitted photons ($N_{\mathrm{em}}$ [-]) and the number of absorbed photons ($N_{\mathrm{abs}}$ [-]):

$$\eta = \frac{N_{\mathrm{em}}}{N_{\mathrm{abs}}} = \frac{k_0 I_{\mathrm{em}}}{I_{\mathrm{ex}}}, \tag{4.1}$$

where $k_0$ [-] is a scaling factor, accounting for the photon energies at the two wavelengths involved, $I_{\mathrm{em}}$ [$\mathrm{Wcm^{-2}}$] is the emission intensity, and $I_{\mathrm{ex}}$ [$\mathrm{Wcm^{-2}}$] is the excitation intensity. A normalized efficiency ($\eta_{\mathrm{norm}}$) is often used to characterize an n-photon upconversion process, e.g., second-harmonic generation and multiphoton fluorescence [19]:

$$\eta_{\mathrm{norm}} = \frac{I_{\mathrm{em}}}{I_{\mathrm{ex}}^{\mathrm{n}}}, \tag{4.2}$$

which has the dimensions of $[\mathrm{cm^2W^{-1}}]^{\mathrm{n}-1}$. However, for upconversion emission based on ETU, the n-power law for the luminescence intensity can become degraded even at moderate excitation intensities.

In a non-saturating excitation regime, the power density dependence of the emission intensity of an n-photon upconversion band can be expressed by:

$$I_{\mathrm{em}} = k_1 I_{\mathrm{ex}}^{\mathrm{n}}, \tag{4.3}$$

where $k_1$ $[\mathrm{cm^2W^{-1}}]^{\mathrm{n}-1}$ is a scaling factor, yielding a slope of n on a double-logarithmic scale. Such power density dependence analysis is widely used to investigate the number of excitation photons needed to generate one emission photon. Nevertheless, as systematically considered by Pollnau et al. [343] and Suyver et al. [344], saturation can occur with increasing excitation power density, which would in turn lead to a decrease in the slope for the same upconversion emission band. This trend can be clearly

seen, for example, in the 800 nm upconversion emission band of core-shell $NaYF_4$:$Yb^{3+}$/$Tm^{3+}$@$NaYF_4$ UCNPs, as illustrated in Figure 4.1. Thus, the normalized efficiency, $\eta_{\text{norm}}$, will not be valid over the entire excitation intensity range of interest. The QY defined in percent in Equation (4.1) is used in this thesis.

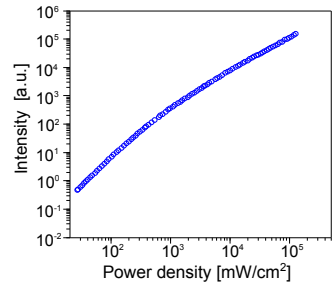


**Figure 4.1.** *The power density dependence of the 800* nm *upconversion emission band of core-shell* $NaYF_4$:$Yb^{3+}$/$Tm^{3+}$@$NaYF_4$ *UCNPs.*

### 4.1.2 Power-density dependence of the quantum yield

Due to the nonlinear dependence of the upconversion emission intensity on the excitation power density, the QY defined in percent will be dependent on the power density, rather than constant [25]. In addition, the degradation of the power law caused by saturation makes this dependence even more complex. For this reason, the linear model for the QY characterization of two-photon upconversion emission, as demonstrated by Faulkner et al. [345], will fail when saturation is present.

The saturation of upconversion emission is governed by the competition between the ETU rate and the linear decay rate for the depletion of the intermediate energy state involved in the upconversion process [343, 344]. This saturation feature has been used to evaluate the quantum efficiency of UCNPs by many researchers [346–350], showing a small slope in the double-logarithmic plot, and a small saturating power density indicating a high QY. However, the use of saturation to assess QY can lead to ambiguous results unless a thorough theoretical analysis is performed.

Numerically solving the rate equations describing upconversion processes and extracting the QY at steady state will, in principle, provide accurate QY data for arbitrary excitation intensities, as demonstrated in Paper **V**. However, this approach is extremely demanding, and may not be feasible in practical applications, because too many parameters are required for the rate equations and some of them are difficult to obtain. An analytical expression describing the excitation-intensity-dependent QY, with few parameters, that can be easily obtained experimentally, will be valuable, although the use of assumptions in achieving such an expression would reduce the accuracy.

### 4.1.3 Two-parameter characterization

$Yb^{3+}$-sensitized two-photon upconversion emission is the most efficient identified so far, and has attracted the greatest interest in biomedical applications. A two-parameter model for QY characterization of such emission, accounting for the saturation property of upconversion process, is proposed in Paper **IV**.

The mechanism of $Yb^{3+}$-sensitized two-photon upconversion emission can be generally depicted by a quasi-three-level model for the main upconversion activators, including $Er^{3+}$, $Tm^{3+}$ and $Ho^{3+}$

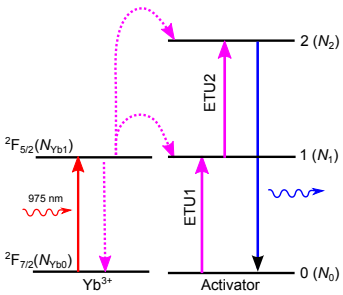


**Figure 4.2.** *Schematic energy level diagrams of the $Yb^{3+}$ and activator ions and the proposed upconversion mechanism following excitation at 975* nm.

[140], as shown in Figure 4.2. The excitation-intensity-dependent behavior of the upconversion emission intensity and QY can be well approximated by the following steady-state rate equations:

$$\frac{\mathrm{d}N_{\mathrm{Yb1}}}{\mathrm{d}t} = \sigma\frac{\rho}{h\nu}N_{\mathrm{Yb0}} - \frac{N_{\mathrm{Yb1}}}{\tau_{\mathrm{Yb1}}} = 0, \tag{4.4a}$$

$$\frac{\mathrm{d}N_1}{\mathrm{d}t} = C_0N_0N_{\mathrm{Yb1}} - C_1N_1N_{\mathrm{Yb1}} - \frac{N_1}{\tau_1} = 0, \tag{4.4b}$$

$$\frac{\mathrm{d}N_2}{\mathrm{d}t} = C_1N_1N_{\mathrm{Yb1}} - \frac{N_2}{\tau_2} = 0. \tag{4.4c}$$

Here, $N_{\mathrm{Yb0,Yb1}}$ [$\mathrm{cm}^{-3}$] are the population densities of the states $^2\mathrm{F}_{7/2}$ and $^2\mathrm{F}_{5/2}$ of $\mathrm{Yb}^{3+}$ ions, respectively, while $N_{0,1,2}$ [$\mathrm{cm}^{-3}$] are the population densities of states 0, 1 and 2 of the activator ions, respectively; $\sigma$ [$\mathrm{cm}^2$] is the absorption cross-section of $\mathrm{Yb}^{3+}$ ions; $\rho$ [$\mathrm{Wcm}^{-2}$] is the excitation power density; $h$ [$\mathrm{m}^2\mathrm{kg/s}$] is Planck's constant; $\nu$ [$\mathrm{s}^{-1}$] is the frequency of the excitation light; $\tau_{1,2}$ [s] are the lifetimes of activator ions in states 1 and 2, respectively, including the contributions of radiative and nonradiative relaxation mechanisms, while $\tau_{\mathrm{Yb1}}$ [s] is the lifetime of $\mathrm{Yb}^{3+}$ ions in the $^2\mathrm{F}_{5/2}$ state; and $C_{0,1}$ [$\mathrm{cm}^3\mathrm{s}^{-1}$] are ETU rates constants characterizing the processes ETU1 and ETU2, respectively.

Algebraically, the QY of two-photon upconversion emission can be described by (see Paper **IV**):

$$\eta = \eta_{\mathrm{s}} \cdot \frac{\rho/\rho_{\mathrm{b}}}{1+\rho/\rho_{\mathrm{b}}}, \tag{4.5}$$

with

$$\eta_{\mathrm{s}} = C_0N_0\tau_{\mathrm{Yb1}}\tau_2/\tau_2^{\mathrm{rad}}, \tag{4.6}$$

and

$$\rho_{\mathrm{b}} = \frac{h\nu}{\tau_1 \cdot C_1\tau_{\mathrm{Yb1}}\sigma N_{\mathrm{Yb0}}}, \tag{4.7}$$

where $\eta_{\mathrm{s}}$ is the maximum attainable QY of the system, $\rho_{\mathrm{b}}$ is the balancing power density, reflecting the excitation intensity dependence of the QY, and $\tau_2^{\mathrm{rad}}$ is the radiative lifetime of state 2. At $\rho_{\mathrm{b}}$, the ETU rate and the linear decay rate contribute equally to the de-excitation of state 1, i.e., $N_1/\tau_1 = C_1N_1N_{\mathrm{Yb1}}$, and the slope efficiency of the excitation-power-density dependence of the upconversion emission intensity on a log-log scale, expressed as (see Paper **IV**):

$$k = 1 + \frac{1}{1+\tau_1 \cdot C_1\tau_{\mathrm{Yb1}}\sigma N_{\mathrm{Yb0}}\rho/h\nu}, \tag{4.8}$$

has a value of 1.5. The terms $\sigma N_{\mathrm{Yb0}}$, $\tau_1$ and $\tau_{\mathrm{Yb1}}$, and $C_1$ characterize the absorption of excitation light by $\mathrm{Yb}^{3+}$ ions, and the retention times of the intermediate state of activator ions and the excited state of $\mathrm{Yb}^{3+}$ ions, respectively, and the energy transfer

rate between excited $Yb^{3+}$ ions and activator ions. The balancing power density is thus a measure of the effectiveness of the upconversion system; a lower value implying better performance. Considering the fact that the upconversion emission is generated through a stepwise process, the term $\eta_s$ can be simply regarded as the probability of reaching state 1 from state 0, while the term $\frac{\rho/\rho_b}{1+\rho/\rho_b}$ regarded as the probability of reaching state 2 from state 1. Experimentally, $\eta_s$ can be obtained by measuring the QY at very high excitation intensity, and $\rho_b$ can be extracted from routine power dependence measurements of upconversion emission intensity.

Experimental QY data can be reasonably well fitted by Equation (4.5), as shown in Figure 4.3. The values of $\eta_s$ and $\rho_b$ are estimated to be 0.91% and 3.8 W/cm$^2$, and 2.6% and 1.3 W/cm$^2$ for the core ($NaYF_4$:$Yb^{3+}$/$Tm^{3+}$) and core-shell ($NaYF_4$:$Yb^{3+}$/$Tm^{3+}$@$NaYF_4$) samples, respectively. The discrepancy could be due to the omission of certain energy transfer processes in the rate equation, and the inaccuracy in the excitation beam size measurement involved in the measurement of the excitation power density.

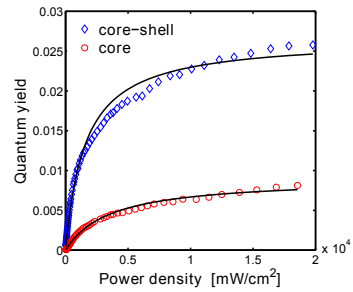


**Figure 4.3.** *Experimentally determined QYs for the 800* nm *upconversion emission band of core $NaYF_4$:$Yb^{3+}$/$Tm^{3+}$ and core-shell $NaYF_4$:$Yb^{3+}$/$Tm^{3+}$@$NaYF_4$ UCNPs. The solid lines are the fitted curves using Equation (4.5).*

### 4.1.4 Experimental measurements

In the early work on QY measurements for upconverting phosphors conducted by Page et al. [25], a CW laser chopped to a 50% duty factor at 100 Hz was employed to facilitate synchronous detection of the signal. However, the study presented in Paper **V** reveals that pulsed excitation is less desirable than CW excitation, because the overall upconversion process is generally slow, and the repeating population/de-population processes of upconversion system under excitation by pulse trains would lead to a smaller apparent QY.

Two types of setup can be used in measuring the QY, i.e., integrating-sphere-based and spectrofluorometer-based. Non-uniform spatial irradiation, typically with a Gaussian profile, is commonly present, when excitation light is illuminating the sample. For linear fluorophores including fluorescent dyes and quantum dots, such non-uniform irradiation would not cause any extra consideration in the QY measurement. However, as the QY is highly power-density-dependent, the non-uniform illumination effect must be compensated for in nonlinear UCNPs, in order to achieve good accuracy. Figure 4.4 presents the calculated photoluminescence intensities as a function of excitation power (Note: not excitation power density) for uniform illumination and a Gaussian distributed illumination. As can be seen, even with the same series of laser output powers, different excitation profiles will result in distinct optical responses of the UCNPs. This effect will lead to large inaccuracy in the interpretation of the results of the QY measurements if one doesn't have precise knowledge of the ex-

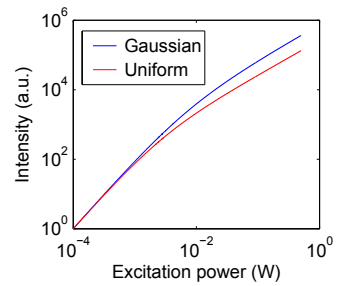


**Figure 4.4.** *Calculated photoluminescence intensities as a function of excitation power under uniform and Gaussian excitation.*

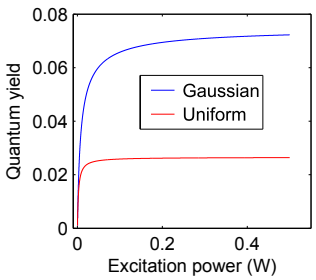


**Figure 4.5.** *Calculated quantum yield as a function of excitation power under uniform and Gaussian excitation.*

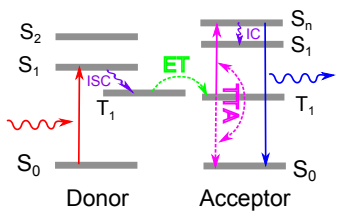


**Figure 4.6.** *Schematic diagram of the triplet-triplet annihilation (TTA) upconversion process. S and T denote singlet states and triplet states, respectively. IC–internal conversion. ISC–intersystem crossing. ET–energy transfer.*

citation beam profile, as illustrated in Figure 4.5, which presents the deduced QYs as a function of output power for two different excitation profiles.

In an integrating-sphere-based setup, it is difficult to determine the true excitation profile that contributes to the finally detected fluorescence signal, since the excitation light repeatedly passes through the sample, generating fluorescence due to reflection from the sphere wall. A spectrofluorometer-based setup was therefore employed instead in the work described in this thesis. A beam profiler was used to measure the excitation profile, and a corresponding compensation procedure was developed to correct for the effect of non-uniform illumination.

In the spectrofluorometer-based setup, a fluorophore with a known QY is required as a reference. The luminescence of fluorescent dye dissolved in a certain solvent has been reported to be dependent on the polarization property of the excitation light [351]. Polarization effects on UCNP suspension are expected to be averaged out due to the random orientation of a large number of nanoparticles, although such an effect could be observed for single nanostructures [352]. The overall influence of the polarization of excitation light on the QY measurements must be corrected for.

Absorption measurements are important for the characterization of QY. Besides absorption, the scattering due to UCNPs will also attenuate the incident excitation light. Two wavelengths, 975 nm and 915 nm, are used for UCNPs to correct for the scattering effect.

A more thorough study report on above effects encountered in the QY measurement of UCNPs is in preparation [353].

### 4.1.5 Extension to triplet-triplet annihilation upconversion

Triplet-triplet annihilation (TTA) based on organic molecules is an even more efficient upconversion mechanism (Figure 4.6) [354, 355]. This process typically converts red or green excitation light into blue emission light. There has been rapid development in such upconversion systems during the past decade, and their applications in biomedical imaging started to appear very recently [356]. Similar to RE-ions-doped UCNPs, TTA-based upconversion emission also exhibits a power-density-dependent QY with saturation. The QYs are usually measured at different excitation power densities [357–360].

In a TTA system, there are two main deactivation channels for the triplet states, namely, spontaneous decay and bimolecular annihilation. Either of these channels could become dominant depending on the excitation power density. Similar to upconversion systems based on RE ions, there exists an balancing excitation intensity, and this balancing point was termed excitation inten-

sity threshold by Monguzzi et al. [361]. This threshold is determined by a few parameters of the constituent molecules. Above this threshold, triplet bimolecular annihilation becomes dominant over spontaneous decay, resulting in efficient upconversion generation. Experimentally, the threshold is extracted by fitting the power density dependence curve of upconversion emission in low and high excitation intensity regimes; the threshold is then given at the intersection of the fitted lines. Monguzzi et al. presented an expression for the excitation-power-density-dependent intensity of upconverted light [362].

As the TTA-based upconversion emission has a similar mechanism to that based on RE ions, the two-parameter QY characterization approach can be applied with some modifications. The dynamics of a typical TTA system can be described by the following rate equations [361]:

$$\frac{\partial T_{\mathrm{D}}}{\partial t} = \alpha(E)\Phi_{\mathrm{ISC}} I_{\mathrm{ex}} - k_{\mathrm{D}}^{\mathrm{T}} T_{\mathrm{D}} - k_{\mathrm{tr}} T_{\mathrm{D}}, \tag{4.9a}$$

$$\frac{\partial T_{\mathrm{A}}}{\partial t} = k_{\mathrm{tr}} T_{\mathrm{D}} - k_{\mathrm{A}}^{\mathrm{T}} T_{\mathrm{A}} - \gamma_{\mathrm{TT}} T_{\mathrm{A}}^2, \tag{4.9b}$$

$$\frac{\partial S_{\mathrm{A}}}{\partial t} = \frac{1}{2} f \gamma_{\mathrm{TT}} T_{\mathrm{A}}^2 - k_{\mathrm{A}}^{\mathrm{S}} S_{\mathrm{A}}, \tag{4.9c}$$

with the same notation as used by Monguzzi et al. [361], and where $\Phi_{\mathrm{ISC}}$ denotes the quantum efficiency of donor intersystem crossing. Back energy transfer from acceptor to donor is not considered here. The steady-state intensity can be expressed as:

$$I = \Phi_{\mathrm{A}} k_{\mathrm{A}}^{\mathrm{S}} S_{\mathrm{A}} = \frac{1}{8} \Phi_{\mathrm{A}} \frac{f}{\gamma_{\mathrm{TT}}} \left[ -1 + \sqrt{1 + \frac{4\alpha(E)\gamma_{\mathrm{TT}} k_{\mathrm{tr}} \Phi_{\mathrm{ISC}} I_{\mathrm{ex}}}{(k_{\mathrm{A}}^{\mathrm{T}})^2 (k_{\mathrm{tr}} + k_{\mathrm{D}}^{\mathrm{T}})}} \right]^2, \tag{4.10}$$

where $\Phi_{\mathrm{A}}$ is the quantum efficiency of acceptor photoluminescence. The slope efficiency on a double logarithmic scale can be described by:

$$k_{\mathrm{TTA}} \equiv \frac{\mathrm{dlog} I}{\mathrm{dlog} I_{\mathrm{ex}}} = 1 + \frac{1}{\sqrt{1 + \frac{4\alpha(E)\gamma_{\mathrm{TT}} k_{\mathrm{tr}} \Phi_{\mathrm{ISC}} I_{\mathrm{ex}}}{(k_{\mathrm{A}}^{\mathrm{T}})^2 (k_{\mathrm{tr}} + k_{\mathrm{D}}^{\mathrm{T}})}}}. \tag{4.11}$$

When the contributions of spontaneous decay and bimolecular annihilation to the deactivation of the acceptor triplet states are equal: $k_{\mathrm{A}}^{\mathrm{T}} T_{\mathrm{A}} = \gamma_{\mathrm{TT}} T_{\mathrm{A}}^2$, the excitation intensity threshold is given by:

$$I_{\mathrm{th}} = \frac{2(k_{\mathrm{A}}^{\mathrm{T}})^2}{\alpha(E)\gamma_{\mathrm{TT}}\Phi_{\mathrm{ISC}}} \left( \frac{k_{\mathrm{tr}} + k_{\mathrm{D}}^{\mathrm{T}}}{k_{\mathrm{tr}}} \right), \tag{4.12}$$

which gives a slope efficiency $k = 4/3$.

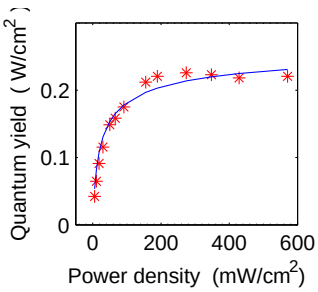


**Figure 4.7.** *Fit to the QY data reported by Kim et al. [360] (*) using Equation (4.13) (solid line).*

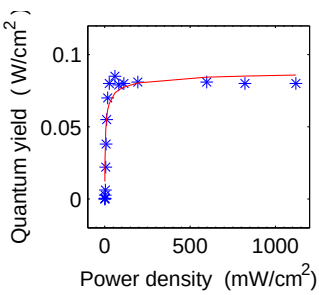


**Figure 4.8.** *Fitting of the QY data reported by Monguzzi et al. [357] (*) using Equation (4.13) (solid line).*

The overall QY of upconversion emission can be obtained from:

$$\eta_{\mathrm{TTA}} \equiv \frac{k_2 I}{\alpha(E) I_{\mathrm{ex}}} = \eta_{\mathrm{TTA}}^{\mathrm{sat}} \cdot \frac{\left(\sqrt{\frac{I_{\mathrm{ex}}}{I_{\mathrm{th}}/8}}\right)^2}{\left(1+\sqrt{1+\frac{I_{\mathrm{ex}}}{I_{\mathrm{th}}/8}}\right)^2}, \tag{4.13}$$

where $k_2$ a parameter correcting for the energy difference between the excitation photon and emission photon, and $\eta_{\mathrm{TTA}}^{\mathrm{sat}}$ is the attainable maximum QY of the system achieved in saturating excitation intensity regime, described by:

$$\eta_{\mathrm{TTA}}^{\mathrm{sat}} = \frac{1}{2} \frac{\Phi_A f \Phi_{\mathrm{ISC}}}{(k_{\mathrm{A}}^{\mathrm{T}})^2} \frac{k_{\mathrm{tr}}}{k_{\mathrm{tr}} + k_{\mathrm{D}}^{\mathrm{T}}}. \tag{4.14}$$

As can be seen in Equation (4.13), parameters $I_{\mathrm{th}}$ and $\eta_{\mathrm{TTA}}^{\mathrm{sat}}$ can be used as two standard indices to describe a TTA system, as they fully characterize the QY, i.e., both the amplitude and the power density dependence.

The QY data for PdOEP/DPA-based TTA systems reported previously [357, 360] are well fitted by Equation (4.13), as shown in Figure 4.7 and Figure 4.8, respectively. The parameters $I_{\mathrm{th}}$ and $\eta_{\mathrm{TTA}}^{\mathrm{sat}}$ were estimated to be approximately 35 mW/cm$^2$ and 27.5%, and 5 mW/cm$^2$ and 9% by fitting these two systems. Interestingly, Equation (4.5) also gave a reasonably good fit to the reported QY data, probably due to the similarity of the upconversion mechanisms in the ETU-based and TTA-based systems.

## 4.2 Excitation scheme optimization

Upconversion emission can be excited using CW lasers or non-coherent lamps with excitation power densities well below 1 W/cm$^2$ [132–134], sometimes as low as ∼50 mW/cm$^2$ [199]. This is a considerable advantage compared to other types of anti-Stokes emission such as second-harmonic generation and two-photon fluorescence, as it alleviates the need for high excitation intensity allowing their use in deep biological tissues. However, the conventional CW excitation scheme is less optimal than pulsed excitation from the perspective of energy conversion and possibility of suppressing the thermal effects of excitation light. Optimization of the excitation scheme for UCNPs will be discussed in this section.

### 4.2.1 Pulsed excitation for higher quantum yield

Due to the excitation power density dependence of the QY of upconverting materials, as shown in Figure 4.3 and Figure 4.7, higher excitation intensity will lead to a higher QY. Considering a CW source and a pulsed source that provide identical average power density, a larger overall QY and thus a larger upconversion signal gain can be expected from the pulsed source, as the excitation

photons are confined to a narrow time window, resulting in an instantly higher excitation power density, as illustrated in Figure 4.9.

Upconversion processes are relatively slow with typical population times on the order of milliseconds [363, 364], because many long-lived intermediate energy states of RE ions are involved. The transient behavior of the upconversion system in each pulse period must be taken into account when evaluating the performance of pulsed excitation. The upconversion system has a lower QY at the very beginning of each pulse than in a later phase at steady state, since the energy states involved are far less populated. Thus, a long rise time of upconversion emission, related to the lifetimes of intermediate energy levels, would reduce some of the benefit of the high excitation power density of pulsed excitation.

The applied average excitation power density is another critical parameter determining the signal gain. If it is already located in a saturating regime, no gain in signal will be obtained by using pulsed excitation, relative to equivalent CW excitation.

It is worth mentioning that pulsed excitation is even better for multi-photon upconversion emission such as blue and ultraviolet emission from $Tm^{3+}$ ions, due to their high-order dependence on excitation power density. Such short wavelength emission has been shown to be very promising in the photoactivation of biomolecules. It is expected that the pulsed excitation approach will facilitate the implementation of NIR-triggered photoactivation in deep tissues, while the depth is limited to only a few millimeters at present [284].

The pulsed excitation approach is described in detail and compared with CW excitation in Paper **V**.

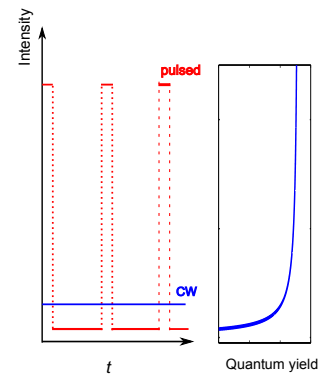


**Figure 4.9.** *Schematic of the benefit of using pulsed excitation for pumping UCNPs. The CW source and pulsed source provide identical power.*

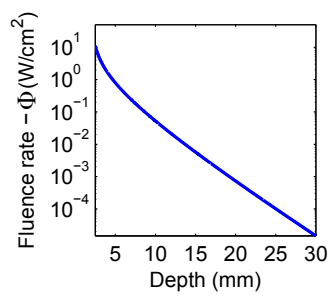


**Figure 4.10.** *Calculated fluence rate at 975 nm with* $\mu_a = 0.7\ \mathrm{cm}^{-1}$ *and* $\mu_s' = 5\ \mathrm{cm}^{-1}$.

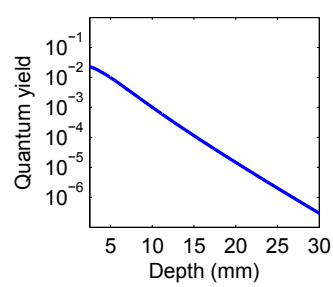


**Figure 4.11.** *Quantum yield for the UCNPs as a function of depth.*

### 4.2.2 Low light limit

The currently available maximum QY of UCNPs, of a few percent, meets the needs for superficial planar imaging. However, significantly lower QYs at low excitation intensities remain a hurdle for the successful applications of UCNPs in deep tissues, where the excitation fluence rate is low due to absorption and scattering by tissue. Figure 4.10 shows the fluence rate of 975 nm light at different depths in a tissue with typical optical properties [365, 366]. The QY of UCNPs at different depths in the same tissue is presented in Figure 4.11. The maximum attainable QY, $\eta_s$, and balancing power density, $\rho_b$, of the UCNPs were assumed to 2.6% and 1.3 W/cm$^2$, respectively. As can be clearly seen, the UCNPs are very inefficient regarding luminescence at a depth of 10 mm, with a QY of around 0.1%. At a depth of 15 mm, the QY is even lower, approximately 0.01%. This would obviously impose a severe limitation on the usable depth of UCNPs in deep tissues, such as diffuse optical imaging, photodynamic therapy and biomolecule remote photoactivation.

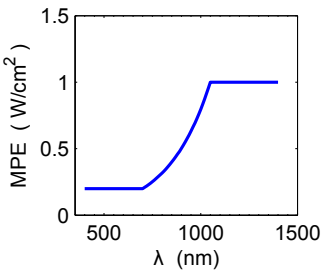


**Figure 4.12.** *The MPE as a function of wavelength for CW laser sources.*

Apart from approaches to improve the efficiency of the materials, such as surface modification with optical antennas including fluorescent dyes [205] and noble metal nanostructures [219], another solution to enhance the upconversion emission is to increase the excitation light intensity. However, this is not possible when using CW excitation due to the risk of tissue damage. This is regulated by the ANSI standard as described below.

### 4.2.3 ANSI standard

For a train consisting of identical pulses, the average power density is the limiting factor. For a square wave with an average power $P$ and a duty cycle $T$, the resulting much higher peak power of $\frac{P}{T}$ is allowed by the ANSI standard. The standard for safe use of lasers established by the Laser Institute of America [367], called the ANSI standard, defines how lasers can be used in bioapplications all over the world. This standard takes into account all possible hazardous effects of exposure to laser light, such as photochemical effects and photothermal effects. In the spectral region of 0.180-0.400 $\mu$m, dual limits apply for photochemical and photothermal effects, while for wavelengths between 0.400 and 1000 $\mu$m, thermal effects are the only concern. The maximum permissible exposure (MPE) is stipulated for all wavelengths, both for CW and pulsed laser sources. Different standards are applied to skin exposure and ocular exposure.

MPEs for skin exposure to a laser beam with wavelengths in the range of 0.400-1.400 $\mu$m are given in Table 4.1. In calculating MPEs for single-pulse lasers, the exposure duration is equal to the pulse duration. For repetitive-pulse lasers, two MPEs are defined: (1) a single-pulse MPE and (2) an average power MPE for thermal and photochemical hazards. The first protects against thermal injury resulting from a single pulse having greater than average power, while the second protects against cumulative photochemical injury and thermal injury due to heat buildup resulting from the average power. A third MPE, i.e., multiple-pulse MPE for thermal hazards, applys only to ocular exposure, which pro-

Table 4.1: Maximum permissible exposure (MPE) of skin to a laser beam. This table is reproduced from Ref. [367]. $C_A$ is a wavelength dependent parameter, $C_A = 10^{2(\lambda-0.700)}$ with $\lambda$ expressed in $\mu$m.

| Wavelength ($\mu$m) | Exposure duration, $t$ (s) | MPE ($\mathrm{J\cdot cm^{-2}}$) | MPE ($\mathrm{W\cdot cm^{-2}}$) |
|---|---|---|---|
| 0.400-1.400 | $10^{-9}$ to $10^{-7}$ | $2C_\mathrm{A}\times10^{-2}$ | |
| 0.400-1.400 | $10^{-7}$ to 10 | $1.1C_\mathrm{A}t^{0.25}$ | |
| 0.400-1.400 | 10 to $3\times10^{4}$ | | $0.2C_\mathrm{A}$ |

tects against sub-threshold pulse-cumulative thermal injury. Figure 4.12 presents the MPEs for skin exposure to CW lasers with different wavelengths. As can be seen, for a CW 975 nm laser, the MPE is around 710 mW/cm$^2$, and around 320 mW/cm$^2$ for 800 nm. It should be noted that the ANSI standard is rather conservative. Considering the optical properties of tissues at these two wavelengths, as discussed in Chapter 2, a higher MPE should be allowed for 800 nm radiation.

### 4.2.4 Single-shot imaging

For single-pulse excitation with a pulse duration in the range of $10^{-7}$–10 s, the MPE [Wcm$^{-2}$] is given by:

$$\mathrm{MPE}_{\mathrm{single-pulse}} = \frac{1.1 C_{\mathrm{A}} t^{0.25}}{t}. \tag{4.15}$$

Figure 4.13 shows the dependence of MPE on pulse duration at a wavelength of 975 nm. As can be seen, a much higher excitation power density is allowed with short pulse durations. This excitation approach enables the use of UCNPs in a more efficient way. Another merit of single-pulse excitation is the significant reduction of the data acquisition time. Today, integration times of ∼10 s are often used for UCNP imaging in deep tissues due to their low QYs. Comparable signal quality can be achieved with much shorter integration times by employing single pulse excitation.

Single-shot imaging using UCNPs is demonstrated in Paper **V**.

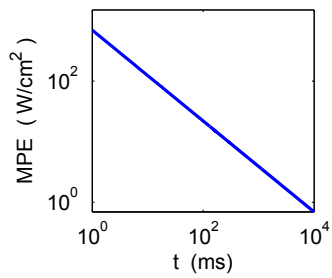


**Figure 4.13.** *The dependence of MPE on pulse duration for pulsed laser sources.*

Chapter 5

# Fluorescence diffuse optical tomography based on upconverting nanoparticles

Fluorescence diffuse optical tomography (FDOT) is a relatively new biomedical imaging modality that can be employed to non-invasively quantify fluorescent biomarkers distributed in biological tissues. This powerful technique has been widely used in preclinical research as well as in clinical cases, e.g., to follow the development of proteases [368], Alzheimer's disease [369], tumors [370], and the effects of various drugs [6]. Due to the general high light scattering of tissue, FDOT suffers from low spatial resolution. Nonlinear UCNPs, with autofluorescence-free detection capacity and super-linear power dependence, are excellent contrast agents for FDOT, leading to unprecedented resolution compared with conventional linear fluorophores. In this chapter, FDOT is discussed in a general framework as the special case of the inverse problem. The advantages of UCNPs as contrast agents for FDOT are also discussed.

## 5.1 The inverse problem

In the field of tissue optics, the aim of solving the inverse problem is to extract the interior optical properties of a medium non-invasively through measurements performed on the tissue boundaries, as illustrated in Figure 5.1. The optical properties in question include the absorption, $\mu_a$ [cm$^{-1}$], and reduced scattering coefficients, $\mu_s'$ [cm$^{-1}$], the diffusion coefficient $D$ [cm], the fluorescence lifetime, $\tau$ [s], and the fluorescence yield (i.e., the product of the QY and the absorption coefficient of the fluorophore), $\eta\mu_{af}$

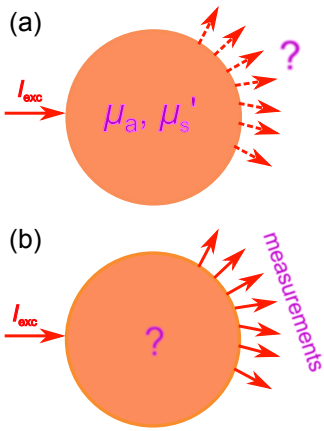


**Figure 5.1.** *The schematic description of (a) the forward problem and (b) the inverse problem.*

[$cm^{-1}$]. As a spatial map of the optical properties within the medium is usually obtained, the method is commonly referred to as diffuse optical tomography. The work described in this thesis concerned with FDOT, in which the spatial distribution of the fluorescence yield is obtained.

### 5.1.1 Measurables, excitation schemes and imaging geometries

#### Measurables

The measurable in FDOT is often the fluorescence intensity at steady state under CW excitation, as this requires a relatively simple setup to acquire fluorescence data.

The temporal signal following short-pulse excitation can also be employed to extract the optical properties of the medium. The detection can be gated, typically on the timescale of ∼100 ps after the time of arrival of a laser pulse on the target of interest, in order to use only the early arriving photons for reconstruction. This yields high spatial resolution [371, 372]. Femtosecond pulse lasers are thus used to provide excitation light in such techniques.

The fluorescence lifetime can be obtained by recording the time-resolved fluorescence intensity, and is typically in the nanosecond regime for fluorescent dyes. The fluorescence lifetime provides excellent contrast, independent of the probe concentration or light path length, but it is dependent on excited-state reactions [373, 374]. These properties of fluorescence lifetimes allow the exploration of the micro-environment of probes in the interior of biological tissues, such as the variation in tissue oxygenation, pH and glucose concentration [100, 375]. In addition, three-dimensional mapping of Förster resonance energy transfer in turbid media can be implemented by using the approach of tomographic lifetime imaging [376–378]. As biological tissues have different optical properties at different wavelengths, they behave as spectral filters when light propagates through them, leading to a shift in intrinsic excitation and the emission spectra of the fluorophores. Thus, multispectral data on both the excitation and emission side are often collected to provide further constraints for FDOT [379–385].

When irradiating tissue with light with a sinusoidally varying amplitude, the collected light signal will also be sinusoidal, with a phase shift and demodulation relative to the source amplitude [386, 387]. The optical properties of the irradiated tissue can be extracted from the recorded phase and modulation response, particularly when multiple modulation frequencies are employed [388].

The use of the measurables discussed above has led to the development of a range of imaging systems for CW, time-domain and frequency domain optical tomography.

### Excitation schemes

A point-like source with a CW output is typically used to provide the excitation energy, while point-like short-pulse laser sources are used for time-resolved measurements [371]. Spatially modulated illumination, developed by Cuccia et al. [389, 390], has also been exploited and has been found to be useful in alleviating the ill-posedness of the optical tomography problem [391–395]. In the frequency domain technique, intensity-modulated laser sources are utilized, irradiating the tissue with sinusoidally varying source power [386, 387].

### Imaging geometries

Imaging geometries can be divided into three main categories: epi-illumination, transillumination, and projection geometries. In the epi-illumination geometry (Figure 5.2(a)), with the source and the detector placed on the same side of the tissue, the sensitivity at shallow depths is superior to that at greater depths. The fluorescence signal is usually considerable if fluorophores are not deeply located, as the fluorescent light will propagate only a relatively short distance before exiting from the surfaces of the tissue. The background from the excitation light is often relatively high, for the same reason. Some large tissues only allow this geometry due to their size, e.g., in fluorescence tomography of most parts of the human body. In the transillumination geometry (Figure 5.2(b)), the source and detector are placed on opposite sides of the tissue. The imaging sensitivity is then higher near the source and the detector than deep in the tissue. The fluorescent light is generally weak, as is the excitation background, due to the attenuation of light by the tissue. In the projection geometry (Figure 5.2(c)), either the source-detector pair or the tissue can be rotated, usually by 360°, yielding a relatively uniform sensitivity throughout the whole tissue.

The appropriate geometry will depend on the application. In very deep tissue, such as the human prostate, other geometries may be necessary, e.g. interstitial measurements, using fibres inserted into the tissue to deliver and collect the light [396].

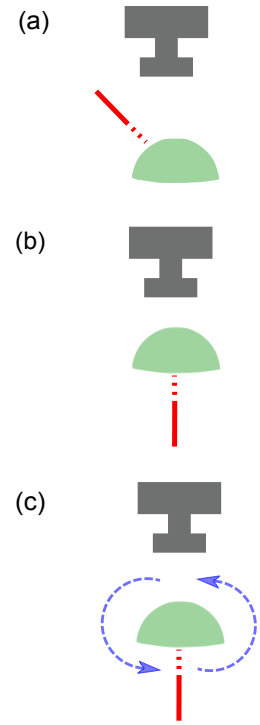


**Figure 5.2.** *Imaging geometries for fluorescence diffuse optical tomography. (a) Epi-illumination. (b) Transillumination. (c) Projection geometry.*

## 5.1.2 The theoretical scheme

In the framework of FDOT, the measurable, denoted by $\mathbf{y}$, is compared with the modeled value $F(\mathbf{x})$, calculated by a forward model. The forward model is given by:

$$F(\mathbf{x}) = \mathcal{M}[\Phi(\mathbf{x})], \tag{5.1}$$

where $\mathcal{M}$ denotes the measurement operator accounting for how the signal is measured, and $\Phi(\mathbf{x})$ is the fluorescence fluence generated by a given fluorophore distribution, $\mathbf{x}$. The forward model

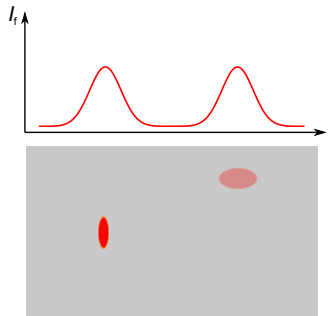


**Figure 5.3.** *Schematic description of the non-uniqueness in fluorescence diffuse optical tomography. Two fluorophore distributions with different concentration at different depths could render the same fluorescence intensity and profile on the surface.*

should describe the light propagation as accurately as possible. Different theoretical models, as described in Chapter 2, can be employed, depending on the case. An objective function is constructed based on the measured data and the modeled value, i.e.:

$$\chi^2 = \|\mathbf{y} - F(\mathbf{x})\|^2. \tag{5.2}$$

The solution is obtained by finding the value of $\mathbf{x}$ giving the minimal value of $\chi^2$, using least-squares minimization.

Due to the high scattering of biological tissues, the problem at hand is fundamentally ill-posed, i.e., the solution is non-unique, and a small perturbation in the data can therefore cause a significant alteration in the solution with minimal $\chi^2$. The origin of the ill-posedness caused by high scattering can be understood by considering the following two facts. (1) A small, deeply located fluorophore could render the same surface fluorescence exitance as a large, shallow one, as illustrated in Figure 5.3; and (2) a perturbation in a small volume inside the tissue causes signal changes in many source-detector projections. In addition, this problem is under-determined, as the number of unknowns usually exceeds the number of measurements. Even if a large data set is obtained, for example, by employing a charge-coupled device as the detector, the problem remains, because only linearly independent measurements contribute to the constraint to the solution.

The ill-posedness and under-determination discussed above make the inversion process unstable, causing the solution to fluctuate considerably. In order to stabilize and smooth the solution, a Tikhonov regularization term is generally included in the objective function [397]:

$$\chi^2 = \|\mathbf{y} - F(\mathbf{x})\|^2 + \lambda\|\mathbf{L}(\mathbf{x} - \mathbf{x}_0)\|^2. \tag{5.3}$$

Here, $\mathbf{L}$ is a regularization matrix, and $\lambda$ is the Tikhonov regularization parameter, giving the weight of the solution norm in the objective function. $\mathbf{x}_0$ is the initial estimate of the fluorophore distribution, often set to zero. The fluorophore distribution is thus reconstructed by minimizing the objective function. The regularization may be performed in different ways, and its meaning will be discussed in detail in Section 5.1.4. Adopting a Euclidean norm provides a solution when the derivative with respect to $\mathbf{x}$ is zero:

$$\frac{\partial \chi^2}{\partial \mathbf{x}} = -2\left[\frac{\partial F}{\partial \mathbf{x}}\right]^T [\mathbf{y} - F(\mathbf{x})] + 2\lambda \mathbf{L}^T\mathbf{L}(\mathbf{x} - \mathbf{x}_0) = 0. \tag{5.4}$$

This problem can be solved in an iterative approach. For iteration $k+1$, Equation (5.4) becomes:

$$\left[\frac{\partial F}{\partial \mathbf{x}}\right]^T [\mathbf{y} - F(\mathbf{x_{k+1}})] - \lambda \mathbf{L}^T\mathbf{L}(\mathbf{x_{k+1}} - \mathbf{x}_0) = 0. \tag{5.5}$$

$F(\mathbf{x_{k+1}})$ is expanded in Taylor series around $\mathbf{x_k}$ and only the first-order terms are retained, i.e.:

$$F(\mathbf{x}_{k+1}) = F(\mathbf{x}_k) + \frac{\partial F}{\partial \mathbf{x}}(\mathbf{x}_{k+1} - \mathbf{x}_k), \tag{5.6}$$

practically meaning that the forward model is linearized around $\mathbf{x}_k$. Insertion of Equation (5.6) into Equation (5.5) yields [398]:

$$[\mathbf{J}^T\mathbf{J} + \lambda\mathbf{L}^T\mathbf{L}]\Delta\mathbf{x} = \mathbf{J}^T\Delta\mathbf{y} - \lambda\mathbf{L}^T\mathbf{L}(\mathbf{x}_k - \mathbf{x}_0), \tag{5.7}$$

where $\mathbf{J} = \frac{\partial F}{\partial \mathbf{x}}$ is the Jacobian matrix, $\Delta\mathbf{x} = \mathbf{x}_{k+1} - \mathbf{x}_k$, is the update for the fluorophore distribution, and $\Delta\mathbf{y} = \mathbf{y} - F(\mathbf{x_k})$ is the difference or misfit between the data and the model in the current iteration. A Levenberg-Marquardt procedure is often applied in the iteration, i.e., assuming $\Delta\mathbf{x} = \mathbf{x}_k - \mathbf{x}_0$ [398, 399], which leads to:

$$\Delta\mathbf{x} = [\mathbf{J}^T\mathbf{J} + \bar{\lambda}\mathbf{L}^T\mathbf{L}]^{-1}\mathbf{J}^T\Delta\mathbf{y}. \tag{5.8}$$

Note $\bar{\lambda} = 2\lambda$.

**Figure 5.4.** *An example of the sensitivity profile between source and detector where regions with higher values will affect the measurement to a higher degree.*

### 5.1.3 The sensitivity matrix

#### Explicit expression

The Jacobian introduced in Equation 5.7 gives the rate of change of the modeled values relative to the parameters. In the calculation of the Jacobian, the adjoint method is employed in order to reduce computational cost [400]. In addition, the Born approximation is usually applied, which neglects the influence of the fluorophore distribution on the excitation field and the emission field [370]. This is valid for low fluorophore concentrations [375]. The explicit expression of the Jacobian can thus be described by:

$$\mathbf{J} = \frac{\partial F}{\partial \mathbf{x}} = \frac{\partial}{\partial \mathbf{x}}(C\Phi_{\mathrm{x}}^{\beta}\mathbf{x}\Phi_{\mathrm{m}}) = C\Phi_{\mathrm{x}}^{\beta}\Phi_{\mathrm{m}}. \tag{5.9}$$

Here, $C$ is a constant accounting for the detection efficiency and emission efficiency of the fluorophore, $\beta$ is a factor describing the excitation power dependence of the fluorophore, where $\beta = 1$ for linear fluorophores and $\beta = 2$ for quadratic fluorophores, $\Phi_{\mathrm{x}}$ is the excitation field, and $\Phi_{\mathrm{m}}$ is the adjoint emission field.

Equation 5.9 implies that equal parameter perturbation at different locations could lead to considerably different changes in the modeled values. The presence of a fluorophore in front of the source or detector is more evident than fluorophores at other locations for each source-detector projection, as illustrated in Figure 5.4. This is the reason why the Jacobian is also referred to as the weight or sensitivity matrix.

The normalized Born approximation, in which the measured fluorescence intensity is normalized by the intensity of the transmitted excitation light, is often used in the inverse problem [401].

The Jacobian is thus normalized in the same way. Such modifications afford advantages such as avoiding absolute photon-field measurements and certain robustness to heterogeneities in the optical properties [402].

#### Singular-value analysis

Singular-value decomposition of the Jacobian is often performed for the purpose of analyzing and optimizing an experimental setup [403–406]. This factorization yields:

$$\mathbf{J} = \mathbf{U}\mathbf{S}\mathbf{V}^T, \tag{5.10}$$

where $\mathbf{U}$ and $\mathbf{V}$ are orthonormal matrices containing the singular vectors of $\mathbf{J}$, and $\mathbf{S}$ is a diagonal matrix containing the singular values of $\mathbf{J}$. The column space of $\mathbf{U}$ is spanned by the detection-space modes, while that of $\mathbf{V}$ is spanned by the image-space modes. The singular values (elements of $\mathbf{J}$) denote how effectively a given image-space mode can be detected with the experimental setup, and thus contribute to the parameter reconstruction [407]. The merit of this method is that it efficiently condenses the information contained in the weight-matrix model into a singular-value spectrum.

In Paper **VIII**, singular-value analysis was performed to verify the usefulness of the data obtained under simultaneous dual-beam excitation for the reconstruction of UCNP distribution.

### 5.1.4 Regularization

The purpose of regularization is to both improve the spatial resolution and reduce the noise in FDOT reconstruction. The difference in the sensitivities at different depths can also be equilibrated by manipulating the regularization. Regularization is controlled by the regularization parameter and the regularization matrix.

#### The regularization parameter

The regularization parameter, $\lambda$, controls the weight given to minimization of the solution norm relative to minimization of the residual norm in Equation (5.3). A large $\lambda$ favors a small solution norm although the residual norm is large, while a small $\lambda$ allows a large solution norm. In addition, $\lambda$ also controls the sensitivity of the regularized solution to perturbations in the weight matrix and the data [408, 409]. Regularization can be viewed as a smoothing of the solution. Generally, a large regularization parameter results in a smooth image with low spatial resolution, while a small regularization parameter can sharpen the solution with noise of high spatial frequency components, as shown in Figure 5.5.

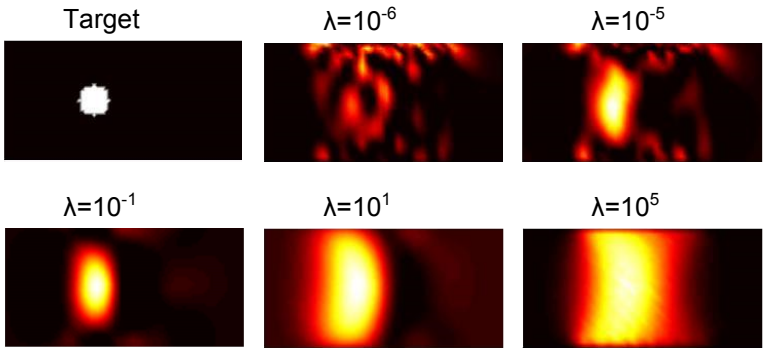


**Figure 5.5.** *The influence of the regularization parameter in standard Tikhonov regularization on the FDOT reconstructions.*

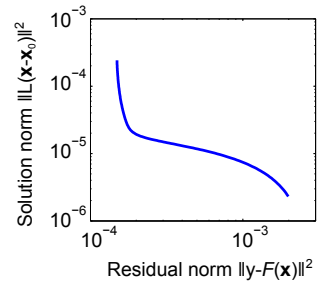


**Figure 5.6.** *The generic L-curve for standard Tikhonov regularization.*

The optimal regularization parameter should be equal to the ratio of the variances of the measurement data and optical properties [398, 410]. However, no such *a prior* information is available generally. Instead, it is most commonly derived empirically. The regularization parameter is often initially set to a high value and is monotonically decreased with increasing iterations. Some techniques based on mathematical principles such as generalized cross-validation [411] and the L-curve technique [412] are useful in choosing an appropriate regularization parameter. The L-curve method is a convenient graphical tool. In this method, the solution norm is plotted versus the residual norm in a log-log plot for different values of $\lambda$, giving a typical "L"-shaped curve, as shown in Figure 5.6. A good regularization parameter is found near the characteristic "corner" of the L-curve [412], as such a value of $\lambda$ yields a trade between a small residual norm and a small solution norm [397]. However, the L-curve method may fail in cases where no well-defined corner exists. The U-curve method, proposed by Krawczyk-Stańdo et al. [413, 414], is also useful in defining the regularization parameter for FDOT [415]. In addition, a neighborhood regularization method was recently proposed, in which multiple regularized solutions, corresponding to a series of adjacent regularization parameters, were combined in a geometric mean to obtain the final solution [416].

For FDOT using nonlinear UCNPs, as described in Paper **VIII** and Paper **VII**, there was no classical L-curve, and the regularization parameter was thus determined by empirical means.

### The regularization matrix

The regularization matrix, **L**, was set to the identity matrix, **I**, in the discussions above, giving the standard Tikhonov regularization. However, different regularization matrices can be chosen. For instance, Pogue et al. used a depth dependent regularization matrix in a cylindrical geometry to compensate for the decrease in sensitivity at greater depths [409]. Liu et al. used a regularization matrix normalized with the 2-norm of columns of the sensitivity matrix to reduce the differences in detection sensitivities [417]. Cao et al. presented an adaptive Tikhonov regularization method, in which the regularization matrix was dynamically updated using the result of the previous iteration to penalize the solutions [418].

Most commonly, **L** is adapted using spatial or spectral *a prior* information obtained from other measurements. X-ray CT [419] and MRI [420] can be incorporated into the FDOT system. The whole volume is divided into different regions according to tissue type, using the anatomical information obtained from the additional imaging modality. Such information is beneficial not only for improving the forward model by providing constraints on the variation in optical properties variation, but also for regularizing the inverse problem. A regularization matrix is accordingly created to control the smoothness and sensitivity of the inverse process. A Laplacian-type of regularization proposed by Brooksby et al. [421] is commonly used, giving the regularization matrix:

$$\mathrm{L}_{i,j} = \begin{cases} 0, & \text{if } i \text{ and } j \text{ are not in the same region,} \\ -1/N, & \text{if } i \text{ and } j \text{ are in the same region,} \\ 1, & \text{if } i = j, \end{cases} \tag{5.11}$$

where $i$ and $j$ are node indices, and $N$ is the number of nodes within the given region (or segment). This method smooths the solution within individual regions, while allowing discontinuities across region borders. A Helmholtz-type structured regularization matrix has also been suggested [422]. Hyde et al. assigned regularization weights to different segments using fluorescence data and anatomic information through a low-dimensional inverse problem [423]. In addition, they considered each FDOT voxel, especially in the vicinity of tissue boundaries, as a mixture of different anatomic regions, due to the difference in resolution of the FDOT and anatomical imaging modality. In this way, they could adjust the regularization level for each node more finely. This method increases smoothing in regions with larger weights, while decreasing smoothing in regions with smaller weights. Ale et al. combined the Laplacian and weighted segments regularization methods, to produce the local Laplacian and Laplacian+Weight-segments methods [424]. All these approaches rely on the assumption that voxels

within the same tissue region should have similar optical properties, and thus the sought quantity varies smoothly.

Multispectral fluorescent emission recordings provide depth information about the fluorophores embedded in tissues [379, 380, 425]. Axelsson et al. presented a method of creating a spatially varying regularization matrix using the intensity ratio of two emission wavelengths [381]. This approach was also employed in the present work (Paper **IX**) with UCNP-mediated FDOT. Both improved resolution and contrast were obtained in the reconstructed images, compared to using standard Tikhonov regularization.

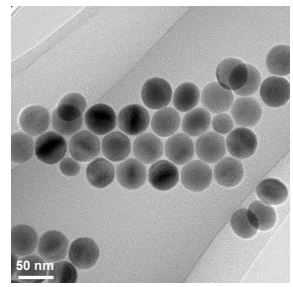


**Figure 5.7.** *Transmission electron microscopy image of core-shell $NaYF_4$:$Yb^{3+}$/$Tm^{3+}$@$NaYF_4$ UCNPs used as the contrast agents in FDOT.*

## 5.2 High-resolution fluorescence diffuse optical tomography using upconverting nanoparticles

Fluorescent dyes and quantum dots are commonly used as contrast agents in FDOT. Recently, UCNPs have been introduced as contrast agents in FDOT [282]. UCNPs have many benefits in FDOT. Both the excitation and emission wavelengths can be tuned to the tissue optical window, where biological tissue has relatively low absorption and scattering. This enables imaging to a considerable depth. Upconversion emissions from UCNPs are anti-Stokes shifted, and this makes the complete separation of upconversion emission from tissue autofluorescence possible by using an appropriate filter system, thus achieving autofluorescence-free imaging, as demonstrated in Paper **VI**. As FDOT is susceptible to noise, the suppression of background tissue autofluorescence leads to reconstructions with high quality [282]. In addition, the nonlinear power dependence of upconversion is also advantageous in FDOT, as will be discussed in detail below. Based on these factors, high-resolution FDOT has been developed using NIR-emitting $Yb^{3+}$/$Tm^{3+}$-codoped nanoparticles.

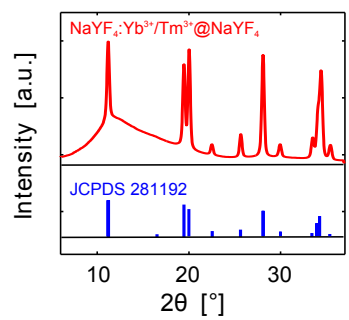


**Figure 5.8.** *X-ray diffraction pattern of the $NaYF_4$:$Yb^{3+}$/$Tm^{3+}$@$NaYF_4$ UCNPs used as the contrast agents in FDOT.*

### 5.2.1 Nanoparticles used in this work

The nanoparticles used in this study were synthesized primarily using the oleate route proposed by the group of Zhang [199, 228, 426] with slight modifications, except in Paper **II**. The particles have a core-shell structure, and the average size can be tuned from 20 nm to 50 nm by varying reaction parameters. Figure 5.7 shows a typical transmission electron microscopy image. The particles appear spherical in shape. The prepared UCNPs have a hexagonal phase, with an X-ray diffraction pattern well consistent with the JCPDS standard card (28-1192), as shown in Figure 5.8. Oleic acid was used as surfactant in the synthesis. The prepared nanoparticles could be well dispersed in commonly used nonpolar solvents, such

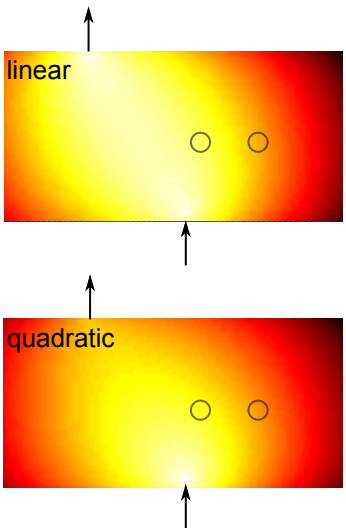


**Figure 5.9.** *Schematic illustration of selective excitation achieved by the steeper gradients of quadratic fluorophores. The circles represent the fluorescent inclusions.*

as hexane, cyclohexane, chloroform and toluene, and are colloidally stable for months without visible agglomeration.

### 5.2.2 Selective excitation

The resolution of far-field fluorescence imaging, i.e., how closely spaced fluorophores can be and still be resolved, is limited to the diffraction limit. An approach commonly used to increase the imaging resolution is to implement selective/localized excitation, as in stimulated emission depletion microscopy [427, 428] and multi-photon fluorescence microscopy [429, 430]. For example, the stimulated emission depletion microscopy employs a depletion beam to inhibit the fluorescence originating from neighboring fluorophores, thus only fluorophores in a localized region are allowed to emit at a certain time. Multi-photon fluorescence microscopy makes use of the nonlinear intensity dependence of fluorophores, giving rise to efficient excitation only near the focus of the excitation beam.

Similarly, upconversion emission provides high spatial resolution, especially in diffuse imaging and tomography, due to its nonlinear nature. Deep in a tissue, the excitation light originating from the source is severely attenuated by tissue absorption and scattering. The resulting fluence rate is usually well below the saturation regime for upconversion emissions. In such circumstances, the two-photon upconversion emission exhibits a quadratic dependence on the excitation intensity, and thus experiences a higher excitation gradient than linear emission, leading to high-resolution diffuse imaging [24].

In the present work (Paper **VII**), high-resolution FDOT was developed with NIR-emitting UCNPs. Two capillaries filled with an UCNP suspension, at a depth of 7 mm from the excitation source, placed 4 mm apart, could still be resolved, while tubes filled with linear fluorophores could only be resolved when seperated by a distance greater than 8 mm. Selective excitation is clearly demonstrated in the sensitivity maps for these two cases, as shown in Figure 5.9.

### 5.2.3 Crosstalk between multiple excitation sources

The nonlinear power dependence of upconversion emissions can be used to increase the information density in a given volume by including simultaneous multibeam excitation. Taking dual-beam excitation as an example, two fluorescence images, recorded during excitation with individual beams at different positions, are useful for image reconstruction. The nonlinearity of upconversion emission opens up the possibility of increasing orthogonal data points

by acquiring a third image under excitation by two beams simultaneously at the two positions, as the emission intensity, $\Gamma$, can be expressed as:

$$\begin{aligned}\Gamma &\propto (\Phi_{x,1} + \Phi_{x,2})^2 \eta \mu_{af} \Phi_m \\ &= (\Phi_{x,1}^2 + \Phi_{x,2}^2 + 2\boldsymbol{\Phi}_{x,\mathbf{1}}\boldsymbol{\Phi}_{x,\mathbf{2}}) \eta \mu_{af} \Phi_m, \end{aligned} \tag{5.12}$$

where $\Phi_{x,1(2)}$ denotes the excitation fluence rates generated by the two beams. The existence of the cross-term makes the new image independent, rather than being a simple linear superposition of the first two. Singular value decomposition analysis of the sensitivity matrices has verified the usefulness of the additional data. This effect was not possible with linear fluorophores. This approach is especially relevant for measurements on small surfaces, such as those found in mice, as sufficient data for an accurate reconstruction can still be obtained. Multibeam FDOT is described in Paper **VIII**.

### 5.2.4 Multispectral regularization

In the multispectral regularization approach, the most probable distance between the fluorophores and the detector is estimated by comparing the detected fluorescence intensity ratio with the modeled value for different emission wavelengths [381], yielding a spatially varying regularization map. Small regularization parameters are assigned to the regions where the fluorophores are mostly likely to be found, in order to increase the spatial resolution, while large parameters are assigned to regions where the fluorophores are not expected, to allow smoothing to reduce artifacts. This approach works best for a single fluorophore inside the tissue, while the small infinite spatial distribution of several fluorophores could make the depth estimate less accurate. The spatial distribution of fluorophores can be reasonably well estimated by repeating the process for all source-dector projections.

A large difference in effective attenuation coefficients at fluorescence wavelengths is preferable in order to increase the depth sensitivity. For biological tissues, this is typically achieved at the blue end of the tissue optical window, making use of the sharp absorption profile of hemoglobin. UCNPs can offer large anti-Stokes shifted emission in a spectral region with large differences in tissue attenuation. In Paper **IX**, core-shell $NaYF_4$:$Yb^{3+}$/$Er^{3+}$@$NaYF_4$ UCNPs, emitting two upconversion bands (540 nm and 660 nm) under excitation of 975 nm, were used in multispectral guided FDOT, yielding significantly better axial resolution than using standard Tikhonov regularization.

A spatially varying regularization map can be obtained using the data acquired with multiple excitation wavelengths in a similar way. UCNPs efficiently excitable by both 975 nm and 808 nm are

now available [148, 149]. More complicated regularization maps can be created by combining multispectral excitation and emission data, in order to provide more constraints and improve the quality of FDOT.

### 5.2.5 Outlook

Although showing great advantages and promise, the relatively weak luminescence from UCNPs is still a limiting factor for their applications in deep tissue regions relying on diffuse light excitation. Besides enhancing the intrinsic luminescence efficiency of UCNPs fundamentally by means of material engineering, progress in the following aspects will greatly increase the applicability of UCNPs in deep tissues:

**Luminescence pathway optimization**. At present, the most notable sensitizer and activator combinations are $Yb^{3+}/Tm^{3+}$ and $Nd^{3+}/Yb^{3+}/Er^{3+}$ [148, 149, 232], for which the excitation wavelength and the main emission wavelength can be 975 nm and 800 nm, and 800 nm and 650 nm, respectively. Both of these two luminescence pathways are close to the optimal for biological applications, especially the one for the $Nd^{3+}/Yb^{3+}/Er^{3+}$ combination, as discussed in Section 3.2.3. If the major upconversion emission band can be tuned to the range of 700–800 nm, it will be more than welcome.

**Excitation enhancement by optical antennas**. Upconversion emission can be significantly enhanced by modifying the surface of UCNPs with dye molecules [205] and noble metal nanostructures [218], as discussed in Section 3.2.2. However, some issues associated with such techniques need to be addressed. Dye molecules are generally photobleached. Surface modification with metal nanostructures is rather demanding, as emission quenching easily becomes dominant if the modification process is not precisely controlled.

**Excitation scheme optimization**. Pulsed excitation including single-pulse excitation, proposed in Paper **V**, proved to be able to break through the low light limit of UCNPs to some extent. In Paper **V**, only square-wave excitation was investigated. A more wisely designed pulse train, taking into account the upconversion dynamics, could enable UCNPs to be used in an even more efficient way. In addition, the combinational use of pulsed excitation approach and optical antenna effect can further increase the applicable depth of UCNPs in biological tissue.

At present, the use of UCNPs in biomedical applications is mainly making use of the response of UCNPs to the excitation

wavelength, i.e., certain emission bands are generated under excitation at one wavelength, and the response to excitation power density, i.e., the nonlinear excitation-power-density dependence of upconversion emission intensity. As an optical system, UCNPs are relatively complex, as many steps are involved in the generation of upconversion emission, and some of them are rather slow, characterized by the long lifetimes of the energy levels of RE ions. The response of UCNPs to time-varying excitation light could provide contrast or other interesting information for biomedical imaging on an easy-to-operate time scale, i.e., $\mu$s–ms. This could be an interesting topic of research.

The use of UCNPs for biomedical imaging is still in its infancy, and most work so far has been for the proof of concept. Functional imaging using UCNPs in different biological models is becoming and will remain a hot research topic in next stage.

# Comments on the Papers

## I Drug quantification in turbid media by fluorescence imaging combined with light-absorption correction using white Monte Carlo simulation

*H. Xie, H. Liu, P. Svenmarker, J. Axelsson, C. T. Xu, S. Gräfe, J. H. Lundeman, H. P. H. Cheng, S. Svanberg, N. Bendsoe, P. E. Andersen, K. Svanberg, S. Andersson-Engels*

The concentration of photosensitizers is a critical parameter in photodynamic therapy, and it is preferable to quantify them using fluorescence techniques as they are noninvasive. However, the detected fluorescence signal generally exhibits a complex dependence on the concentration of photosensitizers deep in the tissue, as different types of tissue have different optical properties. This article describes a procedure for correction of the fluorescence intensity due to the different optical properties of tissues, utilizing time-resolved fluorescence white Monte-Carlo simulations combined with the Beer-Lambert law. The method was validated using data obtained from tissue phantoms and murine tissues.

I proposed the light-absorption-correction procedure, and performed a major part of the data analysis and the implementation of the time-resolved white Monte-Carlo simulations. I made substantial contributions to the preparation of the manuscript.

II **Synthesis of $NaYF_4$:$Yb^{3+}$, $Er^{3+}$ upconverting nanocrystals in a capillary-based continuous microfluidic reaction system**

*H. Liu, O. Jakobsson, C. T. Xu, H. Xie, T. Laurell, S. Andersson-Engels*

The continuous flow synthesis of $NaYF_4$:$Yb^{3+}$,$Er^{3+}$ upconverting nanocrystals was achieved for the first time in a capillary-based microfluidic reaction system. Microfluidic synthesis opens up the possibility of real-time reaction monitoring and scale-up production.

I participated in the planning of the work, and was responsible for the main part of the nanoparticle synthesis and optical characterization. I wrote the manuscript.

III **Upconverting nanoparticles for pre-clinical diffuse optical imaging, microscopy and sensing: Current trends and future challenges**

*C. T. Xu, Q. Zhan, H. Liu, G. Somesfalean, J. Qian, S. He, S. Andersson-Engels*

This is a review article in which the current state of the art of UCNPs and their applications in diffuse imaging, microscopy and sensing are discussed. In addition, future directions and challenges for the development of UCNPs as potential clinical biomedical materials are presented.

I made substantial contributions to the preparation of the manuscript.

IV **Balancing power density based quantum yield characterization of upconverting nanoparticles for arbitrary excitation intensities**

*H. Liu, C. T. Xu, D. Lindgren, H. Xie, D. Thomas, C. Gundlach, S. Andersson-Engels*

The characterization of the excitation-intensity-dependent quantum yield of upconverting nanoparticles is a crucial issue for both the development of upconverting materials and their biomedical applications. In this study, a simple relationship between the quantum yield and excitation intensity was theoretically derived for two-photon upconversion emission. A two-parameter quantum yield characterization approach is proposed, involving the balancing power density and the maximum attainable quantum yield. The results presented in this paper provide a potential standard characterization approach for upconverting nanoparticles regarding energy conversion.

I proposed the quantum yield characterization of UCNPs using balancing power density. I was responsible for the theoretical derivation, the experimental work and the data analysis. I wrote the manuscript.

V **Deep tissue optical imaging of upconverting nanoparticles enabled by exploiting higher intrinsic quantum yield through use of millisecond single pulse excitation with high peak power**

*H. Liu, C. T. Xu, G. Dumlupinar, O. B. Jensen, P. E. Andersen, S. Andersson-Engels*

The low quantum yield of upconverting nanoparticles, especially at low excitation fluence rate, as is typically encountered in biological tissues, constitutes a severe hurdle for biomedical applications of upconverting nanoparticles in deep tissues. This cannot be overcome by increasing the intensity of continuous excitation of the upconverting nanoparticles due to laser safety concerns. A pulsed excitation approach was thus proposed in this study, which has the potential to employing higher intrinsic quantum yield of upconverting nanoparticles using the same amount of excitation energy, thus extending the imaging depth.

I participated in the proposal of the idea, and was responsible for the numerical simulations, the experimental work and the data analysis. I played a major part in the interpretation of the experimental results and prepared the manuscript.

VI **Autofluorescence insensitive imaging using upconverting nanoparticles in scattering media**

*C. T. Xu, N. Svensson, J. Axelsson, P. Svenmarker, G. Somesfalean, G. Chen, H. Liang, H. Liu, Z. Zhang, S. Andersson-Engels*

In this study, autofluorescence-free diffuse optical imaging using upconverting nanoparticles as a type of exogenous luminescent markers was demonstrated in a tissue phantom. It was found that UCNP-mediated imaging led to exceptionally high contrast, compared to conventional downconverting luminescent markers, due to the absence of autofluorescence.

I took part in the nanoparticle synthesis and optical characterization, as well as discussions on the optical imaging experiments.

VII **High-resolution fluorescence diffuse optical tomography developed with nonlinear upconverting nanoparticles**

*C. T. Xu, P. Svenmarker, H. Liu, X. Wu, M. E. Messing, L. R. Wallenberg, S. Andersson-Engels*

In this study, it was demonstrated that the spatial resolution of the FDOT reconstruction images could be significantly improved by using nonlinear upconverting nanoparticles, compared to using conventional linear fluorophores as contrast agents. The improvement was achieved by selective excitation, to some extent, of individual fluorescent targets due to the large excitation gradient, rooted in the nonlinear power density dependence of upconverting nanoparticles.

I took part in the design of the experiments and participated in all parts. I made substantial contributions to the data analysis.

## VIII Multibeam fluorescence diffuse optical tomography using upconverting nanoparticles

*H. Liu, C. T. Xu, S. Andersson-Engels*

In FDOT, the image reconstruction quality is essentially determined by the amount and quality of the information obtained from boundary measurements. In this study, the unique nonlinear power dependence of upconverting nanoparticles was exploited to increase the information density for FDOT. By performing excitation simultaneously with two beams, orthogonal data were obtained when using UCNPs as contrast agents, leading to significantly improved reconstructions. The same behavior could not be observed when using linear fluorophores.

I proposed the use of multiple excitation beams for UCNP-mediated fluorescence diffuse optical tomography in order to increase information density. I participated in planning the work, took part in all the experiments, and prepared the manuscript.

## IX Multispectral guided fluorescence diffuse optical tomography using upconverting nanoparticles

*P. Svenmarker, C. T. Xu, H. Liu, X. Wu, S. Andersson-Engels*

In this study, a spatially varying regularization map was created using multispectral emission information generated using upconverting nanoparticles as contrast agent, and was incorporated as *a priori* information to guide fluorescence diffuse optical tomography. This led to significantly improved resolution and contrast in the reconstructed images.

I contributed substantially to the synthesis and optical characterization of the upconverting nanoparticles. I took part in the preparation of the manuscript.

# Acknowledgements

First of all, I would like to express my deepest gratitude to my supervisor, Professor Stefan Andersson-Engels, who was my mentor throughout this endeavor. I still remember how "green" I was when I started my PhD studies, but thanks to him, I now feel much more confident in scientific research. His patience, guidance and encouragement have been indispensable. Thank you for encouraging me to pursue my own ideas, and for giving me a little "nudge" when necessary. Thank you also for all the illuminating discussions we have had, especially when I was confused or frustrated. Your kindness and support will never be forgotten.

I would also like to express my thanks to my co-supervisor, Professor Thomas Laurell, for giving me the opportunity to "dabble" in the fantastic field of microfluidics, and for his wonderful support and rewarding discussions throughout the period of these studies.

Special thanks also to my mentor, Dr. Gabriel Somesfalean. I am truly grateful to you for introducing me to a splendid world, for your invaluable help in research throughout the years, and for being a good friend.

Sincere thanks also to Professor Peter E. Andersen, for fruitful collaboration, and for organizing the wonderful summer school at Hven.

I would also like to express my gratitude to the Svanberg family. Thank you all for your warm welcome when I set foot in a foreign land. Sune, thank you for organizing the very nice apartment. I will never forget the night when you painted the floor. You painted my family in the bedroom, and painted yourself out, in order to make our living environment even nicer. Thank you also for your truly inspiring and contagious enthusiasm for life and science. Katarina, thank you for always being friendly and helpful, in both professional and personal matters. Emilie

and Kristina, thank you for including my family as members of your family.

Furthermore, I would like to thank my splendid colleagues, past and present, for creating the friendliest of atmospheres. It has really been a pleasure to work with you. Can Xu, I am really grateful for your help in research and for our fruitful discussions and collaboration on many interesting topics, and for your help to my whole family. I have learnt a lot from you about science and life. It is my fortune to have you as a good friend. Haiyan Xie, thank you for your help and company in the first project, and for your positive attitude to life and research. It is simply wonderful to have you as a good friend and an elder sister. Ola Jakobsson, thank you for your invaluable help in the project on microfuidic synthesis of upconverting nanoparticles, and also for your help to my family. The experience of barbecues and making chili oil is unforgettable. Pontus Svenmarker, thank you for your constant help and collaboration in research throughout the years. I would also like to thank Johan Axelsson for his kindness and willingness in solving technical problems; Dmitry Khoptyar, for taking me to my first international measurement campaign at the Technical University of Denmark, and also for organizing many social events; Erik Alerstam, for sharing his passion for science, as well as for carrying out time-of-flight measurements for me; Patrik Lundin, for sharing his experience and knowledge in supervising the wonderful diode laser lab; Nina Reistad, for her kindness and pleasant talks; and Xia Wu, Gökhan Dumplupinar, Björn Thomasson, Arefeh Mousavi, Arman Subash, Alfi Shaharin, and Hugo Söderlund, for being excellent MSc students.

I would like to express my thanks to all present and former members of the Atomic Physics Division for providing a friendly, exciting and stimulating environment to work in. I particularly enjoyed the Friday meetings, the annual Lund Laser Center excursion, St. Lucia celebrations and the julbord!

This thesis could not have been completed without the assistance of my splendid local and international collaboration partners: Sarah Fredriksson, Fredrik Olsson, Anna Gisselsson, Hanna Toftevall, Pontus Kjellman, Rene in 't Zandt, Linda Andersson, Malin Mejare, Nina Rogelius, and collaborators at Genovis AB in Lund, David Lindgren and Maria E. Messing at the Division of Solid State Physics in Lund, Diana Thomas and Carsten Gundlach at MAXLAB in Lund, L. Reine Wallenberg at Polymer and Materials Chemistry/nCHREM in Lund, Guanying Chen and Professor Zhiguo Zhang at Harbin Institute of Technology in China, Qiuqiang Zhan, Professor Sailing He and collaborators at Zhejiang University in China, Ole B. Jensen at

the Department of Photonics Engineering, Technical University of Denmark, and collaborators at Biolitec AG in Jena, Germany. My appreciation also goes to Dr. Hampus Nilsson and Dr. Sven Huldt at the Lund Observatory, and Professor Dan Hessman at the Division of Solid State Physics in Lund, for their assistance in the spectroscopic measurements on upconverting nanoparticles, Professor Jörgen Larsson at the Division of Atomic Physics in Lund for his assistance in the X-ray diffraction measurement on upconverting nanoparticles, Professor Yong Zhang at the Department of Biomedical Engineering, National University of Singapore, and Professor Frank C. J. M. van Veggel at the Department of Chemistry, University of Victoria, Canada, for instructing me about the synthesis of upconverting nanoparticles.

Finally, I would like to express my deepest gratitude to my beloved family and friends for their unconditional support and encouragement, and also for making life colorful and enjoyable. At the end, I would also like to apologize to my beloved sweet daughter. Please forgive me for not having more time and patience to play with you.

# References


[1]. R. Weissleder and U. Mahmood. *Molecular imaging.* Radiology **219**, 316–333 (2001).

[2]. T. F. Massoud and S. S. Gambhir. *Molecular imaging in living subjects: seeing fundamental biological processes in a new light.* Genes Dev. **17**, 545–580 (2003).

[3]. R. Weissleder, C.-H. Tung, U. Mahmood and A. Bogdanov. *In vivo imaging of tumors with protease-activated near-infrared fluorescent probes.* Nat. Biotech. **17**, 375–378 (1999).

[4]. R. M. Hoffman. *The multiple uses of fluorescent proteins to visualize cancer in vivo.* Nat. Rev. Cancer **5**, 796–806 (2005).

[5]. A. Petrovsky, E. Schellenberger, L. Josephson, R. Weissleder and A. Bogdanov. *Near-infrared fluorescent imaging of tumor apoptosis.* Cancer Res. **63**, 1936–1942 (2003).

[6]. V. Ntziachristos, E. A. Schellenberger, J. Ripoll, D. Yessayan, E. Graves, A. Bogdanov, L. Josephson and R. Weissleder. *Visualization of antitumor treatment by means of fluorescence molecular tomography with an annexin V-Cy5.5 conjugate.* Proc. Natl. Acad. Sci. U. S. A. **101**, 12294–12299 (2004).

[7]. V. Ntziachristos, A. G. Yodh, M. Schnall and B. Chance. *Concurrent MRI and diffuse optical tomography of breast after indocyanine green enhancement.* Proc. Natl. Acad. Sci. U. S. A. **97**, 2767–2772 (2000).

[8]. M. Andresen, A. C. Stiel, J. Fölling, D. Wenzel, A. Schönle, A. Egner, C. Eggeling, S. W. Hell and S. Jakobs. *Photoswitchable fluorescent proteins enable monochromatic multilabel imaging and dual color fluorescence nanoscopy.* Nat. Biotechnol. **26**, 1035–1040 (2008).

[9]. M. Chalfie, Y. Tu, G. Euskirchen, W. W. Ward and D. C. Prasher. *Green fluorescent protein as a marker for gene expression.* Science **263**, 802–805 (1994).

[10]. A. M. Smith and S. M. Nie. *Chemical analysis and cellular imaging with quantum dots.* Analyst **129**, 672–677 (2004).

[11]. A. M. Smith, X. H. Gao and S. M. Nie. *Quantum dot nanocrystals for in vivo molecular and cellular imaging.* Photochem. Photobiol. **80**, 377–385 (2004).

[12]. M. Howarth, K. Takao, Y. Hayashi and A. Y. Ting. *Targeting quantum dots to surface proteins in living cells with biotin ligase.* Proc. Natl. Acad. Sci. U. S. A. **102**, 7583–7588 (2005).

[13]. X. Gao and S. R. Dave. *Quantum dots for cancer molecular imaging.* Adv. Exp. Med. Biol. **620**, 57–73 (2007).

[14]. Y. Zhong, N. Kaji, M. Tokeshi and Y. Baba. *Nanobiotechnology: quantum dots in bioimaging.* Expert Rev. Proteomic. **4**, 565–572 (2007).

[15]. X. F. Yu, L. D. Chen, K. Y. Li, Y. Li, S. Xiao, X. Luo, J. Liu, L. Zhou, Y. L. Deng, D. W. Pang and Q. Q. Wang. *Immunofluorescence detection with quantum dot bioconjugates for hepatoma in vivo.* J. Biomed. Opt. **12**, 014008 (2007).

[16]. Y. Xing and J. H. Rao. *Quantum dot bioconjugates for in vitro diagnostics & in vivo imaging.* Cancer Biomark. **4**, 307–319 (2008).

[17]. M. A. Walling, J. A. Novak and J. R. E. Shepard. *Quantum dots for live cell and in vivo imaging.* Int. J. Mol. Sci. **10**, 441–491 (2009).

[18]. S. C. Davis, B. W. Pogue, H. Dehghani and K. D. Paulsen. *Contrast-detail analysis characterizing diffuse optical fluorescence tomography image reconstruction.* J. Biomed. Opt. **10**, 050501 (2005).

[19]. F. Auzel. *Upconversion and anti-Stokes processes with f and d ions in solids.* Chem. Rev. **104**, 139–173 (2004).

[20]. D. K. Chatterjee, E. Zhang and Y. Zhang. *Upconverting nanoparticles for cellular imaging.* NSTI-Nanotech. **2**, 535–538 (2008).

[21]. M. Nyk, R. Kumar, T. Y. Ohulchanskyy, E. J. Bergey and P. N. Prasad. *High contrast in vitro and in vivo photoluminescence bioimaging using near infrared to near infrared up-conversion in $Tm^{3+}$ and $Yb^{3+}$ doped fluoride nanophosphors.* Nano Lett. **8**, 3834–3838 (2008).

[22]. F. Wang, D. Banerjee, Y. Liu, X. Chen and X. Liu. *Upconversion nanoparticles in biological labeling, imaging, and therapy.* Analyst **135**, 1839–1854 (2010).

[23]. J. Zhou, Z. Liu and F. Li. *Upconversion nanophosphors for small-animal imaging.* Chem. Soc. Rev. **41**, 1323–1349 (2012).

[24]. P. Svenmarker, C. T. Xu and S. Andersson-Engels. *Use of nonlinear upconverting nanoparticles provides increased spatial resolution in fluorescence diffuse imaging.* Opt. Lett. **35**, 2789–2791 (2010).

[25]. R. H. Page, K. I. Schaffers, P. A. Waide, J. B. Tassano, S. A. Payne, W. F. Krupke and W. K. Bischel. *Upconversion-pumped luminescence efficiency of rare-earth-doped hosts sensitized with trivalent ytterbium.* J. Opt. Soc. Am. B **15**, 996–1008 (1998).

[26]. A. H. Li, Q. Lü, Z. R. Zheng, L. Sun, W. Z. Wu, W. L. Liu, Y. Q. Yang and T. Q. Lü. *Yellow-green upconversion luminescence of $Dy^{3+}$ ion in $LiNbO_3$ crystal heavily codoped with ZnO.* J. Appl. Phys. **102**, 113102 (2007).

[27]. A. H. Li, Z. R. Zheng, Q. Lü, L. Sun, Y. H. Xu, W. L. Liu, W. Z. Wu, Y. Q. Yang and T. Q. Lü. *Sensitized holmium upconversion emission in $LiNbO_3$ triply doped with $Ho^{3+}$, $Yb^{3+}$, and $Nd^{3+}$.* J. Appl. Phys. **104**, 063526 (2008).

[28]. L. M. Maestro, E. M. Rodriguez, F. Vetrone, R. Naccache, H. L. Ramirez, D. Jaque, J. A. Capobianco and J. G. Solé. *Nanoparticles for highly efficient multiphoton fluorescence bioimaging.* Opt. Express **18**, 23544–23553 (2010).

[29]. C. F. Gainer, G. S. Joshua and M. Romanowski. *Toward the use of two-color emission control in upconverting $NaYF_4$: $Er^{3+}$,$Yb^{3+}$ nanoparticles for biomedical imaging.* Proc. SPIE **8231**, 82310I (2012).

[30]. W. Zhang, F. Ding and S. Y. Chou. *Large enhancement of upconversion luminescence of $NaYF_4$:$Yb^{3+}$/$Er^{3+}$ nanocrystal by 3D plasmonic nano-antennas.* Adv. Mater. **24**, OP236–OP241 (2012).

[31]. C. F. Gainer, G. S. Joshua, C. R. De Silva and M. Romanowski. *Control of green and red upconversion in $NaYF_4$ :$Yb^{3+}$, $Er^{3+}$ nanoparticles by excitation modulation.* J. Mater. Chem. **21**, 18530–18533 (2011).

[32]. J. W. S. B. Rayleigh. *On the light from the sky, its polarization and colour.* Phil. Mag. **41**, 107–120, 274–279 (1871).

[33]. G. Mie. *Beiträge zur optik trüber medien, speziell kolloidaler metallösungen.* Ann. Phys. **330**, 377–445 (1908).

[34]. C. V. Raman. *A new radiation.* Indian J. Phys. **2**, 387–398 (1928).

[35]. L. Brillouin. *Diffusion de la lumière et des rayonnes X par un corps transparent homogéne; Influence del'agitation thermique.* Ann. Phys. **17**, 88 (1922).

[36]. R. Y. Chiao, C. H. Townes and B. P. Stoicheff. *Stimulated Brillouin scattering and coherent generation of intense hypersonic waves.* Phys. Rev. Lett. **12**, 592–595 (1964).

[37]. J. W. S. B. Rayleigh. *On the scattering of light by small particles.* Phil. Mag. **41**, 447–454 (1871).

[38]. S. Prahl. Mie scattering calculator (2012). URL http://omlc.ogi.edu/calc/mie_calc.html.

[39]. L. G. Henyey and J. L. Greenstein. *Diffuse radiation in the galaxy.* Astrophys. J. **93**, 70–83 (1941).

[40]. S. L. Jacques, C. A. Alter and S. A. Prahl. *Angular dependence of HeNe laser light scattering by human dermis.* Lasers Life Sci. **1**, 309–333 (1987).

[41]. T. Tarvainen, V. Kolehmainen, A. Pulkkinen, M. Vauhkonen, M. Schweiger, S. R. Arridge and J. P. Kaipio. *An approximation error approach for compensating for modelling errors between the radiative transfer equation and the diffusion approximation in diffuse optical tomography.* Inverse Probl. **26**, 015005 (2010).

[42]. R. Graaff, J. G. Aarnoudse, J. R. Zijp, P. M. A. Sloot, F. F. M. de Mul, J. Greve and M. H. Koelink. *Reduced light-scattering properties for mixtures of spherical particles: a simple approximation derived from Mie calculations.* Appl. Opt. **31**, 1370–1376 (1992).

[43]. J. R. Mourant, T. Fuselier, J. Boyer, T. M. Johnson and I. J. Bigio. *Predictions and measurements of scattering and absorption over broad wavelength ranges in tissue phantoms.* Appl. Opt. **36**, 949–957 (1997).

[44]. S. L. Jacques. *Optical properties of biological tissues: a review.* Phys. Med. Biol. **58**, R37–R61 (2013).

[45]. W. G. Zijlstra, A. Buursma and O. W. van Assendelft. *Visible and near infrared absorption spectra of human and animal haemoglobin–Determination and application.* VSP BV (2000).

[46]. S. J. Matcher and C. E. Cooper. *Absolute quantification of deoxyhaemoglobin concentration in tissue near infrared spectroscopy.* Phys. Med. Biol. **39**, 1295 (1994).

[47]. L. Kou, D. Labrie and P. Chylek. *Refractive indices of water and ice in the 0.65- to 2.5-μm spectral range.* Appl. Opt. **32**, 3531–3540 (1993).

[48]. R. M. Pope and E. S. Fry. *Absorption spectrum (380–700 nm) of pure water. II. Integrating cavity measurements.* Appl. Opt. **36**, 8710–8723 (1997).

[49]. A. Cerussi, N. Shah, D. Hsiang, A. Durkin, J. Butler and B. J. Tromberg. *In vivo absorption, scattering, and physiologic properties of 58 malignant breast tumors determined by broadband diffuse optical spectroscopy.* J. Biomed. Opt. **11**, 044005 (2006).

[50]. N. Kollias and A. Baqer. *On the assessment of melanin in human skin in vivo.* Photochem. Photobiol. **43**, 49–54 (1986).

[51]. N. Kollias, R. M. Sayre, L. Zeise and M. R. Chedekel. *Photoprotection by melanin.* J. Photochem. Photobiol. B **9**, 135–160 (1991).

[52]. H. Fedorow, F. Tribl, G. Halliday, M. Gerlach, P. Riederer and K. L. Double. *Neuromelanin in human dopamine neurons: Comparison with peripheral melanins and relevance to Parkinson's disease.* Prog. Neu-

robiol. **75**, 109–124 (2005).

[53]. G. M. Hale and M. R. Querry. *Optical constants of water in the 200-nm to 200-µm wavelength region.* Appl. Opt. **12**, 555–563 (1973).

[54]. S. A. Prahl. Optical absorption of hemoglobin (2009). URL http://omlc.ogi.edu/spectra/hemoglobin/index.html.

[55]. R. L. P. van Veen, H. J. C. M. Sterenborg, A. Pifferi, A. Torricelli and R. Cubeddu. *Determination of VIS-NIR absorption coefficients of mammalian fat, with time- and spatially resolved diffuse reflectance and transmission spectroscopy.* OSA Technical Digest (2004).

[56]. Beer. *Bestimmung der absorption des rothen Lichts in farbigen Fflüssigkeiten.* Ann. Phys. **162**, 78–88 (1852).

[57]. D. T. Delpy, M. Cope, P. van der Zee, S. R. Arridge, S. Wray and J. Wyatt. *Estimation of optical pathlength through tissue from direct time of flight measurement.* Phys. Med. Biol. **33**, 1433 (1988).

[58]. A. Sassaroli and S. Fantini. *Comment on the modified Beer-Lambert law for scattering media.* Phys. Med. Biol. **49**, N255–N257 (2004).

[59]. R. Drezek, I. Boiko, M. Follen, R. Richards-Kortum, A. Malpica, K. Sokolov and U. Utzinger. *Understanding the contributions of NADH and collagen to cervical tissue fluorescence spectra: Modeling, measurements, and implications.* J. Biomed. Opt. **6**, 385–396 (2001).

[60]. B. R. Masters, P. T. So and E. Gratton. *Multiphoton excitation fluorescence microscopy and spectroscopy of in vivo human skin.* Biophys. J. **72**, 2405–2412 (1997).

[61]. R. Richards-Kortum and E. Sevick-Muraca. *Quantitative optical spectroscopy for tissue diagnosis.* Annu. Rev. Phys. Chem. **47**, 555–606 (1996).

[62]. M. J. Koehler, K. König, P. Elsner, R. Bückle and M. Kaatz. *In vivo assessment of human skin aging by multiphoton laser scanning tomography.* Opt. Lett. **31**, 2879–2881 (2006).

[63]. I. Georgakoudi, B. C. Jacobson, M. G. Müller, E. E. Sheets, K. Badizadegan, D. L. Carr-Locke, C. P. Crum, C. W. Boone, R. R. Dasari, J. Van Dam and M. S. Feld. *NAD(P)H and collagen as in vivo quantitative fluorescent biomarkers of epithelial precancerous changes.* Cancer Res. **62**, 682–687 (2002).

[64]. N. Billinton and A. W. Knight. *Seeing the wood through the trees: A review of techniques for distinguishing green fluorescent protein from endogenous autofluorescence.* Anal. Biochem. **291**, 175–197 (2001).

[65]. G. R. Cherrick, S. W. Stein, C. M. Leevy and C. S. Davidson. *Indocyanine green - Observations on its physical properties, plasma decay, and hepatic extraction.* J. Clin. Invest. **39**, 592–600 (1960).

[66]. R. Heim, D. C. Prasher and R. Y. Tsien. *Wavelength mutations and posttranslational autoxidation of green fluorescent protein.* Proc. Natl. Acad. Sci. U. S. A. **91**, 12501–12504 (1994).

[67]. N. C. Shaner, M. Z. Lin, M. R. McKeown, P. A. Steinbach, M. W. Hazelwood, K. L.and Davidson and R. Y. Tsien. *Improving the photostability of bright monomeric orange and red fluorescent proteins.* Nat. Meth. **5**, 545–551 (2008).

[68]. L. Ye, K.-T. Yong, L. Liu, I. Roy, R. Hu, J. Zhu, H. Cai, W.-C. Law, J. Liu, K. Wang, J. Liu, Y. Liu, Y. Hu, X. Zhang, M. T. Swihart and P. N. Prasad. *A pilot study in non-human primates shows no adverse response to intravenous injection of quantum dots.* Nat. Nano. **7**, 453–458 (2012).

[69]. Y. Su, M. Hu, C. Fan, Y. He, Q. Li, W. Li, L.-H. Wang, P. Shen and Q. Huang. *The cytotoxicity of CdTe quantum dots and the relative contributions from released cadmium ions and nanoparticle properties.*

Biomaterials **31**, 4829–4834 (2010).

[70]. A. Schuster. *Radiation through a foggy atomsphere.* The Observatory **26**, 379–381 (1903).

[71]. A. Schuster. *Radiation through a foggy atmosphere.* Astrophys. J. **21**, 1–22 (1905).

[72]. S. Chandrasekhar. *Radiative transfer.* Dover publications (1960).

[73]. K. M. Case and P. F. Zweifel. *Linear transport theory.* Addision-Wesley Pub. Co. (1967).

[74]. C. L. Longmire and M. N. Rosenbluth. *Diffusion of charged particles across a magnetic field.* Phys. Rev. **103**, 507–510 (1956).

[75]. R. L. Longini and R. Zdrojkowski. *A note on the theory of backscattering of light by living tissue.* IEEE Transactions on Biomedical Engineering **BME-15**, 4–10 (1968).

[76]. L. Reynolds, C. Johnson and A. Ishimaru. *Diffuse reflectance from a finite blood medium: applications to the modeling of fiber optic catheters.* Appl. Opt. **15**, 2059–2067 (1976).

[77]. A. Ishimaru. *Wave propagation and scattering inrandom media.* Academic Press (1978).

[78]. T. Svensson. *Pharmaceutical and biomedical applications of spectroscopy in the photon migration regime.* PhD thesis Lund University (2008).

[79]. S. R. Arridge and M. Schweiger. *Image reconstruction in optical tomography.* Phil. Trans. R. Soc. Lond. B **352**, 717–726 (1997).

[80]. S. R. Arridge. *TOPICAL REVIEW Optical tomography in medical imaging.* Inverse Probl. **15**, R41–R93 (1999).

[81]. L. C. L. Chin, W. M. Whelan and I. A. Vitkin. *Information content of point radiance measurements in turbid media: implications for interstitial optical property quantification.* Appl. Opt. **45**, 2101–2114 (2006).

[82]. M. Chu, K. Vishwanath, A. D. Klose and H. Dehghani. *Light transport in biological tissue using three-dimensional frequency-domain simplified spherical harmonics equations.* Phys. Med. Biol. **54**, 2493–2509 (2009).

[83]. D. Yang, X. Chen, Z. Peng, X. Wang, J. Ripoll, J. Wang and J. Liang. *Light transport in turbid media with non-scattering, low-scattering and high absorption heterogeneities based on hybrid simplified spherical harmonics with radiosity model.* Biomed. Opt. Express **4**, 2209–2223 (2013).

[84]. J. B. Domínguez and Y. Bérubé-Lauziére. *Diffuse light propagation in biological media by a time-domain parabolic simplified spherical harmonics approximation with ray-divergence effects.* Appl. Opt. **49**, 1414–1429 (2010).

[85]. L. Zhang, J. Li, X. Yi, H. Zhao and F. Gao. *Analytical solutions to the simplified spherical harmonics equations using eigen decompositions.* Opt. Lett. **38**, 5462–5465 (2013).

[86]. A. Liemert and A. Kienle. *Analytical solutions of the simplified spherical harmonics equations.* Opt. Lett. **35**, 3507–3509 (2010).

[87]. K. Peng, X. Gao, X. Qu, N. Ren, X. Chen, X. He, X. Wang, J. Liang and J. Tian. *Graphics processing unit parallel accelerated solution of the discrete ordinates for photon transport in biological tissues.* Appl. Opt. **50**, 3808–3823 (2011).

[88]. B. C. Wilson and G. Adam. *A Monte Carlo model for the absorption and flux distributions of light in tissue.* Med. Phys. **10**, 824–830 (1983).

[89]. L. Wang, S. L. Jacques and L. Zheng. *MCML-Monte Carlo modeling of light transport in multi-layered tissues.* Comput. Meth. Programs Biomed. **47**, 131–146 (1995).

[90]. E. Alerstam. *Optical spectroscopy of turbid media: time-domain measurements and accelerated Monte Carlo modelling.* PhD thesis Lund University (2011).

[91]. E. Alerstam. *Anisotropic diffusive transport: a rigorous theory for connecting microscopic scattering and macroscopic transport properties.* arXiv:1311.3603v3 (2013).

[92]. M. Schweiger, S. R. Arridge, M. Hiraoka and D. T. Delpy. *The finite element method for the propagation of light in scattering media: boundary and source conditions.* Med. Phys. **22**, 1779–1792 (1995).

[93]. J. B. Fishkin, S. Fantini, M. J. vandeVen and E. Gratton. *Gigahertz photon density waves in a turbid medium: Theory and experiments.* Phys. Rev. E **53**, 2307–2319 (1996).

[94]. L. Martí-López, J. C. Hebden and J. B. Domínguez. *Estimates of minimum pulse width and maximum modulation frequency for diffusion optical tomography.* Opt. Lasers Eng. **44**, 1172–1184 (2006).

[95]. G. Alexandrakis, T. J. Farrell and M. S. Patterson. *Accuracy of the diffusion approximation in determining the optical properties of a two-layer turbid medium.* Appl. Opt. **37**, 7401–7409 (1998).

[96]. S. L. Jacques and B. W. Pogue. *Tutorial on diffuse light transport.* J. Biomed. Opt. **13**, 041302 (2008).

[97]. T. Durduran, A. G. Yodh, B. Chance and D. A. Boas. *Does the photon-diffusion coefficient depend on absorption?* J. Opt. Soc. Am. A **14**, 3358–3365 (1997).

[98]. A. Zhang, D. Piao, C. F. Bunting and B. W. Pogue. *Photon diffusion in a homogeneous medium bounded externally or internally by an infinitely long circular cylindrical applicator. I. Steady-state theory.* J. Opt. Soc. Am. A **27**, 648–662 (2010).

[99]. A. J. Welch and M. J. C. Gemert. *Optical-thermal response of laser irradiated tissue, second edition.* Springer (2010).

[100]. D. Y. Paithankar, A. U. Chen, B. W. Pogue, M. S. Patterson and E. M. Sevick-Muraca. *Imaging of fluorescent yield and lifetime from multiply scattered light reemitted from random media.* Appl. Opt. **36**, 2260–2272 (1997).

[101]. A. Soubret and V. Ntziachristos. *Fluorescence molecular tomography in the presence of background fluorescence.* Phys. Med. Biol. **51**, 3983–4001 (2006).

[102]. R. A. J. Groenhuis, H. A. Ferwerda and J. J. Ten Bosch. *Scattering and absorption of turbid materials determined from reflection measurements. 1: Theory.* Appl. Opt. **22**, 2456–2462 (1983).

[103]. M. Keijzer, W. M. Star and P. R. M. Storchi. *Optical diffusion in layered media.* Appl. Opt. **27**, 1820–1824 (1988).

[104]. M. S. Patterson, B. Chance and B. C. Wilson. *Time resolved reflectance and transmittance for the non-invasive measurement of tissue optical properties.* Appl. Opt. **28**, 2331–2336 (1989).

[105]. T. J. Farrell, M. S. Patterson and B. C. Wilson. *A diffusion theory model of spatially resolved, steady-state diffuse reflectance for the non-invasive determination of tissue optical properties in vivo.* Med. Phys. **19**, 879–888 (1992).

[106]. S. R. Arridge, M. Cope and D. T. Delpy. *The theoretical basis for the determination of optical pathlengths in tissue: temporal and frequency analysis.* Phys. Med. Biol. **37**, 1531–1560 (1992).

[107]. D. Contini, F. Martelli and G. Zaccanti. *Photon migration through a turbid slab described by a model based on diffusion approximation. I. Theory.* Appl. Opt. **36**, 4587–4599 (1997).

[108]. F. Martelli, D. Contini, A. Taddeucci and G. Zaccanti. *Photon migration through a turbid slab described by a model based on diffusion approximation. II. Comparison with Monte Carlo results.* Appl. Opt. **36**, 4600–4612 (1997).

[109]. E. Alerstam, S. Andersson-Engels and T. Svensson. *White Monte Carlo for time-resolved photon migration.* J. Biomed. Opt. **13**, 041304 (2008).

[110]. E. Alerstam, T. Svensson and S. Andersson-Engels. *Parallel computing with graphics processing units for high-speed Monte Carlo simulation of photon migration.* J. Biomed. Opt. **13**, 060504 (2008).

[111]. S. A. Prahl, M. Keijzer, S. L. Jacques and A. J. Welch. *A Monte Carlo model of light propagation in tissue.* **IS 5**, 102–111 (1989).

[112]. J. Swartling, A. Pifferi, A. M. K. Enejder and S. Andersson-Engels. *Accelerated Monte Carlo models to simulate fluorescence spectra from layered tissues.* J. Opt. Soc. Am. A **20**, 714–727 (2003).

[113]. X. Teng, Y. Zhu, W. Wei, S. Wang, J. Huang, R. Naccache, W. Hu, A. I. Y. Tok, Y. Han, Q. Zhang, Q. Fan, W. Huang, J. A. Capobianco and L. Huang. *Lanthanide-doped $Na_xScF_{3+x}$ nanocrystals: Crystal structure evolution and multicolor tuning.* J. Am. Chem. Soc. **134**, 8340–8343 (2012).

[114]. Q. M. Huang, J. C. Yu, E. Ma and K. M. Lin. *Synthesis and characterization of highly efficient near-infrared upconversion $Sc^{3+}/Er^{3+}/Yb^{3+}$ tridoped $NaYF_4$.* J. Phys. Chem. C **114**, 4719–4724 (2010).

[115]. D. Hartree. *The Calculation of atomic Structures.* John Wiley & Sons Ltd., New York (1957).

[116]. J. C. Slater. *Quantum theory of atomic structure.* McGraw-Hill, New York (1960).

[117]. X. Xu and M. Su, editors. *Luminescence and luminescent materials (in Chinese).* Chemical Industry Press (China) (2004).

[118]. G. H. Dieke and H. M. Crosswhite. *The spectra of the doubly and triply Ionized rare earths.* Appl. Opt. **2**, 675–686 (1963).

[119]. W. T. Carnall, G. L. Goodman, K. Rajnak and R. S. Rana. *A systematic analysis of the spectra of the lanthanides doped Into single-crystal $LaF_3$.* J. Chem. Phys. **90**, 3443–3457 (1989).

[120]. G. Liu. *Spectroscopic properties of rare earths in optical materials* chapter Electronic energy level structure. Springer (2005).

[121]. B. Henderson and G. F. Imbusch. *Optical Spectroscopy for Inorganic Solids.* Oxford Univ Press Inc (1989).

[122]. G. W. Burdick, S. M. Crooks and M. F. Reid. *Ambiguities in the parametrization of $4f^N-4f^N$ electric-dipole transition intensities.* Phys. Rev. B **59**, R7789–R7792 (1999).

[123]. D. J. Newman and G. Balasubramanian. *Parametrization of rare-earth ion transition intensities.* J. Phys. C **8**, 37–44 (1975).

[124]. M. F. Reid and F. S. Richardson. *Lanthanide 4f→4f electric dipole intensity theory.* J. Phys. Chem. **88**, 3579–3586 (1984).

[125]. B. R. Judd. *Optical absorption intensities of rare-earth ions.* Phys. Rev. **127**, 750–761 (1962).

[126]. G. S. Ofelt. *Intensities of crystal spectra of rare-earth ions.* J. Chem. Phys. **37**, 511–520 (1962).

[127]. M. P. Hehlen, M. G. Brik and K. W. Kramer. *50th anniversary of the Judd-Ofelt theory: An experimentalist's view of the formalism and its application.* J. Lumin. **136**, 221–239 (2013).

[128]. M. F. Reid. *Spectroscopic properties of rare earths in optical materials* chapter Transition Intensities. Springer (2005).

[129]. G. Chen, H. Liu, G. Somesfalean, Y. Sheng, H. Liang, Z. Zhang, Q. Sun and F. Wang. *Enhancement of the upconversion radiation in $Y_2O_3$: $Er^{3+}$ nanocrystals by codoping with $Li^+$ ions.* Appl. Phys. Lett. **92**, 113114 (2008).

[130]. G. Chen, H. Liu, H. Liang, G. Somesfalean and Z. Zhang. *Upconversion emission enhancement in $Yb^{3+}/Er^{3+}$-codoped $Y_2O_3$ nanocrystals by tridoping with $Li^+$ Ions.* J. Chem. Phys. C **112**, 12030–12036 (2008).

[131]. N. Bloembergen. *Solid state infrared quantum counters.* Phys. Rev. Lett. **2**, 84–85 (1959).

[132]. F. Auzel. *Compteur quantique par transfert d'energie entre deux ions de terres rares dans un tungstate mixte et dans un verre.* C. R. Acad. Sci. Paris B **262**, 1016–1019 (1966).

[133]. F. Auzel. *Compteur quantique par transfert d'energie de $Yb^{3+}$ a $Tm^{3+}$ dans un tungstate mixte et dans verre germanate.* C. R. Acad. Sci. Paris B **263**, 819–821 (1966).

[134]. V. V. Ovsyankin and P. P. Feofilov. *Mechanism of summation of electronic excitations in activated crystals.* JETP Lett. **3**, 494–497 (1966).

[135]. T. Förster. *Zwischenmolekulare energiewanderung und fluoreszenz.* Ann. Phys. **437**, 55–75 (1948).

[136]. D. L. Dexter. *A theory of sensitized luminescence in solids.* J. Chem. Phys. **21**, 836–850 (1953).

[137]. M. Inokuti and F. Hirayama. *Influence of energy transfer by the exchange mechanism on donor luminescence.* J. Chem. Phys. **43**, 1978–1989 (1965).

[138]. T. Kushida. *Energy transfer and cooperative optical transitions in rare-earth doped inorganic materials. II. Comparison with experiments.* J. Phys. Soc. Jpn. **34**, 1327–1333 (1973).

[139]. Pouradier, J. F. and Auzel, F. *Calcul des probabilités des transferts d'énergie entre ions de terres rares. I. une méthode de calcul unifiée utilisant des méthodes tensorielles standard.* J. Phys. France **39**, 825–831 (1978).

[140]. J. C. Wright. *Up-conversion and excited state energy transfer in rare-earth doped materials.* Top. Appl. Phys. **15**, 239–295 (1976).

[141]. F. Auzel. *Multiphonon-assisted anti-Stokes and Stokes fluorescence of triply ionized rare-earth ions.* Phys. Rev. B **13**, 2809–2817 (1976).

[142]. V. V. Ovsyakin and P. P. Feofilov. *Cooperative sensitization of luminescence in crystals activated with rare earth ions.* JETP Lett. **4**, 317–318 (1966).

[143]. T. Miyakawa and D. L. Dexter. *Cooperative and stepwise excitation of luminescence: Trivalent rare-earth ions in $Yb^{3+}$-sensitized crystals.* Phys. Rev. B **1**, 70–80 (1970).

[144]. M. Yokota and O. Tanimoto. *Effects of diffusion on energy transfer by resonance.* J. Phys. Soc. Jpn. **22**, 779–784 (1967).

[145]. M. J. Weber. *Luminescence decay by energy migration and transfer: Observation of diffusion-limited relaxation.* Phys. Rev. B **4**, 2932–2939 (1971).

[146]. W. J. C. Grant. *Role of rate equations in the theory of luminescent energy transfer.* Phys. Rev. B **4**, 648–663 (1971).

[147]. F. Wang, R. Deng, J. Wang, Q. Wang, Y. Han, H. Zhu, X. Chen and X. Liu. *Tuning upconversion through energy migration in core-shell nanoparticles.* Nat. Mater. **10**, 968–973 (2011).

[148]. X. Xie, N. Gao, R. Deng, Q. Sun, Q. Xu and X. Liu. *Mechanistic investigation of photon upconversion in $Nd^{3+}$-sensitized core-shell nanoparticles.* J. Am. Chem. Soc. **135**, 12608–12611 (2013).

[149]. Y.-F. Wang, G.-Y. Liu, L.-D. Sun, J.-W. Xiao, J.-C. Zhou and C.-H. Yan. *$Nd^{3+}$-sensitized upconversion nanophosphors: efficient in vivo bioimaging probes with minimized heating effect.* ACS Nano **7**, 7200–7206 (2013).

[150]. F. W. Ostermayer and L. G. Van Uitert. *Cooperative energy transfer from $Yb^{3+}$ to $Tb^{3+}$ in $YF_3$.* Phys. Rev. B **1**, 4208–4212 (1970).

[151]. H. Liang, G. Chen, L. Li, Y. Liu, F. Qin and Z. Zhang. *Upconversion luminescence in $Yb^{3+}/Tb^{3+}$-codoped monodisperse $NaYF_4$ nanocrystals.* Opt. Commun. **282**, 3028 – 3031 (2009).

[152]. E. Nakazawa and S. Shionoya. *Cooperative luminescence in $YbPO_4$.* Phys. Rev. Lett. **25**, 1710–1712 (1970).

[153]. F. Auzel, D. Meichenin, F. Pellé and P. Goldner. *Cooperative luminescence as a defining process for RE-ions clustering in glasses and crystals.* Opt. Mater. **4**, 35–41 (1994).

[154]. J. S. Chivian, W. E. Case and D. D. Eden. *The photon avalanche: A new phenomenon in $Pr^{3+}$-based infrared quantum counters.* Appl. Phys. Lett. **35**, 124–125 (1979).

[155]. M. F. Joubert, S. Guy and B. Jacquier. *Model of the photon-avalanche effect.* Phys. Rev. B **48**, 10031–10037 (1993).

[156]. M. F. Joubert. *Photon avalanche upconversion in rare earth laser materials.* Opt. Mater. **11**, 181–203 (1999).

[157]. R. Scheps. *Upconversion laser processes.* Prog. Quantum. Electron. **20**, 271 – 358 (1996).

[158]. Ph. Goldner and F. Pellé. *Photon avalanche fluorescence and lasers.* Opt. Mater. **5**, 239–249 (1996).

[159]. S. Sivakumar, F. C. J. M van Veggel and P. S. May. *Near-Infrared (NIR) to red and green up-conversion emission from silica sol-gel thin films made with $La_{0.45}Yb_{0.50}Er_{0.05}F_3$ nanoparticles, hetero-looping-enhanced energy transfer (Hetero-LEET): A new up-conversion process.* J. Am. Chem. Soc. **129**, 620–625 (2007).

[160]. G. Chen, H. Liang, H. Liu, G. Somesfalean and Z. Zhang. *Anomalous power dependence of upconversion emissions in $Gd_2O_3$: $Er^{3+}$ nanocrystals under diode laser excitation of 970 nm.* J. Appl. Phys. **105**, 114315 (2009).

[161]. E. Downing, L. Hesselink, J. Ralston and R. Macfarlane. *A three-color, solid-state, three-dimensional display.* Science **273**, 1185–1189 (1996).

[162]. G. Blasse and B. C. Grabmaier. *Luminescent materials.* Springer-Verlag Berlin Heidelberg (1994).

[163]. F. Wang and X. Liu. *Recent advances in the chemistry of lanthanide-doped upconversion nanocrystals.* Chem. Soc. Rev. **38**, 976–989 (2009).

[164]. J. M. F. Vandijk and M. F. H. Schuurmans. *On the nonradiative and radiative decay-rates and a modified exponential energy-gap law for 4f-4f transitions in rare-earth ions.* J. Chem. Phys. **78**, 5317–5323 (1983).

[165]. K. W. Krämer, D. Biner, G. Frei, H. U. Güdel, M. P. Hehlen and S. R. Lüthi. *Hexagonal sodium yttrium fluoride based green and blue emitting upconversion phosphors.* Chem. Mater. **16**, 1244–1251 (2004).

[166]. S. Heer, K. Kömpe, H. U. Güdel and M. Haase. *Highly efficient multicolour upconversion emission in transparent colloids of lanthanide-doped $NaYF_4$ nanocrystals.* Adv. Mater. **16**, 2102–2105 (2004).

[167]. D. K. Chatterjee, M. K. Gnanasammandhan and Y. Zhang. *Small upconverting fluorescent nanoparticles for biomedical applications.* Small **6**, 2781–2795 (2010).

[168]. A. Gnach and A. Bednarkiewicz. *Lanthanide-doped up-converting nanoparticles: Merits and challenges.* Nano Today **7**, 532–563 (2012).

[169]. G. Wang, Q. Peng and Y. Li. *Upconversion luminescence of monodisperse $CaF_2$:$Yb^{3+}$/$Er^{3+}$ nanocrystals.* J. Am. Chem. Soc. **131**, 14200–14201 (2009).

[170]. M. Ito, C. Goutaudier, Y. Guyot, K. Lebbou, T. Fukuda and G. Boulon. *Crystal growth, $Yb^{3+}$ spectroscopy, concentration quenching analysis and potentiality of laser emission in $Ca_{1-X}Yb_XF_{2+X}$.* J. Phys.: Condens. Matter **16**, 1501–1521 (2004).

[171]. N.-N. Dong, M. Pedroni, F. Piccinelli, G. Conti, A. Sbarbati, J. E. Ramírez-Hernández, L. M. Maestro, M. C. Iglesias-de la Cruz, F. Sanz-Rodriguez, A. Juarranz, F. Chen, F. Vetrone, J. A. Capobianco, J. G. Solé, M. Bettinelli, D. Jaque and A. Speghini. *NIR-to-NIR two-photon excited $CaF_2$:$Tm^{3+}$,$Yb^{3+}$ nanoparticles: multifunctional nanoprobes for highly penetrating fluorescence bio-imaging.* ACS Nano **5**, 8665–8671 (2011).

[172]. G. Chen, J. Shen, T. Y. Ohulchanskyy, N. J. Patel, A. Kutikov, Z. Li, J. Song, R. K. Pandey, H. Ågren, P. N. Prasad and G. Han. *($\alpha$-$NaYbF_4$:$Tm^{3+}$)/$CaF_2$ core/shell nanoparticles with efficient near-Infrared to near-infrared upconversion for high-contrast deep tissue bioimaging.* ACS Nano **6**, 8280–8287 (2012).

[173]. J. Shen, G. Chen, T. Y. Ohulchanskyy, S. J. Kesseli, S. Buchholz, Z. Li, P. N. Prasad and G. Han. *Tunable near infrared to ultraviolet upconversion luminescence enhancement in ($\alpha$-$NaYbF_4$:$Tm^{3+}$)/$CaF_2$ core/shell nanoparticles for in situ real-time recorded biocompatible photoactivation.* Small **9**, 3213–3217 (2013).

[174]. F. Shi, J. Wang, X. Zhai, D. Zhao and W. Qin. *Facile synthesis of $\beta$-$NaLuF_4$ : Yb/Tm hexagonal nanoplates with intense ultraviolet upconversion luminescence.* CrystEngComm **13**, 3782–3787 (2011).

[175]. Q. Liu, Y. Sun, T. Yang, W. Feng, C. Li and F. Li. *Sub-10 nm hexagonal lanthanide-doped $NaLuF_4$ upconversion nanocrystals for sensitive bioimaging in vivo.* J. Am. Chem. Soc. **133**, 17122–17125 (2011).

[176]. J. Zhou, X. Zhu, M. Chen, Y. Sun and F. Li. *Water-stable $NaLuF_4$-based upconversion nanophosphors with long-term validity for multimodal lymphatic imaging.* Biomaterials **33**, 6201–6210 (2012).

[177]. T. S. Yang, Y. Sun, Q. Liu, W. Feng, P. Y. Yang and F. Y. Li. *Cubic sub-20 nm $NaLuF_4$-based upconversion nanophosphors for high-contrast bioimaging in different animal species.* Biomaterials **33**, 3733–3742 (2012).

[178]. S. Zeng, J. Xiao, Q. Yang and J. Hao. *Bi-functional $NaLuF_4$:$Gd^{3+}$/$Yb^{3+}$/$Tm^{3+}$ nanocrystals: structure controlled synthesis, near-infrared upconversion emission and tunable magnetic properties.* J. Mater. Chem. **22**, 9870–9874 (2012).

[179]. Y. Yang, Y. Sun, T. Cao, J. Peng, Y. Liu, Y. Wu, W. Feng, Y. Zhang and F. Li. *Hydrothermal synthesis of $NaLuF_4$: $^{153}Sm,Yb,Tm$ nanoparticles and their application in dual-modality upconversion luminescence and SPECT bioimaging.* Biomaterials **34**, 774 – 783 (2013).

[180]. N. Niu, P. Yang, F. He, X. Zhang, S. Gai, C. Li and J. Lin. *Tunable multicolor and bright white emission of one-dimensional $NaLuF_4$:$Yb^{3+}$,$Ln^{3+}$ (Ln = Er, Tm, Ho, Er/Tm, Tm/Ho) microstructures.* J. Mater. Chem. **22**, 10889–10899 (2012).

[181]. Y. Li, J. Zhang, Y. Luo, X. Zhang, Z. Hao and X. Wang. *Color control and white light generation of upconversion luminescence by operating dopant concentrations and pump densities in $Yb^{3+}$, $Er^{3+}$ and $Tm^{3+}$ tri-doped $Lu_2O_3$ nanocrystals.* J. Mater. Chem. **21**, 2895–2900 (2011).

[182]. F. Wang, Y. Han, C. S. Lim, Y. Lu, J. Wang, J. Xu, H. Chen, C. Zhang, M. Hong and X. Liu. *Simultaneous phase and size control of upconversion nanocrystals through lanthanide doping.* Nature **463**, 1061–1065

(2010).

[183]. F. Wang and X. Liu. *Upconversion multicolor fine-tuning: Visible to near-infrared emission from lanthanide-doped $NaYF_4$ nanoparticles.* J. Am. Chem. Soc. **130**, 5642–5643 (2008).

[184]. G. Chen, Y. Liu, Y. Zhang, G. Somesfalean, Z. Zhang, Q. Sun and F. Wang. *Bright white upconversion luminescence in rare-earth-ion-doped $Y_2O_3$ nanocrystals.* Appl. Phys. Lett. **91**, 133103 (2007).

[185]. G. Chen, H. Liu, G. Somesfalean, H. Liang and Z. Zhang. *Upconversion emission tuning from green to red in $Yb^{3+}/Ho^{3+}$-codoped $NaYF_4$ nanocrystals by tridoping with $Ce^{3+}$ ions.* Nanotechnology **20**, 385704 (2009).

[186]. N. Rakov, G. S. Maciel, M. L. Sundheimer, L. de S. Menezes, A. S. L. Gomes, Y. Messaddeq, F. C. Cassanjes, G. Poirier and S. J. L. Ribeiro. *Blue upconversion enhancement by a factor of 200 in $Tm^{3+}$-doped tellurite glass by codoping with $Nd^{3+}$ ions.* J. Appl. Phys. **92**, 6337–6339 (2002).

[187]. T. S. Hauck, A. A. Ghazani and W. C. W. Chan. *Assessing the effect of surface chemistry on gold nanorod uptake, toxicity, and gene expression in mammalian cells.* Small **4**, 153–159 (2008).

[188]. F. Zhao, Y. Zhao, Y. Liu, X. Chang, C. Chen and Y. Zhao. *Cellular uptake, intracellular trafficking, and cytotoxicity of nanomaterials.* Small **7**, 1322–1337 (2011).

[189]. H. Kobayashi, M. Ogawa, R. Alford, P. L. Choyke and Y. Urano. *New strategies for fluorescent probe design in medical diagnostic imaging.* Chem. Rev. **110**, 2620–2640 (2010).

[190]. J. A. Champion and S. Mitragotri. *Role of target geometry in phagocytosis.* Proc. Natl. Acad. Sci. U. S. A. **103**, 4930–4934 (2006).

[191]. A. Verma and F. Stellacci. *Effect of surface properties on nanoparticle-cell interactions.* Small **6**, 12–21 (2010).

[192]. Y. Qiu, Y. Liu, L. Wang, L. Xu, R. Bai, Y. Ji, X. Wu, Y. Zhao, Y. Li and C. Chen. *Surface chemistry and aspect ratio mediated cellular uptake of Au nanorods.* Biomaterials **31**, 7606–7619 (2010).

[193]. J.-C. Boyer and F. C. J. M. van Veggel. *Absolute quantum yield measurements of colloidal $NaYF_4$: $Er^{3+}$, $Yb^{3+}$ upconverting nanoparticles.* Nanoscale **2**, 1417–1419 (2010).

[194]. G. Yi, H. Lu, S. Zhao, Y. Ge, W. Yang, D. Chen and L.-H. Guo. *Synthesis, characterization, and biological application of size-controlled nanocrystalline $NaYF_4$:Yb,Er infrared-to-visible up-conversion phosphors.* Nano Lett. **4**, 2191–2196 (2004).

[195]. X. Wang, J. Zhuang, Q. Peng and Y. D. Li. *A general strategy for nanocrystal synthesis.* Nature **437**, 121–124 (2005).

[196]. J.-C. Boyer, L. A. Cuccia and J. A. Capobianco. *Synthesis of colloidal upconverting $NaYF_4$: $Er^{3+}/Yb^{3+}$ and $Tm^{3+}/Yb^{3+}$ monodisperse nanocrystals.* Nano Lett. **7**, 847–852 (2007).

[197]. H.-X. Mai, Y.-W. Zhang, R. Si, Z.-G. Yan, L.-D. Sun, L.-P. You and C.-H. Yan. *High-quality sodium rare-earth fluoride nanocrystals: Controlled synthesis and optical properties.* J. Am. Chem. Soc. **128**, 6426–6436 (2006).

[198]. G. S. Yi and G. M. Chow. *Synthesis of hexagonal-phase $NaYF_4$:Yb,Er and $NaYF_4$:Yb,Tm nanocrystals with efficient up-conversion fluorescence.* Adv. Funct. Mater. **16**, 2324–2329 (2006).

[199]. Z. Li and Y. Zhang. *An efficient and user-friendly method for the synthesis of hexagonal-phase $NaYF_4$ :Yb, Er/Tm nanocrystals with controllable shape and upconversion fluorescence.* Nanotechnology **19**, 345606 (2008).

[200]. A. D. Ostrowski, E. M. Chan, D. J. Gargas, E. M. Katz, G. Han, P. J. Schuck, D. J. Milliron and B. E. Cohen. *Controlled synthesis and single-particle imaging of bright, sub-10 nm lanthanide-doped upconverting nanocrystals.* ACS Nano **6**, 2686–2692 (2012).

[201]. W. Zheng, S. Y. Zhou, Z. Chen, P. Hu, Y. S. Liu, D. T. Tu, H. M. Zhu, R. F. Li, M. D. Huang and X. Y. Chen. *Sub-10 nm lanthanide-doped $CaF_2$ nanoprobes for time-resolved luminescent biodetection.* Angew. Chem. Int. Ed. **52**, 6671–6676 (2013).

[202]. Q. Liu, W. Feng, T. Yang, T. Yi and F. Li. *Upconversion luminescence imaging of cells and small animals.* Nat. Protocols **8**, 2033–2044 (2013).

[203]. E. M. Chan, C. Xu, A. W. Mao, G. Han, J. S. Owen, B. E. Cohen and D. J. Milliron. *Reproducible, high-throughput synthesis of colloidal nanocrystals for optimization in multidimensional parameter space.* Nano Lett. **10**, 1874–1885 (2010).

[204]. H.-Q. Wang and T. Nann. *Monodisperse upconverting nanocrystals by microwave-assisted synthesis.* ACS Nano **3**, 3804–3808 (2009).

[205]. W. Zou, C. Visser, J. A. Maduro, M. S. Pshenichnikov and J. C. Hummelen. *Broadband dye-sensitized upconversion of near-infrared light.* Nat. Photon. **6**, 560–564 (2012).

[206]. G. Chen, T. Y. Ohulchanskyy, R. Kumar, H. Ågren and P. N. Prasad. *Ultrasmall monodisperse $NaYF_4$:$Yb^{3+}$/$Tm^{3+}$ nanocrystals with enhanced near-infrared to near-infrared upconversion photoluminescence.* ACS Nano **4**, 3163–3168 (2010).

[207]. H. Liang, Y. Zheng, L. Wu, L. Liu, Z. Zhang and W. Cao. *Enhancing upconversion emissions of $NaTm_{0.02}Yb_xY_{0.98-x}F_4$ nanocrystals through increasing $Yb^{3+}$ doping.* J. Lumin. **131**, 1802 – 1806 (2011).

[208]. F. Vetrone, J.-C. Boyer, J. A. Capobianco, A. Speghini and M. Bettinelli. *Significance of $Yb^{3+}$ concentration on the upconversion mechanisms in codoped $Y_2O_3$: $Er^{3+}$, $Yb^{3+}$ nanocrystals.* J. Appl. Phys. **96**, 661–667 (2004).

[209]. F. Vetrone, R. Naccache, V. Mahalingam, C. G. Morgan and J. A. Capobianco. *The active-core/active-shell approach: A strategy to enhance the upconversion luminescence in lanthanide-doped nanoparticles.* Adv. Funct. Mater. **19**, 2924–2929 (2009).

[210]. D. Yang, C. Li, G. Li, M. Shang, X. Kang and J. Lin. *Colloidal synthesis and remarkable enhancement of the upconversion luminescence of $BaGdF_5$:$Yb^{3+}$/$Er^{3+}$ nanoparticles by active-shell modification.* J. Mater. Chem. **21**, 5923–5927 (2011).

[211]. B. Zhou, L. Tao, Y. H. Tsang and W. Jin. *Core-shell nanoarchitecture: a strategy to significantly enhance white-light upconversion of lanthanide-doped nanoparticles.* J. Mater. Chem. C **1**, 4313–4318 (2013).

[212]. R. Esteban, M. Laroche and J.-J. Greffet. *Influence of metallic nanoparticles on upconversion processes.* J. Appl. Phys. **105**, 033107 (2009).

[213]. M. Saboktakin, X. Ye, S. J. Oh, S.-H. Hong, A. T. Fafarman, U. K. Chettiar, N. Engheta, C. B. Murray and C. R. Kagan. *Metal-enhanced upconversion luminescence tunable through metal nanoparticle-nanophosphor separation.* ACS Nano **6**, 8758–8766 (2012).

[214]. M. Saboktakin, X. Ye, U. K. Chettiar, N. Engheta, C. B. Murray and C. R. Kagan. *Plasmonic enhancement of nanophosphor upconversion luminescence in Au nanohole arrays.* ACS Nano **7**, 7186–7192 (2013).

[215]. L. Sudheendra, V. Ortalan, S. Dey, N. D. Browning and I. M. Kennedy. *Plasmonic enhanced emissions from cubic $NaYF_4$:Yb:Er/Tm nanophosphors.* Chem. Mater. **23**, 2987–2993 (2011).

[216]. Z. Q. Li, S. Chen, J. J. Li, Q. Q. Liu, Z. Sun, Z. B. Wang and S. M. Huang. *Plasmon-enhanced upconversion fluorescence in $NaYF_4$:Yb/Er/Gd nanorods coated with Au nanoparticles or nanoshells.* J. Appl. Phys. **111**, 014310 (2012).

[217]. W. Xu, Y. Zhu, X. Chen, J. Wang, L. Tao, S. Xu, T. Liu and H. Song. *A novel strategy for improving upconversion luminescence of $NaYF_4$:Yb, Er nanocrystals by coupling with hybrids of silver plasmon nanostructures and poly(methyl methacrylate) photonic crystals.* Nano Research **6**, 1–13 (2013).

[218]. A. Priyam, N. M Idris and Y. Zhang. *Gold nanoshell coated $NaYF_4$ nanoparticles for simultaneously enhanced upconversion fluorescence and darkfield imaging.* J. Mater. Chem. **22**, 960–965 (2012).

[219]. W. Ge, X. R. Zhang, M. Liu, Z. W. Lei, R. J. Knize and Yalin Liu. *Distance dependence of gold-enhanced upconversion luminescence in $Au/SiO_2/Y_2O_3$:$Yb^{3+}$, $Er^{3+}$ nanoparticles.* Theranostics **3**, 282–288 (2013).

[220]. X. Yu, M. Li, M. Xie, L. Chen, Y. Li and Q. Wang. *Dopant-controlled synthesis of water-soluble hexagonal $NaYF_4$ nanorods with efficient upconversion fluorescence for multicolor bioimaging.* Nano Research **3**, 51–60 (2010).

[221]. D. Chen, P. Huang, Y. Yu, F. Huang, A. Yang and Y. Wang. *Dopant-induced phase transition: a new strategy of synthesizing hexagonal upconversion $NaYF_4$ at low temperature.* Chem. Commun. **47**, 5801–5803 (2011).

[222]. Y. Bai, K. Yang, Y. Wang, X. Zhang and Y. Song. *Enhancement of the upconversion photoluminescence intensity in $Li^+$ and $Er^{3+}$ codoped $Y_3O_3$ nanocrystals.* Opt. Commun. **281**, 2930–2932 (2008).

[223]. Q. Dou and Y. Zhang. *Tuning of the structure and emission spectra of upconversion nanocrystals by alkali ion doping.* Langmuir **27**, 13236–13241 (2011).

[224]. F. Wang, J. Wang and X. Liu. *Direct evidence of a surface quenching effect on size-dependent luminescence of upconversion nanoparticles.* Angew. Chem. Int. Ed. **49**, 7456–7460 (2010).

[225]. A. Kar and A. Patra. *Impacts of core-shell structures on properties of lanthanide-based nanocrystals: crystal phase, lattice strain, downconversion, upconversion and energy transfer.* Nanoscale **4**, 3608–3619 (2012).

[226]. Q. Su, S. Han, X. Xie, H. Zhu, H. Chen, C.-K. Chen, R.-S. Liu, X. Chen, F. Wang and X. Liu. *The effect of surface coating on energy migration-mediated upconversion.* J. Am. Chem. Soc. **134**, 20849–20857 (2012).

[227]. C. Zhang and J. Y. Lee. *Prevalence of anisotropic shell growth in rare earth core-shell upconversion nanocrystals.* ACS Nano **7**, 4393–4402 (2013).

[228]. Z. Li, Y. Zhang and S. Jiang. *Multicolor core/shell-structured upconversion fluorescent nanoparticles.* Adv. Mater. **20**, 4765–4769 (2008).

[229]. H.-S. Qian and Y. Zhang. *Synthesis of hexagonal-phase core-shell $NaYF_4$ nanocrystals with tunable upconversion fluorescence.* Langmuir **24**, 12123–12125 (2008).

[230]. X. Liu, X. Kong, Y. Zhang, L. Tu, Y. Wang, Q. Zeng, C. Li, Z. Shi and H. Zhang. *Breakthrough in concentration quenching threshold of upconversion luminescence via spatial separation of the emitter doping area for bio-applications.* Chem. Commun. **47**, 11957–11959 (2011).

[231]. Q. Zhan, J. Qian, H. Liang, G. Somesfalean, D. Wang, S. He, Z. Zhang and S. Andersson-Engels. *Using 915 nm laser excited $Tm^{3+}/Er^{3+}/Ho^{3+}$-Doped $NaYbF_4$ upconversion nanoparticles for in*

*vitro and deeper in vivo bioimaging without overheating irradiation.* ACS Nano **5**, 3744–3757 (2011).

[232]. J. Shen, G. Chen, A.-M. Vu, W. Fan, O. S. Bilsel, C.-C. Chang and G. Han. *Engineering the upconversion nanoparticle excitation wavelength: Cascade sensitization of tri-doped upconversion colloidal nanoparticles at 800 nm.* Adv. Opt. Mater. **1**, 644–650 (2013).

[233]. G. Tian, Z. Gu, L. Zhou, W. Yin, X. Liu, L. Yan, S. Jin, W. Ren, G. Xing, S. Li and Y. Zhao. *$Mn^{2+}$ dopant-controlled synthesis of $NaYF_4$:Yb/Er upconversion nanoparticles for in vivo imaging and drug delivery.* Adv. Mater. **24**, 1226–1231 (2012).

[234]. G. Chen, Y. Zhang, G. Somesfalean, Z. Zhang, Q. Sun and F. Wang. *Two-color upconversion in rare-earth-ion-doped $ZrO_2$ nanocrystals.* Appl. Phys. Lett. **89**, 163105 (2006).

[235]. F. Wang, D. K. Chatterjee, Z. Li, Y. Zhang, X. Fan and M. Wang. *Synthesis of polyethylenimine/$NaYF_4$ nanoparticles with upconversion fluorescence.* Nanotechnology **17**, 5786 (2006).

[236]. J. Zeng, Z. Li, J. Su, L. Wang, R. Yan and Y. Li. *Synthesis of complex rare earth fluoride nanocrystal phosphors.* Nanotechnology **17**, 3549 (2006).

[237]. Y. Wei, F. Lu, X. Zhang and D. Chen. *Polyol-mediated synthesis and luminescence of lanthanide-doped $NaYF_4$ nanocrystal upconversion phosphors.* J. Alloys Compd. **455**, 376–384 (2008).

[238]. L. Xiong, Z. Chen, M. Yu, F. Li, C. Liu and C. Huang. *Synthesis, characterization, and in vivo targeted imaging of amine-functionalized rare-earth up-converting nanophosphors.* Biomaterials **30**, 5592–5600 (2009).

[239]. C. Chen, L.-D. Sun, Z.-X. Li, L.-L. Li, J. Zhang, Y.-W. Zhang and C.-H. Yan. *Ionic liquid-based route to spherical $NaYF_4$ nanoclusters with the assistance of microwave radiation and their multicolor upconversion luminescence.* Langmuir **26**, 8797–8803 (2010).

[240]. R. Naccache, F. Vetrone, V. Mahalingam, L. A. Cuccia and J. A. Capobianco. *Controlled synthesis and water dispersibility of hexagonal phase $NaGdF_4$:$Ho^{3+}$/$Yb^{3+}$ nanoparticles.* Chem. Mater. **21**, 717–723 (2009).

[241]. J.-C. Boyer, M.-P. Manseau, J. I. Murray and F. C. J. M. van Veggel. *Surface modification of upconverting $NaYF_4$ nanoparticles with PEG-phosphate ligands for NIR (800 nm) biolabeling within the biological window.* Langmuir **26**, 1157–1164 (2010).

[242]. N. J. J. Johnson, N. M. Sangeetha, J.-C. Boyer and F. C. J. M. van Veggel. *Facile ligand-exchange with polyvinylpyrrolidone and subsequent silica coating of hydrophobic upconverting $\beta$-$NaYF4$:$Yb^{3+}$/$Er^{3+}$ nanoparticles.* Nanoscale **2**, 771–777 (2010).

[243]. J. Jin, Y.-J. Gu, C. W.-Y. Man, J. Cheng, Z. Xu, Y. Zhang, H. Wang, V. H.-Y. Lee, S. H. Cheng and W.-T. Wong. *Polymer-coated $NaYF_4$:$Yb^{3+}$, $Er^{3+}$ upconversion nanoparticles for charge-dependent cellular imaging.* ACS Nano **5**, 7838–7847 (2011).

[244]. Z. Chen, H. Chen, H. Hu, M. Yu, F. Li, Q. Zhang, Z. Zhou, T. Yi and C. Huang. *Versatile synthesis strategy for carboxylic acid-functionalized upconverting nanophosphors as biological labels.* J. Am. Chem. Soc. **130**, 3023–3029 (2008).

[245]. H. P. Zhou, C. H. Xu, W. Sun and C. H. Yan. *Clean and flexible modification strategy for carboxyl/aldehyde-functionalized upconversion nanoparticles and their optical applications.* Adv. Funct. Mater. **19**, 3892–3900 (2009).

[246]. G. S. Yi and G. M. Chow. *Water-soluble $NaYF_4$: Yb,Er(Tm)/$NaYF_4$/polymer core/shell/shell nanoparticles with*

*significant enhancement of upconversion fluorescence.* Chem. Mater. **19**, 341–343 (2007).

[247]. Z. Li and Y. Zhang. *Monodisperse silica-coated polyvinylpyrrolidone/$NaYF_4$ nanocrystals with multicolor upconversion fluorescence emission.* Angew. Chem. Int. Ed. **45**, 7732–7735 (2006).

[248]. R. A. Jalil and Y. Zhang. *Biocompatibility of silica coated $NaYF_4$ upconversion fluorescent nanocrystals.* Biomaterials **29**, 4122–4128 (2008).

[249]. Z. Liu, G. Yi, H. Zhang, J. Ding, Y. Zhang and J. Xue. *Monodisperse silica nanoparticles encapsulating upconversion fluorescent and superparamagnetic nanocrystals.* Chem. Commun. pp 694–696 (2008).

[250]. H. S. Qian, H. C. Guo, P. C. L. Ho, R. Mahendran and Y. Zhang. *Mesoporous-silica-coated up-conversion fluorescent nanoparticles for photodynamic therapy.* Small **5**, 2285–2290 (2009).

[251]. G. Jiang, J. Pichaandi, N. J. J. Johnson, R. D. Burke and F. C. J. M. van Veggel. *An effective polymer cross-linking strategy to obtain stable dispersions of upconverting $NaYF_4$ nanoparticles in buffers and biological growth media for biolabeling applications.* Langmuir **28**, 3239–3247 (2012).

[252]. J. B. Ma, P. Huang, M. He, L. Y. Pan, Z. J. Zhou, L. L. Peng, G. Gao and D. X. Cui. *Folic acid-conjugated $LaF_3$:Yb,Tm@$SiO_2$ nanoprobes for targeting dual-modality imaging of upconversion luminescence and X-ray computed tomography.* J. Phys. Chem. B **116**, 14062–14070 (2012).

[253]. L. Xiong, Z. Chen, Q. Tian, T. Cao, C. Xu and F. Li. *High contrast upconversion luminescence targeted imaging in vivo using peptide-labeled nanophosphors.* Anal. Chem. **81**, 8687–8694 (2009).

[254]. K. Kuningas, T. Rantanen, T. Ukonaho, T. Lovgren and T. Soukka. *Homogeneous assay technology based on upconverting phosphors.* Anal. Chem. **77**, 7348–7355 (2005).

[255]. H. Lu, G. Yi, S. Zhao, D. Chen, L.-H. Guo and J. Cheng. *Synthesis and characterization of multi-functional nanoparticles possessing magnetic, up-conversion fluorescence and bio-affinity properties.* J. Mater. Chem. **14**, 1336–1341 (2004).

[256]. K. Yu, Y. Cui, C. S. Li, M. B. Zaman, R. Wilkins, X. H. Wu and J. Y. Ouyang. *Optical response of CdSe quantum dots to Cesium-137 Gamma-Ray radiation.* J. Nanosci. Nanotechnol. **10**, 1819–1824 (2010).

[257]. L. L. Li, P. W. Wu, K. Hwang and Y. Lu. *An exceptionally simple strategy for DNA-functionalized up-conversion nanoparticles as biocompatible agents for nanoassembly, DNA delivery, and imaging.* J. Am. Chem. Soc. **135**, 2411–2414 (2013).

[258]. H. Päkkilä, M. Ylihärsilä, S. Lahtinen, L. Hattara, N. Salminen, R. Arppe, M. Lastusaari, P. Saviranta and T. Soukka. *Quantitative multianalyte microarray immunoassay utilizing upconverting phosphor technology.* Anal. Chem. **84**, 8628–8634 (2012).

[259]. R. Madru, P. Svenmarker, C. Ingvar, F. Stahlberg, S. Andersson-Engels, L. Knutsson and S.-E. Strand. *Development of a hybrid nanoprobe for triple-modality MR/SPECT/Optical fluorescence imaging.* submitted (2014).

[260]. Y. Liu, K. Ai, J. Liu, Q. Yuan, Y. He and L. Lu. *A high-performance ytterbium-based nanoparticulate contrast agent for in vivo X-Ray computed tomography imaging.* Angew. Chem. Int. Ed. **51**, 1437–1442 (2012).

[261]. A. Xia, M. Chen, Y. Gao, D. Wu, W. Feng and F. Li. *$Gd^{3+}$ complex-*

*modified $NaLuF_4$-based upconversion nanophosphors for trimodality imaging of NIR-to-NIR upconversion luminescence, X-Ray computed tomography and magnetic resonance.* Biomaterials **33**, 5394 – 5405 (2012).

[262]. H. Xing, W. Bu, S. Zhang, X. Zheng, M. Li, F. Chen, Q. He, L. Zhou, W. Peng, Y. Hua and J. Shi. *Multifunctional nanoprobes for upconversion fluorescence, MR and CT trimodal imaging.* Biomaterials **33**, 1079–1089 (2012).

[263]. H. Xing, W. Bu, Q. Ren, X. Zheng, M. Li, S. Zhang, H. Qu, Z. Wang, Y. Hua, K. Zhao, L. Zhou, W. Peng and J. Shi. *A $NaYbF_4:Tm^{3+}$ nanoprobe for CT and NIR-to-NIR fluorescent bimodal imaging.* Biomaterials **33**, 5384–5393 (2012).

[264]. R. Kumar, M. Nyk, T. Y. Ohulchanskyy, C. A. Flask and P. N. Prasad. *Combined optical and MR bioimaging using rare earth ion doped $NaYF_4$ nanocrystals.* Adv. Funct. Mater. **19**, 853–859 (2009).

[265]. Z. Li, Y. Zhang, B. Shuter and N. M. Idris. *Hybrid lanthanide nanoparticles with paramagnetic shell coated on upconversion fluorescent nanocrystals.* Langmuir **25**, 12015–12018 (2009).

[266]. Y. Il Park, J. H. Kim, K. T. Lee, K. S. Jeon, H. Bin Na, J. H. Yu, H. M. Kim, N. Lee, S. H. Choi, S. I. Baik, H. Kim, S. P. Park, B. J. Park, Y. W. Kim, S. H. Lee, S. Y. Yoon, I. C. Song, W. K. Moon, Y. D. Suh and T. Hyeon. *Nonblinking and nonbleaching upconverting nanoparticles as an optical imaging nanoprobe and T1 magnetic resonance imaging contrast agent.* Adv. Mater. **21**, 4467–4471 (2009).

[267]. J. Shen, L.-D. Sun, Y.-W. Zhang and C.-H. Yan. *Superparamagnetic and upconversion emitting $Fe_3O_4/NaYF_4$: Yb,Er hetero-nanoparticles via a crosslinker anchoring strategy.* Chem. Commun. **46**, 5731–5733 (2010).

[268]. C. C. Mi, J. P. Zhang, H. Y. Gao, X. L. Wu, M. Wang, Y. F. Wu, Y. Q. Di, Z. R. Xu, C. B. Mao and S. K. Xu. *Multifunctional nanocomposites of superparamagnetic ($Fe_3O_4$) and NIR-responsive rare earth-doped up-conversion fluorescent ($NaYF_4$: Yb, Er) nanoparticles and their applications in biolabeling and fluorescent imaging of cancer cells.* Nanoscale **2**, 1141–1148 (2010).

[269]. C. N. Zhong, P. A. P. Yang, X. B. Li, C. X. Li, D. Wang, S. L. Gai and J. Lin. *Monodisperse bifunctional $Fe_3O_4$@$NaGdF_4$:Yb/Er@$NaGdF_4$:Yb/Er core-shell nanoparticles.* RSC Adv. **2**, 3194–3197 (2012).

[270]. X. Zhu, J. Zhou, M. Chen, M. Shi, W. Feng and F. Li. *Core-shell $Fe_3O_4$@$NaLuF_4$:Yb,Er/Tm nanostructure for MRI, CT and upconversion luminescence tri-modality imaging.* Biomaterials **33**, 4618–4627 (2012).

[271]. J. Zhou, M. X. Yu, Y. Sun, X. Z. Zhang, X. J. Zhu, Z. H. Wu, D. M. Wu and F. Y. Li. *Fluorine-18-labeled $Gd^{3+}/Yb^{3+}/Er^{3+}$ co-doped $NaYF_4$ nanophosphors for multimodality PET/MR/UCL imaging.* Biomaterials **32**, 1148–1156 (2011).

[272]. Q. Liu, M. Chen, Y. Sun, G. Chen, T. Yang, Y. Gao, X. Zhang and F. Li. *Multifunctional rare-earth self-assembled nanosystem for trimodal upconversion luminescence /fluorescence /positron emission tomography imaging.* Biomaterials **32**, 8243–8253 (2011).

[273]. Y. Sun, M. Yu, S. Liang, Y. Zhang, C. Li, T. Mou, W. Yang, X. Zhang, B. Li, C. Huang and F. Li. *Fluorine-18 labeled rare-earth nanoparticles for positron emission tomography (PET) imaging of sentinel lymph node.* Biomaterials **32**, 2999–3007 (2011).

[274]. J. Lee, T. S. Lee, J. Ryu, S. Hong, M. Kang, K. Im, J. H. Kang, S. M. Lim, S. Park and R. Song. *RGD peptide-conjugated multimodal*

*$NaGdF_4:Yb^{3+}/Er^{3+}$ nanophosphors for upconversion luminescence, MR, and PET imaging of tumor angiogenesis.* J. Nucl. Med. **54**, 96–103 (2013).

[275]. Y. Sun, Q. Liu, J. J. Peng, W. Feng, Y. J. Zhang, P. Y. Yang and F. Y. Li. *Radioisotope post-labeling upconversion nanophosphors for in vivo quantitative tracking.* Biomaterials **34**, 2289–2295 (2013).

[276]. Y. Sun, X. Zhu, J. Peng and F. Li. *Core-shell lanthanide upconversion nanophosphors as four-modal probes for tumor angiogenesis imaging.* ACS Nano **7**, 11290–11300 (2013).

[277]. C. Vinegoni, D. Razansky, S. A. Hilderbrand, F. W. Shao, V. Ntziachristos and R. Weissleder. *Transillumination fluorescence imaging in mice using biocompatible upconverting nanoparticles.* Opt. Lett. **34**, 2566–2568 (2009).

[278]. Z. Tian, G. Chen, X. Li, H. Liang, Y. Li, Z. Zhang and Y. Tian. *Autofluorescence-free in vivo multicolor imaging using upconversion fluoride nanocrystals.* Lasers Med. Sci. **25**, 479–484 (2010).

[279]. S. Wu, G. Han, D. J. Milliron, S. Aloni, V. Altoe, D. V. Talapin, B. E. Cohen and P. J. Schuck. *Non-blinking and photostable upconverted luminescence from single lanthanide-doped nanocrystals.* Proc. Natl. Acad. Sci. U. S. A. **106**, 10917–10921 (2009).

[280]. F. Vetrone, R. Naccache, A. Zamarrón, A. J. de la Fuente, F. Sanz-Rodríguez, L. M. Maestro, E. M. Rodriguez, D. Jaque, J. G. Solé and J. A. Capobianco. *Temperature sensing using fluorescent nanothermometers.* ACS Nano **4**, 3254–3258 (2010).

[281]. N. M. Idris, Z. Li, L. Ye, E. K. Wei Sim, R. Mahendran, P. C. L. Ho and Y. Zhang. *Tracking transplanted cells in live animal using upconversion fluorescent nanoparticles.* Biomaterials **30**, 5104–5113 (2009).

[282]. C. T. Xu, J. Axelsson and S. Andersson-Engels. *Fluorescence diffuse optical tomography using upconverting nanoparticles.* Appl. Phys. Lett. **94**, 251107–251107–3 (2009).

[283]. T. Soukka, T. Rantanen and K. Kuningas. *Photon upconversion in homogeneous fluorescence-based bioanalytical assays.* Ann. N. Y. Acad. Sci. **1130**, 188–200 (2008).

[284]. M. K. G. Jayakumar, N. M. Idris and Y. Zhang. *Remote activation of biomolecules in deep tissues using near-infrared-to-UV upconversion nanotransducers.* Proc. Natl. Acad. Sci. U. S. A. **109**, 8483–8488 (2012).

[285]. C. J. Carling, J.-C. Boyer and N. R. Branda. *Remote-control photoswitching using NIR light.* J. Am. Chem. Soc. **131**, 10838–10839 (2009).

[286]. C. J. Carling, F. Nourmohammadian, J. C. Boyer and N. R. Branda. *Remote-control photorelease of caged compounds using near-infrared light and upconverting nanoparticles.* Angew. Chem. Int. Ed. **49**, 3782–3785 (2010).

[287]. G. Shan, H. Assaaoudi and G. P. Demopoulos. *Enhanced performance of dye-sensitized solar cells by utilization of an external, bifunctional layer consisting of uniform $\beta$-$NaYF4:Er^{3+}/Yb^{3+}$ nanoplatelets.* ACS Appl. Mater. Interfaces **3**, 3239–3243 (2011).

[288]. A. Ivaturi, S. K. W. MacDougall, R. Martín-Rodríguez, M. Quintanilla, J. Marques-Hueso, K. W. Krämer, A. Meijerink and B. S. Richards. *Optimizing infrared to near infrared upconversion quantum yield of $\beta$-$NaYF_4:Er^{3+}$ in fluoropolymer matrix for photovoltaic devices.* J. Appl. Phys. **114**, 013505 (2013).

[289]. L. T. Su, S. K. Karuturi, J. S. Luo, L. J. Liu, X. F. Liu, J. Guo, T. C. Sum, R. R. Deng, H. J. Fan, X. G. Liu and A. I. Y. Tok. *Photon upconversion in hetero-nanostructured photoanodes for enhanced near-infrared light harvesting.* Adv. Mater. **25**, 1603–1607 (2013).

[290]. X. Huang, S. Han, W. Huang and X. Liu. *Enhancing solar cell efficiency: the search for luminescent materials as spectral converters.* Chem. Soc. Rev. **42**, 173–201 (2013).

[291]. G. Chen, J. Seo, C. Yang and P. N. Prasad. *Nanochemistry and nanomaterials for photovoltaics.* Chem. Soc. Rev. **42**, 8304–8338 (2013).

[292]. W. Qin, D. Zhang, D. Zhao, L. Wang and K. Zheng. *Near-infrared photocatalysis based on $YF_3$: $Yb^{3+}, Tm^{3+}/TiO_2$ core/shell nanoparticles.* Chem. Commun. **46**, 2304–2306 (2010).

[293]. M. Zhang, Y. Lin, T. J. Mullen, W.-F. Lin, L.-D. Sun, C.-H. Yan, T. E. Patten, D. Wang and G.-Y. Liu. *Improving Hematite's solar water splitting efficiency by incorporating rare-earth upconversion nanomaterials.* J. Phys. Chem. Lett. **3**, 3188–3192 (2012).

[294]. Y. Zhang and Z. Hong. *Synthesis of lanthanide-doped $NaYF_4@TiO_2$ core-shell composites with highly crystalline and tunable $TiO_2$ shells under mild conditions and their upconversion-based photocatalysis.* Nanoscale **5**, 8930–8933 (2013).

[295]. D.-X. Xu, Z.-W. Lian, M.-L. Fu, B. Yuan, J.-W. Shi and H.-J. Cui. *Advanced near-infrared-driven photocatalyst: Fabrication, characterization, and photocatalytic performance of $\beta$-$NaYF_2$:$Yb^{3+}, Tm^{3+}@TiO_2$ core@shell microcrystals.* Appl. Catalysis B: Environ. **142–143**, 377–386 (2013).

[296]. J. Park, D.-H. Lim, H.-J. Lim, T. Kwon, J.-S. Choi, S. Jeong, I.-H. Choi and J. Cheon. *Size dependent macrophage responses and toxicological effects of Ag nanoparticles.* Chem. Commun. **47**, 4382–4384 (2011).

[297]. B. D. Chithrani, A. A. Ghazani and W. C. W. Chan. *Determining the size and shape dependence of gold nanoparticle uptake into mammalian cells.* Nano Lett. **6**, 662–668 (2006).

[298]. C. M. Goodman, C. D. McCusker, T. Yilmaz and V. M. Rotello. *Toxicity of gold nanoparticles functionalized with cationic and anionic side chains.* Bioconjugate Chem. **15**, 897–900 (2004).

[299]. B. Ballou, B. C. Lagerholm, L. A. Ernst, M. P. Bruchez and A. S. Waggoner. *Noninvasive imaging of quantum dots in mice.* Bioconjugate Chem. **15**, 79–86 (2004).

[300]. S. Harper, C. Usenko, J. E. Hutchison, B. L. S. Maddux and R. L. Tanguay. *In vivo biodistribution and toxicity depends on nanomaterial composition, size, surface functionalisation and route of exposure.* J. Exp. Nanosci. **3**, 195–206 (2008).

[301]. Y. Liu, Y. Zhao, B. Sun and C. Chen. *Understanding the toxicity of carbon nanotubes.* Acc. Chem. Res. **46**, 702–713 (2013).

[302]. S. Liu, L. Wei, L. Hao, N. Fang, M. W. Chang, R. Xu, Y. Yang and Y. Chen. *Sharper and faster "nano darts" kill more bacteria: A study of antibacterial activity of individually dispersed pristine single-walled carbon nanotube.* ACS Nano **3**, 3891–3902 (2009).

[303]. V. E. Kagan, N. V. Konduru, W. Feng, B. L. Allen, J. Conroy, Y. Volkov, I. I. Vlasova, N. A. Belikova, N. Yanamala, A. Kapralov, Y. Y. Tyurina, J. Shi, E. R. Kisin, A. R. Murray, J. Franks, D. Stolz, P. Gou, J. Klein-Seetharaman, B. Fadeel, A. Star and A. A. Shvedova. *Carbon nanotubes degraded by neutrophil myeloperoxidase induce less pulmonary inflammation.* Nat. Nano. **5**, 354–359 (2010).

[304]. C. D. Walkey and W. C. W. Chan. *Understanding and controlling the interaction of nanomaterials with proteins in a physiological environment.* Chem. Soc. Rev. **41**, 2780–2799 (2012).

[305]. Y. Xu, X. Lin and C. Chen. *Key factors influencing the Toxicity of nanomaterials.* Chin. Sci. Bull. **58**, 2466–2478 (2013).

[306]. J. Shan, J. Chen, J. Meng, J. Collins, W. Soboyejo, J. S. Friedberg and

Y. Ju. *Biofunctionalization, cytotoxicity, and cell uptake of lanthanide doped hydrophobically ligated $NaYF_4$ upconversion nanophosphors.* J. Appl. Phys. **104**, 094308 (2008).

[307]. L. Zhao, A. Kutikov, J. Shen, C. Duan, J. Song and G. Han. *Stem Cell Labeling using Polyethylenimine Conjugated ($\alpha$-$NaYbF_4$:$Tm^{3+}$)/$CaF_2$ Upconversion Nanoparticles.* Theranostics **3**, 249–257 (2013).

[308]. L. Xiong, T. Yang, Y. Yang, C. Xu and F. Li. *Long-term in vivo biodistribution imaging and toxicity of polyacrylic acid-coated upconversion nanophosphors.* Biomaterials **31**, 7078–7085 (2010).

[309]. T. Cao, Y. Yang, Y. Sun, Y. Wu, Y. Gao, W. Feng and F. Li. *Biodistribution of sub-10 nm PEG-modified radioactive/upconversion nanoparticles.* Biomaterials **34**, 7127–7134 (2013).

[310]. J.-C. Zhou, Z.-L. Yang, W. Dong, R.-J. Tang, L.-D. Sun and C.-H. Yan. *Bioimaging and toxicity assessments of near-infrared upconversion luminescent $NaYF_4$:Yb,Tm nanocrystals.* Biomaterials **32**, 9059–9067 (2011).

[311]. K. Wang, J. Ma, M. He, G. Gao, H. Xu, J. Sang, Y. Wang, B. Zhao and D. Cui. *Toxicity assessments of near-infrared upconversion luminescent $LaF_3$:Yb,Er in early development of zebrafish embryos.* Theranostics **3**, 258–266 (2013).

[312]. H. J. M. A. A. Zijlmans, J. Bonnet, J. Burton, K. Kardos, T. Vail, R. S. Niedbala and H. J. Tanke. *Detection of cell and tissue surface antigens using up-converting phosphors: A new reporter technology.* Anal. Biochem. **267**, 30 – 36 (1999).

[313]. L. Yu, Y. Lu, N. Man, S.-H. Yu and L.-P. Wen. *Rare earth oxide nanocrystals induce autophagy in HeLa cells.* Small **5**, 2784–2787 (2009).

[314]. M. Wang, C. Mi, Y. Zhang, J. Liu, F. Li, C. Mao and S. Xu. *NIR-responsive silica-coated $NaYbF_4$:Er/Tm/Ho upconversion fluorescent nanoparticles with tunable emission colors and their applications in immunolabeling and fluorescent imaging of cancer cells.* J. Phys. Chem. C **113**, 19021–19027 (2009).

[315]. M. Wang, C. Mi, W. Wang, C. Liu, Y. Wu, Z. Xu, C. Mao and S. Xu. *Immunolabeling and NIR-excited fluorescent imaging of HeLa cells by using $NaYF_4$:Yb,Er upconversion nanoparticles.* ACS Nano **3**, 1580–1586 (2009).

[316]. S. Jiang and Y. Zhang. *Upconversion nanoparticle-based FRET system for study of siRNA in live cells.* Langmuir **26**, 6689–6694 (2010).

[317]. J. Pichaandi, J.-C. Boyer, K. R. Delaney and F. C. J. M. van Veggel. *Two-photon upconversion laser (scanning and wide-field) microscopy using $Ln^{3+}$-doped $NaYF_4$ upconverting nanocrystals: A critical evaluation of their performance and potential in bioimaging.* J. Phys. Chem. C **115**, 19054–19064 (2011).

[318]. K. Kuningas, T. Ukonaho, H. Päkkilä, T. Rantanen, J. Rosenberg, T. Lövgren and T. Soukka. *Upconversion fluorescence resonance energy transfer in a homogeneous immunoassay for estradiol.* Anal. Chem. **78**, 4690–4696 (2006).

[319]. T. Rantanen, H. Pakkila, L. Jamsen, K. Kuningas, T. Ukonaho, T. Lovgren and T. Soukka. *Tandem dye acceptor used to enhance upconversion fluorescence resonance energy transfer in homogeneous assays.* Anal. Chem. **79**, 6312–6318 (2007).

[320]. T. Rantanen, M.-L. Jarvenpaa, J. Vuojola, K. Kuningas and T. Soukka. *Fluorescence-quenching-based enzyme-activity assay by using photon upconversion.* Angew. Chem. Int. Ed. **47**, 3811–3813 (2008).

[321]. T. Rantanen, M.-L. Jarvenpaa, J. Vuojola, R. Arppe, K. Kuningas and

T. Soukka. *Upconverting phosphors in a dual-parameter LRET-based hybridization assay.* Analyst **134**, 1713–1716 (2009).

[322]. Y. Wang, P. Shen, C. Li, Y. Wang and Z. Liu. *Upconversion fluorescence resonance energy transfer based biosensor for ultrasensitive detection of matrix metalloproteinase-2 in blood.* Anal. Chem. **84**, 1466–1473 (2012).

[323]. F. van de Rijke, H. Zijlmans, S. Li, T. Vail, A. K. Raap, R. S. Niedbala and H. J. Tanke. *Up-converting phosphor reporters for nucleic acid microarrays.* Nat. Biotech. **19**, 273–276 (2001).

[324]. P. L. A. M. Corstjens, M. Zuiderwijk, A. Brink, S. Li, H. Feindt, R. S. Niedbala and H. J. Tanke. *Use of up-converting phosphor reporters in lateral-flow assays to detect specific nucleic acid sequences: A rapid, sensitive DNA test to identify human papillomavirus type 16 infection.* Clin. Chem. **47**, 1885–1893 (2001).

[325]. P. L. A. M. Corstjens, M. Zuiderwijk, M. Nilsson, H. Feindt, R. S. Niedbala and H. J. Tanke. *Lateral-flow and up-converting phosphor reporters to detect single-stranded nucleic acids in a sandwich-hybridization assay.* Anal. Biochem. **312**, 191–200 (2003).

[326]. L. Wang and Y. Li. *Green upconversion nanocrystals for DNA detection.* Chem. Commun. pp 2557–2559 (2006).

[327]. M. Wang, W. Hou, C. Mi, W. Wang, Z. Xu, H. Teng, C. Mao and S. Xu. *Immunoassay of goat antihuman immunoglobulin G antibody based on luminescence resonance energy transfer between near-infrared responsive $NaYF_4$:Yb, Er upconversion fluorescent nanoparticles and gold nanoparticles.* Anal. Chem. **81**, 8783–8789 (2009).

[328]. J. Zhang, C. Mi, H. Wu, H. Huang, C. Mao and S. Xu. *Synthesis of $NaYF_4$:Yb/Er/Gd up-conversion luminescent nanoparticles and luminescence resonance energy transfer-based protein detection.* Anal. Biochem. **421**, 673–679 (2012).

[329]. P. Bao, A. G. Frutos, C. Greef, J. Lahiri, U. Muller, T. C. Peterson, L. Warden and X. Y. Xie. *High-sensitivity detection of DNA hybridization on microarrays using resonance light scattering.* Anal. Chem. **74**, 1792–1797 (2002).

[330]. C. H. Liu and D. P. Chen. *Detection of DNA hybridization based on the quenching of upconversion fluorescence of $NaYF_4$: Yb, Er Nanospheres.* Progress On Post-genome Technologies, Proceedings pp 76–78 (2009).

[331]. H. Guo and S. Sun. *Lanthanide-doped upconverting phosphors for bioassay and therapy.* Nanoscale **4**, 6692–6706 (2012).

[332]. Z. Zhou, H. Hu, H. Yang, T. Yi, K. Huang, M. Yu, F. Li and C. Huang. *Up-conversion luminescent switch based on photochromic diarylethene and rare-earth nanophosphors.* Chem. Commun. pp 4786–4788 (2008).

[333]. J.-C. Boyer, C. J. Carling, B. D. Gates and N. R. Branda. *Two-way photoswitching using one type of near-infrared light, upconverting nanoparticles, and changing only the light intensity.* J. Am. Chem. Soc. **132**, 15766–15772 (2010).

[334]. J.-C. Boyer, C. J. Carling, S. Y. Chua, D. Wilson, B. Johnsen, D. Baillie and N. R. Branda. *Photomodulation of fluorescent upconverting nanoparticle markers in live organisms by using molecular switches.* Chem. Eur. J. **18**, 3122–3126 (2012).

[335]. J. V. Garcia, J. P. Yang, D. K. Shen, C. Yao, X. M. Li, R. Wang, G. D. Stucky, D. Y. Zhao, P. C. Ford and F. Zhang. *NIR-triggered release of caged nitric oxide using upconverting nanostructured materials.* Small **8**, 3800–3805 (2012).

[336]. Y. M. Yang, F. Liu, X. G. Liu and B. G. Xing. *NIR light controlled*

*photorelease of siRNA and its targeted intracellular delivery based on upconversion nanoparticles.* Nanoscale **5**, 231–238 (2013).

[337]. Y. M. Yang, Q. Shao, R. R. Deng, C. Wang, X. Teng, K. Cheng, Z. Cheng, L. Huang, Z. Liu, X. G. Liu and B. G. Xing. *In vitro and in vivo uncaging and bioluminescence imaging by using photocaged upconversion nanoparticles.* Angew. Chem. Int. Ed. **51**, 3125–3129 (2012).

[338]. B. Yan, J.-C. Boyer, N. R. Branda and Y. Zhao. *Near-infrared light-triggered dissociation of block copolymer micelles using upconverting nanoparticles.* J. Am. Chem. Soc. **133**, 19714–19717 (2011).

[339]. B. Yan, J.-C. Boyer, D. Habault, N. R. Branda and Y. Zhao. *Near infrared light triggered release of biomacromolecules from hydrogels loaded with upconversion nanoparticles.* J. Am. Chem. Soc. **134**, 16558–16561 (2012).

[340]. Y. Matsushita-Ishiodori, M. Morinaga, K. Watanabe and T. Ohtsuki. *Near-infrared light-directed RNAi using a photosensitive carrier molecule.* Bioconjugate Chem. **24**, 1669–1673 (2013).

[341]. M. L. Viger, M. Grossman, N. Fomina and A. Almutairi. *Low power upconverted near-IR light for efficient polymeric nanoparticle degradation and cargo release.* Adv. Mater. **25**, 3733–3738 (2013).

[342]. Q. Xiao, Y. Ji, Z. Xiao, Y. Zhang, H. Lin and Q. Wang. *Novel multifunctional $NaYF_4$:$Er^{3+}$,$Yb^{3+}$/PEGDA hybrid microspheres: NIR-light-activated photopolymerization and drug delivery.* Chem. Commun. **49**, 1527–1529 (2013).

[343]. M. Pollnau, D. R. Gamelin, S. R. Lüthi, H. U. Güdel and M. P. Hehlen. *Power dependence of upconversion luminescence in lanthanide and transition-metal-ion systems.* Phys. Rev. B **61**, 3337–3346 (2000).

[344]. J. F. Suyver, A. Aebischer, S. García-Revilla, P. Gerner and H. U. Güdel. *Anomalous power dependence of sensitized upconversion luminescence.* Phys. Rev. B **71**, 125123 (2005).

[345]. D. O. Faulkner, S. Petrov, D. D. Perovic, N. P. Kherani and G. A. Ozin. *Absolute quantum yields in $NaYF_4$:Er,Yb upconverters - synthesis temperature and power dependence.* J. Mater. Chem. **22**, 24330–24334 (2012).

[346]. Y. Lei, H. Song, L. Yang, L. Yu, Z. Liu, G. Pan, X Bai and L. Fan. *Upconversion luminescence, intensity saturation effect, and thermal effect in $Gd_2O_3$: $Er^{3+}$,$Yb^{3+}$ nanowires.* J. Chem. Phys. **123**, 174710 (2005).

[347]. J. Shan, M. Uddi, R. Wei, N. Yao and Y. Ju. *The hidden effects of particle shape and criteria for evaluating the upconversion luminescence of the lanthanide doped nanophosphors.* J. Phys. Chem. C **114**, 2452–2461 (2010).

[348]. G. Chen, C. Yang, B. Aghahadi, H. Liang, Y. Liu, L. Li and Z. Zhang. *Ultraviolet-blue upconversion emissions of $Ho^{3+}$ ions.* J. Opt. Soc. Am. B **27**, 1158–1164 (2010).

[349]. A. Yin, Y. Zhang, L. Sun and C. Yan. *Colloidal synthesis and blue based multicolor upconversion emissions of size and composition controlled monodisperse hexagonal $NaYF_4$: Yb,Tm nanocrystals.* Nanoscale **2**, 953–959 (2010).

[350]. G. Chen, T. Y. Ohulchanskyy, A. Kachynski, H. Ågren and P. N. Prasad. *Intense visible and near-infrared upconversion photoluminescence in colloidal $LiYF_4$:$Er^{3+}$ nanocrystals under excitation at 1490 nm.* ACS Nano **5**, 4981–4986 (2011).

[351]. K. Rurack. *Fluorescence quantum yields: Methods of determination and standards.* In Ute Resch-Genger, editor, *Springer Series on Fluorescence* vol. 5 pp 101–145. Springer Berlin Heidelberg (2008).

[352]. J. Zhou, G. Chen, E Wu, G. Bi, B. Wu, Y. Teng, S. Zhou and J. Qiu.

*Ultrasensitive polarized up-conversion of $Tm^{3+}$-$Yb^{3+}$ doped $\beta$-$NaYF_4$ single nanorod.* Nano Lett. **13**, 2241–2246 (2013).

[353]. B. Thomasson et al. *Towards accurate quantum yield characterization of upconverting nanoparticles.* manuscript in preparation (2014).

[354]. C. A. Parker, C. G. Hatchard and T. A. Joyce. *Selective and mutual sensitization of delayed fluorescence.* Nature **205**, 1282–1284 (1965).

[355]. S. Baluschev, T. Miteva, V. Yakutkin, G. Nelles, A. Yasuda and G. Wegner. *Up-conversion fluorescence: Noncoherent excitation by sunlight.* Phys. Rev. Lett. **97**, 143903 (2006).

[356]. Q. Liu, T. Yang, W. Feng and F. Li. *Blue-emissive upconversion nanoparticles for low-power-excited bioimaging in vivo.* J. Am. Chem. Soc. **134**, 5390–5397 (2012).

[357]. A. Monguzzi, M. Frigoli, C. Larpent, R. Tubino and F. Meinardi. *Low-power-photon up-conversion in dual-dye-loaded polymer nanoparticles.* Adv. Funct. Mater. **22**, 139–143 (2012).

[358]. A. Monguzzi, F. Bianchi, A. Bianchi, M. Mauri, R. Simonutti, R. Ruffo, R. Tubino and F. Meinardi. *High efficiency up-converting single phase elastomers for photon managing applications.* Adv. Energy Mater. **3**, 680–686 (2013).

[359]. J.-H. Kim and J.-H. Kim. *Encapsulated triplet-triplet annihilation-based upconversion in the aqueous phase for sub-band-gap semiconductor photocatalysis.* J. Am. Chem. Soc. **134**, 17478–17481 (2012).

[360]. J.-H. Kim, F. Deng, F. N. Castellano and J.-H. Kim. *High efficiency low-power upconverting soft materials.* Chem. Mater. **24**, 2250–2252 (2012).

[361]. A. Monguzzi, J. Mezyk, F. Scotognella, R. Tubino and F. Meinardi. *Upconversion-induced fluorescence in multicomponent systems: Steady-state excitation power threshold.* Phys. Rev. B **78**, 195112 (2008).

[362]. A. Monguzzi, R. Tubino, S. Hoseinkhani, M. Campione and F. Meinardi. *Low power, non-coherent sensitized photon up-conversion: modelling and perspectives.* Phys. Chem. Chem. Phys. **14**, 4322–4332 (2012).

[363]. A. F. H. Librantz, L. Gomes, L. C. Courrol, I. M. Ranieri and S. L. Baldochi. *Population inversion of $^1G_4$ excited state of $Tm^{3+}$ investigated by means of numerical solutions of the rate equations system in Yb:Tm:Nd:$LiYF_4$ crystal.* J. Appl. Phys. **105**, 113503 (2009).

[364]. A. Braud, S. Girard, J. L. Doualan, M. Thuau, R. Moncorg'e and A. M. Tkachuk. *Energy-transfer processes in Yb:Tm-doped $KY_3F_{10}$, $LiYF_4$ and $BaY_2F_8$ single crystals for laser operation at 1.5 and 2.3 $\mu$m.* Phys. Rev. B **61**, 5280–5292 (2000).

[365]. G. Alexandrakis, F. R. Rannou and A. F. Chatziioannou. *Tomographic bioluminescence imaging by use of a combined optical-PET (OPET) system: a computer simulation feasibility study.* Phys. Med. Biol. **50**, 4225–4241 (2005).

[366]. T. Svensson, S. Andersson-Engels, M. Einarsdottir and K. Svanberg. *In vivo optical characterization of human prostate tissue using near-infrared time-resolved spectroscopy.* J. Biomed. Opt. **12**, 014022 (2007).

[367]. Laser Institute of America. *Americal National Standard for Safe Use of Lasers* (2000). *in ANSI Z136.1-2000* (Laser Institute of America, Orlando, Florida, 2000).

[368]. V. Ntziachristos, C. Tung, C. Bremer and R. Weissleder. *Fluorescence molecular tomography resolves protease activity in vivo.* Nat. Med. **8**, 757–760 (2002).

[369]. D. Hyde, R. de Kleine, S. A. MacLaurin, E. Miller, D. H. Brooks,

T. Krucker and V. Ntziachristos. *Hybrid FMT-CT imaging of amyloid-beta plaques in a murine Alzheimer's disease model.* Neuroimage **44**, 1304–1311 (2009).

[370]. A. Corlu, R. Choe, T. Durduran, M. A. Rosen, M. Schweiger, S. R. Arridge, M. D. Schnall and A. G. Yodh. *Three-dimensional in vivo fluorescence diffuse optical tomography of breast cancer in humans.* Opt. Express **15**, 6696–6716 (2007).

[371]. M. J. Niedre, R. H. de Kleine, E. Aikawa, D. G. Kirsch, R. Weissleder and V. Ntziachristos. *Early photon tomography allows fluorescence detection of lung carcinomas and disease progression in mice in vivo.* Proc. Natl. Acad. Sci. U. S. A. **105**, 19126–19131 (2008).

[372]. F. Leblond, H. Dehghani, D. Kepshire and B. W. Pogue. *Early-photon fluorescence tomography: spatial resolution improvements and noise stability considerations.* J. Opt. Soc. Am. A **26**, 1444–1457 (2009).

[373]. P. I. H. Bastiaens and A. Squire. *Fluorescence lifetime imaging microscopy: spatial resolution of biochemical processes in the cell.* Trends Cell Biol. **9**, 48–52 (1999).

[374]. L. Zhao, K. Abe, M. Barroso and X. Intes. *Active wide-field illumination for high-throughput fluorescence lifetime imaging.* Opt. Lett. **38**, 3976–3979 (2013).

[375]. M. A. O'Leary, D. A. Boas, X. D. Li, B. Chance and A. G. Yodh. *Fluorescence lifetime imaging in turbid media.* Opt. Lett. **21**, 158–160 (1996).

[376]. J. McGinty, V. Y. Soloviev, K. B. Tahir, R. Laine, D. W. Stuckey, J. V. Hajnal, A. Sardini, P. M. W. French and S. R. Arridge. *Three-dimensional imaging of Förster resonance energy transfer in heterogeneous turbid media by tomographic fluorescent lifetime imaging.* Opt. Lett. **34**, 2772–2774 (2009).

[377]. V. Gaind, S. Kularatne, P. S. Low and K. J. Webb. *Deep-tissue imaging of intramolecular fluorescence resonance energy-transfer parameters.* Opt. Lett. **35**, 1314–1316 (2010).

[378]. K. Abe, L. Zhao, A. Periasamy, X. Intes and M. Barroso. *Non-invasive in vivo imaging of near infrared-labeled transferrin in breast cancer cells and tumors using fluorescence lifetime FRET.* PLOS ONE **8**, e80269 (2013).

[379]. J. Swartling, J. Svensson, D. Bengtsson, K. Terike and S. Andersson-Engels. *Fluorescence spectra provide information on the depth of fluorescent lesions in tissue.* Appl. Opt. **44**, 1934–1941 (2005).

[380]. J. Svensson and S. Andersson-Engels. *Modeling of spectral changes for depth localization of fluorescent inclusion.* Opt. Express **13**, 4263–4274 (2005).

[381]. J. Axelsson, J. Svensson and S. Andersson-Engels. *Spatially varying regularization based on spectrally resolved fluorescence emission in fluorescence molecular tomography.* Opt. Express **15**, 13574–13584 (2007).

[382]. A. D. Zacharopoulos, P. Svenmarker, J. Axelsson, M. Schweiger, S. R. Arridge and S. Andersson-Engels. *A matrix-free algorithm for multiple wavelength fluorescence tomography.* Opt. Express **17**, 3042–3051 (2009).

[383]. A. D. Klose. *Hyperspectral excitation-resolved fluorescence tomography of quantum dots.* Opt. Lett. **34**, 2477–2479 (2009).

[384]. A. J. Chaudhari, S. Ahn, R. Levenson, R. D. Badawi, S. R. Cherry and R. M. Leahy. *Excitation spectroscopy in multispectral optical fluorescence tomography: methodology, feasibility and computer simulation studies.* Phys. Med. Biol. **54**, 4687–4704 (2009).

[385]. A. D. Klose and T. Pöschinger. *Excitation-resolved fluorescence tomog-*

*raphy with simplified spherical harmonics equations.* Phys. Med. Biol. **56**, 1443 (2011).

[386]. J. B. Fishkin and E. Gratton. *Propagation of photon-density waves in strongly scattering media containing an absorbing semi-infinite plane bounded by a straight edge.* J. Opt. Soc. Am. A **10**, 127–140 (1993).

[387]. B. J. Tromberg, L. O. Svaasand, T.-T. Tsay and R. C. Haskell. *Properties of photon density waves in multiple-scattering media.* Appl. Opt. **32**, 607–616 (1993).

[388]. T. H. Pham, O. Coquoz, J. B. Fishkin, E. Anderson and B. J. Tromberg. *Broad bandwidth frequency domain instrument for quantitative tissue optical spectroscopy.* Rev. Sci. Instrum. **71**, 2500–2513 (2000).

[389]. D. J. Cuccia, F. Bevilacqua, A. J. Durkin and B. J. Tromberg. *Modulated imaging: quantitative analysis and tomography of turbid media in the spatial-frequency domain.* Opt. Lett. **30**, 1354–1356 (2005).

[390]. D. J. Cuccia, F. B., A. J. Durkin, F. R. Ayers and B. J. Tromberg. *Quantitation and mapping of tissue optical properties using modulated imaging.* J. Biomed. Opt. **14**, 024012 (2009).

[391]. A. Joshi, W. Bangerth and E. M. Sevick-Muraca. *Non-contact fluorescence optical tomography with scanning patterned illumination.* Opt. Express **14**, 6516–6534 (2006).

[392]. V. Lukic, V. A. Markel and J. C. Schotland. *Optical tomography with structured illumination.* Opt. Lett. **34**, 983–985 (2009).

[393]. J. Dutta, S. Ahn, A. A. Joshi and R. M. Leahy. *Optimal illumination patterns for fluorescence tomography.* 2009 IEEE International Symposium on Biomedical Imaging: From Nano to Macro pp 1275–1278 (2009).

[394]. J. Dutta, S. Ahn, A. A. Joshi and R. M. Leahy. *Illumination pattern optimization for fluorescence tomography: theory and simulation studies.* Phys. Med. Biol. **55**, 2961–2982 (2010).

[395]. N. Ducros, C. D'andrea, G. Valentini, T. Rudge, S. R. Arridge and A. Bassi. *Full-wavelet approach for fluorescence diffuse optical tomography with structured illumination.* Opt. Lett. **35**, 3676–3678 (2010).

[396]. J. Axelsson, J. Swartling and S. Andersson-Engels. *In vivo photosensitizer tomography inside the human prostate.* Opt. Lett. **34**, 232–234 (2009).

[397]. P. C. Hansen. *Analysis of discrete ill-posed problems by means of the L-Curve.* SIAM Review **34**, 561–580 (1992).

[398]. P. K. Yalavarthy, B. W. Pogue, H. Dehghani and K. D. Paulsen. *Weight-matrix structured regularization provides optimal generalized least-squares estimate in diffuse optical tomography.* Med. Phys. **34**, 2085–2098 (2007).

[399]. H. Dehghani, M. E. Eames, P. K. Yalavarthy, S. C. Davis, S. Srinivasan, C. M. Carpenter, B. W. Pogue and K. D. Paulsen. *Near infrared optical tomography using NIRFAST: Algorithm for numerical model and image reconstruction.* Commun. Numer. Methods Eng. **25**, 711–732 (2009).

[400]. S. R. Arridge and M. Schweiger. *Photon-measurement density functions. Part 2: Finite-element-method calculations.* Appl. Opt. **34**, 8026–8037 (1995).

[401]. V. Ntziachristos and R. Weissleder. *Experimental three-dimensional fluorescence reconstruction of diffuse media by use of a normalized Born approximation.* Opt. Lett. **26**, 893–895 (2001).

[402]. A. Soubret, J. Ripoll and V. Ntziachristos. *Accuracy of fluorescent tomography in the presence of heterogeneities: Study of the normalized Born ratio.* IEEE Trans. Med. Imaging **24**, 1377–1386 (2005).

[403]. J. P. Culver, V. Ntziachristos, M. J. Holboke and A. G. Yodh. *Optimization of optode arrangements for diffuse optical tomography: A singular-value analysis.* Opt. Lett. **26**, 701–703 (2001).

[404]. H. Xu, H. Dehghani, B. W. Pogue, R. Springett, K. D. Paulsen and J. F. Dunn. *Near-infrared imaging in the small animal brain: optimization of fiber positions.* J. Biomed. Opt. **8**, 102–110 (2003).

[405]. T. Lasser and V. Ntziachristos. *Optimization of 360◦ projection fluorescence molecular tomography.* Med. Image Anal. **11**, 389–399 (2007).

[406]. F. Leblond, K. M. Tichauer and B. W. Pogue. *Singular value decomposition metrics show limitations of detector design in diffuse fluorescence tomography.* Biomed. Opt. Express **1**, 1514–1531 (2010).

[407]. E. E. Graves, J. P. Culver, J. Ripoll, R. Weissleder and V. Ntziachristos. *Singular-value analysis and optimization of experimental parameters in fluorescence molecular tomography.* J. Opt. Soc. Am. A **21**, 231–241 (2004).

[408]. P. C. Hansen. *REGULARIZATION TOOLS: A Matlab package for analysis and solution of discrete ill-posed problems.* Numer. Algorithms **6**, 1–35 (1994).

[409]. B. W. Pogue, T. O. McBride, J. Prewitt, U. L. Österberg and K. D. Paulsen. *Spatially variant regularization improves diffuse optical tomography.* Appl. Opt. **38**, 2950–2961 (1999).

[410]. H. Dehghani, S. Srinivasan, B. W. Pogue and A. Gibson. *Numerical modelling and image reconstruction in diffuse optical tomography.* Phil. Trans. R. Soc. A **367**, 3073–3093 (2009).

[411]. H. R. Busby and D. M. Trujillo. *Optimal regularization of an inverse dynamics problem.* Comput. Struct. **63**, 243–248 (1997).

[412]. P. Hansen and D. O'Leary. *The use of the L-curve in the regularization of discrete ill-posed problems.* SIAM J. Sci. Comput. **14**, 1487–1503 (1993).

[413]. D. Krawczyk-Stańdo and M. Rudnicki. *Regularization parameter selection in discrete ill-posed problems-The use of the U-curve.* Int. J. Appl. Math. Comput. Sci. **17**, 157–164 (2007).

[414]. D. Krawczyk-Stańdo and M. Rudnicki. *The use of L-curve and U-curve in inverse electromagnetic modelling.* In Slawomir Wiak, Andrzej Krawczyk and Ivo Dolezel, editors, *Intelligent Computer Techniques in Applied Electromagnetics* vol. 119 of *Studies in Computational Intelligence* pp 73–82. Springer Berlin Heidelberg (2008).

[415]. J. Chamorro-Servent, J. Aguirre, J. Ripoll, J. J. Vaquero and M. Desco. *Feasibility of U-curve method to select the regularization parameter for fluorescence diffuse optical tomography in phantom and small animal studies.* Opt. Express **19**, 11490–11506 (2011).

[416]. M. Li, X. Cao, F. Liu, B. Zhang, J. Luo and J. Bai. *Reconstruction of fluorescence molecular tomography using a neighborhood regularization.* IEEE Trans. Biomed. Engineering **59**, 1799–1803 (2012).

[417]. F. Liu, M. Li, B. Zhang, J. Luo and J. Bai. *Weighted depth compensation algorithm for fluorescence molecular tomography reconstruction.* Appl. Opt. **51**, 8883–8892 (2012).

[418]. X. Cao, B. Zhang, X. Wang, F. Liu, K. Liu, J. W. Luo and J. Bai. *An adaptive Tikhonov regularization method for fluorescence molecular tomography.* Med. Biol. Eng. Comput. **51**, 849–858 (2013).

[419]. Y. Lin, W. C. Barber, J. S. Iwanczyk, W. Roeck, O. Nalcioglu and G. Gulsen. *Quantitative fluorescence tomography using a combined tri-modality FT/DOT/XCT system.* Opt. Express **18**, 7835–7850 (2010).

[420]. S. C. Davis, H. Dehghani, J. Wang, S. Jiang, B. W. Pogue and K. D. Paulsen. *Image-guided diffuse optical fluorescence tomography imple-*

*mented with Laplacian-type regularization.* Opt. Express **15**, 4066–4082 (2007).

[421]. B. Brooksby, S. Jiang, H. Dehghani, B. W. Pogue, K. D. Paulsen, J. Weaver, C. Kogel and S. P. Poplack. *Combining near-infrared tomography and magnetic resonance imaging to study in vivo breast tissue: implementation of a Laplacian-type regularization to incorporate magnetic resonance structure.* J. Biomed. Opt. **10** (2005).

[422]. P. K. Yalavarthy, B. W. Pogue, H. Dehghani, C. M. Carpenter, S. Jiang and K. D. Paulsen. *Structural information within regularization matrices improves near infrared diffuse optical tomography.* Opt. Express **15**, 8043–8058 (2007).

[423]. D. Hyde, E. L. Miller, D. H. Brooks and Vasilis Ntziachristos. *Data specific spatially varying regularization for multimodal fluorescence molecular tomography.* IEEE Trans. Med. Imaging **29**, 365–374 (2010).

[424]. A. Ale, R. B. Schulz, A. Sarantopoulos and V. Ntziachristos. *Imaging performance of a hybrid x-ray computed tomography-fluorescence molecular tomography system using priors.* Med. Phys. **37**, 1976–1986 (2010).

[425]. F. Leblond, Z. Ovanesyan, S. C. Davis, P. A. Valdés, A. Kim, A. Hartov, B. C. Wilson, B. W. Pogue, K. D. Paulsen and D. W. Roberts. *Analytic expression of fluorescence ratio detection correlates with depth in multispectral sub-surface imaging.* Phys. Med. Biol. **56**, 6823– (2011).

[426]. H.-S. Qian and Y. Zhang. *Synthesis of hexagonal-phase core-shell $NaYF_4$ nanocrystals with tunable upconversion fluorescence.* Langmuir **24**, 12123–12125 (2008).

[427]. S. W. Hell and J. Wichmann. *Breaking the diffraction resolution limit by stimulated-emission: stimulated-emission-depletion fluorescence microscopy.* Opt. Lett. **19**, 780–782 (1994).

[428]. V. Westphal, S. O. Rizzoli, M. A. Lauterbach, D. Kamin, R. Jahn and S. W. Hell. *Video-rate far-field optical nanoscopy dissects synaptic vesicle movement.* Science **320**, 246–249 (2008).

[429]. F. Helmchen and W. Denk. *Deep tissue two-photon microscopy.* Nat. Methods **2**, 932–940 (2005).

[430]. E. J. Sánchez, L. Novotny and X. S. Xie. *Near-field fluorescence microscopy based on two-photon excitation with metal tips.* Phys. Rev. Lett. **82**, 4014–4017 (1999).

# Papers

# Paper I

**Drug quantification in turbid media by fluorescence imaging combined with light-absorption correction using white Monte Carlo simulation**

H. Xie, H. Liu, P. Svenmarker, J. Axelsson, C. T. Xu, S. Gräfe, J. H. Lundeman, H. P. H. Cheng, S. Svanberg, N. Bendsoe, P. E. Andersen, K. Svanberg, S. Andersson-Engels.

*Journal of Biomedical Optics* **16(6)**, 066002-1 - 066002-11 (2011).

Journal of Biomedical Optics 16(6), 066002 (June 2011)

# Drug quantification in turbid media by fluorescence imaging combined with light-absorption correction using white Monte Carlo simulations

**Haiyan Xie,[a] Haichun Liu,[a] Pontus Svenmarker,[a] Johan Axelsson,[a] Can T. Xu,[a] Susanna Gräfe,[b] Jesper Holm Lundeman,[c] Haynes Pak Hay Cheng,[c] Sune Svanberg,[a] Niels Bendsoe,[d] Peter E. Andersen,[c] Katarina Svanberg,[e] and Stefan Andersson-Engels[a]**

[a]Lund University, Department of Physics, P.O. Box 118, SE-221 00, Lund, Sweden
[b]Biolitec AG, Research and Development, D-077 45, Jena, Germany
[c]Technical University of Denmark, DTU Fotonik, DK-4000, Roskilde, Denmark
[d]Lund University Hospital, Department of Dermatology and Venereology, SE-221 85, Lund, Sweden
[e]Lund University Hospital, Department of Oncology, SE-221 85, Lund, Sweden

**Abstract.** Accurate quantification of photosensitizers is in many cases a critical issue in photodynamic therapy. As a noninvasive and sensitive tool, fluorescence imaging has attracted particular interest for quantification in pre-clinical research. However, due to the absorption of excitation and emission light by turbid media, such as biological tissue, the detected fluorescence signal does not have a simple and unique dependence on the fluorophore concentration for different tissues, but depends in a complex way on other parameters as well. For this reason, little has been done on drug quantification *in vivo* by the fluorescence imaging technique. In this paper we present a novel approach to compensate for the light absorption in homogeneous turbid media both for the excitation and emission light, utilizing time-resolved fluorescence white Monte Carlo simulations combined with the Beer–Lambert law. This method shows that the corrected fluorescence intensity is almost proportional to the absolute fluorophore concentration. The results on controllable tissue phantoms and murine tissues are presented and show good correlations between the evaluated fluorescence intensities after the light-absorption correction and absolute fluorophore concentrations. These results suggest that the technique potentially provides the means to quantify the fluorophore concentration from fluorescence images.  [DOI: 10.1117/1.3585675]

Keywords: fluorescence; imaging; biomedical optics; tissues; optical properties; absorption; Monte Carlo; photon migration.

Paper 11047R received Feb. 2, 2011; revised manuscript received Apr. 6, 2011; accepted for publication Apr. 8, 2011; published online Jun. 1, 2011.

## 1 Introduction

Photodynamic therapy (PDT) has been clinically accepted to treat certain types of malignant tumors as well as some non-malignant diseases.[1,2] In PDT a photosensitizer (PS) is administrated either systemically or topically. It is activated by irradiating appropriate light to the sensitized tumor. As the PS absorbs light, the gained energy can be transferred to nearby oxygen molecules, leading to the formation of highly reactive oxygen radicals and thereafter tissue damage. PDT is a nonthermal photochemical reaction, which requires the presence of a photosensitizing agent (i.e., PS), oxygen and light, simultaneously. In PDT, quantification of the PS in a noninvasive way is in many cases a critical issue, since light dosimetry, irradiation parameters, and therapeutic outcome depends significantly on the PS quantities distributed in the region of interest (ROI).

Various techniques have been proposed to quantify the PS concentration. In *ex vivo* animal experiments, high performance liquid chromatography (HPLC) of excised tissues is conventionally used as a gold standard for quantitative analysis of the PS concentration as well as for its pharmacokinetic behavior.[3] Optical techniques can offer alternatives and be used *in vivo*. Among these techniques, absorption spectroscopy[4–7] provides a noninvasive tool for PS concentration studies. However, it suffers from a relatively poor detection sensitivity, limiting its applicability.[4] Most photosensitizing agents are, however, fluorescent, providing another possibility for measuring its concentration. Fluorescence has already been extensively used for tumor localization and to assess treatment progression during diagnostic screening or image-guided surgery to improve clinical decision-making and the therapeutic outcome (see e.g., Refs. 8–11).

Fluorescence spectroscopy (either in the point-monitoring or imaging mode) can also be used as a tool for PS concentration measurements.[4,12–15] No tissue excision would be required in contrast to HPLC. Thus, it may constitute a tool for minimally invasive quantification studies providing *in vivo* capabilities. In these types of measurements, it is, however, a challenge to reduce the influence of the attenuation of the probing light. The signal depends not only on the concentration of the fluorophore but also on the optical properties, the detection geometry, and the tissue autofluorescence [i.e., the fluorescence from endogenous tissue fluorophores such as collagen or nicotinamide adenine dinucleotide (NADH)[16]], etc. Ultimately, these dependencies tend to decrease the correlation coefficient between the fluorescence signal and the true PS concentration.

Address all correspondence to: Haiyan Xie, Lund University, Department of Physics, P.O. Box 118, 22100 Lund, Sweden. Tel: 0046-46-222 3119; Fax: 0046-46-222 4250; E-mail: haiyan.xie@fysik.lth.se.

1083-3668/2011/16(6)/066002/11/$25.00 © 2011 SPIE

An alternative method would be to perform a tomographic reconstruction [fluorescence diffuse optical tomography-(FDOT)]. Such a procedure would obtain the fluorescence signal per unit volume tissue compensated for the light attenuation. The reconstruction is achieved by fitting the collected boundary fluence for multiple source-detector pairs to a forward propagation model, for example, the diffusion model. This somewhat limits the geometries possible in the measurements. Furthermore, FDOT suffers from the requirement of a sophisticated system, greatly increasing the system expense. Moreover, an increased computation time, usually unknown background, and that the reconstruction algorithm most often is very ill-conditioned makes the technique difficult to use in practice.[17–20] Image ratiometric quantification is therefore a commonly used method[12] to correct for these properties. Svensson et al. have suggested and shown that an image ratio of the fluorescence signal from the PS over tissue autofluorescence signal could provide a capability in real-time PS quantification in a defined murine organ.[21] However, different organs do not show the same dependence, probably due to their different optical properties. In Ref. 13, a double fluorescence/reflectance ratio was calculated for two different excitation sources. The excitation wavelengths were chosen to match the maximum and minimum of the fluorophore absorption spectrum. In this way, it was possible to compensate for the optical properties, and to obtain a signal that is only weakly dependent on these properties. This approach requires a sharp edge in the fluorophore absorption in order to facilitate a proper normalization. In Ref. 22, Themelis et al. employed a single fluorescence/remittance ratio approach to correct for the light attenuation effects. They managed to improve the correlation between the fluorescence intensity and fluorophore concentration approximately from 2.5:1 to 1.6:1 for the epi-illumination imaging and from 1.8:1 to 1.2:1 for the transillumination imaging at a five-fold absorption variation for the phantoms they constructed. None of these techniques compensates adequately for the absorption at both excitation and emission wavelengths. The ratio-based methods are thus generally limited to certain special cases.

In this paper we present a novel model-based light-absorption correction approach to obtain the fluorescence intensity originating from the fluorophores to accurately quantify the PS concentrations from the 2D fluorescence images. This method utilizes time-resolved fluorescence white Monte Carlo (FWMC) simulations in combination with the Beer–Lambert law for light absorption. It takes into account details of the light propagation in homogeneous turbid media and thus does not require separate multispectral fluorescence measurements. The results on tissue-like phantoms containing Rhodamine 6G and organs of mice following systemic administration of a liposomal formulation of meso-tetra hydroxyphenyl chlorin (m-THPC), are presented and show an almost linear response of the corrected fluorescence intensities to the chemically extracted fluorophore concentrations measured from HPLC, regardless of the tissue optical properties. The sensitivity of the results to the optical properties variation of the media in the model are also presented.

## 2 Materials and Methods

The light-absorption correction method based on 2D fluorescence images was first validated with a set of well controlled tissue-like phantoms containing the fluorescent dye Rhodamine 6G. Then the PS concentration was evaluated in excised murine tissues and compared to the results from the gold standard in terms of HPLC analysis of extracted tissue samples.

### 2.1 *Phantom Preparation*

Twenty homogeneous liquid tissue phantoms were prepared by mixing water (192.3 ml), Intralipid (Fresenius Kabi, Uppsala, Sweden; 200 mg/ml, 7.3 ml), India ink (Pelican Fount, Hannover, Germany; 1:100 stock solution prepared in our lab, 0 ml, 0.5 ml, 1.0 ml, 1.5 ml, respectively), and Rhodamine 6G, a fluorescent dye with similar emission spectra to fluorescent proteins (Lambda Physik, Göttingen, Germany; a concentration of 10 $\mu$m solution, 0.2 ml, 0.5 ml, 1.0 ml, 1.5 ml, 2.0 ml, respectively). The ranges of ink and dye concentrations were chosen to match the absorption and fluorescence for small animals for both the excitation and emission wavelengths.[23] Each phantom was placed in a cylindric glass container. The thickness of the phantom was 3.1 cm. The absorption and reduced scattering coefficient were measured with a time-of-flight (TOF) spectroscopy system, described in detail elsewhere.[24] The coefficients were measured at two wavelengths (632 and 660 nm). The absorption could be assumed constant over the wavelength range of interest, with the India ink as the absorber. For the reduced scattering, we assumed the relation

$$\mu_s'(\lambda) = a \cdot \lambda^{-b}, \tag{1}$$

where the parameters $a$ and $b$ were determined from the measurements. The anisotropy factor was assumed to be 0.87 at these two wavelengths.[25]

### 2.2 *Photosensitizer*

In the animal measurement, Fospeg® (Biolitec AG, Jena, Germany), a liposomal formulation of the active ingredient m-THPC, or temoporfin, was employed as the PS.[26,27] Liposomes are designed as carrier and delivery systems with the aim of improving the tumor accumulation behavior of the PS during PDT. The PS was diluted in 50 $\mu$l of 5% glucose. All compounds were stored at 4°C in the darkness. The extinction coefficients and fluorescence emission spectrum of m-THPC dissolved in ethanol were measured using a conventional spectrofluorometer (HORIBA Jobin Yvon GmbH, Unterhaching, Germany).

### 2.3 *Animal Model*

The study was performed on 30 female NMRI nu/nu mice (Harlan Winkelmann GmbH, Borchen, Germany). All animal experiments were carried out in compliance with the guidelines established by European Council Directive 86/909/EC and had been approved by the Thüringer Landesamt für Lebensmittelsicherheit und Verbraucherschutz, Weimar. A suspension of HT29 human colorectal carcinoma cells (0.1 ml of $8\times10^7$ cells/ml in 5% aqueous glucose solution) was inoculated subcutaneously 13 days before the measurements into the left and right hind thigh of six- to eight-week-old mice, weighing 22 to 25 g.

The optical properties for various murine tissues used in our data evaluation for some discrete wavelengths were obtained from Ref. 23. The reduced scattering coefficient was then extrapolated using Eq. (1). The absorption coefficient was

approximated in a similar way as a weighted sum of the concentrations of the blood (both oxy- and deoxy-hemoglobin) and water volume fractions in the organs, i.e.,

$$\mu_a(\lambda) = C_{\text{diff}}(\lambda, R_{\text{vessel}}) \cdot S_B \cdot [x\mu_{a_{HbO_2}}(\lambda) + (1-x)\mu_{a_{Hb}}(\lambda)] + S_W \cdot \mu_{a_W}(\lambda), \quad (2)$$

where $\mu_{a_{HbO_2}}(\lambda)$, $\mu_{a_{Hb}}(\lambda)$, and $\mu_{a_W}(\lambda)$ were the spectral absorption coefficients of oxy-haemoglobin ($HbO_2$), deoxy-haemoglobin (Hb) and water, respectively. $x = HbO_2/(HbO_2 + Hb)$. $S_B$ and $S_W$ were blood and water volume fractions, respectively in the different mouse organs. The factor, $C_{\text{diff}}(\lambda, R_{\text{vessel}})$, was introduced to extend the applicability of the diffusion theory in homogeneous media to shorter wavelengths than 650 nm, due to the fact that blood is not a homogeneously distributed absorber but a strong absorber concentrated in the discrete blood vessels.[28] The mean vessel radius, $R_{\text{vessel}}$, was set to 60 $\mu$m.[29] Numerical values for all parameters in the model were selected as in Ref. 23. Finally, the anisotropic factor was set to be 0.8 at both the excitation and emission wavelength.[30]

### 2.4 *Animal Procedures*

Fospeg® was injected into the tail vein of the mice 13 days after the tumor cell inoculation, when the tumors had reached a surface diameter of approximately 5 to 8 mm, and protruded approximately 2 to 3 mm above the skin surface. After injection of Fospeg®, the mice were kept in the dark and given food *ad libidum* until the experiment was performed. The animals were then sacrificed at different times (0.5, 2, 4, 8, and 18 h) after the PS injection. Blood was removed rapidly by cardiac puncture and organs (muscle, liver, kidney, and lung) were excised for fluorescence imaging measurements followed by HPLC analysis. Five mice without PS injection were used as controls.

### 2.5 *HPLC Analysis*

Immediately following the fluorescence imaging, the tissue samples were snap frozen and stored in the darkness until analyzed using chemical extraction and HPLC analysis. In preparation for the HPLC analysis, tissue samples were homogenized by cutting into small pieces, freeze dried for 24 h using a freeze dryer (Alpha 1-4 LSC, Martin Christ Gefriertrocknungsanlagen GmbH, Osterode am Harz, Germany), mixed with methanol and dimethyl sulfoxide (3:5, volume:volume), and continuously shaken for at least 12 h in a vortex mixer (Merck Eurolab, MELB 1719, Lutterworth, UK) operating at 2400 rpm. All samples were then spun at 16,000 rpm in a centrifuge (Microfuge, Heraeus, Germany) during 5 min. 1.0 ml of each supernatant was transferred to an HPLC vial. Details of the sample preparations and HPLC analysis are described in Refs. 21 and 31. The results from the HPLC method of the excised tissue were used as gold standard for determining the drug concentrations. These values were correlated to the animal fluorescence measurements.

### 2.6 *Fluorescence Imaging Measurements*

Fluorescence images were acquired using the setup schematically depicted in Fig. 1. The excitation light was coupled into an optical fiber. The distal end of the fiber was positioned to obtain either a transillumination or an epi-fluorescence geometry.

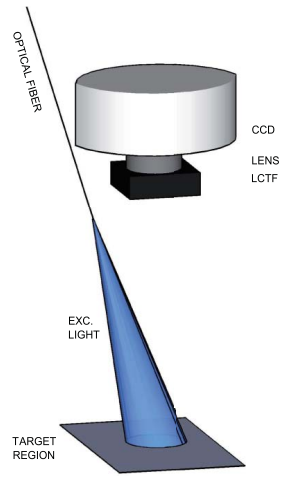


**Fig. 1** Schematic picture showing the fluorescence imaging setup. The distal end of the fiber was positioned to obtain either a transillumination or an epi-fluorescence geometry.

For the phantom experiments, Rhodamine 6G was excited by an Nd:YAG laser (Viasho VA-I-N-532–200mW, Beijing, China) at 532 nm with a spot size of 3 mm in diameter from the bottom of the container. The fluorescence was spectrally filtered using a liquid crystal tunable filter (LCTF VIS 20-35, Varispec, CRI, Inc., Woburn, California). Images of transmitted fluorescence were acquired with the LCTF set to 600 nm, using a charge-coupled device (CCD) camera (Andor iXon DU-897, Belfast, Ireland) with a standard camera lens (50 mm focal length and f/1.8, Nikon, Tokyo, Japan). To suppress the transmitted laser light from reaching the camera, a long-pass, cut-off color-glass filter (OG-550, Schott Inc., W. Germany) was fixed between the sample and the LCTF.

For the animal measurement, a continuous-wave laser source at 405 nm developed at DTU Fotonik was used for excitation of the PS. It was based on a frequency doubled tapered diode amplifier placed in an external grating cavity with Littrow feedback, described in Ref. 32. The entire laser system was built on a breadboard and placed on a mobile cart. The output power was 130 mW, out of which 70% was coupled into and delivered through an optical fiber mounted above the target. The spot size on the tissue was approximately 4 cm in diameter. The fluorescence images were captured by the CCD camera with the LCTF set to 652 nm (corresponding to m-THPC fluorescence peak) and 525 nm (tissue autofluorescence), respectively.

The fluorescence images were acquired in a dimmed room to avoid any artifacts from background light. Background images without the excitation light were also acquired using the same filter wavelength.

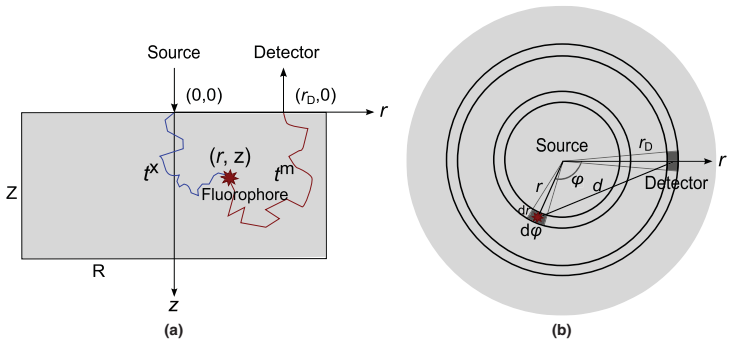


**Fig. 2** Schematic diagram of the geometry used for fluorescence white Monte Carlo simulations. (a) The medium is divided into volume elements using small grids along the $r$ and $z$ axes. Similarly, time is divided into intervals with a size of $dt$. (b) View of the coordinate system used to calculate the convolution of excitation and emission light for a slab of thickness $dz$ at $z$, where $d = (r^2 + r_D^2 + 2rr_D\cos\varphi)^{1/2}$.

### 2.7 *Evaluation Procedure*

The background image was subtracted pixel by pixel from each fluorescence image. The fluorescence intensity for an image was normalized with respect to the exposure time. Prior to the correction, all images obtained were cropped to the size of the ROI corresponding to the area where the fluorescence signal was measured for the phantom or the entire organ. Then the fluorescence intensity was computed as the average over each investigated sample.

#### 2.7.1 *Image ratio*

The PS concentration within each animal organ was quantified by calculating a dimensionless contrast function resulting from forming a spectral ratio between the two detection bands:

$$R = F_{\text{image}}(652\text{ nm})/F_{\text{image}}(525\text{ nm}), \tag{3}$$

where $F_{\text{image}}(652\text{ nm})$ and $F_{\text{image}}(525\text{ nm})$ denote the mean value of the fluorescence intensities within the ROI at the two wavelengths for each animal tissue sample.

#### 2.7.2 *Light absorption correction*

For a series of nonabsorbing media with the same scattering coefficient and geometry but containing a different amount of fluorescence molecules (uniformly distributed), the fluorescence escaping from the surface is proportional to the concentration of the fluorophores. However, different media usually have different absorption coefficients, leading to different absorbed fractions both for the excitation and emission light. As a result, the fluorescence signal detected thus normally shows a strong dependence on the tissue type in addition to the fluorophore concentration. In principle, the absorptions of both the excitation and emission light can be compensated for by the Beer–Lambert law, if the temporal distribution of the escaping fluorescence is known. Thus, the linear dependence of the fluorescence intensity on fluorophore concentration could be reconstructed, independent on tissue type (or optical properties).

The temporal distribution of the fluorescence was simulated by a reverse-emission accelerated Monte Carlo (MC) approach,[33] which accelerated the fluorescence MC simulations considerably. To further save computation time, the method was modified and combined with the white Monte Carlo (WMC) simulation approach. The principle of WMC is explained in detail in Ref. 24. The WMC approach accelerates multispectral simulations as the solution for one set of optical properties (corresponding to one wavelength) can be rescaled to another set. This makes it only necessary to conduct one simulation run, independent of the number of wavelengths of interest. The simulation time can thus be greatly shortened, especially when modeling tissue fluorescence, where multiple wavelengths and different sets of optical properties are involved.

The medium simulated was assumed to be homogeneous and the fluorescent molecules to be uniformly distributed. The geometry used for the simulation is a cylinder with a radius of $R$ and height of $Z$, as shown in Fig. 2. The optical properties of the medium at the excitation wavelength are described by the absorption coefficient $\mu_a^x$, the scattering coefficient $\mu_s^x$, and the anisotropy factor $g^x$. The corresponding parameters at the emission wavelength are $\mu_a^m$, $\mu_s^m$, and $g^m$, respectively. Furthermore, we define $t^x$ as the time an excitation photon takes from the excitation light source to exciting a fluorophore, and $t^m$ the time an emission photon takes from the fluorophore to the detector on the medium surface. For a nonabsorbing white medium with certain scattering coefficients $\mu_s^x$ and $\mu_s^m$, the fluorescence intensities detected at a radial position $r_D$ after time $t^x$ and $t^m$ are denoted as $F_W(r_D, t^x, t^m)$, the short term of $F_W(\mu_a^x = 0, \mu_a^m = 0, \mu_s^x, \mu_s^m, r_D, t^x, t^m)$. It could be simulated through a reverse-emission accelerated FWMC procedure, as defined in Ref. 33, by setting $\mu_a^x$ and $\mu_a^m$ to zero and convolving over space.

$$F_{\text{W}}(r_{\text{D}}, t^{\text{x}}, t^{\text{m}}) = \int_0^Z \mathrm{d}z \int_0^R \mathrm{d}r \int_0^{2\pi} \mathrm{d}\varphi A_{\text{W}}\left(\mu_{\text{a}}^{\text{x}} = 0, \mu_{\text{s}}^{\text{x}}, r, z, t^{\text{x}}\right) \times \phi_{\text{eff}}(r, \varphi, z) E_{\text{W}}\left(\mu_{\text{a}}^{\text{m}} = 0, \mu_{\text{s}}^{\text{m}}, d, z, t^{\text{m}}\right), \tag{4}$$

where $A_W(\mu_a^x = 0, \mu_s^x, r, z, t^x)$ is the probability per unit volume and unit time for an excitation photon to be absorbed at a fluorophore position $(r, \varphi, z)$, after a time delay $t^x$ from the injection point; $E_W(\mu_a^m = 0, \mu_s^m, d, z, t^m)$ is the probability

**Table 1** Input parameters for white Monte Carlo simulations.

| | | | Grid resolution | | | Grid size | | | |
|---|---|---|---|---|---|---|---|---|---|
| | No. photons | $\phi_{\text{eff}}$ | dz ($\mu$m) | dr ($\mu$m) | dt (ps) | nz | nr | $nt_1$ | $nt_2$ |
| Phantoms | $2\times10^6$ | 0.25 | 500 | 500 | 10 | 61 | 120 | 400 | 400 |
| Murine tissues | $10^7$ | 0.25 | 40 | 40 | 1 | 125 | 200 | 150 | 150 |

per unit volume and unit time to detect a fluorescence photon which originates from the fluorescence emission point which is located at a radial distance $d$ and a depth $z$, after a delay $t^m$; $\phi_{\text{eff}}(r, \varphi, z)$ is the effective quantum yield, which is a constant in time and space and proportional to the fluorophore concentration. In our evaluation the decay of the fluorophore is assumed to be negligible. Values of input parameters used for the WMC simulations are stated in Table 1.

In the experiments, the excitation light was distributed over the medium surface. This effect was taken into account by

$$F_W^*(r_D, t^x, t^m) = F_W(r_D, t^x, t^m) \otimes S_{\text{Beam}}, \tag{5}$$

where $\otimes$ denotes the convolution, and $S_{\text{Beam}}$ is the beam intensity profile on the medium surface.

If absorption is added to this white medium at both excitation and emission, the corresponding fluorescence intensities, $F_A^*(r_D, t^x, t^m)$, can be derived analytically from $F_W^*(r_D, t^x, t^m)$ using the Beer–Lambert law:

$$F_{\text{A}}^*(r_{\text{D}}, t^{\text{x}}, t^{\text{m}}) = F_{\text{W}}^*(r_{\text{D}}, t^{\text{x}}, t^{\text{m}}) \exp\left[-\mu_{\text{a}}^{\text{x}} v t^{\text{x}}\right] \exp\left[-\mu_{\text{a}}^{\text{m}} v t^{\text{m}}\right], \tag{6}$$

where $v = c/n$ is the light speed in the medium with a refractive index $n$. Integrating over the time, we will get a signal corresponding to the recorded fluorescence signal from a pixel at a radius $r_D$, or a Cartesian position $(x, y)$ in the image, where $r_D = (x^2 + y^2)^{1/2}$. We denote this $F_{\text{image}}(x, y)$:

$$F_{\text{image}}(x, y) = F_{\text{image}}(r_{\text{D}}) = \int_{t^{\text{x}}} \int_{t^{\text{m}}} F_{\text{A}}^*(r_{\text{D}}, t^{\text{x}}, t^{\text{m}}) \mathrm{d}t^{\text{x}} \mathrm{d}t^{\text{m}}. \tag{7}$$

Then the total intensity from the image can be obtained by summing up all over the pixels:

$$F_{\text{image}} = \sum_{x,y} F_{\text{image}}(x, y). \tag{8}$$

By defining a calculated correction factor

$$\Delta \equiv \frac{\int_{t^{\text{x}}} \int_{t^{\text{m}}} \oint_{\text{ROI}} F_{\text{W}}^*(r_{\text{D}}, t^{\text{x}}, t^{\text{m}}) \mathrm{d}t^{\text{x}} \mathrm{d}t^{\text{m}} \mathrm{d}s}{F_{\text{image}}}, \tag{9}$$

where $s$ denotes the surface integral, and ROI is the evaluated region of interest from which the fluorescence is measured, we get

$$F_{\text{image}} \cdot \Delta \propto \int_{t^{\text{x}}} \int_{t^{\text{m}}} \oint_{\text{ROI}} F_{\text{W}}^*(r_{\text{D}}, t^{\text{x}}, t^{\text{m}}) \mathrm{d}t^{\text{x}} \mathrm{d}t^{\text{m}} \mathrm{d}s \propto \phi_{\text{eff}} \propto \text{Conc}, \tag{10}$$

where Conc is the fluorophore concentration to be determined. This indicates the corrected fluorescence intensity, $F_{\text{image}} \cdot \Delta$, will be proportional to the fluorophore concentration.

## 3 Results

### 3.1 *Time-Resolved Fluorescence Distribution from the FWMC Simulations*

The simulated temporal distribution of the fluorescence signal $F(r_D, t^x, t^m, z_D)$ is plotted in Fig. 3. This corresponds to the detected signal at a surface of the simulated phantom at a radial distance $r_D = 5.0$ mm, where $z_D$ indicates if the detector is at the bottom (the left column, $z_D = 3.1$ cm, corresponding to the transillumination geometry) or the top surface (the right column,

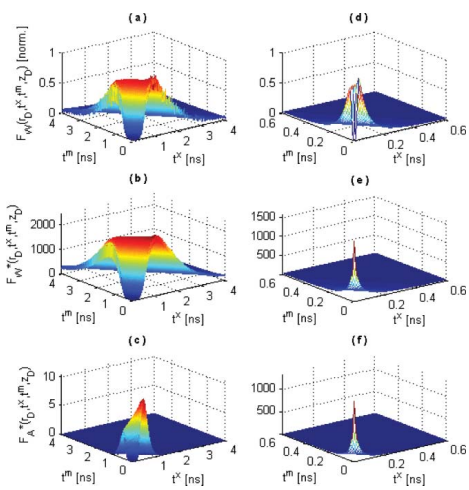


**Fig. 3** Simulated temporal distribution of the fluorescence for the phantom at $r_D = 5.0$ mm. The left column illustrates the fluorescence at $Z_D = 3.1$ cm, i.e., for the transillumination geometry. The fluorescence intensity has been normalized to its peak signal. The right column shows the corresponding data at $Z_D = 0$, i.e., for the epi-fluorescence geometry. The top row show the results for a white medium when all the incident photons were injected at the origin; in (b) and (e) a uniform flat beam was incident all over the surface of this white medium; while in (c) and (f) an absorption of $\mu_a^x = \mu_a^m = 0.37$ cm$^{-1}$ is added. In the simulations, reduced scattering coefficients of $\mu_s'^x = 10.07$ cm$^{-1}$ and $\mu_s'^m = 8.30$ cm$^{-1}$ were used. Values of the other parameters are listed in Table 1.

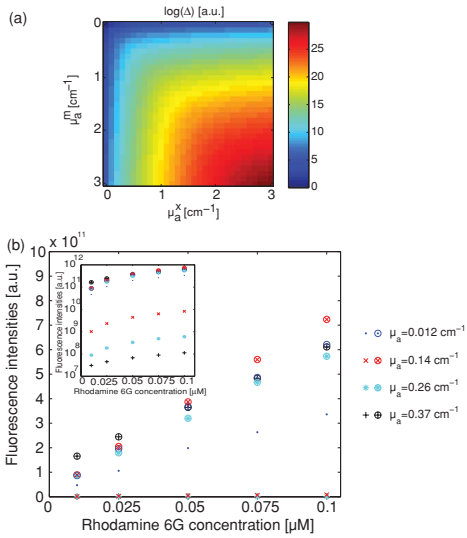


**Fig. 4** (a) Dependence of the correction factor on phantom absorption coefficients for the transillumination geometry. (b) Scatter plots showing the fluorescence signals captured at 600 nm before (markers without circles) and after (with circles) the light-absorption correction versus the true dye concentrations for liquid tissue-like phantoms, where the absorption coefficients are the same at the 532-nm excitation and 600-nm emission, i.e., $\mu_a = \mu_a^x = \mu_a^m$. The inset shows the same data in the semi-log scale.

$z_D = 0$ cm, the epi-fluorescence geometry). The subplots in the top row show the results for a point source at the top center of a white medium, i.e., with zero-absorption. It can be seen that most of the excitation light has a large probability to be absorbed and the fluorescence reaches the detector within a much longer time in the transillumination geometry [Fig. 3(a)] than in the epi-fluorescence geometry [Fig. 3(d)]. For a flat light source with uniform power distribution irradiating all over the surface of the white medium, the fluorescence signal in the point source case was convolved with the beam intensity profile on the total surface. The result of that is shown in the middle row. The signal is increased by a factor of approximately one thousand. When a certain absorption was added to the white medium, Eq. (6) was applied to calculate the absorbed light. The results are illustrated in the bottom row. Photons with a long traveling time are absorbed, resulting in a decreased fluorescence signal.

For the phantom, the total simulation time is approximately 3 h for one single FWMC process, running on a Intel Duo Core 2-GHz processor. For the smaller grids corresponding to the animal case, the simulation time is approximately 10 h.

### 3.2 *Phantom Measurements*

Our light-absorption correction method was first tested on homogeneous well-controlled tissue-like phantoms. From the TOF measurement, the absorption coefficients of the phantoms with

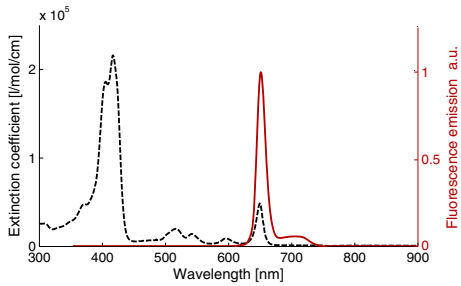


**Fig. 5** The extinction coefficients (dashed line) and the fluorescence emission spectrum (solid line) of m-THPC when excited at 405 nm in ethanol.

the same ink concentration were the same at both 532 and 600 nm, as the India ink absorption is very flat over this wavelength range. For different ink concentrations, the results were 0.37, 0.26, 0.14, and 0.012 cm$^{-1}$, respectively. The reduced scattering coefficients were measured and extrapolated to be 10.10 cm$^{-1}$ at 532 nm and 8.30 cm$^{-1}$ at 600 nm.

The simulated dependence of the correction factor on different absorption coefficients at the excitation and emission wavelength is shown in Fig. 4(a). For the four sets of phantoms with different absorptions, the correction factor was $\Delta = 5303$, 949, 87, and 2, respectively. The large variation in $\Delta$ illustrates that the fluorescence signal from the surface is heavily dependent on the optical properties of the absorbing medium. Figure 4(b) shows the correlation between the fluorescence signal and the fluorescent dye (Rhodamine 6G) concentrations before and after the light-absorption correction, respectively. The markers without circles represent the raw signals directly from the images, while the markers with circles representing the corrected fluorescence intensities, which were achieved by multiplying the measured fluorescence from the images by the corresponding simulated $\Delta$. The correlation between the fluorescence signal and the fluorophore concentration is dramatically improved from 3000:1 to 1.3:1.

### 3.3 *Animal Measurements*

The extinction coefficients and fluorescence emission spectrum of m-THPC dissolved in ethanol are plotted in Fig. 5, which shows a high extinction coefficient at 405 nm and strong fluorescent emission at 652 nm.

For the animal measurements, the data from the HPLC method were regarded as the absolute PS concentrations. Figure 6 shows some fluorescence images of the murine organs *ex vivo*, acquired from the imaging setup. Both the image spectral ratio [$F_{\text{image}}(652\text{ nm})/F_{\text{image}}(525\text{ nm})$] and light-absorption correction method [$F_{\text{image}}(652\text{ nm}) \cdot \Delta$] were evaluated for the different types of murine organs. The results are shown in Figs. 7 and 8. The subplots on the left of Figs. 7 and 8 show the correlations between the raw fluorescence signals at 652 nm directly from the images and the PS concentrations. The slope of the linear fit varies from 5900 for muscle to 720 for lung (8.3:1). That is to say, no universal correlation curve could adequately fit

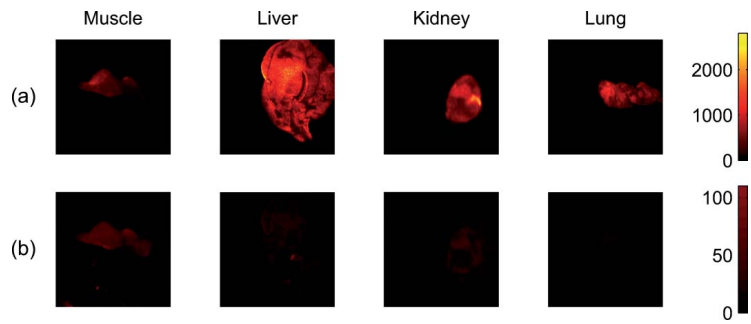


**Fig. 6** Fluorescence images of some animal organs *ex vivo* captured at different emission wavelengths with an exposure time of 11 s. The color bars indicate fluorescence intensity after background subtraction. (a) The top row shows the images taken with the LCTF set to 652 nm (corresponding to the maximal drug fluorescence), while (b) the bottom row shows the images at 525 nm (tissue autofluorescence).

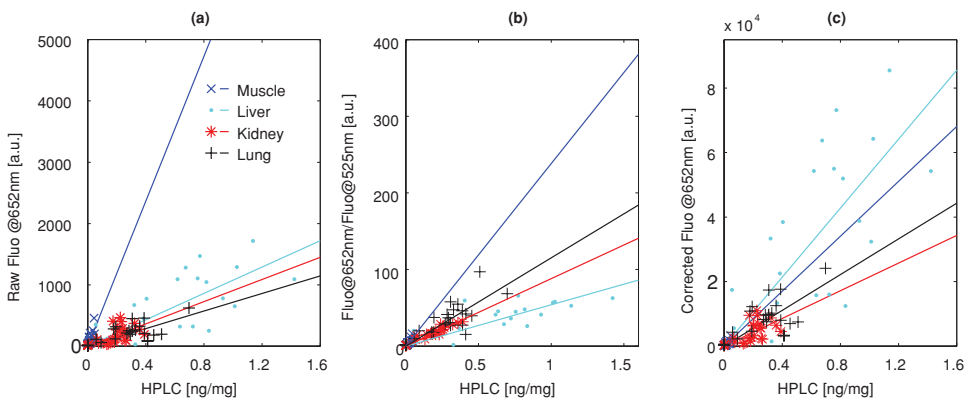


**Fig. 7** Scatter plots showing (a) the fluorescence signals captured at 652 nm versus the HPLC values for individual organs, where a linear fit of the data points for each type of organs (solid line) is also shown; (b) the spectral ratio of the fluorescence intensities at 652 nm to that at 525 nm; and (c) the fluorescence signals after the light-absorption correction versus the HPLC values.

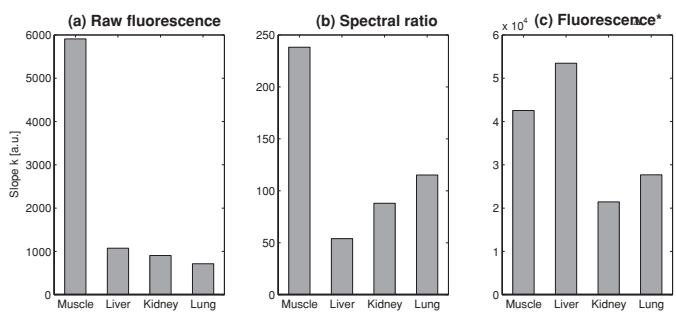


**Fig. 8** Comparison of the linear fit slopes between the fluorescence signals and the HPLC values. The methods are the same as stated in Fig. 7.

**Table 2** Optical properties of different organs.

| Organs | $\mu_a^x(\text{cm}^{-1})$ | $\mu_a^m(\text{cm}^{-1})$ | $\mu_s^x(\text{cm}^{-1})$ | $\mu_s^m(\text{cm}^{-1})$ | $g^x = g^m(-)$ |
|---|---|---|---|---|---|
| Muscle | 6.2 | 0.4 | 88.7 | 23.0 | 0.8 |
| Liver | 26.5 | 1.8 | 57.5 | 34.9 | 0.8 |
| Kidney | 4.9 | 0.3 | 240.9 | 117.4 | 0.8 |
| Lung | 13.5 | 0.6 | 142.0 | 110.0 | 0.8 |

the fluorescence imaging data and the HPLC values, mainly due to the varying optical properties of the tissue under investigation. As shown in the middle columns, the slope from the spectral ratio varies from 240 for muscle to 60 for liver (4.4:1). After the absorbed light is compensated for, using the optical properties of a different type of murine organs listed in Table 2, the result on the right shows the slope varying from 53,500 for liver to 21,400 for lung (2.5:1).

## 4 Discussion

The simulated time-resolved fluorescence signal provides us with a clear picture of how the excitation and emitted photons migrate in the medium. With the information of the photomigration time, one can simulate the amount of light which is absorbed within the turbid medium, using the proposed absorption correction method. As demonstrated with tissue-like phantoms in Fig. 4(b), the correlation between the corrected (intrinsic) fluorescence signal and the dye concentration has been dramatically improved by approximately 2000-fold in comparison to the uncorrected signal, when absorption of the phantoms was varied over a wide range (approximately by a factor of 30). However, the corrected correlation is not a perfect single line (about 30% error in the correlation) for different sets of optical properties. This results mainly from about a 10% relative error in the optical properties measured by the TOF spectroscopy system.[34] Therefore, we tested the sensitivity of $\Delta$ due to the error in the measured optical properties by altering them to a $\pm 10\%$ variation, while the other parameters remained the same in the simulations. How $\Delta$ is affected for the set of phantoms with the highest absorption and scattering coefficients ($\mu_a^x = \mu_a^m = 0.37\,\text{cm}^{-1}$, $\mu_s'^x = 10.10\,\text{cm}^{-1}$, $\mu_s'^m = 8.30\,\text{cm}^{-1}$) is shown in Tables 3 and 4, respectively. The relative change in $\Delta$ is within the range of $-18\%$ to $+36\%$. For the other phantoms, a smaller variation in $\Delta$ was obtained for lower values of the optical properties. Provided more accurate optical properties, one could expect a better correlation between the fluorescence and fluorophore concentrations. In addition, photobleaching of Rhodamine 6G (which also could provide an error) is not relevant due to the low light fluence and short acquisition time used.

For the animal study, Fospeg® content *ex vivo* in murine organs was quantified. This drug contains the active ingredient m-THPC, and therefore is interesting as a PDT sensitizer. The observed signal level directly from the fluorescence imaging measurement is affected by many factors. It generally leads to a poor correlation between the signal level and drug concentration, as shown in Figs. 7(a) and 8(a). The fitted linear slope of the raw fluorescence signals at 652 nm varies drastically between different organs. The large variations in the raw signals indicate that absorption caused by tissue should be taken into account to allow quantification of the PS in the tissue samples. Tissue absorption at the interesting wavelengths is mostly dependent on the amount of hemoglobin (both oxy- and deoxy-hemoglobin) in the tissue. The high absorbance in lung, kidney, and liver is caused by high blood contents, attenuating both the excitation and emission light. This effect explains the lower slope of the correlation curves for these organs as compared to those for muscle and skin. The detailed selectivity and biodistribution of Fospeg® following systemic administration were studied separately in Ref. 31.

To compensate for the tissue absorbed light, the optical properties for different murine organs need to be known. Values from literatures vary a lot and seem not fully consistent between tissue types. The large variation in literature values results from the fact that measurements were performed on tissues from different species, *in vitro* or *in vivo*, and at a great variety of sample preparation techniques and other experimental conditions. In the preparation period of the tissue samples in this study, bleeding during organ removal caused partial loss of the blood resulting in a variation of absorption coefficient even for the same type of tissues. As mentioned above, we do not have the precise values of the tissue optical properties. Instead, the tabulated values from Ref. 23 were used. They could only be interpreted as reasonable but rough estimates of the true mouse tissue optical properties. This is one of the main reasons why the correlation is not as good as that for the phantom. The sensitivity of the correction factor to tissue absorption coefficients are also examined for the liver with highest absorption ($\mu_a^x = 26.5\,\text{cm}^{-1}$, $\mu_a^m = 1.8\,\text{cm}^{-1}$, $\mu_s'^x = 11.5\,\text{cm}^{-1}$, $\mu_s'^m = 7.0\,\text{cm}^{-1}$). In Table 5, the absorption coefficients have been altered by $\pm 30\%$, resulting in a variation in $\Delta$ from $-34\%$ to $+41\%$. Apparently this variation is less sensitive than that of the phantoms due to the much shorter migration pathlengths the photons spend in the epi-fluorescence geometry. Furthermore, if the tissue optical properties could be measured individually for each tissue investigated, simultaneously with the fluorescence imaging measurements, the correlation could be further improved.

The absorption correction method proposed in this study is based on assumptions that the fluorescent drug is homogeneously distributed within these tissues, and that all tissues have homogeneous optical properties. Unfortunately very little is known about distribution of this new drug following system-

**Table 3** Sensitivity of the simulated correction factor to absorption coefficients of the phantoms.

| | $(\mu_a^x, \mu_a^m)$ | $(\mu_a^x - 10\%, \mu_a^m)$ | $(\mu_a^x + 10\%, \mu_a^m)$ | $(\mu_a^x, \mu_a^m - 10\%)$ | $(\mu_a^x, \mu_a^m + 10\%)$ |
|---|---|---|---|---|---|
| Variation in $\Delta$ | 0 | $-23\%$ | $+26\%$ | $-27\%$ | $+32\%$ |

**Table 4** Sensitivity of the simulated correction factor to scattering coefficients of the phantoms.

| | $(\mu_s'^x, \mu_s'^m)$ | $(\mu_s'^x - 10\%, \mu_s'^m)$ | $(\mu_s'^x + 10\%, \mu_s'^m)$ | $(\mu_s'^x, \mu_s'^m - 10\%)$ | $(\mu_s'^x, \mu_s'^m + 10\%)$ |
|---|---|---|---|---|---|
| Variation in $\Delta$ | 0 | −22% | +25% | −18% | +19% |

atic administration. Nonetheless, we believe it is reasonable to assume a homogeneous fluorophore distribution. The assumptions are based on the following considerations and facts. First, the drug was systemically administrated to the animals. This suggests, in a first order approximation, a relatively homogeneous distribution in the tissues. Second, the time delays between drug injection and the measurements are relatively long in this study, again suggesting a relatively homogenous distribution. In addition, the tumors in this study are relatively small without visible necrotic regions that would cause an inhomogenous distribution. Actually, the inhomogeneity of the fluorescence can somehow be examined from the spatial distribution of the fluorescence ratio analyzed. From the fluorescence ratio image, a rather homogeneously fluorescence is present across the organ surface. Any spatial variation in raw data images for a single wavelength is mostly due to nonuniform illumination, variations in the distance, and the angle between the tissue surface and light source. In this study the fluorescence measurements are correlated with absolute drug concentration using chemical extraction and HPLC analysis, where the tissues were homogenized in preparation and the results were considered as a gold standard. This technique also relies on a homogeneous distribution.

It is known that the fluorescence intensity sometimes exhibits local variations in certain tissue structures due to light reabsorption or fluctuations in fluorescence yield due to the local fluorophore environment. The intra-animal variation in mTHPC concentration has been investigated by Kruijt et al. They investigated intratumoral localization of Foslip® (a different liposomal formulation of mTHPC in rat liver).[35] For short drug-light intervals, the drug is vascularly targeted, whereas longer time periods (>3 h) enable the PS to diffuse into the nearby tissues.[3] They found an overall homogeneous distribution of mTHPC on the macroscopic scale, while it was heterogeneous on a submillimeter spatial scale. The macroscopic fluorescence imaging setup and chemical extraction do not have the spatial resolution to pick up such a small spatial heterogeneity. Instead these techniques averaged the fluorescence intensities and homogenized the tissues in the chemical extraction. In fact, the absorption coefficient of animal tissues at 405-nm excitation wavelength is on the order of tens of $cm^{-1}$. When the fluorescence is excited at 405 nm, the effective penetration depth into tissue is typically on the order of hundreds of micrometers. In practice we are sampling a relatively small volume of tissues. This might also decrease the correlation between the fluorescence signal and PS concentration.

Tissue autofluorescence could be another issue to slightly influence the measured fluorescence intensities and thus the resulting correlation. When excited by UV- or blue radiation, tissue autofluorescence has a broad spectrum without any distinct spectral features and slightly overlaps the drug fluorescence signals. The cross-talk will give a background in the detection. Johansson et al.,[4] and Svensson et al.[21] discussed how the influence of this cross-talk can be minimized for fluorophore assessments. In this work, another approach to handle the tissue autofluorescence was employed, using a dimensionless contrast function, namely the fluorescence ratio between the m-THPC emission peak at 652 nm and the strongest tissue autofluorescence at 525 nm, to study the drug concentrations. This approach improves the correlation between the fluorescence signals and the absolute drug content, yet not good enough, as shown in Figs. 7(b) and 8(b). To reduce the tissue autofluorescence, fluorescence imaging in the near-infrared was utilized in Ref. 22, since autofluorescence is much smaller than in the visible. Furthermore, a halogen lamp for white-light color imaging was employed to get the attenuation image, which had to be selected where the fluorophore of interest does not fluoresce. Therefore, the ratio-based quantification method has a quite strict limit on the spectral bands. It can not be applied in general cases. A significant advantage of the now proposed light-absorption correction method is that it does not have strict requirements on the spectral bands as in the ratiometric quantification methods.

Photodegradation of Temoporfin over time is usually expected in the fluorescence measurement, in particular in relation to the ultimate goal of using this technique for quantification of PS concentration during PDT. Normally photobleaching depends much on irradiance. Bendsoe et al. reported a photobleaching of about 30% to 35% after 200 s in a liposome formulation based on dipalmitoylphosphatidylcholine of m-THPC, with an irradiation of 20 $J/cm^2$ at 652-nm excitation.[36] In comparison, the fluence rate is 7 $mW/cm^2$ at 405-nm excitation in our measurement, which should translate in that the photodegradation is negligible within the imaging acquisition time (11 s). Based on this point, the light-induced changes in the resulting absolute PS concentration, which was obtained from HPLC analysis after fluorescence measurement, is also at an acceptable

**Table 5** Sensitivity of the simulated correction factor to absorption coefficients of murine livers.

| | $(\mu_a^x, \mu_a^m)$ | $(\mu_a^x - 30\%, \mu_a^m)$ | $(\mu_a^x + 30\%, \mu_a^m)$ | $(\mu_a^x, \mu_a^m - 30\%)$ | $(\mu_a^x, \mu_a^m + 30\%)$ |
|---|---|---|---|---|---|
| Variation in $\Delta$ | 0 | −34% | +41% | −10% | +9% |

level. It is worthwhile to point out that the fluorophore lifetime does not influence the correlation in the model at all, since the absorbed light depends only on the photon migration time.

## 5 Conclusion

In conclusion, this paper has shown that the fluorescence imaging technique can be used as a noninvasive and sensitive tool to quantify the fluorescent markers in homogeneous turbid media, using the novel light-absorption correction approach combining the fluorescence imaging and FWMC simulations. The results on both the well-controlled tissue-like phantoms and *ex vivo* animal tissues have shown that this method provides an acceptable quantification of fluorescent molecule markers in media with known geometry and optical properties at both the excitation and emission wavelengths. An improved linear correlation with the true concentrations is obtained independent of the tissue optical properties, since this method efficiently compensates for light attenuation and thus more directly relates to the intrinsic fluorescence signal levels from the fluorophores. This approach offers the advantages of minimizing the dependence on the tissue optical properties, a very low concentration detection limit, and wide spectral bands. The sensitivity of the results to the medium optical properties variation are presented and discussed, in order to point toward the possible future improvement of this technique.

In future work, it is highly desirable to combine the sensitivity of the fluorescence imaging technique with the tissue optical properties measurements to constitute an even better and more reliable fluorophore concentration estimate. The absorption correction and image ratio methods could also be combined to compensate for tissue autofluorescence.

### *Acknowledgments*

The authors are grateful to Biolitec AG for the realization of animal studies, HPLC analysis of tissue samples, and providing photosensitizer formulations (a drug they have a commercial interest in), and to Erik Alerstam for his assistance with the time-of-flight measurements. This work was funded by the EUBrighter project (FP6-IST-035266) (all groups), and a Linnaeus grant for the Lund Laser Center.

1. A. Johansson and S. Andersson-Engels, Chapter 8 in *Laser Imaging and Manipulation in Cell Biology*, pp. 167–199, Wiley-VCH, Verlag (2010).
2. K. Svanberg, N. Bendsoe, J. Axelsson, S. Andersson-Engels, and S. Svanberg, "Photodynamic therapy: superficial and interstitial illumination," *J. Biomed. Opt.* **15**(4), 041502 (2010).
3. H.-P. Lassalle, D. Dumas, S. Gräfe, M.-A. D'Hallewin, F. Guillemin, and L. Bezdetnaya, "Correlation between in vivo pharmacokinetics, intratumoral distribution and photodynamic efficiency of liposomal mTHPC," *J. Controlled Release* **134**(2), 118–124 (2009).
4. A. Johansson, J. Svensson, N. Bendsoe, K. Svanberg, E. Alexandratou, M. Kyriazi, D. Yova, S. Gräfe, T. Trebst, and S. Andersson-Engels, "Fluorescence and absorption assessment of a lipid mTHPC formulation following topical application in a non-melanotic skin tumor model," *J. Biomed. Opt.* **12**(3), 034026 (2007).
5. J. R. Mourant, I. J. Bigio, D. A. Jack, T. M. Johnson, and H. D. Miller, "Measuring absorption coefficients in small volumes of highly scattering media: source-detector separations for which path lengths do not depend on scattering properties," *Appl. Opt.* **36**(22), 5655–5661 (1997).
6. J. R. Mourant, T. M. Johnson, G. Los, and I. J. Bigio, "Non-invasive measurement of chemotherapy drug concentrations in tissue: preliminary demonstrations of in vivo measurements," *Phys. Med. Biol.* **44**(5), 1397–1417 (1999).
7. L. Lilge, C. O'Carroll, and B. Wilson, "A solubilization technique for photosensitizer quantification in ex vivo tissue samples," *J. Photochem. Photobiol. B: Biol.* **39**(3), 229–235 (1997).
8. D. Jocham, H. Stepp, and R. Waidelich, "Photodynamic diagnosis in urology: state-of-the-art," *Eur. Urol.* **53**(6), 1138–1150 (2008).
9. Q. T. Nguyen, E. S. Olson, T. A. Aguilera, T. Jiang, M. Scadeng, L. G. Ellies, and R. Y. Tsien, "Surgery with molecular fluorescence imaging using activatable cell-penetrating peptides decreases residual cancer and improves survival," *Proc. Nat. Acad. Sci. USA* **107**(9), 4317–4322 (2010).
10. M. S. Eljamel, "Fluorescence image-guided surgery of brain tumors: Explained step-by-step," *Photodiagn. Photodyn. Ther.* **5**(4), 260–263 (2008).
11. N. Haj-Hosseini, J. Richter, S. Andersson-Engels, and K. Wårdell, "Optical touch pointer for fluorescence guided glioblastoma resection using 5-aminolevulinic acid," *Lasers Surg. Med.* **42**, 9–14 (2010).
12. A. Bogaards, H. Sterenborg, and B. Wilson, "In vivo quantification of fluorescent molecular markers in real-time: A review to evaluate the performance of five existing methods," *Photodiagn. Photodyn. Ther.* **4**(3), 170–178 (2007).
13. A. Bogaards, H. Sterenborg, J. Trachtenberg, B. Wilson, and L. Lilge, "In vivo quantification of fluorescent molecular markers in real-time by ratio imaging for diagnostic screening and image-guided surgery," *Lasers Surg. Med.* **39**(7), 605–613 (2007).
14. H. Stepp, T. Beck, W. Beyer, C. Pfaller, M. Schuppler, R. Sroka, and R. Baumgartner, "Measurement of fluorophore concentration in turbid media by a single optical fiber," *Med. Laser Appl.* **22**(1), 23–34 (2007).
15. M. M. Korol', A. S. Slesar', M. V. Parkhots, A. Y. Khairullina, and T. V. Ol'shanskaya, "Determination of photosensitizer concentration in biological tissues from diffuse reflectance and fluorescence," *J. Appl. Spectrosc.* **76**(2), 260–267 (2009).
16. C. T. Xu, N. Svensson, J. Axelsson, P. Svenmarker, G. Somesfalean, G. Chen, H. Liang, H. Liu, Z. Zhang, and S. Andersson-Engels, "Autofluorescence insensitive imaging using upconverting nanocrystals in scattering media," *Appl. Phys. Lett.* **93**(17), 171103 (2008).
17. V. Ntziachristos, J. Ripoll, L. V. Wang, and R. Weissleder, "Looking and listening to light: the evolution of whole-body photonic imaging," *Nat. Biotech.* **23**, 313–320 (2005).
18. V. Ntziachristos, "Fluorescence molecular imaging," *Annu. Rev. Biomed. Eng.* **8**(1), 1–33 (2006).
19. L. Sampath, W. Wang, and E. M. Sevick-Muraca, "Near infrared fluorescent optical imaging for nodal staging," *J. Biomed. Opt.* **13**(4), 041312 (2008).
20. C. T. Xu, J. Axelsson, and S. Andersson-Engels, "Fluorescence diffuse optical tomography using upconverting nanoparticles," *Appl. Phys. Lett.* **94**(25), 251107 (2009).
21. J. Svensson, A. Johansson, S. Gräfe, B. Gitter, T. Trebst, N. Bendsoe, S. Andersson-Engels, and K. Svanberg, "Tumor selectivity at short times following systemic administration of a liposomal temoporfin formulation in a murine tumor model," *Photochem. Photobiol.* **83**(5), 1211–1219 (2007).
22. G. Themelis, J. S. Yoo, K.-S. Soh, R. Schulz, and V. Ntziachristos, "Real-time intraoperative fluorescence imaging system using light-absorption correction," *J. Biomed. Opt.* **14**(6), 064012 (2009).
23. G. Alexandrakis, F. R. Rannou, and A. F. Chatziioannou, "Tomographic bioluminescence imaging by use of a combined optical-PET (OPET) system: a computer simulation feasibility study," *Phys. Med. Biol.* **50**(17), 4225–4241 (2005).
24. E. Alerstam, S. Andersson-Engels, and T. Svensson, "White Monte Carlo for time-resolved photon migration," *J. Biomed. Opt.* **13**(4), 041304 (2008).
25. H. J. van Staveren, C. J. M. Moes, J. van Marie, S. A. Prahl, and M. J. C. van Gemert, "Light scattering in Intralipid-10% in the wavelength range of 400-1100 nm," *Appl. Opt.* **30**, 4507–4514 (1991).
26. V. Engelhardt, B. Krammer, and K. Plaetzer, "Antibacterial photodynamic therapy using water-soluble formulations of hypericin or mTHPC is effective in inactivation of Staphylococcus aureus," *Photochem. Photobiol. Sci.* **9**(1), 365–369 (2010).

27. J. Buchholz, B. Kaser-Hotz, T. Khan, C. Rohrer Bley, K. Melzer, R. A. Schwendener, M. Roos, and H. Walt, "Optimizing photodynamic therapy: in vivo pharmacokinetics of liposomal meta-(tetrahydroxyphenyl)chlorin in feline squamous cell carcinoma," *Clin. Cancer Res.* **11**(20), 7538–7544 (2005).
28. R. L. P. van Veen, W. Verkruysse, and H. J. C. M. Sterenborg, "Diffuse-reflectance spectroscopy from 500 to 1060 nm by correction for inhomogeneously distributed absorbers," *Opt. Lett.* **27**(4), 246–248 (2002).
29. L. O. Svaasand, E. J. Fiskerstrand, G. Kopstad, L. T. Norvang, E. K. Svaasand, J. S. Nelson, and M. W. Berns, "Therapeutic response during pulsed laser treatment of port-wine stains: Dependence on vessel diameter and depth in dermis," *Lasers Med. Sci.* **10**, 235–243 (1995).
30. Z. Xu, J. Liu, and Y. L. Kim, "Diffuse light suppression of back-directional gating imaging in high anisotropic media," *J. Biomed. Opt.* **14**(3), 030510 (2009).
31. H. Xie, P. Svenmarker, S. Andersson-Engels, et al. "Pharmacokinetic and biodistribution study following systemic administration of Fospeg–a pegylated liposomal temoporfin formulation in a murine model," in preparation.
32. J. H. Lundeman, O. B. Jensen, P. E. Andersen, S. Andersson-Engels, B. Sumpf, G. Erbert, and P. M. Petersen, "High power 404 nm source based on second harmonic generation in PPKTP of a tapered external feedback diode laser," *Opt. Express* **16**(4), 2486–2493 (2008).
33. J. Swartling, A. Pifferi, A. M.K. Enejder, and S. Andersson-Engels, "Accelerated Monte Carlo models to simulate fluorescence spectra from layered tissues," *J. Opt. Soc. Am. A* **20**(4), 714–727 (2003).
34. E. Alerstam, S. Andersson-Engels, and T. Svensson, "Improved accuracy in time-resolved diffuse reflectance spectroscopy," *Opt. Express* **16**, 10440–10454 (2008).
35. B. Kruijt, S. Kascakova, H. S. de Bruijn, A. van der Ploeg-van den Heuvel, H. J. C. M. Sterenborg, and D. J. Robinson, "In vivo quantification of chromophore concentration using fluorescence differential path length spectroscopy," *J. Biomed. Opt.* **14**(3), 034022 (2009).
36. N. Bendsoe, L. Persson, A. Johansson, J. Axelsson, J. Svensson, S. Gräfe, S. Svanberg, and K. Svanberg, "Fluorescence monitoring of a topically applied liposomal temoporfin formulation and photodynamic therapy of nonpigmented skin malignancies," *J. Environ. Pathol. Toxicol. Oncol.* **26**(2), 117–126 (2007).

# Paper II

**Synthesis of $NaYF_4$:$Yb^{3+}$, $Er^{3+}$ upconverting nanocrystals in a capillary-based continuous microfluidic reaction system**

H. Liu, O. Jakobsson, C. T. Xu, H. Xie, T. Laurell, S. Andersson-Engels.

*Proc. of SPIE* **7909**, 790917-1 - 790917-6 (2011).

# Synthesis of $NaYF_4 : Yb^{3+}, Er^{3+}$ upconverting nanocrystals in a capillary-based continuous microfluidic reaction system

Haichun Liu[1], Ola Jakobsson[2], Can T. Xu[1], Haiyan Xie[1], Thomas Laurell[2,3], and Stefan Andersson-Engels[1]

[1]Department of Physics, Lund University, P. O. Box 118, S-221 00, Lund, Sweden;
[2]Department of Electrical Measurements, Lund University, P. O. Box 118, S-221 00, Lund, Sweden;
[3]Department of Biomedical Engineering, Dongguk University, Seoul, South Korea

## ABSTRACT

We report for the first time continuous flow synthesis of $NaYF_4 : Yb^{3+}, Er^{3+}$ upconverting nanocrystals in a capillary-based microfluidic reaction system. Two sequential temperature steps were employed for heating with an initial high temperature (180 °C) step to burst nuclei and a subsequent low temperature (110 °C) step to promote growth of the nanocrystals in order to obtain high-performance nanocrystals. The prepared nanocrystals exhibit green and red emissions under excitation of 974 nm diode laser. Our research opens the door for the synthesis of upconverting nanocrystals in microfluidic systems.

**Keywords:** upconverting nanocrystals, continuous flow, microfluidic

## 1. INTRODUCTION

Upconverting nanocrystals doped with lanthanide ions have drawn much attention due to their potential as optical imaging probes in biomedical applications. These contrast agents have several advantages over conventional fluorescent biomarkers (e.g., organic dyes and semiconductor nanocrystals), such as dramatically reduced autofluorescence from cells or tissues, better light penetration depth, no photo-damage to living organisms, and higher spatial resolution in the captured images.[1–3] Upconverting nanocrystals have come to be widely used in such diverse fields as, luminescence microscopy,[4] reflectance and transillumination imaging of biological tissues,[5–7] and fluorescence diffuse optical tomography[8,9]during the last decade.

Among upconverting nanomaterials, lanthanide-ions-doped $NaYF_4$ nanocrystals ($NaYF_4 : Yb^{3+}, Er^{3+}/Tm^{3+}$) have been demonstrated to be the most efficient to date. Many efforts are being made in order to develop efficient and less complex methods for synthesizing high quality and monodispersed $NaYF_4 : Yb^{3+}, Er^{3+}/Tm^{3+}$ nanocrystals for various biomedical applications. Currently, $NaYF_4$ nanocrystals are mainly synthesized in batch-control modes in small volumes, for example, using the hydrothermal method,[10] solvothermal method,[11] microwave synthesis,[12] and pyrolysis of trifluoroacetates.[13] Although achievements have been made, batch reactors often suffer from the disability to rapidly establish homogenous reaction conditions, e.g., during temperature changes. This problem is commonly addressed by minimizing reactor volumes, thus leading to a negative impact on the production rate. It is also difficult to implement fast screening and optimize the synthesis conditions in batch modes.[14]

Microfluidic reaction systems offer a solution to these challenges and have an increasingly important role in the synthesis of nanocrystals as highly controlled thermal and stoichiometric microenvironments can be obtained in the synthesis process.[15] Particularly the synthesis of quantum dots was early targeted, and the strategy of using microfluidic reactors was first presented by Edel J.B. et al, at Imperial College London in 2002.[16] In this paper, we report continuous flow based synthesis of $NaYF_4 : Yb^{3+}, Er^{3+}$ nanocrystals in a capillary-based microfluidic reaction system. In order to obtain high-performance nanocrystals, a typical synthesis scheme for colloidal nanocrystals was utilized, which separated the nucleation and growth phase of the nanocrystals by employing two temperature steps.[17,18]

Further author information: (Send correspondence to Haichun Liu)
Haichun Liu: E-mail: haichun.liu@fysik.lth.se, Telephone: +46 46 222 7471

Colloidal Quantum Dots/Nanocrystals for Biomedical Applications VI, edited by Wolfgang J. Parak, Kenji Yamamoto, Marek Osinski, Proc. of SPIE Vol. 7909, 790917 · © 2011 SPIE · CCC code: 1605-7422/11/$18 · doi: 10.1117/12.874348

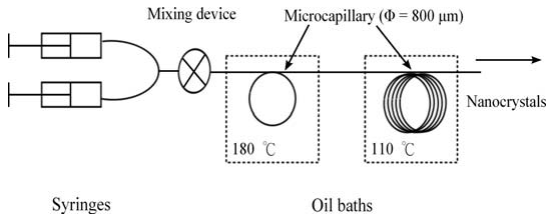


Fig. 1. Scheme of the experimental setup.

## 2. EXPERIMENTAL

### 2.1 Chemicals

All chemicals were purchased from Sigma-Aldrich, Ltd., and used as received without further purification. $Ln_2O_3$ (Ln = Y, Yb, Er) (99.99%), NaF (99.9%), and $HNO_3$ (70%) were used as precursor materials, while polyethylene glycol (PEG, 99%) with an average molecular weight of 200 g/mol and ethylene glycol (EG, 99%) were used as the solvents. Oleic acid (OA, 90%) was used as the surfactant.

### 2.2 Synthesis of $NaYF_4$ nanocrystals

In the preparation of stock solutions, first $Ln(NO_3)_3 \cdot 6H_2O$ (Ln = Y, Yb, Er) were prepared by dissolving $Y_2O_3$, $Yb_2O_3$ and $Er_2O_3$ in $HNO_3$, respectively, followed by evaporative crystallization of the solutions. Stoichiometric amounts of $Ln(NO_3)_3 \cdot 6H_2O$ were subsequently dissolved in EG or PEG under vigorous stirring to form a clear solution with 0.01 M $Ln^{3+}$ and a molar ratio of $Y^{3+}$:$Yb^{3+}$:$Er^{3+}$ 78:20:2. The NaF EG solution with a concentration of 0.03 M was obtained in the same way. In the synthesis of sample A, the $Ln^{3+}$ and NaF EG solutions were aspirated in two syringes respectively and injected into a coaxial mixing device by syringe pumps. The mixing of the two solutions was diffusion limited and no active mixing was introduced. Then the mixture was injected into a polytetrafluoroethylene microcapillary with an inner diameter of 800 $\mu$m and heated in a 180 °C oil bath, and subsequently heated in a 110 °C oil bath. Retention times of the reaction mixture in the two oil baths were determined by the flow rates and capillary lengths. The flow rates of $Ln^{3+}$ and NaF solutions were 50 $\mu$l/min and 200 $\mu$l/min, respectively, while the capillary lengths in the first and second oil bath were 8 cm and 100 cm, respectively, resulting in retention times of 10 s in the first oil bath and 120 s in the second oil bath. The product were collected from the outlet of the capillary in a test tube. A schematic representation of the reaction system is shown in Fig. 1. In the synthesis of sample B, the PEG solution of lanthanide ions with the same concentration and molar ratio of lanthanide ions was used to replace corresponding EG solution, and OA was further added in with a volume ratio of OA/PEG 1:1. The nanocrystals were separated by diluting the obtained suspension using acetone followed by centrifugation, and washed using ethanol and deionized water for several times. The nanocrystals were finally redispersed in ethanol for further characterization.

### 2.3 Characterization

The size and morphology of the nanocrystals were observed using a JEOL 3000SFF transmission electron microscope (TEM). Samples were prepared by placing a drop of ethanol dispersed nanocrystals on the surface of a copper specimen grid coated with a perforated carbon film. The fluorescence spectra were recorded on a USB 6500 Ocean Optics spectrometer equipped with a 974 nm diode laser as the excitation source with nanocrystals redispersed in ethanol.

## 3. RESULTS AND DISCUSSION

In Fig. 2 the shapes of the $NaYF_4 : Yb^{3+}, Er^{3+}$ nanocrystals are shown. As also shown in Fig. 2 (a), the nanocrystals synthesized without the presence of OA (sample A) show rod-like shapes. Although these rod-like shaped nanocrystals have a broad length distribution, they have a relative narrow diameter distribution ($16.0 \pm 3.2$ nm). This suggests that the rod-like nanocrystals were probably formed by the connection of spherical

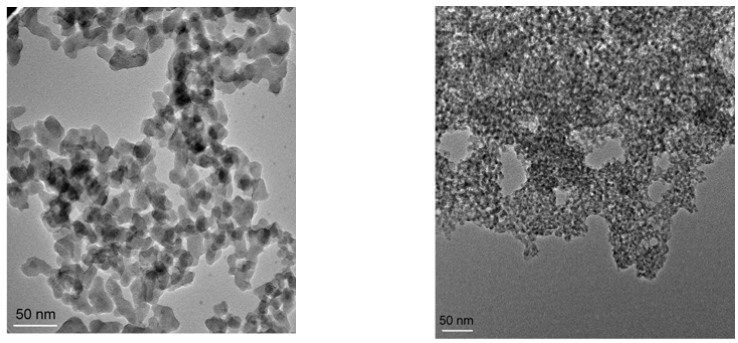


(a) (b)

Fig. 2. TEM images of (a) sample A and (b)sample B.

or ellipsoidal precursors synthesized in the microcapillary, as reported in the synthesis of worm and chain-like metal nanoparticles in Ref.19. One possible reason is that the growth of nanocrystals were not properly quenched due to the lack of protection of surfactants. In view of this, OA was added in the subsequent experiment, the product of which was shown in Fig. 2 (b). As can be seen, the synthesized nanocrystals (sample B) show more regular shapes and have much smaller size (less than 10 nm) as compared to sample A. However, they tend to aggregate when dispersed in ethanol, probably due to the adsorption of OA on the surface of the nanocrystals. These results reveals that OA can be employed to modify the shape and size of upconverting nanocrystals in the microfluidic reaction. The influence of OA on the microfluidic synthesis of upconverting nanocrystals is currently being thoroughly investigated, and the postprocessing procedures are being improved in order to wash and redisperse the nanocrystals.

The upconversion fluorescence spectra of sample A and B under excitation of 974 nm are presented in Fig. 3 (a) and (b), respectively. As seen, both sample A and B have dominant red emissions, while sample A has a much larger red/green emission ratio (10:1), which can be explained by the difference in the size and morphology of the nanocrystals obtained in the two different batches. The emission bands can easily be assigned to intra-4f electronic transitions of the $Er^{3+}$ ions. The green emissions between 510 and 530 nm and between 530 and 570 nm were assigned to the $^2H_{11/2} \rightarrow ^4 I_{15/2}$ and $^4S_{3/2} \rightarrow ^4 I_{15/2}$ transitions, respectively. The red emission between 635 and 700 nm originated from the $^4F_{9/2} \rightarrow ^4 I_{15/2}$ transition.[20]

In order to determine the number of photons responsible for the upconversion mechanism, the dependence of the upconversion emissions of sample A on the excitation power was investigated. As presented in Fig. 4, both the green and red upconversion emission intensities demonstrated second order power dependence at low excitation densities, indicating a two-photon upconversion mechanism. The power dependencies of $Er^{3+}$ upconversion emissions became linear at high excitation densities due to "saturation"of the upconversion processes.[21] The upconversion emissions of sample B have similar power dependences, not shown here.

The upconversion excitation pathways in the $Yb^{3+}/Er^{3+}$ system are well-known and are shown in Fig. 5. The $Er^{3+}$ ions are firstly excited to $^4I_{11/2}$ via an energy transfer from $Yb^{3+}$ ions in $^2F_{5/2}$ state. A second 974 nm photon, or energy transfer from $Yb^{3+}$ ions can then pump $Er^{3+}$ ions to the $^4F_{7/2}$ level. Subsequently the $Er^{3+}$ ions undergo a multi-phonon assisted relaxation to the $^2H_{11/2}$ and $^4S_{3/2}$ levels and the green emissions occur via transitions of $^2H_{11/2}/^4S_{3/2} \rightarrow ^4 I_{15/2}$. Alternatively, the ions can further relax and populate the $^4F_{9/2}$ leading to the red emission via transition of $^4F_{9/2} \rightarrow ^4 I_{15/2}$.[20]

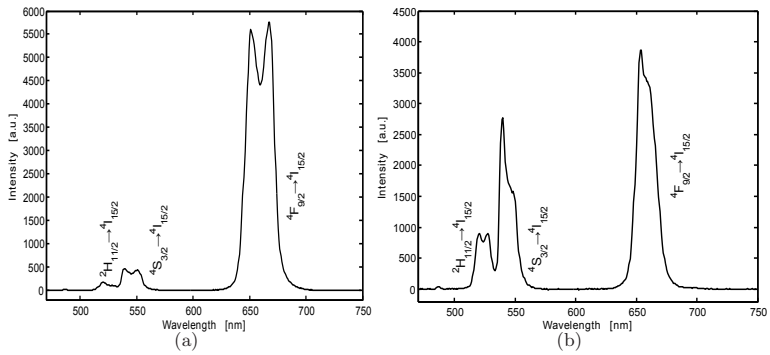


Fig. 3. Measured upconvertsion emission in $NaYF_4 : Yb^{3+}, Er^{3+}$ nanocrystals under excitation of 974 nm diode laser.

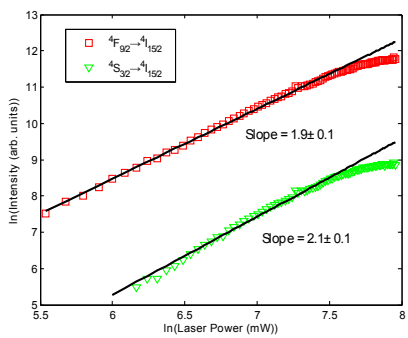


Fig. 4. Power dependence of the upconversion emissions of sample A when excited at 974 nm.

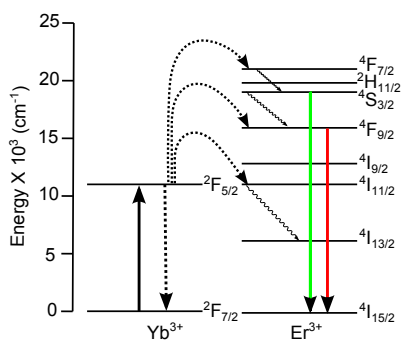


Fig. 5. The energy level diagrams of the $Er^{3+}$ and $Yb^{3+}$ dopant ions and the upconversion mechanisms for the green and red emissions under excitation of 974 nm diode laser. The solid, dotted, and curly arrows represent emission, energy transfer, and multiphonon relaxation processes, respectively.

## 4. CONCLUSIONS

The $NaYF_4 : Yb^{3+}, Er^{3+}$ nanocrystals were successfully synthesized in a capillary-based continuous microfluidic reaction system. The nanocrystals prepared without the presence of OA shows rod-like shapes with a large length distribution but a relative narrow diameter distribution. The shape and size of the nanocrystals can be dramatically modified by addition of surfactant OA. The prepared nanocrystals can emit green and red upconversion emissions under excitation of 974 nm, and both the green and red emissions originate from two-photon processes. On-going research targets the further improvements of the upconverting nanocrystals synthesis process.

## ACKNOWLEDGMENTS

This work was supported by a Swedish Research Council grant (VR 2007-4214) and a Linnaeus grant for the Lund Laser Centre.

## REFERENCES

[1] Auzel, F., "Upconversion and anti-stokes processes with f and d ions in solids," *Chem. Rev.* **104**(1), 139–173 (2004).

[2] Xu, C. T., Svensson, N., Axelsson, J., Svenmarker, P., Somesfalean, G., Chen, G., Liang, H., Liu, H., Zhang, Z., and Andersson-Engels, S., "Autofluorescence insensitive imaging using upconverting nanocrystals in scattering media," *Appl. Phys. Lett.* **93**(17), 171103 (2008).

[3] Svenmarker, P., Xu, C. T., and Andersson-Engels, S., "Use of nonlinear upconverting nanoparticles provides increased spatial resolution in fluorescence diffuse imaging," *Opt. Lett.* **35**(16), 2789–2791 (2010).

[4] Yu, M., Li, F., and Chen, Z., "Laser scanning up-conversion luminescence microscopy for imaging cells labeled with rare-earth nanophosphors," *Anal. Chem.* **81**(3), 930–935 (2009).

[5] Nyk, M., Kumar, R., Ohulchanskyy, T. Y., Bergey, E. J., and Prasad, P. N., "High contrast in vitro and in vivo photoluminescence bioimaging using near infrared to near infrared up-conversion in $Tm^{3+}$ and $Yb^{3+}$ doped fluoride nanophosphors," *Nano Lett.* **8**(11), 3834–3838 (2008).

[6] Chatterjee, D., Rufaihah, A., and Zhang, Y., "Upconversion fluorescence imaging of cells and small animals using lanthanide doped nanocrystals," *Biomaterials* **29**(7), 937–943 (2008).

[7] Vinegoni, C., Razansky, D., Hilderbrand, S. A., Shao, F., Ntziachristos, V., and Weissleder, R., "Transillumination fluorescence imaging in mice using biocompatible upconverting nanoparticles," *Opt. Lett.* **34**(17), 2566–2568 (2009).

[8] Xu, C. T., Axelsson, J., and Andersson-Engels, S., "Fluorescence diffuse optical tomography using upconverting nanoparticles," *Appl. Phys. Lett.* **94**(25), 251107 (2009).

[9] Liu, H., Xu, C. T., and Andersson-Engels, S., "Multibeam fluorescence diffuse optical tomography using upconverting nanoparticles," *Opt. Lett.* **35**(5), 718–720 (2010).

[10] Sun, Y., Chen, Y., Tian, L., Yu, Y., Kong, X., Zhao, J., and Zhang, H., "Controlled synthesis and morphology dependent upconversion luminescence of $NaYF_4 : Yb, Er$ nanocrystals," *Nanotechnology* **18**(27), 275609 (2007).

[11] Wang, L. and Li, Y., "Controlled synthesis and luminescence of lanthanide doped $NaYF_4$ nanocrystals," *Chem. Mater.* **19**(4), 727–734 (2007).

[12] Wang, H.-Q. and Nann, T., "Monodisperse upconverting nanocrystals by microwave-assisted synthesis," *ACS Nano* **3**(11), 3804–3808 (2009).

[13] Boyer, J.-C., Cuccia, L. A., and Capobianco, J. A., "Synthesis of colloidal upconverting $NaYF_4 : Er^{3+}/Yb^{3+}$ and $Tm^{3+}/Yb^{3+}$ monodisperse nanocrystals," *Nano Lett.* **7**(3), 847–852 (2007).

[14] Song, Y., Hormes, J., and Kumar, C. S. S. R., "Microfluidic synthesis of nanomaterials," *Small* **4**(6), 698–711 (2008).

[15] Marre, S. and Jensen, K. F., "Synthesis of micro and nanostructures in microfluidic systems," *Chem. Soc. Rev.* **39**(3), 1183–1202 (2010).

[16] Edel, J. B., Fortt, R., deMello, J. C., and deMello, A. J., "Microfluidic routes to the controlled production of nanoparticles," *Chem. Commun.* (10), 1136–1137 (2002).

[17] Yin, Y. and Alivisatos, A. P., "Colloidal nanocrystal synthesis and the organic-inorganic interface," *Nature* **437**(7059), 664–670 (2005).

[18] Zhu, X., Zhang, Q., Li, Y., and Wang, H., "Redispersible and water-soluble $LaF_3 : Ce, Tb$ nanocrystals via a microfluidic reactor with temperature steps," *J. Mater. Chem.* **18**(42), 5060–5062 (2008).

[19] Song, Y., Sun, Q., Zhang, T., Jin, P., and Han, L., "Synthesis of worm and chain-like nanoparticles by a microfluidic reactor process," *J. Nanopart. Res.* **12**(7), 2689–2697 (2010).

[20] Suyver, J. F., Grimm, J., van Veen, M. K., Biner, D., Kramer, K. W., and Güdel, H. U., "Upconversion spectroscopy and properties of $NaYF_4$ doped with $Er^{3+}$, $Tm^{3+}$ and/or $Yb^{3+}$," *J. Lumin.* **117**(1), 1–12 (2006).

[21] Suyver, J. F., Aebischer, A., García-Revilla, S., Gerner, P., and Güdel, H. U., "Anomalous power dependence of sensitized upconversion luminescence," *Phys. Rev. B* **71**(12), 125123 (2005).

# Paper III

**Upconverting nanoparticles for pre-clinical diffuse optical imaging, microscopy and sensing: Current trends and future challenges**

C. T. Xu, Q. Zhan, H. Liu, G. Somesfalean, J. Qian, S. He, S. Andersson-Engels.

*Laser & Photonics Reviews* **7(5)**, 663-697 (2013).

Laser Photonics Rev. **7,** No. 5, 663–697 (2013) / **DOI** 10.1002/lpor.201200052

LASER & PHOTONICS REVIEWS

**Abstract** Upconverting nanoparticles (UCNPs) are a class of recently developed luminescent biomarkers that – in several aspects – are superior to organic dyes and quantum dots. UCNPs can emit spectrally narrow anti-Stokes shifted light with quantum yields which greatly exceed those of two-photon dyes for fluence rates relevant for deep tissue imaging. Compared with conventionally used Stokes-shifting fluorophores, UCNP-based imaging systems can acquire completely autofluorescence-free data with superb contrast. For diffuse optical imaging, the multiphoton process involved in the upconversion process can be used to obtain images with unprecedented resolution. These unique properties make UCNPs extremely attractive in the field of biophotonics. UCNPs have already been applied in microscopy, small-animal imaging, multi-modal imaging, highly sensitive bioassays, temperature sensing and photodynamic therapy. In this review, the current state-of-the-art UCNPs and their applications for diffuse imaging, microscopy and sensing targeted towards solving essential biological issues are discussed.

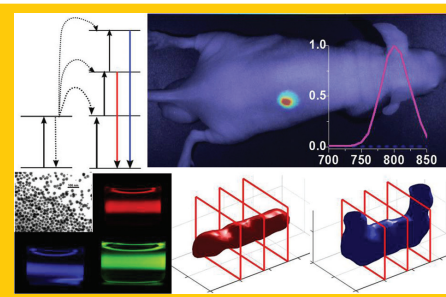


REVIEW ARTICLE

# Upconverting nanoparticles for pre-clinical diffuse optical imaging, microscopy and sensing: Current trends and future challenges

**Can T. Xu[1,3,**], Qiuqiang Zhan[2,3,4,**], Haichun Liu[1,3], Gabriel Somesfalean[1,2,3], Jun Qian[2,3], Sailing He[2,3,4], and Stefan Andersson-Engels[1,3,*]**

## 1. Introduction

Upconverting nanoparticles (UCNPs) constitute a novel type of contrast agent with highly interesting and unique properties for luminescence bioimaging. The aim of this review paper is to illustrate the great potential of this emerging field. The phenomenon of upconverting luminescence has been studied for decades, with the earliest experimental works presented in, e.g., Refs. [1, 2]. The idea originated from Bloembergen in 1959 [3], who proposed that infrared (IR) light could be detected by sequential stepwise absorption of an ion in a solid material. An extensive review of the early work was given by Auzel in 2004 [4]. Most efforts were focused on rare-earth (RE) ions doped into a lattice host. Such ions are ideal because they exhibit very long lifetimes for the intermediate states in the upconversion excitation chain, which are essential for increasing the probability of sequential excitations. The reasons for the long lifetimes are that intra 4*f* level transitions are parity forbidden (being relaxed a bit due to the crystal field of the host lattice) and that excited *f*-levels are shielded by outer electrons. The host crystals are usually oxides or fluorides. Especially fluoride lattices exhibit low phonon energies which reduces multiphonon relaxation of the ions, also of importance to ensure long lifetimes of the intermediate states. The importance of the host properties for the upconversion (UC) process, e.g., the low multiphonon relaxation, is the reason why it is difficult to achieve efficient UC in aqueous solutions [5].

Submicron luminescent particles based on UC were introduced for biomedical assays in the middle of the 90s [6–9]. They displayed a better sensitivity (a factor of

[1] Department of Physics, Lund University, Box 118, 221 00 Lund, Sweden
[2] Centre for Optical and Electromagnetic Research, State Key Laboratory of Modern Optical Instrumentation, Zhejiang University (ZJU), Hangzhou 310058, China
[3] Joint Research Center of Photonics, ZJU-Royal Institute of Technology-Lund University, Hangzhou 310058, China
[4] ZJU-SCNU Joint Research Center of Photonics, South China Academy of Advanced Optoelectronics, South China Normal University (SCNU), 510006 Guangzhou, China
[**] These authors contributed equally to this work.
[*] Corresponding author(s): e-mail: stefan.andersson-engels@fysik.lth.se

LASER & PHOTONICS REVIEWS



10 improvement) than conventional luminescent reporters, which is most likely caused by the absence of sample autofluorescence background. It was known from the early beginning that host materials doped with two types of ions – sensitizers and activators – were the most efficient [10–12]. With the upconverting materials attracting an increasing amount of interest, further efforts were invested into the understanding of the UC process, leading to particles that were acceptable both in terms of size and brightness for *in-vivo* biomedical studies [13–16]. The power dependence of the UC signal ($I$) was known to be $I \propto I_{ex}^{n}$, where $n$ is the number of photons absorbed in the process, and $I_{ex}$ is the power density of the excitation light. Later, it was realized that this relationship is only valid in a limited range of power densities, as saturation alters the power dependence and the efficiency was shown to have a more complex power-density-dependent behavior for high power densities [17, 18].

During the last few years, the great potential of UCNPs for *in vitro* and *in vivo* use in, e.g., tissue microscopy applications and also deep tissue imaging and tomography, is becoming obvious [19]. Today, the research topic of *upconverting nanoparticles for biomedical applications* is extremely popular, in particular related to optical bioimaging. Much progress has been made in developing nanoparticles with outstanding properties, motivated by the huge interest for biomedical applications. In this review, recent and present trends in *optical imaging, microscopy and sensing using upconverting nanoparticles* are discussed, with emphasis placed on the biological applicability rather than the nanoparticle materials. Recent reviews which focus more on the properties of the UCNPs themselves can be found in, e.g., Refs. [20–23].

This review paper will first introduce the UCNPs and how they are synthesized. This section will be followed by a discussion on means to characterize these particles and determine their most interesting properties. The importance of careful characterization of their luminescence efficiency in a reproducible manner will be stressed, as this appears to be neglected in the literature, making it difficult to compare results from different studies. Furthermore, the necessary surface modifications for *in vitro* and *in vivo* applications, and health issues related to UCNPs are discussed. Finally, the central theme of this review is developed, i.e., biomedical applications of UCNPs which is followed by a discussion of the outlook as well as the present and future challenges.

## 2. Composition and synthesis

Upconverting materials have been known and studied over a long period of time, however, only recently have they become interesting for biomedical applications. For this reason, there are still plenty of unexplored aspects of the UCNPs which can lead to improved and optimized properties for biomedical applications. In this section, the composition and synthesis methods for UCNPs used in biomedical imaging will be briefly reviewed.

UCNPs are generally comprised of an inorganic host doped with a sensitizer and an activator. The dopants, especially the activator, are usually incorporated into the host lattice at a low doping concentration in order to avoid quenching caused by undesired cross relaxations [24, 25]. Efficient UC emissions can be obtained by manipulating the energy transfer between the sensitizer and the activator with the assistance of the host lattice [4]. The sensitizer, which displays a considerable absorption cross-section, absorbs the energy from the excitation light, and transfers it to the activator, mainly through non-radiative and phonon-assisted processes. During the last decade, many kinds of UCNPs which incorporate RE ions into various host materials have been developed [26–36]. However, up to date, efficient UC emissions with good potential in bioapplications have only been observed in very few dopant-host combinations, such as $NaYF_4$:$Yb^{3+}$/$Er^{3+}$, $NaYF_4$:$Yb^{3+}$/$Ho^{3+}$ and $NaYF_4$:$Yb^{3+}$/$Tm^{3+}$ [37, 38].

Well-crystallized nanoparticles are highly desirable in biological applications as luminescence markers, since they can exert a strong field on the doped ions and energy losses caused by crystal defects can be minimized. Uneven components of the field increase the $f - f$ transition probabilities of the dopant ions [39, 40], resulting in efficient UC emissions [41, 42]. The crystal structure of the host thus plays an important role in the process of UC emission, as it determines the crystal field and the doping concentration [43–47]. $NaYF_4$ UCNPs constitute a good example of this, since $NaYF_4$ exists in two polymorphs at ambient pressure: cubic ($\alpha$) phase (metastable high-temperature phase) and hexagonal ($\beta$) phase (thermodynamically stable low-temperature phase) [48, 49], which are closely related to the quantum yield (QY). The $\beta$-$NaYF_4$ UCNPs have approximately one order of magnitude higher QY than their $\alpha$-phase counterparts [43, 44, 50, 51]. Due to the stringent requirements on the crystallinity and phase purity of the host materials, during the last decade, considerable efforts have been invested into developing synthesis methods which yield highly crystalline structures for efficient UC emissions.

In the following, the three most important aspects that determine the quality of UCNPs will be discussed, i.e., the commonly used host materials, activators and sensitizers; the typical synthesis methods; as well as the phase-and-size control approaches.

### *2.1. Host materials, activators and sensitizers*

#### 2.1.1. Host materials

Host materials play a key role in UC emissions. Ideal host materials should be transparent in the spectral range of interest, have high optical damage threshold and chemical stability. They are also required to have low lattice phonon energies in order to minimize non-radiative energy losses. Fluorides satisfy these conditions and are commonly used as host materials for UCNPs due to their relatively low phonon energies ($\sim$350 $cm^{-1}$). Oxides have also been

 

REVIEW ARTICLE



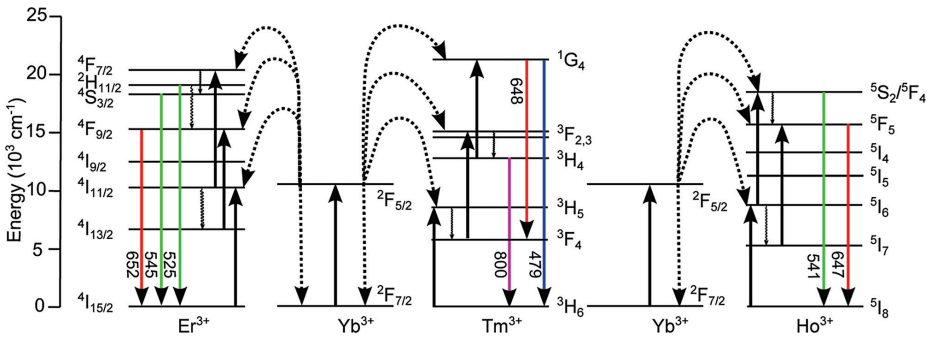


**Figure 1** (online color at: www.lpr-journal.org) Energy level structure and proposed UC mechanisms of the $Yb^{3+}$, $Er^{3+}$/ $Tm^{3+}$/$Ho^{3+}$ co-doped UCNPs under excitation at 975 nm.

extensively investigated in the past decades, however, this is of more historical reasons as they have relatively large phonon energies (∼500–700 cm$^{-1}$). In addition, the host materials should have lattices which matches well with the dopant ions in order to achieve high doping levels. All trivalent RE ions, alkaline earth ions (e.g., $Ca^{2+}$, $Sr^{2+}$ and $Ba^{2+}$) and some transition metal ions (e.g., $Zr^{4+}$, $Ti^{4+}$, and $Mn^{2+}$) exhibit similar ionic sizes. Therefore, inorganic compounds, especially oxides and fluorides, containing these ions are suitable host materials for RE ions. $Y_2O_3$ [16, 52], $Gd_2O_3$ [53], $Y_2O_2S$ [54], $LaF_3$ [55–57], $NaYF_4$ [13, 58–68], $NaGdF_4$ [69–72], $CaF_2$ [73–76], $NaLuF_4$ [31, 77, 78] and $Na_xScF_{3+x}$ [79] are typical UC host materials. RE-doped fluoride UCNPs, which exhibit low phonon energies and high chemical stability are currently the most efficient in generating UC luminescence, and have shown great potential as contrast agents in the field of bioimaging. Thus, they will be given more emphasis in this review.

### 2.1.2. Activators

Upconversion emissions are theoretically expected from most RE ions. However, under low excitation power densities, efficient UC emissions can only be generated by very few RE ions, such as $Er^{3+}$, $Ho^{3+}$ and $Tm^{3+}$. This is due to the ladder-like arrangement of their energy states and good match with commercially available high-power diode lasers (Fig. 1). For example, $Er^{3+}$ ions have mainly three UC emissions bands, including two green emission bands at around 525 nm and 545 nm originating from the transitions $^2H_{11/2} \rightarrow {}^4I_{15/2}$ and $^4S_{3/2} \rightarrow {}^4I_{15/2}$, respectively, and a red emission band at around 652 nm originating from the transition $^4F_{9/2} \rightarrow {}^4I_{15/2}$ [80]. The $Ho^{3+}$ ions have two main UC bands of green and red emission at 541 and 647 nm, corresponding to the transitions $^5S_2/^5F_4 \rightarrow {}^5I_8$ and $^5F_5 \rightarrow {}^5I_8$, respectively [81]. The main UC band of the $Tm^{3+}$ ions is in the near infrared (NIR) range at around 800 nm, originating from the transition $^3H_4 \rightarrow {}^3H_6$ [82]. This NIR UC band is located within the "window of optical transparency"for biological tissues, in which both light absorption and scattering are significantly reduced. This feature makes $Tm^{3+}$-doped UCNPs particularly interesting for imaging of deeply located bio-targets. The $Tm^{3+}$ ions have another two generally less efficient UC emission bands at around 479 and 648 nm, generated by the transitions $^1G_4 \rightarrow {}^3H_6$ and $^1G_4 \rightarrow {}^3F_4$, respectively [82]. The blue emission band is less suitable for bioimaging due to much higher light absorption and scattering in biological tissues at this wavelength. The intensity ratio between different UC bands is host and doping concentration dependent, even for the same activator.

For other RE ions, Wang et al. [83] has made pioneering work to exploit their UC emission ability. They suggested a general approach for realizing efficient UC emissions through gadolinium sublattice-mediated energy migration, by incorporating a set of RE ions into separated layers at precisely defined concentrations. In this way, they have demonstrated efficient UC emissions from a wide range of activators, such as $Tb^{3+}$, $Eu^{3+}$, $Dy^{3+}$ and $Sm^{3+}$. Generally, the doping concentration of activators is relatively low (usually $< 2$ mol%) in order to minimize cross-relaxation energy losses.

### 2.1.3. Sensitizers

In single-doped nanoparticles, the efficiencies of UC emissions are relatively low. This is due to the difficulty in finding an equilibrium point for minimizing the quenching effect by reducing the RE-ion concentration, and maximizing the absorption of pump energy by increasing its concentration. To enhance the UC luminescence efficiency, a sensitizer with a sufficiently large absorption cross-section in the NIR region is usually incorporated together with the activator. Certainly, it is required that efficient energy transfer between the sensitizer and activator can occur. These types of sensitizers can be called direct sensitizers. For

LASER & PHOTONICS REVIEWS



example, $Yb^{3+}$ fulfills the condition and is commonly used as UC direct sensitizer for $Er^{3+}$, $Ho^{3+}$ and $Tm^{3+}$ under excitation by 975 nm light. The optimal concentration of $Yb^{3+}$ is dependent on the host and the activator [84], but is usually kept high (∼20% for fluoride nanoparticles). Another type of sensitizers, called indirect sensitizers, are used to quench and enhance certain emission bands. For instance, $Nd^{3+}$, $Ce^{3+}$ and $Ho^{3+}$ have been used as co-sensitizers to enhance the blue emission band of $Tm^{3+}$, red emission band of $Ho^{3+}$ and NIR emission band of $Tm^{3+}$, respectively [81, 85, 86]. It should be noted that the cations of the host materials themselves can be used as indirect sensitizers, as indicated in recent reports [83, 87].

Up to date, most efforts have been devoted to developing $Yb^{3+}$-sensitized UCNPs pumped at around 975 nm. Although biological tissues have relatively small scattering at this wavelength, the applications of this type of UCNPs are still limited in biomedical imaging, due to the non-negligible absorption of water, which comprises the major part of biological tissues. In view of this and benefiting from the development of commercially available high-power tunable laser sources, the research on the sensitization capability of different RE-ions excited by different pump wavelengths constitutes an interesting topic. Such research could eventually lead to the emergence of a new group of UC materials.

## 2.2. Synthesis methods

A large number of methods have been developed in order to fabricate high-quality fluoride UCNPs, including the co-precipitation method [58], the hydro(solvo)thermal method [65], the thermal decompositon method [61], the two-phase synthesis [88–90], the hydrothermal *in-situ* conversion route [31, 45, 91], and the ionic liquids-based syntehsis [92–94]. This review mainly focuses on the thermal decomposition and hydro(solvo)thermal methods, which are the most widely used as they can offer precise control over the phase, shape and size of fluoride UCNPs. For other synthesis approaches, the readers are directed to other reviews [23, 25, 38, 95–97].

### 2.2.1. Thermal decomposition method

In a typical thermal decomposition procedure, metal trifluoroacetates are thermally decomposed to corresponding metal fluorides. Zhang et al. [55] first reported the synthesis of single-crystalline and monodisperse $LaF_3$ triangular nanoplates *via* the thermal decomposition of lanthanum trifluoroacetates ($La(CF_3COO)_3$) in a mixture of oleic acid (OA) and octadecene (ODE). The approach was later developed as a general route to synthesize high-quality $REF_3$ and $NaREF_4$ nanoparticles [61, 62, 67, 80, 98] (Fig. 2(a-b)).

In this approach, ODE with a high boiling temperature (315 °C) is used to provide a high-temperature environment, while OA having a good coordinate capability, is acting as the coordinating solvent which aids in capping the surface of UCNPs to prevent agglomeration. Besides OA, oleylamine (OM), trioctyphosphine (TOP) and trictylphosphine oxide (TOPO) have also been used as capping agents in the synthesis of UC fluoride nanoparticles [14, 64, 98]. Due to the use of RE and sodium trifluoroacetic precursors, the decomposition method inevitably generates some toxic by-products such as trifluoroacetic anhydride $(CF_3CO)_2O$, trifluoroacetyl fluoride $CF_3CF_2COF$, carbonyl difluoride $COF_2$ and tetrafluoroethylene $C_2F_4$ [80], with apparent safety concerns. Wei et al. [99] reported a more friendly thermal decomposition method for synthesizing $\alpha$- and $\beta$-$NaYF_4$ UCNPs by empolying RE-oleate complexes and NaF as precursors. The decomposition method has also been extended to synthesize other RE fluorides, such as $LiREF_4$ [100–103], $KREF_4$ [100, 101], $KRE_3F_{10}$ [104], $MF_2$ (M = Mg, Ca, and Sr) [74], and $BaREF_5$ [100, 105].

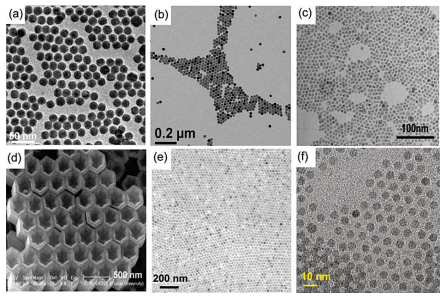


**Figure 2** (online color at: www.lpr-journal.org) TEM images of $NaREF_4$ nanocrystals synthesized by the thermal decomposition method and the hydro(solvo)thermal method. (Adapted with permission from Refs. [61, 65, 66, 80, 110] and [126]. Copyright 2006,2007,2007,2007,2008,2012, American Chemical Society, Wiley-VCH Verlag GmbH & Co. KGaA, Weinheim, and IOP Publishing Ltd.)

Although the thermal decomposition method is an efficient approach in synthesizing high-quality and monodisperse UCNPs, it has some disadvantages, including the harsh conditions needed (∼300 °C, anhydrous, oxygen-free and inert gas protection), expensive and toxic metal precursors, and hazardous by-products—as mentioned above. Additionally, post-synthesis processes are required to introduce hydrophilic and biocompatible coatings on these nanoparticles due to the presence of hydrophobic capping ligands on the surface of the UCNPs.

### 2.2.2. Hydro(solvo)thermal method

The hydro(solvo)thermal method is a typical solution-based chemical synthesis approach in which reactions occur in a sealed environment under high pressure and temperature, usually above the critical point of the solvent in order to increase the solubility and reactivity of the inorganic substances. In a typical synthesis procedure, RE and fluoride precursors, solvents and certain surfactants are mixed

 

REVIEW ARTICLE



and then heated in a specialized reaction vessel known as an autoclave. HF, $NH_4F$, NaF and $NH_4HF_2$ are typical fluoride precursors, while RE nitrates, chlorides and oxides are typical RE precursors. Ethylenediamine tetraacetic acid (EDTA), cetyltrimethylammonuim bromide (CTAB), OA and trisodium citrate (TSC) are commonly used as surfactants. Wang et al. [106] first reported a liquid-solid-solution (LSS) strategy for synthesizing high-quality RE fluoride colloid nanoparticles, based on a general phase transfer and separation mechanism occuring at the interfaces of the liquid, solid, and solution phases present during the synthesis. This approach was further developed as an effective method to synthesize RE fluoride UCNPs [59,65,107,108] (Fig. 2(c)). Wang et al. [13] developed a one-step synthesis of polyethylenimine (PEI)-coated $NaYF_4$:Yb,Er/Tm UCNPs *via* a solvothermal approach. The prepared nanoparticles were hydrophilic and biocompatible directly after production due to the free amine groups capped on the surface of the UCNPs, thus, no further surface modification and functionalization were needed. Zhang et al. [66, 109] reported the synthesis of uniform nanostructured $\beta$-$NaREF_4$ arrays by an OA-assisted hydrothermal route without the assistance of templates, applied fields, and undercoating on substrates (Fig. 2(d)). Li et al. [68, 110] reported a novel user-friendly solvothermal-like method in a glass flask rather than in a sealed autoclave for fabricating high quality hexagonal-phase $NaYF_4$:Yb,Er/Tm nanoparticles without the use of excess fluoride reactants (Fig. 2(e)). This synthesis strategy has been widely used in the synthesis of fluoride UCNPs [42, 83, 111–115].

Possible advantages of the hydro(solvo)thermal method include cost-effective raw materials, excellent control over the crystalline phase, particle size and shape under much lower reaction temperatures (generally below 200 °C). Disadvantages of this method include the need for long reaction time (hours-days) and specialized reaction vessels. In addition, surface modifications are usually likewise required because of the insufficient hydrophilicity of the prepared UCNPs in most cases.

The optimization of the synthesis parameters is generally very time-consuming, and the relatively long reaction time makes it even more challenging. Recent work conducted by Wang et al. [116] and Chan et al. [51] showed great progress along these lines. Wang et al. greatly shortened the reaction time to 5 min by employing microwave heating. This microwave-assisted approach has been further developed and is currently another widely used approach for producing high quality fluoride UCNPs [117–119]. Chan et al. used a different approach and developed a parallel reaction workstation called WANDA (workstation for automated nanomaterials discovery and analysis) for reproducible and high-throughput synthesis of colloidal nanocrystals including $NaYF_4$ UCNPs [51].

Although the above discussed batch-control methods are proved to be efficient in the synthesis of UCNPs and enable control over the phase, size and shape, they are not of complete satisfaction. Inherent to batch-control methods, it is difficult to monitor the UCNPs in real time and accordingly control their growth by adjusting experimental parameters. Microfluidic methods have been shown to be excellent in the synthesis of nanostructures including QDs, gold and silver nanoparticles [120–124]. Despite this, currently very few attempts have been made to synthesize UCNPs in microfluidic systems [125]. In the reported microfluidic synthesis, the reaction time, limited by the final length of the microchannel or capillary, seems to retard the formation of uniform UCNPs with desired hexagonal phase, and the prepared UCNPs suffer from aggregation problems probably due to the absence of proper surfactants during the synthesis. Further studies are therefore required.

### 2.3. Phase and size control

Control of the crystal structure of the fluorides is critical to achieve a high QY. It has been shown that in the thermal decomposition and hydro(solvo)thermal synthesis approaches, $\alpha$-phase $NaYF_4$ nanoparticles are generally first formed, and then $\beta$-phase can be formed through $\alpha \rightarrow \beta$ phase transition by overcoming the free-energy barrier [61, 126]. Hence, any method which could facilitate such a phase transition is helpful in obtaining $\beta$-$NaYF_4$ nanoparticles. Here, several commonly used methods for the phase control of $NaYF_4$ UCNPs will be summarized.

(a) Controlling the reaction temperature and time

Generally, prolonged reaction time and high temperature are needed to overcome the free-energy barrier for the $\alpha \rightarrow \beta$ phase transition [59, 61, 127]. Usually, a reaction time of at least 30 minutes and temperatures of 290-310 °C are needed in order to obtain hexagonal $NaYF_4$ UCNPs [110, 126].

(b) Adjusting the molar ratio of $Na^+/RE^{3+}$ and $F^-/RE^{3+}$

$\beta$-$NaYF_4$ is disfavored under most conditions, except within a narrow window in which the 1:1:4 stoichiometry of $Na^+$, $RE^{3+}$, and $F^-$ is strictly maintained [29, 126], indicated by the phase diagrams of bulk sodium yttrium fluoride [48]. However, influenced by the mechanisms of $Na^+$, $RE^{3+}$, and $F^-$ liberations, previous reports have suggested that higher $Na^+/RE^{3+}$ and $F^-/RE^{3+}$ reactant ratios favor the formation of $\beta$-$NaYF_4$ [61,128–130]. Thus, when using different $Na^+$ and $F^-$ sources, different reactant ratios may be required to promote the $\alpha \rightarrow \beta$ phase transition.

(c) Ligand-mediated phase transition

Wei et al. [67] found that EDTA molecules capping on the surface of the UCNPs could suppress the cubic-to-hexagonal phase transition, prohibiting transformation from the $\alpha$-phase to $\beta$-phase, even when annealed at 600 °C for 5 hours. OA was also found to be in favor of the formation of cubic-phase UCNPs, because negatively charged oleate ligands strongly binds electrostatically to the positively charged (100) surfaces of small $\alpha$-$NaYF_4$ particles and stabilizes the $\alpha$-phase relative to $\beta$-phase [51,63,98,126]. OM can mediate the phase transition

LASER & PHOTONICS REVIEWS



from cubic to hexagonal [63, 126], while TOP can be used as combined ligands together with OA and ODE to change the surface energy and control particle phase and shape. A ligand formed between oleate and TOP at high temperature promotes the phase transition from cubic to hexagonal [64, 128]. TOPO was found to be able to reduce the energy barrier of the $\alpha \rightarrow \beta$ phase transition, thus, it can be used as a single solvent, both a boiling solvent and a capping reagent, to control crystalline growth by providing a broad temperature window for the $\beta$-$NaYF_4$ UCNPs [14].

(d) Lanthanide and transition metal ions doping

Yu et al. [131] and Wang et al. [114] reported that lanthanide dopants with larger ionic radius, such as $La^{3+}$, $Ce^{3+}$, and $Gd^{3+}$, can decrease the energy barrier and tip the balance in favor of the formation of $\beta$-$NaYF_4$. Chen et al. [47] reported that $Ti^{4+}$ doping induced $\alpha \rightarrow \beta$ phase transition in a liquid-solid-solution reaction system at as low temperature as 130 °C. Tian et al. [132] reported a facile strategy for controlling the phase ($\beta \rightarrow \alpha$) and UC emission behavior (green $\rightarrow$ red) of $NaYF_4$:Yb/Er UCNPs through $Mn^{2+}$ ion doping.

Varying the parameters mentioned in the above procedures will also affect the size of UCNPs. Thus, the control over the crystalline phase is always accompanied with the control over the size. The size is an aspect of significance which influences the uptake, biodistribution and clearance of nanoparticles in living organisms. Although research on how the size of UCNPs influences their uptake in cell or animal models is limited, a large amount of effort has been devoted towards the control of the size in order to produce UCNPs with various diameters which are needed for different biomedical applications [63, 77, 109, 114]. For, in particular, *in vivo* imaging applications, nanoparticles are usually required to have comparable sizes to the targeted molecules, in the range of 4–10 nm for most membrane and globular proteins [133]. Significantly larger nanoparticles may have limited accessibility to smaller subcellular structures, perturb trafficking patterns, retard diffusion, interfere with protein functions or binding events, or alter pharmacokinetics [134–136]. Smaller nanoparticles means lower brightness and thus the challenge is to synthesize UCNPs small enough while maintaining their brightness. Much progress has been made in producing sub-10 nm $NaYF_4$ nanoparticles [77, 126, 137]. Most notable of these studies has been the determination of the window for synthesis of sub-10 nm $\beta$-$NaYF_4$ by Ostrowski et al. [126]. They described the conditions for controlled synthesis of protein-size $\beta$-$NaYF_4$ from 4.5 to 15 nm in diameter with efficient UC emissions, by varying the concentration of basic surfactants (OA and OM), $Y^{3+}/F^-$ ratio, and reaction temperature (Fig. 2(f)).

It is noteworthy to point out that the phase and size control of fluoride UCNPs often requires a precise control over many experimental parameters, since the phases are affected by multiple factors instead of a single one. In addition, the above approaches can be employed synthetically in order to obtain desired products with reasonable conditions [77]. To fully meet the demands of different sized UCNPs for various applications, approaches for phase and size control need to be further explored.

## 3. Optical properties and characterization

In contrast to traditional fluorescent biomarkers, UCNPs can be excited by NIR rather than ultraviolet (UV) radiation, thereby significantly minimizing photo damage of biological specimens and maximizing the penetration depth of the excitation light. The anti-Stokes nature of the UC emissions enables autofluorescence-free detection which results in excellent signal-to-noise ratio (SNR) and improved detection sensitivity. Distinguished from other anti-Stokes processes – including second harmonic generation, multi-photon absorption and anti-Stokes Raman scattering – UC emissions are based on real intermediate states, thus allowing for more efficient frequency conversion. This means that UC emissions can occur under moderate light intensities, which is often a basic requirement in biological studies. UCNPs can be excited by compact, inexpensive and low-power (1–1000 W/cm$^2$) NIR lasers. UCNPs show non-blinking characteristics under continuous irradiation and are resistant to photobleaching as well as photochemical degradation. Additional advantages of UCNPs include narrow and well-defined emission peaks, a large anti-Stokes shift, and convenient emission color tuning [81, 84, 138].

The UC photoluminescence spectra of the UCNPs constitute one of their most important characteristics and typical luminescence spectra are presented in Fig. 3. Since the discovery of the UC phenomenon in the 1960's, extensive efforts have been invested into the research of the UC emission mechanisms. To date, several basic processes have been identified, including ground state absorption (GSA), excited state absorption (ESA), energy transfer upconversion (ETU), cross relaxation (CR) and cooperative

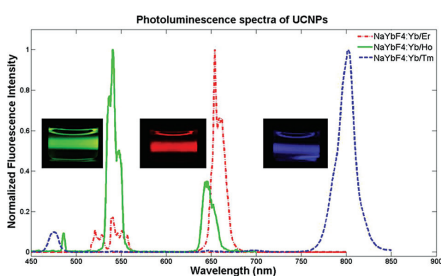


**Figure 3** (online color at: www.lpr-journal.org) Photoluminescence spectra emitted by UCNPs doped with different RE-ions. The $NaYbF_4$:$Yb^{3+}/Er^{3+}/Ho^{3+}/Tm^{3+}$ nanoparticles are suspended in a chloroform solution and being irradiated by a 915-nm diode laser with a power density of 500 mW/cm$^2$. (Reprinted with permission from Ref. [139]. Copyright 2011, American Chemical Society.)

REVIEW ARTICLE



sensitization (CS) [4]. Through the combined action of these processes, complex multi-photon UC phenomena – including photon avalanche (PA) – and anti-Stokes spectra can be achieved. The details of UC mechanisms have been summarized in previous reviews [4, 140].

### 3.1. Rate equation analysis

In principle, the UC process can be quantitatively expressed by a set of coupled differential equations describing the population density, $N_i$, of each lanthanide $4f^N$ manifold, taking into account all population and depopulation rates involved [141–143]:

$$\begin{aligned}\frac{dN_i}{dt} &= \sum \text{population rate} - \sum \text{depopulation rate} \\ &= \sum_j N_j\left(A_{ji}^{ED} + A_{ji}^{MD}\right) + N_{i+1}W_{i+1,i}^{NR} \\ &\quad + \sum_{ij,kl} N_j N_i C_{ji,lk}^{ET} - \sum_j N_i\left(A_{ij}^{ED} + A_{ij}^{MD}\right) \\ &\quad - N_i W_{i,i-1}^{NR} - \sum_{ij,kl} N_i N_k C_{ij,kl}^{ET} \qquad (1)\end{aligned}$$

where $A_{ij}^{ED}$ and $A_{ij}^{MD}$ are Einstein coefficients for electric dipole (ED) and magnetic dipole (MD) radiative transitions from manifold $i$ to $j$; $W_{i,i-1}^{NR}$ is the nonradiative multiphonon relaxation (MPR) rate constant from manifold $i$ to $i-1$; $C_{ij,kl}^{ET}$ is the microscopic energy transfer parameter for the transfer of energy *via* the donor transition $i \rightarrow j$ and the acceptor $k \rightarrow l$ transition. In this model, the interactions among more than two ions (such as the CS process) are not considered. The intensity of any given UC emission peak is proportional to the product of the population density of the emitting state and the microscopic rate constants for the radiative transition. Obviously, these rate constants play critical roles in depicting the UC emissions. Once they are known, the characteristics of UC emissions, including the QYs and spectral purities, can be obtained by calculation directly, as shown in a recent work of Chan et al. [142]. This model can also be used to determine critical energy transfer transitions involved in UC process [142]. However, the use of this model is demanding mainly due to the difficulty in determining the rate constants, although in theory the ED, MD transition rates and energy transfer rate $C_{ij,kl}^{ET}$ can be calculated using the Judd-Ofelt theory [39, 40], while the quantum mechanical magnetic dipole operator [144] and the nonradiative MPR can be treated with a modified energy gap law [145]. Thus, this model is usually simplified to only include the major transitions and MPR processes identified by previous studies.

The investigation on the time dependent behavior of UC emissions is a good way to verify the validity of the proposed UC pathways, and the rate constants could be extracted by fitting the measured time-dependent emission intensity with time-dependent rate equations [146–148]. There are very few reports on the use of this approach on UCNPs in the literature and an interesting topic could be to correlate the microscopic rate constants and the reaction conditions in order to guide the synthesis of UCNPs.

### 3.2. Power dependence

In addition to studying the time-resolved behavior of UC emissions, power dependence analysis of UC emission intensity under CW excitation, combined with steady-state rate equation analysis, also provides useful information for the UC mechanism. A theoretical model for this was systematized by Pollnau et al. and Suyver et al. [17, 18], and is now one of the most important aspects of the optical characterization of UCNPs. Briefly, the UC emission intensity, $I$, is related to the absorbed excitation power density, $I_{ex}$, by the following equation

$$I \propto I_{ex}^{n}. \qquad (2)$$

By plotting the emission intensity versus the excitation power density in a double-logarithmic diagram, the order $n$ of the UC process, i.e., the number of pump photons required to excite the emitting state, can be obtained by the slope of the power dependence curve. This slope indicates the multi-photon nature of the UC emission. An example of the power dependence of the NIR UC emission for $Tm^{3+}$ is shown in Fig. 4 together with the corresponding UC spectrum, indicating that this UC emission line originates from a two-photon process.

It should be noted that the power density dependence of the UC emission described by Eq. ((2)) is only valid under weak excitation power densities and will become more

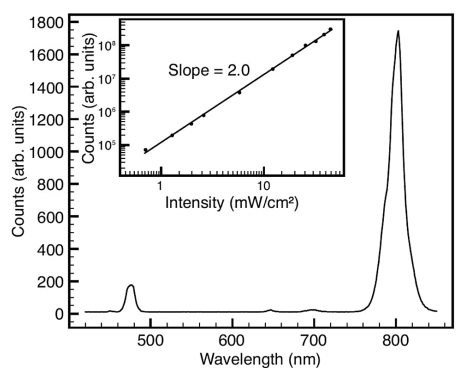


**Figure 4** Emission spectrum recorded for $NaYF_4$:$Yb^{3+}$/$Tm^{3+}$ nanoparticles under 980-nm excitation with an intensity of 6 W/cm$^2$. The inset shows the pump-power dependence of the interesting 800 nm line measured under low intensities. (Reprinted with permission from Ref. [19]. Copyright 2008, American Institute of Physics.)

LASER & PHOTONICS REVIEWS



complicated for higher excitation power densities due to the competition between the ETU rate (excitation power density dependent) and the linear decay rate in the individual excitation steps. The slope of the power dependence curve is known to decrease with increasing excitation power density. When the excitation intensity is high enough such that saturation of the intermediate energy state involved in the UC process occurs, the two-photon UC luminescence will appear with a slope of 1 [17]. Smaller slopes and saturation power densities are often used to indirectly indicate better performance of UCNPs in energy upconversion [103, 149].

### 3.3. Quantum yield

The QY measurement constitutes another important aspect in the optical characterization of UCNPs, playing a crucial role for their practical applications. The QY is generally defined as the ratio between the number of the emitted UC photons and the number of absorbed excitation photons. Currently, QY measurements on UCNPs are directly adapted from the QY characterization of conventional fluorescent materials, such as fluorescent dyes and QDs. Two different experimental setups can be employed: a spectrofluorometer-based setup and an integrating-sphere-based setup. The former needs a fluorophore with known QY as a reference, while the latter is self-calibrated. Different from linear fluorescent dyes and QDs, the QYs of UCNPs are power density dependent rather than constant [150, 151]. Thus, the determination of the excitation power density is critical for QY measurements on UCNPs. In an integrating-sphere-based setup, it is typically challenging to determine the true excitation power-density, since the excitation light repeatedly passes through the sample due to reflections from the wall of the sphere, which could lead to errors in the measurements. Compared with an integrating-sphere-based setup, determining the excitation power density of a spectrofluorometer-based setup is much more straight forward.

Reports in the literature on the absolute QY of UCNPs are generally very scarce [50, 150–152]. Page et al. [150] measured the QYs of several UC phosphors using an integrating-sphere-based setup. For bulk $NaYF_4$:$Yb^{3+}$/$Tm^{3+}$ material, they determined the power conversion factor of the blue emission band to be $2 \times 10^{-4}$ at an excitation intensity of 1 W/cm$^2$. Size-dependent effects have also been considered by Boyer et al. [50] for $Yb^{3+}$/$Er^{3+}$ co-doped $NaYF_4$ nanoparticles, where 10 times lower QY of core–shell nanoparticles (30 nm) as compared with bulk material was found under an excitation intensity of 150 W/cm$^2$. Recently, Xu et al. [151] measured the QY of $NaYF_4$:$Yb^{3+}$/$Tm^{3+}$@$NaYF_4$ core–shell nanoparticles using a spectrofluorometer-based setup and reached a value of 3.5% under an excitation intensity of 78 W/cm$^2$, as illustrated in Fig. 5. For comparison, the QYs of the most efficient two-photon dyes were simulated under identical experimental conditions and are also shown in the same figure. It can be seen that the required excitation intensity is

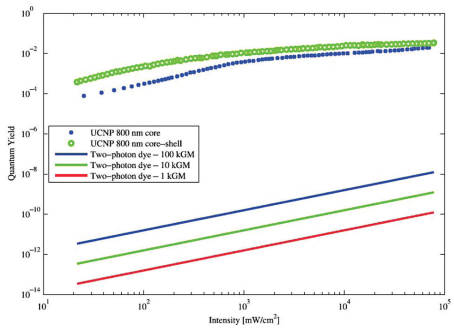


**Figure 5** (online color at: www.lpr-journal.org) Quantum yield of the 800 nm emission band in core-shell $NaYF_4$:$Yb^{3+}$/$Tm^{3+}$@$NaYF_4$ nanoparticles and core nanoparticles $NaYF_4$:$Yb^{3+}$/$Tm^{3+}$. The quantum yield increases linearly with the excitation intensity until a saturation point, from which the quantum yield approaches a constant value. Solid lines show simulated corresponding QYs for highly efficient two-photon dyes under identical experimental conditions. (Reprinted with permission from Ref. [151]. Copyright 2012, American Chemical Society.)

clearly too high to be used in scattering tissues. The reason is that these dyes require simultaneous absorption of two photons *via* a virtual state, in contrast to UCNPs, which display long-lived real intermediate states.

An important aspect of proper QY measurements is to make it possible to compare the results between different studies. However, up to date, the QY characterization on UCNPs still does not follow a harmonized protocol, instead the QYs are usually provided at one specific power density, ignoring their power density dependencies [50, 77, 126]. As mentioned above, UCNPs are different from conventional Stokes-shifting fluorophores, since saturation can occur due to competition between ETU and linear decay. This leads to QYs that in general have complex power density dependent behaviors. Thus, the reported QYs from different studies are not directly comparable. Here we propose a protocol for a standardized QY measurement for UCNPs, where the whole power density dependence is measured in order to provide complete information on the UC energy conversion system. In addition, the intensity of the excitation light generally has an inhomogeneous rather than a "top hat"distribution. This inhomogeneity should also be compensated in order to provide accurate QY information. If possible, finding a few parameters which are able to characterize both the absolute QY and the change on excitation power density are also highly desirable. Such a careful characterization of the luminescence efficiency in a reproducible way – which appears to be neglected in the literature – would make direct comparisons between results from different studies possible. This would stimulate the further development of the UCNPs, improving their performance and lead to more optimized synthesis methods.

 

REVIEW ARTICLE

Laser Photonics Rev. **7,** No. 5 (2013) 

### 3.4. Enhancement of upconversion efficiency

In most cases, the emission efficiency of UCNPs is relatively low because of two reasons: (1) non-radiative decay due to surface defects and (2) two-photon nonlinear processes. Hexagonal phase $NaYF_4$ UCNPs usually have one order of magnitude higher QY than their cubic counterparts. Thus, by phase control approaches UCNPs with enhanced UC efficiency can be obtained. Another trivial method to increase the QY is to synthesize larger UCNPs. Smaller particles have larger surface-to-volume-ratio, which naturally leads to more defects. Ions on or near the surface of the UCNPs are sensitive to the local environments, thereby causing higher non-radiative energy losses. However, the maximum size of UCNPs for specific applications is normally limited. Therefore, this approach is not generally valid. Other versatile approaches will be presented as follow.

#### 3.4.1. Ion doping and composition tuning

Ion doping can modify the crystal field surrounding doped RE ions, thus changing the UC emission intensity by altering the transition probabilities of the RE ions. Introduced by Chen et al. [16, 153] and Bai et al. [154–156], $Li^+$-doping was found to be able to enhance the UC emission in oxide UCNPs. In some recent reports [116, 157] it was shown that $Li^+$ -doping gives similar results in fluoride UCNPs. $Ho^{3+}$ -doping is found to enhance the NIR UC emission of $Tm^{3+}$ [86]. Composition tuning is another commonly used approach to enhance the QY, where the recent work of Chen et al. [137] is a good example.

#### 3.4.2. Coating with a shielding layer

A shield layer on the surface of the UCNPs can reduce crystal defects and protect the active optical ions from the coupling with vibrational modes in the solvent, thereby reducing the non-radiative energy losses [42]. The shell could be either inert (i.e., with no optical active ions) or active (i.e., containing active ions, mainly $Yb^{3+}$). For example, increased QYs were observed after growing of an undoped $NaYF_4$ shell over $Er^{3+}$- or $Tm^{3+}$-doped core UCNPs [50, 151]. In another report, a 50-fold higher QY was observed for sub-10 nm UCNPs, and the emission from 9-nm core-shell UCNPs was larger than that of comparable 37-nm cores when normalized to the absorbance at 980 nm [126]. For the use of active shells, examples include comparison of the pure $BaGdF_5$:$Yb^{3+}$/$Er^{3+}$ core with the active-shell coated counterparts, where it was shown that the luminescence intensity could be enhanced by several hundreds of times [158]. In another report, a significant increase in the UC intensity was measured in $NaGdF_4$:$Er^{3+}$, $Yb^{3+}$@$NaGdF_4$:$Yb^{3+}$ mol 20% active-core/active-shell UCNPs compared to $NaGdF_4$:$Er^{3+}$,$Yb^{3+}$@$NaGdF_4$ active-core/inert-shell and $NaGdF_4$:$Er^{3+}$/$Yb^{3+}$ core-only nanoparticles [159]. In addition, by spatially separating dopant ions using a layer (laminated) structure, the effect of the concentration quenching can be suppressed, and an enhancement of the UC emission can be expected [83, 159, 160].

#### 3.4.3. Surface plasmonics coupling

It is well known that the unique surface plasmon properties of metallic structures can be exploited to enhance the fluorescence from adjacent fluorophores (organic dyes and inorganic QDs) [161, 162]. Similarly, surface plasmons with strong local field can also be used to enhance the efficiency of UC emission [163, 164]. Zhang et al. and Sudheendra et al. have successfully attached gold nanoparticles onto UCNPs to modulate the UC emission [165, 166]. A specifically designed plasmonic gold surface coupling with 980-nm radiation was shown to clearly enhance NIR-to-visible upconversion luminescence from the nanocrystalline layer [167]. It is very important to study the surface plasmon enhancement mechannism at single nanoparticle level in order to provide an optimal design of hybrid UCNPs and metallic nanoparticles. Schietinger et al. coupled single $NaYF_4$:$Yb^{3+}$/$Er^{3+}$ nanocrystals with gold nanospheres (30 and 60 nm in diameter) to enhance UC emission in a combined optical and atomic force microscopy (AFM) system, gaining an overall enhancement factor of 3.8 [168]. Time-resolved measurements revealed that both the excitation and the emission processes are influenced by the coupling to plasmon resonance in the gold nanospheres. Several studies have shown that the separation critically determines whether enhancement or quenching eventually dominates [161, 169]. The enhancement of UC emission is highly spectral dependent. A more-photon-involved UC process resulted in a larger enhancement factor under the same excitation power density [170].

The enhancement is known to result from the modification of the radiative and nonradiative decay rates and the enhancement of the excitation intensity by the localized surface plasmonic resonance of metallic nanostructures [163, 168, 171, 172]. However, some details remain unknown, e.g., is the change of decay rates or the increase of excitation intensity contributing the most to the enhancement of the intrinsic QY of the nanocrystals, and by how much the ultimate (maximum achievable) intrinsic QY will be increased due to the change of the decay rates (the enhancement of the excitation intensity will not change the ultimate intrinsic QY). Further experimental studies on the QY enhancement are needed. Regarding the QY of the system, although it always tends to increase due to the enhanced local field, the enhancement is, however, related with the intrinsic power-density dependent QY of the crystal. Thus the understanding of the influence of the surface plasmonic coupling on the intrinsic QY could address questions related to the amount of gain that can be expected.

Although the UC emission enhancement depends on the fourth or higher power of the local field, solid theoretical analysis revealed much weaker gains than that of Raman enhancement [163]. Furthermore, chemical sample

LASER & PHOTONICS REVIEWS



preparation and precise physical control are essential to ensure a satisfactory enhancement, making the process complicated and demanding. Thus, considerable challenges involved in using metallic nanoparticles to enhance UC emission for biodetection remains and there is a strong need of simplifed and reproducible synthesis strategies.

## 4. Surface modification

Similar to other nanosized biomarkers, UCNPs also need to be water dispersible, highly stable, biocompatible, sensitive and biotargeting for successful bio-applicability. However, most of the commonly used UCNPs were synthesized using oil-phase methods which render UCNPs with no intrinsic aqueous dispersibility and functional organic groups on the surface. Recently, several single-step synthesis methods, mainly including polyol process [173,174], one-pot synthesis assisted by hydrophilic ligands [175,176], hydrothermal microemulsion synthesis [177] and ionic liquid-based synthesis [94,178], have been developed to directly synthesize hydrophilic UCNPs. However, it is still very demanding to obtain monodisperse and hydrophilic UCNPs with small size *via* single-step methods, although they simplify the reaction procedure and reduce the post-processing. For hydrophobic UCNP synthesis strategies, it is easier to control the size, morphology, phase and crystallinity of the UCNPs, and the procedure of post-processing is straight forward and controllable. Furthermore, the directly synthesized hydrophilic UCNPs without any treatment also show toxicity to cells, tissues or whole organisms. Therefore, UCNPs synthesized from hydrophobic methods are still the most commonly used in biological applications. In the following, more emphasis will be placed on how to re-process the as-synthesized hydrophobic UCNPs into a hydrophilic state with high stability, high biocompatibility and bioconjugation platform.

### *4.1. Hydrophilic processing of UCNPs*

In general, a multitude of methods exist for converting hydrophobic UCNPs into a hydrophilic state [38]. Here, four main methods commonly found in the literature are summarized: ligand exchange, ligand oxidation, silanization and ligand free. These methods are versatile and do not have any obvious side effects upon the morphology, size, composition, crystallization and optical properties of the resulting UCNPs.

#### 4.1.1. Ligand exchange

Ligand exchange is an effective method for modificating the surface of nanoparticles. When the hydrophobic ligands on the as-prepared nanoparticles are replaced by some hydrophilic ligands, the nanoparticles will become water dispersible. Due to the surfactant OA adsorbed on the surface, UCNPs contain a large number of carboxyl groups (–COOH), which strongly interact with RE ions. Therefore, for the OA-coated UCNPs, multichelated ligands or an excess of single-chelated ligands are required to exchange the OA ligands. In recently reported works, poly(ethyleneglycol) (PEG) [139, 179], 3-mercaptopropionic acid (3-MSA) [82], 5-mercaptosuccinic acid (MSA) [139], polyacrylic acid (PAA) [71, 180, 181] and citrate have been used to replace the OA ligands *via* ligand exchange. These replacement processes are simple, highly repeatable and do not change the unique optical properties of UCNPs in any significant way. These commonly used organic molecules all carry functional groups and facilitate further biofunctionalization and bioconjugation. For UCNPs which are coated by charged organic molecules, it is possible to add an additional polymer coating of opposite charge. Once the UCNPs become water dispersible, further process could be performed. Recently Zhan et al. [139] proposed to encapsulate negatively charged MSA-UCNPs using positively charged polyallylamine hydrochloride (PAH). The significant decrease of OA, the MSA encapsulation and PAH coating were confirmed by Zeta potential measurements and Fourier transform infrared (FTIR) spectroscopy, as shown in Fig. 6. This attraction is based on electrostatic interaction. Repeated coating *via* this attraction can be useful and this approach is called layer-by-layer method [182], which, however, normally requires repeated coating and complicated washing procedure.

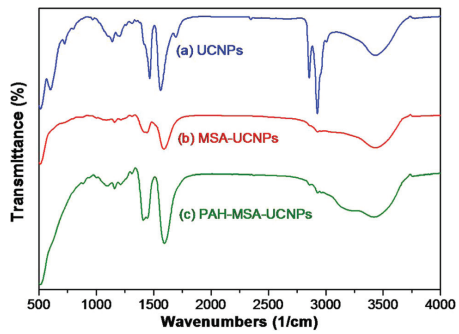


**Figure 6** (online color at: www.lpr-journal.org) FTIR spectra of (a) OA-capped $NaYbF_4:Yb^{3+}/Er^{3+}$ sample, (b) MSA-$NaYbF_4:Yb^{3+}/Er^{3+}$ and (c) PAH-MSA- $NaYbF_4:Yb^{3+}/Er^{3+}$.The alternation of FTIR spectrum peaks (corresponding to the specific chemical bonds) revealed the process of surface modification.(Reprinted with permission from Ref. [139]. Copyright 2011, American Chemical Society.)

#### 4.1.2. Ligand oxidation

Apart from ligand exchange, OA ligands on the surface of the UCNPs can also be oxidized into azelaic acids

 

REVIEW ARTICLE

Laser Photonics Rev. **7,** No. 5 (2013) 

($HOOC(CH_2)_7COOH$), which results in the generation of free carboxylic acid groups on the surface. After ligand oxidation, the OA-coated UCNPs will become water dispersible. A strong oxidizing agent is very important for the effective ligand oxidation process. In 2008, the group of F.Y. Li proposed a simple and versatile strategy for direct oxidization of OA ligands without any intermediate procedures using a strong oxidizing reagent named Lemieux-von Rudloff reagent [16,183]. Naccache et al. [71] proposed the utilization of permanganate/periodate to oxidize and break the double bond of the long OA C18 chain with the –COOH moiety maintained, facilitating better dispersibility in water. The OA ligands could also be directly oxidized by ozone – a clean and readily available strong oxidant – under specific conditions, which enabled the presence of –COOH or –CHO groups on the surface [184]. These oxidization reactions were reported to have no significant negative effect on the chemical and optical properties of UCNP, and the introduction of carboxylic or aldehyde groups not only rendered high water dispersibility, but also facilitated further bioconjugation with biomolecules through covalent methods. It is worth to point out that this method involves oxidation of the double C=C bond of the ligand, and thus the types of available ligands are limited and dependent on the used surfactants. Other disadvantages of the oxidation strategy include the long reaction times and the low yields.

#### 4.1.3. Silanization

Silicate systems have been used to synthesize bulk, film, and particle silicate mesoporous structures for a wide range of applications. As one of the most frequently used methods of surface modification for nanoparticles, silica coating is highly stable (chemically inert), biocompatible, optically transparent and offers nanometer-precision thicknesses. It is also suitable for use as a coating material for UCNPs [185]. In recent years, the group of Y. Zhang has employed silica to encapsulate hydrophobic OA-coated UCNPs [90, 111, 186–191]. Surface silanization methods can flexibly offer abundant functional groups (e.g., –COOH, $–NH_2$, –SH, *etc*.) and thus satisfy various needs of conjugation with biological molecules. The most commonly used approach of silica coating is the reversed microemulsion system, which is based on a homogeneous mixture of water, oil, surfactant and tetraethyl orthosilicate (TEOS) [115, 192]. This method can precisely control the silica shell thickness *via* altering the reagent amount or the reaction time, which is very useful to control the distance between the nanoparticles and the molecules of interest [115, 193]. Furthermore, another advantage of silica coating is that mesoporous silica shell can be easily obtained and greatly facilitates the loading of drugs and biomolecules onto the surface of UCNPs. Thus, such surface modification of the UCNPs can allow drug delivery to specific cells or receptors. An representative application is to employ mesoporous-silica-shell-coated UCNPs as nanocarriers for PDT drugs [194].

#### 4.1.4. Ligand free

The surface OA ligands of $NaYF_4$:$Yb^{3+}$,$Er^{3+}$ nanoparticles could be released by thorough washing using excess ethanol [90] and HCl [195] under ultrasonic treatment. This ligand-free method is very simple and was proposed very recently. UCNPs without any ligand on the surface are highly water dispersible. However, the problem would be that biofunctionalization and bioconjugation is nontrivial due to the lack of functional groups on the surface. A solution to efficiently biofunctionalize these ligand free UCNPs would be the key.

#### 4.1.5. The impact of surface modification on optical properties

The described surface modification methods have different applicabilities due to their distinctive features, and thus the method selection should rely on the specific application of interest. As previously discussed, a large number of successful bioapplications of UCNPs were substantially demonstrated with the assist of these surface modification methods. It is reasonable to believe that these methods are essential and effective, and they hardly have considerable side effect on the optical properties of UCNPs. However, it is still of significance to investigate the impact of these processes on the luminescence intensity in order to improve or maintain their brightness. In very recent years, there have been an increasing number of studies revealing the impact of surface modification on the optical proterties of UCNPs, although they are not covered in most review papers. According to some reports, the luminescence intensity, to some extent, was actually decreased after treatment with certain modification processes [113, 115, 196, 197]. As a case of point, decreased luminescence intensity can be observed for PAA-coated UCNPs due to the interaction between the surface of UCNPs and PAA [196, 197]. Besides, in the silanization method the silica shell can slightly scatter both excitation and emission light and thus weaken the luminescence to some extent [115]. The type of solvent is also an important factor affecting the brightness. UCNPs dispersed in aqueous solvent were reported to have a decreased brightness when compared to the same UCNPs dispersed in organic solvent [113]. The reason is that water molecules have high energy vibrational modes, which probably results in an increased nonradiative relaxation of the excited states and thus an overall quenching of the luminescence [113]. These problems could be overcome partially by a protective shell of $NaYF_4$, which has low phonon energy and can act as an isolation layer in order to greatly weaken the negative interaction between UCNPs and surface ligands/local environment [113, 196]. The other strategies of enhancing QY previously discussed in section 3 can also be exerted to compensate the possible brightness decrease caused by surface modification and aqueous solvent. The key is to keep or even improve the unique optical properties of UCNPs while performing surface modification.

LASER & PHOTONICS REVIEWS



### *4.2. Surface functionalization of UCNPs*

The previously mentioned surface modifications of UCNPs enable their dispersion and stability in aqueous solutions. This post-treatment is quite indispensable for hydrophobic UCNPs, but not sufficient for further bioapplications. In most applications, including bioimaging, biosensing and biotherapy, UCNPs also need to be capable of targeting specific cell lines, tumors or biomolecules. Living cells do not interact directly with the assistant biomaterials, but with the proteins or molecules adsorbed on their surface. Thus, it is needed to develop a bioconjugation of UCNPs interacting with such proteins and molecules. After the surface modification, UCNPs either gain functional groups (e.g., carboxyl, amino, thiol, *etc*.) or are strongly charged (positive/negative) on the surface, which both enable them to conjugate with various biological or polymeric molecules. In the field of bionanotechnology, there exists several well-known approaches for bioconjugation of nanoparticles with biomolecules. Generally, these biomolecules can be bioconjugated to the surface of UCNPs *via* physical interaction (e.g., electrostatic adsorption) or chemical interaction (e.g., covalent link).

As one of the most commonly used procedures, the electrostatic adsorption method is straightforward and effective *via* non-covalent forces. Zhan et al. [139] successfully conjugated positively charged PAH-UCNPs with negatively charged antibodies (anti-CEA8 with isoelectric point (pI) in the range pH 5.8–6.5) in phosphate buffer solution (PBS) (pH 7.4). Without chemical bonding, the proteins or molecules attached on the surface of UCNPs will not change or lose their activity. Non-specific binding cannot be eliminated in the case of physical methods. In comparison, chemical binding is more specific and also more complicated to perform. Chemical binding needs to make use of covalent interaction between some specific functional group pairs, such as, a carboxylic acid and a primary amine to form an amide bond, two thiols to form a disulfide bond, a thiol and a maleimide to form a thioether bond, and an aldehyde group and a hydrazide group to form a hydrazide bond [23]. Covalent binding of biomolecules often requires some intermediate process and are assisted with some linker agents. As a case of point, EDC (ethyl(dimethylaminopropyl) carbodiimide) and Sulfo-NHS (N-hydroxysulfosuccinimide) are always employed to couple amino and carboxyl, conjugating surface modified UCNPs and biomolecules [182, 198, 199]. The effectiveness of this strategy relies on the precise control of the molar ratio of the reagent molecules. In addition, there are many other useful bioconjugation strategies. As a very popular protein binding mechanism, biotin binding to streptavidin were also introduced to the bioapplications of UCNPs [200, 201]. Some peptides bearing –COOH, including RGD (arginine–glycine–asparatic acid) and CTX (chlorotoxin)), were directly conjugated to the surface of $–NH_2$ modified UCNPs for desired function activity [199, 202]. DNA and folic acid (FA) were also successfully used to directly bioconjugate UCNPs to specifically target cancer cells [187, 201].

## 5. Toxicity and health issues

Despite all of the advantages of UCNPs as compared to conventional fluorophores, in order for them to be an attractive choice for biological imaging studies, it is obviously of utmost importance that the toxicity and potential health issues are thoroughly investigated. Even though UCNPs have not been available for very long, the importance of this topic has already attracted a great amount of interest. Most of the studies have focused on *in vitro* cytotoxicity, however, results concerning long-term effects within small animals have recently started to appear. In this section, a few of the most important results concerning the cytotoxicity of UCNPs will be highlighted.

Following the increasing interest of UCNPs, several studies of *in-vitro* cytotoxicity of UCNPs have been conducted. Already in 2008, Chatterjee et al. [203] used murine stem cells to assess the cell biocompatibility of PEI-coated UCNPs, while Shan et al. [204] studied the toxicity of silica coated UCNPs in human osteosarcoma (HOS) cells, using the methylthiazol tetrazolium (MTT) assay to evaluate the cytotoxicity. Both of these early studies found the cytotoxicity to be very low. To date, the cytotoxicity of a large number of both human and animal cell lines have been studied, including HeLa cells [177], human glioblastoma (U87MG) cells [199], human nasopharyngeal epidermal carcinoma (KB) cells [205], and human hepatic (L02) cells [206]. An example of the cell viability of HeLa, KB and L02 cells are shown in Fig. 7. Currently, no severe adverse effects have been found that can be directly related to the UCNPs, indicating them to be of high biocompatibility.

An important aspect that *in-vitro* cell studies cannot provide an immediate answer to is the biodistribution and clearance of UCNPs following an injection into an animal. The long-term biodistribution of intravenously injected UCNPs has been reported by Xiong et al. [205]. In this study, the animals were followed for 115 days and the results showed that the UCNPs mainly accumulate within the spleen and liver. Furthermore, the UCNPs were found to have a clearing time longer than 7 days, in contrast to a previous study which showed a more rapid clearance speed [186]. This shows that sample preparation is of high importance in order to determine the pharmacokinetics of the UCNPs within an organism. However, perhaps more importantly, for these

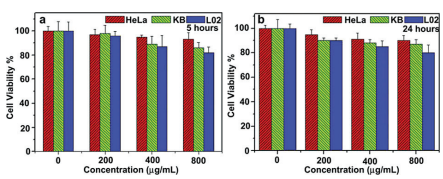


**Figure 7** (online color at: www.lpr-journal.org) *In vitro* cell viability of HeLa, KB and L02 cells incubated with UCNP-OA-CDT at different concentration for 5 (a) and 24 h (b), respectively. (Reprinted with permission from Ref. [206]. Copyright 2008, Elsevier Ltd.)

REVIEW ARTICLE

Laser Photonics Rev. **7,** No. 5 (2013) 

studies, no significant toxicity effects could be seen in the animals under the moderate doses (∼15 mg/kg) used.

In addition to the studies of small animals, systematic investigation of the effects upon Caenorhabditis elegans (C. elegans) has also been recently conducted [207]. The worms were fed with a mixture of B-growth media and UCNPs, and the toxicity assessments were based on green fluorescent protein (GFP) expression, life span, egg production, egg viability, and growth rate. The results showed no significant differences between the worms fed with the mixture of B-growth media and UCNPs compared with those fed with only B-growth media.

Predicting the toxicity and health issues associated with nanoparticles in a general manner is very difficult. Since the toxicity is not only related to the composition of the nanoparticles (including surface modification), it is clear that the properties of the bulk material very seldom can be directly translated to the nanometer scale. For example, size-dependent factors and the local environment within an organism will play a significant role in the pharmacokinetics of the nanoparticles. For the case of UCNPs, the material itself is still relatively new and despite the current studies showing no significant toxicity effects, further studies on an even longer time scale are certainly required before they can be applied in clinical settings. For example, it is known that RE elements could induce autophagy in HeLa cells, which is a common biological effect for the lanthanide elements [208]. It is also worth to point out that for the purpose of small-animal studies, the effects on a very long time scale may not be of extreme importance. Similarly, the use of experimental drugs on patients carrying terminal diseases is approved in certain regions of the world, e.g., Europe. Thus, even though the effects on a very long time scale may not be clear at this time, there are still numerous of compelling *in-vivo* applications of UCNPs.

## 6. Applications of UCNPs

In recent years, UCNPs have attracted remarkable attention in the biophotonics area due to their merits of autofluorescence free, large anti-Stokes shifts, sharp emission bandwidths, high resistance to photobleaching, nonblinking emission behavior, deep detection ability and high spatial resolution. As shown in Fig. 8, UCNPs have widely been employed in *in vitro* cell microscopy, *in vivo* animal diffuse imaging, luminescence diffuse optical tomograpy, *in vivo* multimodal animal imaging (MRI/PET), highly sensitive bioassays (luminescence resonance energy transfer (LRET)), *in vitro* temperature sensing and photodynamic therapy (PDT). In the following, all the above biological applications will be covered and discusssed in detail.

### *6.1. Bioassays*

Bioassay techniques are of fundamental importance in bioanalytical chemistry and biological sciences. They can offer qualitative assessment or measurement of the presence, amount and the functional activity of the analyte, which can be a drug, a biochemical substance or a cell in an organism under study. Concerning single biomolecule detection or nano-scale bioprocess monitoring, the SNR performance of the employed bioassays is very critical and needs further improvements. UCNPs can facilitate the weak signal detection due to the improved SNR as compared to conventional fluorophores. Therefore, in recent years, UCNPs have gained much popularity in applications towards bioassays. In the year of 2001, Corstjens et al. [209] developed UCNP-based lateral-flow bioassays to identify Human Papillomavirus type 16 infection *via* detection of specific nucleic acid sequences. Later, the same group further applied UCNPs in immunohistochemistry in lateral flow assay formats, and in immunochromatographic assays for human chorionic gonadotropin [210]. A host of UCNP-based nucleic acid assay has also been exploited by Tanke et al. and coworkers to achieve a detection limit of 1 ng/ml oligonucleotides [54]. A sensitive luminescent bioassay for the simultaneous detection of Salmonella Typhimurium and Staphylococcus Aureus was developed for both recognition and element concentration evaluation [211]. UCNP-based assays are highly sensitive, inexpensive, allow for multiplexing, and are suitable for quantitative detection. Successful on-site detection with UCNP-based assays and portable readers has been performed in Europe for the detection of drugs abuse *via* oral fluids. These reports show the very large potential of the UCNP-based bioassay in biochemical testing.

As one of the most powerful bioassay tools, FRET (Förster resonance energy transfer)-based assays are advantageous in detecting bioaffinity interactions and conformational changes of biomolecules on nanometer scale

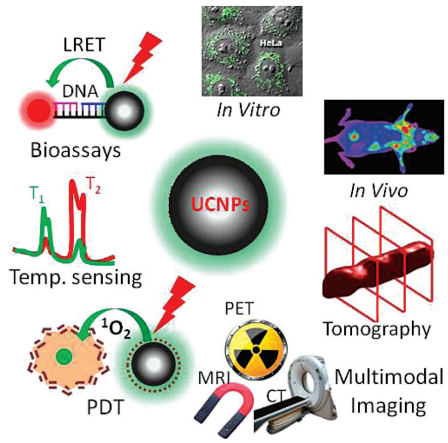


**Figure 8** (online color at: www.lpr-journal.org) Schematic summary of biological applications using UCNPs.

LASER & PHOTONICS REVIEWS



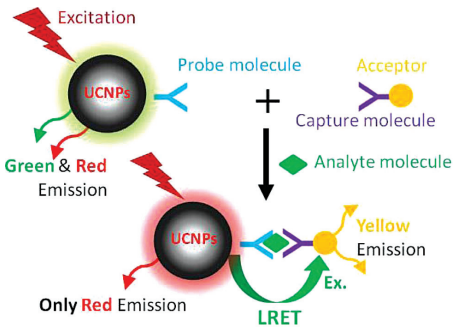


**Figure 9** (online color at: www.lpr-journal.org) Principles of UCNP-based LRET: a UCNP donor produces anti-Stokes emission at 530–550 nm upon excitation. Consequently, it can excite the attached acceptors *via* FRET process. The intensity of the sensitized emission from the acceptor measured around 600 nm is proportional to the analyte concentration in the reaction. Biomolecules here could be RNA, DNA, antigen/antibody and various proteins (depending on the type of biorecognition).

(< 10 nm) [211]. Here, UCNP-based probes could assist in circumventing some of the challenges with traditional FRET system caused by the commonly used downconversion organic dyes or QDs. The cross-talk between the donor and acceptor absorption and/or emission spectra probably disables the detection of the weak FRET signals. A significant overlap between these spectra could lead either to direct excitation of the acceptor by the excitation light of the donor or to incomplete discrimination between acceptor and donor emissions. Another limiting factor in traditional FRET is that the background autofluorescence of biological materials caused by the excitation light could disable the detection of weak FRET signals. Such drawbacks limit the efficiency and feasibility of FRET and could be overcome by using UCNPs as donors because of their large anti-Stokes shifted and narrow-band emission. As a derivative of FRET, the working principle of upconversion luminescence RET (LRET) is schematically introduced in Fig. 9. The group of Soukka has performed several studies on UCNP-based LRET bioassays [200, 212–215]. In 2005, they developed a novel homogeneous upconversion LRET assay technology and its potential was well demonstrated [200]. Since then they applied this technology in many applications, such as immunoassay for E2 (17$\beta$-estradiol) in serum [212], enzyme activity assay [214], dual-parameter DNA hybridization assay [215]. A highly sensitive nucleotide sensor has also been exploited with a detection limit of 1.3 nm [201, 216]. Very recently, UCNP-based LRET was used to perform detection of Matrix Metalloproteinase, which is a very important biomarker in blood, while, also challenging for sensitive and selective detection [211]. These examples clearly demonstrate that upconversion LRET can extend the applications of FRET technique and enable the realization of effective and highly sensitive assays to be utilized in diagnostic applications and also in high-throughput screening approaches. As a donor, UCNPs with two-photon emission processes have a relatively low quantum yield compared to the downconversion donors of traditional FRET. Further enhancement of the UCNP luminescence will improve the detection limit of the UCNP-based LRET.

### 6.2. Optical thermometry

As a property of the Boltzmann distribution, the relative intensity of the different emission bands of UCNPs will be dependent on the surrounding temperature. For this reason, UCNPs have been proposed as sensitive nanothermometers. For the UC emission bands originating from two states in close proximity, separated by an energy gap of $\Delta E$ (usually on the order of several hundred wavenumbers), a thermal equilibrium exists governed by the Boltzmann factor [217]:

$$\frac{I_1}{I_2} = C \cdot \exp(-\Delta E / kT), \tag{3}$$

where $I_1$ and $I_2$ are the integrated intensities of the emissions from the higher state and the lower state, respectively; $C$ is a constant which depends on the degeneracy, spontaneous emission rate, and photon energies of the emitting states in the host materials; $k$ is the Boltzmann constant, and $T$ is the absolute temperature. Up to date, several emission bands of different activators have been used in temperature sensing, including the green emission bands of $Er^{3+}$ [219–225] and $Ho^{3+}$ [226], red emission bands of $Er^{3+}$ [227], and blue emission bands of $Tm^{3+}$ [228]. In addition, the ratio between two well-separated emission bands has also been used as temperature-sensitive measurables [218, 229]. A theoretical model is, however, needed to evaluate such information.

Recently, optical thermometry based on UCNPs has been used in cell models. Vetrone et al. [217] reported the use of green UC emissions from $NaYF_4:Yb^{3+}, Er^{3+}$ nanoparticles for temperature sensing in HeLa cervical cancer cells (Fig. 10(a)). In this study, the excitation light at 920 nm with excitation intensity well below 0.5 kW/cm$^2$ was used in order to avoid any pump-induced heating. Fischer et al. [218] reported the use of the same kind of nanoparticles for temperature sensing in human embryo kidney cells (Fig. 10(b)).

It is worth pointing out that the ratiometric optical thermometry using UCNPs, although reliable, is primarily applicable for superficial imaging. When the UCNPs are embedded in biological tissue, the luminescence light will be spectrally distorted by absorption and scattering of the tissue. The intensity ratio of two emission bands can thus not directly be related to a temperature. In addition, considering different power-density dependencies of various UC emission bands, even in superficial imaging, optical thermometry based on the use of two well-separated UC bands

 

REVIEW ARTICLE



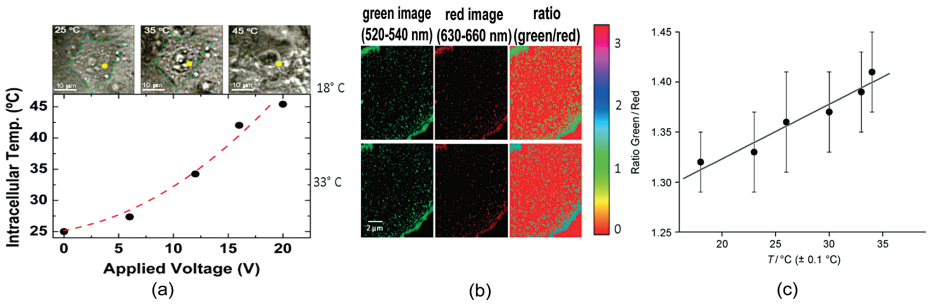


**Figure 10** (online color at: www.lpr-journal.org) Temperature sensing using $NaYF_4$ :$Yb^{3+}$, $Er^{3+}$ nanoparticles in cell models. (a) Top: Optical transmission images of an individual HeLa cell at three inner temperatures. Cell death is observed at 45°C. Bottom: Temperature of the HeLa cell, determined by the fluorescence intensity ratio of the $NaYF_4$ :$Yb^{3+}$, $Er^{3+}$ UCNPs at 525 and 545 nm, as a function of the applied voltage. (b) Temperature-dependent images of human embryo kidney (HEK) cells transfected with $NaYF_4$ :$Yb^{3+}$, $Er^{3+}$ UCNPs showing sub-micrometer resolution. (c) Calibration plot for the temperature-sensitive nanoparticles inside HEK cells (Adapted with permission from ref. [217] and [218]. Copyright 2010, 2011, Wiley-VCH Verlag GmbH & Co. KGaA, Weinheim, and American Chemical Society.)

is difficult because of a general lack of adequate control of the excitation intensity.

### *6.3. Optical Microscopy*

Photoluminescence microscopy using either organic dyes or fluorescent nanoparticles can offer high resolution and sensitivity, thus constituting a powerful tool for biological studies as well as clinical medical applications. Microscopy techniques vary a lot depending on the involved emissive features. Due to their unique properties, UCNP-based microscopy exhibits a lot of advantages over other traditional fluorophores.

#### 6.3.1. Ideal properties for single molecule imaging

Due to the multiphoton excitation process involved, UCNP-based microscopy can yield high resolution images under CW excitation. In most cases, a Gaussian beam of light is used to excite the emissive samples and this Gaussian intensity profile (unsaturated level) of the excitation beam can be expressed as

$$I_{ex}(r) = I_0 \cdot \exp\left(\frac{-2r^2}{\omega_0^2}\right) \qquad (4)$$

where $r$ is the radial distance from the center axis of the beam, $\omega_0$ the beam waist size, and $I_0$ the center intensity. The power dependence of multiphoton process is nonlinear, which can be seen in Eq. ((2)). Thus the corresponding emission intensity profiles *via* one-photon (linear/conventional fluorescent dyes), two-photon and three-photon processes

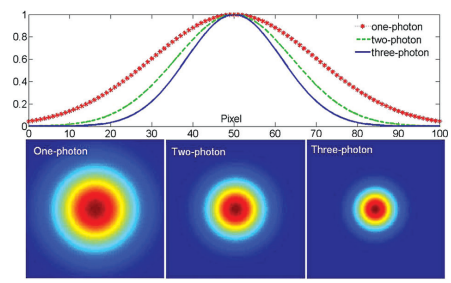


**Figure 11** (online color at: www.lpr-journal.org) Calculated photoluminescence intensity profiles upon excitation by a Gaussian beam for three cases: one-photon (conventional fluorophores), two-photon (red and green emission of UCNP) and three-photon luminescence (blue emission of UCNP).

(nonlinear upconverting nanoparticles) are shown in Fig. 11. Apparently such nonlinear power dependence can be exploited to improve the spatial resolution in microscopy applications. Apart from their anti-Stokes emission characteristics, UCNPs are highly photostable and display non-blinking emission in contrast to quantum dots. Compared with the traditional organic dyes (red and blue emission in Fig. 12c), UCNPs (green emission in Fig. 12c) exhibit exceptional photostability after the same long-time exposure to the excitation [230]. As shown in Fig. 12b the time-resolved emission intensity did not show on/off behavior for single UCNPs [231]. The absence of photobleaching and photoblinking enables rapid and precise tracking of single UCNPs. Thus, individual UCNPs possess such ideal properties suitable for single nanoparticle imaging [72, 126, 231], as shown in Fig. 12d. To use sin-

LASER & PHOTONICS REVIEWS



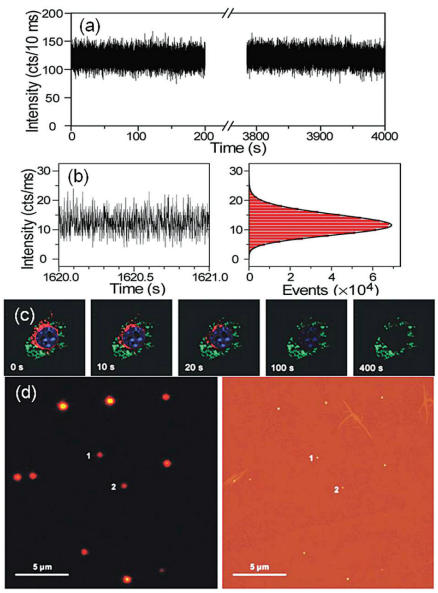


**Figure 12** (online color at: www.lpr-journal.org) Nonbleaching and nonblinking behavior of UCNPs: (a) Photostability of a single UCNP under long-time monitoring; (b) time-resolved emission of UCNP, suggesting no on/off behavior; (c) simultaneous excitations were provided by CW lasers at 405, 543, and 980 nm with powers of approximately 1.6, 0.13, and 19 mW in the focal plane, respectively; (d) Single particle imaging of UCNPs: luminescence image (left) and AFM image (right) of the UCNPs dispersed on the cover slip.(Adapted with permission from Refs. [72, 230, 231], Copyright 2009, National Academy of Sciences, American Chemical Society and John Wiley & Sons, Inc.)

gle UCNPs for probing single proteins, the particles should be small enough in order not to affect the protein itself. However, smaller nanoparticles also means less emission light. Very recently, Ostrowskigrow et al. [126] reported on the successful synthesis of light-emitting nanocrystals small enough not to disrupt cell activity but bright enough for single detection, enabling single protein imaging. This breakthrough will broaden the applications of UCNPs, such as mapping single proteins moving through a cell, neurons cell interaction, and the process in brain cells connecting together to form a synapse.

With the merit of single particles imaging, UCNP can be envisaged as a superresolution probe. Generally, superresolution can be realized using centroid localization and computer rendering as long as the detected light spots in the microscopy field of view are confirmed from single or separate nanoparticles. It is well known that photoswitchable emission or blinking behavior are the paramount for successful excitation of a single fluorophore molecule in organic dyes or a single QD in superresolution imaging systems (e.g., PALM (photoactivated localization microscopy), STORM (stochastic optical reconstruction microscopy)) [232, 233]. For the case of multiple UCNPs in close proximity of each other, differentiation is not possible due to the fact that they have no dark/activate states or stochastic blinking. To develop other time-division mechanisms for exciting UCNPs is challenging but required to address this problem. Different from single-molecule-imaging based superresolution microscopy, STED (stimulated emission depletion) and SIM (structure illumination microscopy) superresolution technologies break through the diffraction limit optically instead of using photobleaching or blinking properties [234, 235]. It is reasonable to envisage that UCNP with many unique optical properties can be an ideal probe for these modalities.

### 6.3.2. *In vitro* non-specific imaging for cells

In 1999, Zijlmans et al. [8] demonstrated for the first time UCNP-based high-contrast bioimaging. In their work $Y_2O_2S:Yb^{3+}/Tm^{3+}$ particles were used to study the distribution of prostate specific antigen in paraffin-embedded human prostate tissue. At that time, the size of upconversion particles was in the range of hundreds of nanometers, and surface modification engineering was in its infancy. In recent years, with the improvement of the UCNP performance, UCNP-based microscopy techniques have been widely exploited for high-resolution and high-contrast imaging of cellular specimens. Non-targeting UCNPs are found to be attached to the membrane or to be endocytosed by various cell lines incubated with those UCNPs. In 2008, Nyk et al. [82] successfully employed MSA-UCNPs to label Panc 1 cells to produce high-contrast images. PEG and some polymers modified UCNPs can also be utilized for *in vitro* nonspecific cell imaging [236]. For non-specific binding, two main interaction mechanisms are electrostatic interactions and ligand interactions with cell membranes. Non-specific binding depends on the charge and hydrophobicity of a ligand, but the dependence has not yet been clarified. Very recently, Jin et al. [181] prepared three types of polymer-coated UCNPs, which resulted in the discovery that positively charged PEI-UCNP have enhanced cellular uptake, more than its neutral and negative counterparts as shown in Fig. 13(b)–(d). UCNPs doped with RE elements could induce autophagy in HeLa cells and it is a common biological effect for RE elements with this process being dose and time dependent [208]. Nonspecific binding can, however, also occur for molecules or cell lines of no interest for the study, and thus this process is not suitable for targeted diagnosis and therapy.

### 6.3.3. *In vitro* specific imaging for cells

Having obvious advantages over non-specific binding imaging, specific imaging of tumor cells has been

 

REVIEW ARTICLE

Laser Photonics Rev. **7,** No. 5 (2013) 

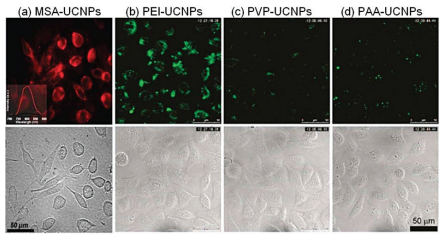


**Figure 13** (online color at: www.lpr-journal.org) (a) MSA-UCNP-incubated non-specific cell imaging; (b)–(d) Charge-dependent cellular imaging (PEI-UCNPs, PVP-UCNPs, PAA-UCNPs); photoluminescence images (upper row) and bright field images (bottom row).(Reprinted with permission from Ref. [82]. Copyright 2008; [236], Copyright 2009, American Chemical Society.)

widely studied using surface-functionalized UCNPs *via* biomolecular recognition. In 2009, Wang et al. [189, 198] proposed anti-CEA8 conjugated UCNPs to perform cell imaging. Zhan et al. [139] have recently performed a set of solid control experiments and demonstrated that $NaYF_4$:$Yb^{3+}$/$Er(Ho)^{3+}$ nanoparticles conjugated with anti-CEA8 antibody can be utilized for highly specific binding and imaging of HeLa cells with antigen expressed on the cell membrane, as shown in Fig. 14. In their report, the as-synthesized OA-capped UCNPs were first rendered aqueous dispersible through MSA encapsulation. Then negatively charged MSA-UCNPs were further polymer-coated through physical adsorption by positively charged PAH, which allows for antibody protein bioconjugation. Other representative work have been reported by Zhang et al. [177, 187], where FA-modified UCNPs were introduced to specifically bind to the folate receptor overexpressed by cancer cells for targeted imaging. High-affinity polypeptide have in recent years been shown to be effective agents for probing biological systems with high specificity. Utilized as peptides, RGD-conjugated UCNPs have been successfully used for cell targeted imaging [199,237]. Yu et al. [202] conjugated PEI-coated $NaYF_4$: $Yb^{3+}$, $Er^{3+}$/$Ce^{3+}$ with recombinant chlorotoxin – a typical peptide neurotoxin that could bind with high specificity to many types of cancer cells – and incubated the modified UCNPs with C6 glioma cells for targeted imaging. Utilized as target agents, UCNPs could also be nanocarriers and indicators for some molecules and drugs. In a recent report, Zhang et al. [238, 239] used UCNPs for the intracellular investigation of small-interference (siRNA) in living cells. Their results have shown that UCNPs are capable of delivering and tracking siRNA.

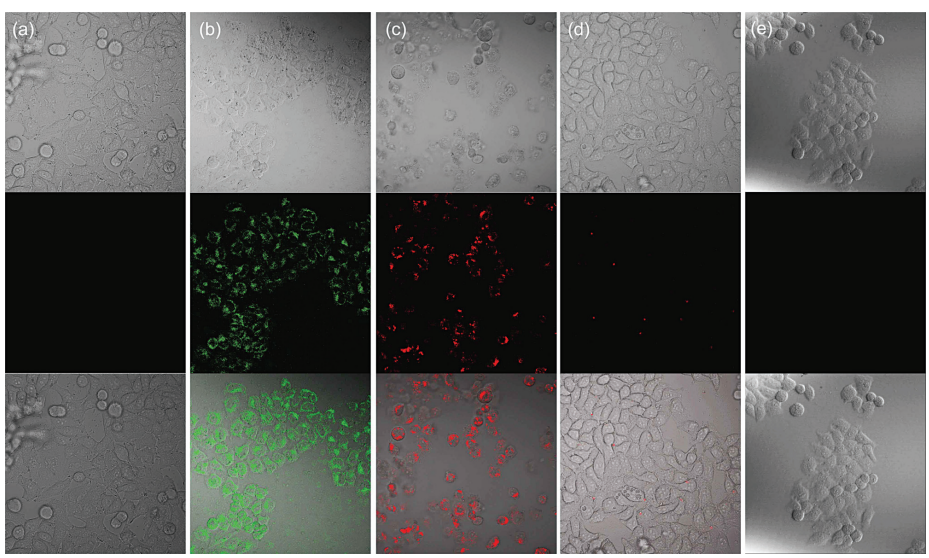


**Figure 14** (online color at: www.lpr-journal.org) In vitro cancer cell imaging using 915-nm laser-excited UCNPs: images of HeLa cells separately incubated with (a) blank, (b) anti-CEA8-$NaYbF_4$:$Yb^{3+}$/$Ho^{3+}$, (c) anti-CEA8-$NaYbF_4$:$Yb^{3+}$/$Er^{3+}$, (d) $NaYbF_4$:$Yb^{3+}$/$Er^{3+}$, and (e) anti-CEA8-$NaYbF_4$:$Yb^{3+}$/$Er^{3+}$ in the presence of 10-fold excess unlabeled antiCEA8. Bright field images (upper-row), photoluminescence images (middle-row) and superimposed images(bottom-row). (Reprinted with permission from Ref. [139]. Copyright 2011, American Chemical Society.)

LASER & PHOTONICS REVIEWS



In principle, the long lifetime in emissive organic dyes and nanoparticles would result in a relatively low photoluminescence intensity under the unsaturated power density level. Due to very long phosphorescence lifetime (millisecond to microsecond) and relatively low QY, UCNP-based microscopy requires relatively low scanning speed to obtain high lateral resolution [240]. Saturated excitation could speed up the scanning while preserving the same lateral resolution. However, in this case it is difficult to obtain a satisfactory axial resolution as the 3D sectioning ability of multiphoton processes will be significantly affected. Another drawback of UCNP-based laser scanning microscopy is that in the cases of 3D spatial scanning, emission wavelength scanning or real-time monitoring, the cell sample has to be exposed to excitation for several minutes or even hours of time [139]. Thus, it is not possible to record very quick bioprocesses. Wide field microscopy could be an alternative method for time-consuming laser scanning upconversion microscopy [82, 240]. Up to date, almost all excitation wavelengths for UCNP applications were selected around 980 nm. It is worth pointing out that light around 980 nm suffers from an intrinsic disadvantage: water – being the most significant ingredient of animal and human body – heavily absorbs light around this wavelength. In the cases of long-time scanning, the excitation light of 980 nm can significantly heat up the cell growth medium, which probably results in damage to the cells, as shown in Fig. 15. Alternatively, Zhan et al. have proposed the use of excitation light around 920 nm (where the optical absorption coefficient of water is much lower and the excitation can still occur effectively) to replace 980-nm light in order to avoid cell damage [139].

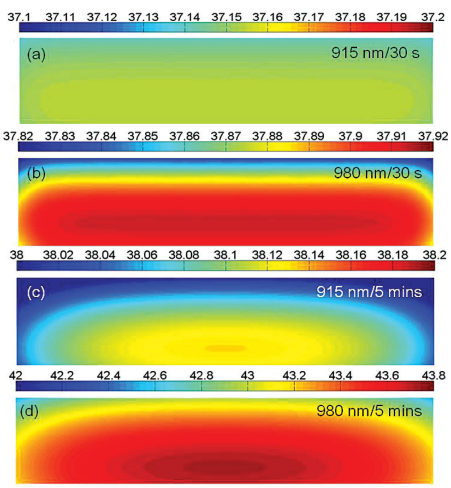


**Figure 15** (online color at: www.lpr-journal.org) Calculated results of cell-in-celldish imaging model: excitation laser induced temperature elevation (°C) after (a, b) 30 s and (c, d) 5 min of irradiation with (a, c) a 915 nm laser and (b, d) a 980 nm laser(power 300mW).(Adapted with permission from Ref. [139]. Copyright 2011, American Chemical Society.)

### *6.4. Diffuse optical imaging*

As is the case for novel microscopy techniques, deep-tissue diffuse optical imaging (DOI) has over the last decades also attracted an increasing amount of attention [241–244]. Compared with conventional non-invasive imaging systems, such as X-ray computed tomography (CT), magnetic resonance imaging (MRI), and Positron emission tomography (PET), optical imaging systems are fast, compact and very sensitive to luminescent contrast agents. However, due to the relatively high scattering and absorption of light in tissue, the penetration depth is typically limited to $\leq 10$ cm [243, 245]. Although the penetration depth may seem to be a severe limitation, DOI has already been applied to monitor a wide range of biological processes and systems in both small animals and humans. In small animals, DOI has, for example, been used to follow the development in time of Alzheimer's disease [246], brain metabolism [247], proteases [248] and various drug effects [249]. In humans, DOI has, for example, been employed to monitor and detect breast cancer tumors [250–254], brain activity and brain metabolism [252, 255]. However, the images obtained from DOI techniques can be of relatively poor quality due to a number of reasons, including endogenous background tissue autofluorescence, the diffusive nature of light propagation in tissue, and the ill-posedness of the mathematical problem formulation. In this section, we will focus on luminescence/fluorescence diffuse imaging, and in particular luminescence/fluorescence diffuse optical tomography (LDOT/FDOT) and discuss how the upconversion luminescence (UCL) of UCNPs can be applied to obtain images of superior qualities as compared to conventional Stokes-shifting contrast agents.

#### 6.4.1. Autofluorescence of tissue

Biological tissue contains a large number of endogenous fluorophores. The fluorophores can either be components of the tissue structural matrix, for example, collagen and elastin, or be formed during metabolism processes, for example, nicotinamide adenine dinucleotide (NADH) and flavins [256, 257]. Although the fluorophores are individually well known, any given tissue, however, typically consists of a mixture of a large number of endogenous fluorophores. The distribution and optical characteristics of the fluorophores within the tissues are not only dependent on the tissue type, but also on the chemical environment as well as the metabolic state at the cellular level. By measuring the changes in the autofluorescence spectra, it is possible, for example, to perform cancer diagnostics [258–260]. However, for diffuse optical imaging, and in particular

 

REVIEW ARTICLE

Laser Photonics Rev. **7,** No. 5 (2013) 

luminescence diffuse optical imaging employing an exogenous contrast agent, the ever-present tissue autofluorescence will certainly deteriorate the signal-to-background ratio and limit the sensitivity of the system, and can at the same time cause severe artifacts in the reconstructed tomographs [261].

In order to obtain accurate representations of the fluorophore distribution as well as to increase the sensitivities, significant efforts have been invested to develop methods to overcome the tissue autofluorescence. Suggested approaches include subtraction-methods which model the tissue autofluorescence [262], time-domain separation using fluorophores with suitable lifetimes [263], spectral unmixing and multispectral methods [264, 265], transillumination and normalized approaches [266], and large Stokes-shifting markers, such as QDs [265, 267]. Although these methods can reduce the effects of unwanted tissue autofluorescence, they are usually associated with complex instrumentation and heavy computational needs. The use of UCNPs can, however, completely eliminate the tissue autofluorescence since the emission from endogenous fluorophores is Stokes shifted, as shown in Fig. 16 [19, 38, 199, 236]. As illustrated in Fig. 17, this will significantly reduce the numbers of artifacts in the particularly sensitive LDOT problem [268, 269]. Furthermore, in contrast to the approaches discussed above, a system using UCNPs is very straightforward to implement and does not require any complex instrumentation in terms of, for example, excitation-light rejection due to the large anti-Stokes shift and the narrow bandwidth of the emission.

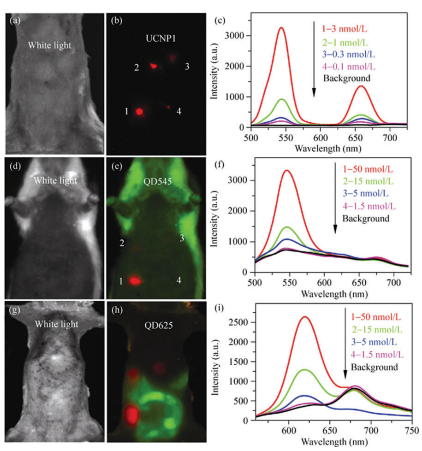


**Figure 16** (online color at: www.lpr-journal.org) Comparison of imaging sensitivities between UCNPs and QDs: (a) a white light image of a mouse subcutaneously injected with various concentrations of UCNP1; (b) an in vivo UCL image of the injected mouse; (c) UCL emission spectra recorded at the injection sites; (d) and (g) white light images of mice subcutaneously injected with QDs; (e) spectrally-resolved fluorescence images of a QD545-injected mouse and (h) a QD625 injected mouse (red and green colors represent QD fluorescence and autofluorescence, respectively); (f) and (i) fluorescence spectra recorded at the QD injection sites (the fluorescence spectra of 1.5 nmol/L QDs were nearly identical to the background spectra). (Reprinted with permission from Ref. [236]. Copyright 2010, Tsinghua University Press and Springer-Verlag Berlin Heidelberg.)

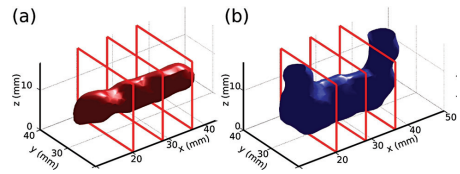


**Figure 17** (online color at: www.lpr-journal.org) LDOT reconstruction of two cylindrical luminescent targets in a tissue phantom. (a) Reconstruction using UCNPs. (b) Reconstruction using rhodamine 6G. It is demonstrated that the presence of even a weak autofluorescent background can cause severe artifacts in the tomographic reconstructions due to the ill-conditioned mathematical formulation. (Reprinted with permission from Ref. [269]. Copyright 2009, American Institute of Physics.)

### 6.4.2. Improving image quality by exploiting the nonlinear power dependence

In addition to the anti-Stokes shifted emission, it has been shown that the nonlinear power dependence of the UC emission can be further exploited to enhance both the quality and the contrast of the resulting images. Since the emissions utilized in diffuse imaging correspond typically to two-photon processes, this can be used to confine the excitation volume, leading to an increase in the spatial resolution. The enhancement of the spatial resolution has been demonstrated for the case of diffuse planar imaging [270] as well as LDOT [151] (Fig. 18). Related to the case of microscopy, the improved spatial resolution can be explained by considering the sensitivity profiles for a given source-detector pair, shown in Fig. 19. It is clear that a multi-photon process will cause a confinement of the sensitivity profiles, thus effectively resulting in selective excitation of each individual luminescent target within the medium. From Fig. 19, it can also be realized that not only will the lateral resolution be improved, but also the axial resolution. This is due to the fact that the resolution strongly depends on the gradient in the sensitivity profiles, and such sharp gradients can be found along all spatial dimensions when nonlinear fluorophores are employed.

An interesting aspect of the nonlinear power dependence of the UCNPs is their potential to increase the information density from a given volume by carefully designing the excitation scheme to include multi-beam excitation. This was demonstrated by Liu et al. [271], where it was shown that the use of two excitation beams

LASER & PHOTONICS REVIEWS



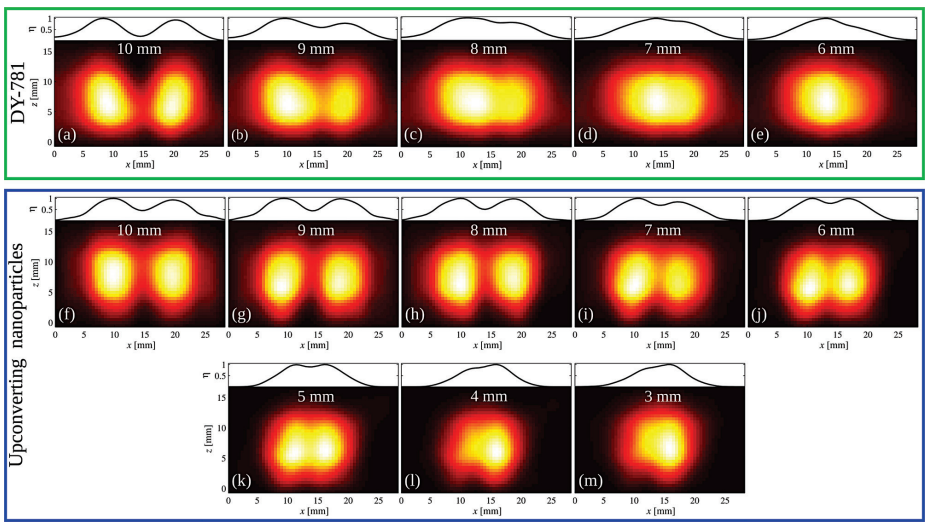


**Figure 18** (online color at: www.lpr-journal.org) Experimental results demonstrating that due to the two-photon-dependent emission, the use of UCNPs can significantly increase the ultimate spatial resolution obtainable in LDOT. The experiments were carried out in tissue phantoms, and two glass tubes filled with either DY-781 dye or UCNPs were placed with different center-to-center separation to evaluate the spatial resolution obtained. (Reprinted with permission from Ref. [151]. Copyright 2012, American Chemical Society.)

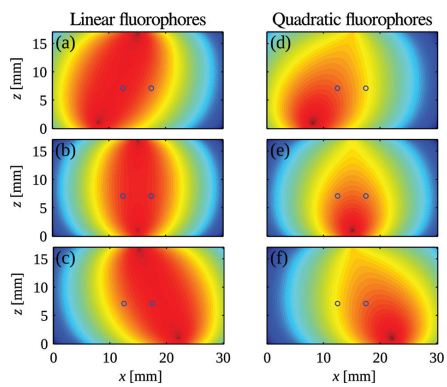


**Figure 19** (online color at: www.lpr-journal.org) Simulated sensitivity profiles for three different source positions and a fixed detector position. The sharp gradients associated with UCNPs (quadratic luminescence markers), enable LDOT reconstructions with superior spatial resolutions as compared with conventional fluorophores (linear luminescence markers). (Reprinted with permission from Ref. [151]. Copyright 2012, American Chemical Society.)

results in a luminescence intensity which can be expressed as

$$\Gamma \propto (I_1 + I_2)^2 = I_1^2 + I_2^2 + 2I_1I_2, \tag{5}$$

where $\Gamma$ is the detected luminescence intensity and $I_{1,2}$ denote the excitation intensities of the two beams. It can be seen that in contrast to conventional linear fluorophores, the use of two excitation beams for a quadratic luminescent marker results in a cross term which contains additional information of the distribution. Figure 20 shows the effect of including the cross term in the reconstructions, which makes clear that the inclusion of the cross term results in a much more correct representation of the true UCNP distribution. Furthermore, by using even more excitation beams, it should be possible to extract additional orthogonal information. Although the benefits may diminish and the system complexity will increase for more excitation beams, this approach should still be very relevant for measurements on small surfaces, such as those found on mice. Using the UCNPs, even a small surface can provide sufficient data for an accurate reconstruction, whereas the amount of orthogonal data points while employing a conventional fluorophore may be very limited.

 

REVIEW ARTICLE



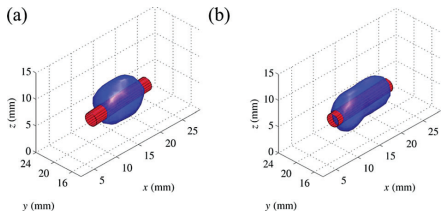


**Figure 20** (online color at: www.lpr-journal.org) Experimental results demonstrating that a dual-beam excitation scheme can be used for UCNPs to extract additional spatial information facilitating FDOT reconstructions of higher qualities. (a) Single-beam setup. (b) Dual-beam setup. (Reprinted with permission from Ref. [271]. (Copyright 2010, Optical Society of America).

### 6.4.3. Improving the penetration depth and avoiding overheating

As has been previously discussed, few reports present the efficiency of UCNPs in absolute terms [50, 151]. However, it is relatively safe to conclude that compared with conventional dye molecules, the QY of UCNPs is usually a few orders of magnitude lower. In most cases, the absence of background tissue autofluorescence will still produce images that are superior to those produced with autofluorescence-sensitive fluorophores. However, the maximum depth that can be imaged while employing UCNPs is of course ultimately limited by the QY as well as the attenuation of the excitation and the emission light in biological tissue. As previously mentioned, the most commonly excitation light (975 nm) can be strongly absorbed by the water in tissue, which may result in limited penetration depth as well as overheating. It is of importance to systematically investigate these issues in order to optimize UCNP-based optical imaging. Recently, it has been demonstrated that by shifting the excitation wavelength to the absorption band of $Yb^{3+}$ at 915 nm, it is possible to increase the penetration depth as the absorption of water is lower than the typically employed absorption band at 975 nm [139]. The experimental and calculated results shown in Fig. 21 both confirm that 915 nm laser excitation is advantageous for deep tissue imaging as compared to 980-nm laser excitation. This is highly relevant when imaging tissue types which contain a high water content, not only to increase the penetration depth but also to avoid the need of excessive laser intensities that may cause tissue heating and damage [159]. The possible overheating effect induced by 980-nm laser irradiation during UCNP-based diffuse imaging was computationally and experimentally studied by Zhan et al. [139]. As shown in Fig. 22, the *in vivo* experimental results of a mouse show that overheating of the mouse can clearly be induced by 980-nm laser irradiation, which can be effectively overcome by using a 915 nm laser. However, it is worth to point out that the absorption of $Yb^{3+}$ at 915 nm is significantly lower and thus the shift of the excitation wavelength is most relevant for water-dense tissues at depths greater than approximately 1.5 cm. The current limitation in absorption motivates the further development of UCNPs. If a more efficient upconversion process can be enabled in the 915-nm region, the penetration depth could be enhanced by several times as compared with excitation at 975 nm.

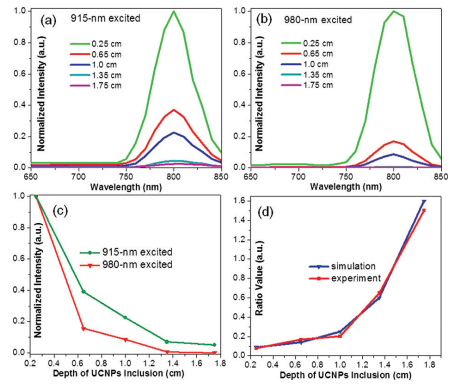


**Figure 21** (online color at: www.lpr-journal.org) Comparison of the UCNP photoluminescence intensity under excitation by 915 nm and 980 nm, respectively, for different UCNP inclusion depths. It is shown that the intensity decreases much slower under excitation by 915 nm (a) as compared to 980 nm (b). (c) Line plots showing the intensity as a function of depth for fixed excitation conditions. (d) Ratio of the absolute photoluminescence intensity under excitation by 915 nm and 980 nm, respectively. (Reprinted with permission from Ref. [139]. Copyright 2011, American Chemical Society.)

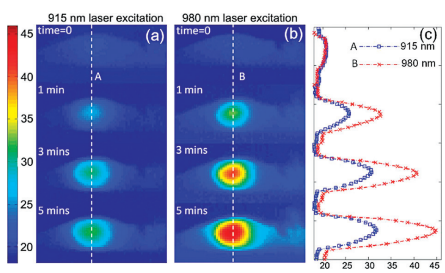


**Figure 22** (online color at: www.lpr-journal.org) *In vivo* temperature (°C) monitoring for (a) a 915-nm laser irradiated mouse and (b) a 980-nm laser irradiated mouse and (c) the corresponding temperature line profiles (curve A and B in (c) corresponding to line A in (a) and line B in (b), respectively). The experiment was performed under a stable room temperature of 18 °C. (Reprinted with permission from Ref. [139]. Copyright 2011, American Chemical Society.)

LASER & PHOTONICS REVIEWS



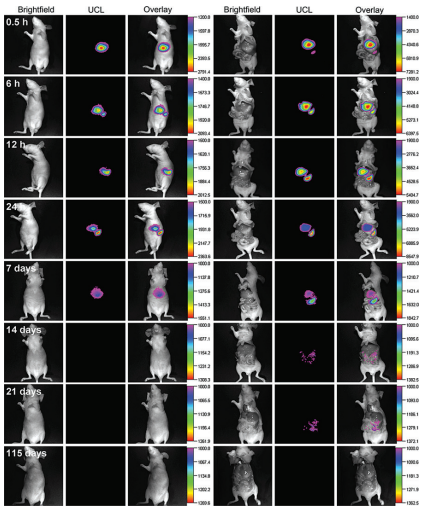


**Figure 23** (online color at: www.lpr-journal.org) Real-time *in vivo* upconversion luminescence (UCL) imaging of athymic nude mice with intravenous injection of PAA-UCNPs (15 mg/kg) at different time points. Column 3: overlays of UCL and brightfield images of mice. Column 6: overlays of UCL and brightfield images of dissected mice. (Reprinted with permission from Ref. [205]. Copyright 2010, Elsevier Ltd.)

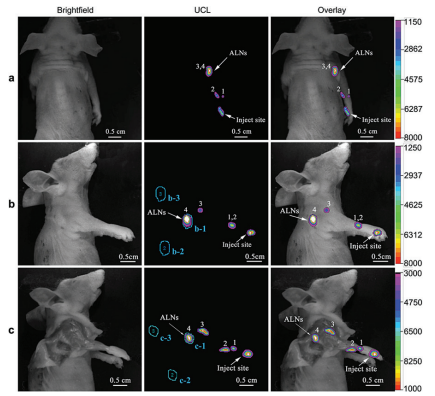


**Figure 24** (online color at: www.lpr-journal.org) *In vivo* lymphatic drainage UCL imaging at 800 nm was clearly detected at four different draining lymph basins (1, 2, 3, 4) along the right antebrachium of the nude mouse. Detection of upconversion luminescence in the different positions, prostrate (a) or lateral (b) position, after injection of 20 mL (1 mg/mL) UCNPs-OAAA into the paw of the nude mouse for 20 min. (c) The lymphatic drainage UCL imaging after removal of skin and fatty tissues was also measured. All images were acquired under the same instrumental conditions (power density of 120 mW/cm$^2$ and temperature at 25 °C on the surface of the mouse). The mean luminescence intensity of the regions of interest (blue areas) of ROI 1 (specific uptake), ROI 2 (nonspecific uptake) and ROI 3 (background) were selected for the *in vivo* SNR calculation. (Reprinted with permission from Ref. [274]. Copyright 2011, Elsevier Ltd.)

### 6.4.4. Small-animal imaging

The rapid development of UCNPs has made them viable for employment in *in-vivo* small-animal imaging. To date, several aspects within small-animal imaging have been studied with the use of UCNPs. Early studies involved imaging of subcutaneous injections [139, 272], and biodistribution of UCNPs. Salthouse et al. [273] studied the accumulation of UCNPs in mice following a tail vein injection and showed that PEG-coated UCNPs with no specific targeting accumulate primarily within the liver and spleen of the animals. This was later confirmed by Xiong et al. [205] using polyacrylic acid (PAA) modified UCNPs, see Fig. 23. In addition, long clearing times were found and the UCNPs could still be observed 7 days post injection in an *in-vivo* setting [205].

Mapping of the lymphatic systems within small animals is another research topic that has been of great interest for UCNPs. Knowledge of the lymphatic system is important to predict the spread of certain kinds of cancer metastasis. Due to the small sizes of the sentinel nodes, it can be difficult to accurately detect and quantify the distribution of fluorophores if autofluorescence is present. Thus, UCNPs are very promising for this application where imaging of the lymphatic vessels and lymphatic nodes has been demonstrated [236, 274, 275]. As demonstrated in Fig. 24, by using UCNPs codoped with different RE ions, it is possible to optically separate injections at different times and sites with virtually no cross talks, enabling means to probe and separate movement speeds.

For targeting of specific tissue types, such as cancer tumors, several approaches exist. The use of FA to label UCNPs for the targeting of folate receptor overexpressing cell lines, for example, HeLa and KB, is among the first to be employed in an *in vivo* setting [177]. Using nude mice bearing a HeLa tumor on the hind leg, it was demonstrated that specific targeting could be achieved and imaged *in vivo* after intravenous injection of the UCNPs. Other reports on targeting methods include peptide labeling, which could provide a more efficient uptake *in vivo* [199, 202]. The specificity was found to be very good and the lack of background tissue autofluorescence resulted in SNRs which were comparable with those found in bioluminescence imaging.

The long-time stability of UCNPs in biological environments has also enabled the possibility to perform live cell tracking of transplanted cells in an animal [112]. Traditionally, cell monitoring of transplanted cells is performed

 

REVIEW ARTICLE

Laser Photonics Rev. **7,** No. 5 (2013) 

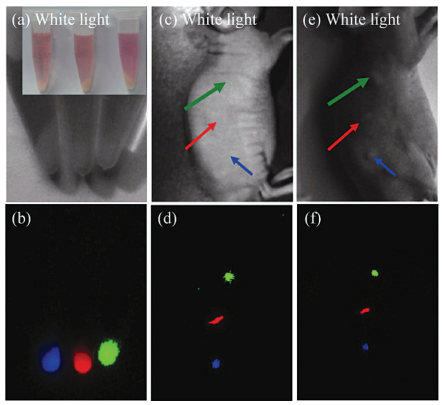


**Figure 25** (online color at: www.lpr-journal.org) Multicolor *in vivo* cancer cell tracking and imaging. White light (a) and UCL (b) images of KB cell (a human carcinoma cell line) pellets after incubation with three colors of UCNPs for 24 h. Excess UCNPs were completely removed by extensive washing. Substantial cellular uptake of UCNPs was evidenced by the bright UCL signals from the cell pellets. White light (c) and UCL (d) images of a nude mouse immediately after subcutaneous injection with three KB cell suspensions labeled by different colors of UCNPs. White light (e) and UCL (f) images of the same mouse one week after cancer cell injection. Three tumors developed on the injected sites and were clearly visualized by the three-color UCL imaging. (Reprinted with permission from Ref. [236]. Copyright 2010, Tsinghua University Press and Springer-Verlag Berlin Heidelberg.)

using histology since the staining agents used typically operate within the UV–blue range of the spectrum. As known, light at these wavelengths has extremely high attenuation and thus *in-vivo* imaging is difficult except for very superficial targets. In addition, these dyes are highly sensitive to photobleaching, which sets a limit on the time span for longitudinal studies in contrast to the stable UCNPs. Idris et al. [112] first demonstrated the use of UCNPs for both *in-vitro* and *in-vivo* tracking of stem cells over a time span of more than one week using confocal microscopy. On the macroscopic scale, Cheng et al. [236] have shown that human cancer cells can be tracked after injection into an animal and the further development of the tumor itself can also be monitored (Fig. 25).

## 6.5. Photodynamic therapy

Photodynamic therapy (PDT) is a treatment modality that has gained clinical acceptance and is now in many places a first line treatment for selected indications, including non-melanoma skin cancer [276]. For other indications, PDT is still being developed and evaluated. In particular, efforts are made towards developing PDT for solid and deeply located malignancies [277,278], antibacterial and anti-fungal treatment [279,280].

Another area of great interest in connection to photodynamic actions is drug delivery. Berg et al. [281, 282] have developed photochemical internalization (PCI) as a technique to assist drug delivery into cells. Photodynamic reactions are used here to destroy the membrane of a vesicle after endocytosis, and consequently to release its content into the intracellular liquid.

Recently, a number of studies have been conducted to evaluate whether UCNPs could be beneficial for PDT, especially due to the long excitation wavelength which provides good light penetration. Commonly used drugs for PDT typically require light in the visible region, however, the penetration depth at these wavelengths is clearly a limiting factor. The strong need to shift the excitation wavelength to the NIR region is therefore motivated. The optimal region for penetrating biological tissue resides around 800 to 1 μm. However, these NIR photons have too low energy to generate $^1O_2$. Efforts have been invested into using two-photon absorption to enable the use of NIR photons for PDT [283]. Unfortunately, the usefulness of this technique for deep-tissue PDT is limited by the required intensities for two-photon absorption. As UC processes in UCNPs are efficient, they should be more suitable for the use of deep-tissue PDT as compared to two-photon dyes. The use of UCNPs for PDT was already reported in 2007 by Zhang et al. [194]. The obtained efficiency for generation of $^1O_2$ was, however, very low, although it was envisaged that the rapid development of UCNP materials in general will significantly enhance the efficiency. Several approaches have since been developed to obtain sufficient efficiency to enable deep-tissue PDT [187, 188, 284–287]. These approaches include the encapsulation of the photosensitizer within mesoporous nanoparticles to overcome the hydrophobic properties of many photosensitizers, thus enabling a broader range of photosensitizer drugs. However, most demonstrations have been on cell plates in a microscopic environment and further studies are certainly required to investigate the applicability of deep-tissue PDT using UCNPs.

### 6.5.1. Dosimetry

For deep-tissue PDT with the currently available photosensitizers, it is of utmost importance to understand the light-tissue interaction in order to provide a useful dosimetry [288–290]. Various kinds of photosensitizers are available, and we do not intend to review the current state-of-the-art photosensitizers. Instead, using simple calculations, we would like to highlight the importance of understanding light-tissue interaction in order to estimate the outcome of a treatment.

For simplicity, we will assume an infinite homogeneous medium and a conservative light-dose threshold of 1 J/cm$^2$ to reach a satisfactory treatment. The distribution of light for a source of power $P_0$ for steady state diffusion is given

LASER & PHOTONICS REVIEWS



by [291]

$$\phi(r) = \frac{P_0}{4\pi Dr} e^{-\mu_{\text{eff}} r}, \quad (6)$$

where $D = 1/3(\mu_a + \mu_s')$ is the diffusion coefficient, $\mu_a$ the absorption coefficient, $\mu_s'$ the reduced scattering coefficient, $\mu_{\text{eff}} = (\mu_a/D)^{1/2}$, and $r$ denotes the distance from the source. Using this well-known and simple relationship, we will show that the time needed to reach a threshold dose for various $r$, i.e., distances or depths from the source, can be estimated.

We assume that the photosensitizer drug is excited in the red wavelength region (∼660 nm), which coincides well with the emissions of the commonly used activators. By knowing the tissue optical properties at this excitation wavelength, it is thus possible to calculate the light distribution and hence the time needed to reach a threshold dose. In the following, we assume PDT treatment of human prostate tissue with $\mu_a(660\,\text{nm}) = 0.5\ \text{cm}^{-1}$ and $\mu_s'(660\,\text{nm}) = 9\ \text{cm}^{-1}$ [292]. The treatment time needed when using UCNPs will be determined by the absorbed fraction, the QY of the UCNPs as well as the energy transfer efficiency from the UCNPs to the photosensitizers. These numbers are difficult to assess in a general manner, and we assume in these quick estimates that all excitation light is absorbed, an energy transfer efficiency of 1 and a QY that is similar of that presented in Fig. 5. The UC fluence rate can thus be expressed as

$$\phi_{\text{em}} = \phi_{\text{ex}} \eta(\phi_{\text{ex}}) \frac{\lambda_{\text{em}}}{\lambda_{\text{ex}}}, \quad (7)$$

where $\eta$ denotes the QY, and the subscripts ex and em denote the excitation light and the emission light, respectively. Furthermore, we can estimate the optical properties at the excitation wavelength of UCNPs at 975 nm [245,292] to be $\mu_a(975\text{nm}) = 0.7\ \text{cm}^{-1}$ and $\mu_s'(975\text{nm}) = 5\ \text{cm}^{-1}$. Using these values we can then again calculate the treatment time needed to reach a threshold dose for UCNP-mediated PDT.

Figure 26(a) shows the calculated fluence rates of the excitation light at 660 nm and 975 nm, with the inset showing the corresponding QYs for each excitation depth for the UCNPs. The strength of the source was chosen to be 500 mW and the QY of the UCNPs was obtained by a linear fit (in a log-log scale) of the low-intensity values from previously published work [151]. The time needed to reach a threshold dose for direct excitation of the photosensitizer and UCNP-mediated PDT is shown in Fig. 26(b). A few conclusions can be immediately drawn from these results. Firstly, for prostate tissue, the attenuation factor of light at 660 nm and 975 nm is similar. This certainly depends on the tissue type, with prostate tissue being relatively rich of hemoglobin and water. However, even for tissue types with less amount of water and hemoglobin, the difference in the fluence rates between the two excitation wavelengths will still be relatively negligible for depths less than 1 cm. Perhaps the most remarkable result is the treatment time that will be needed if UCNPs are used to excite the photosensitizer drugs. From Fig. 26, it can be seen that the treatment time while using UCNPs will be at least 4 orders of magnitude longer. This treatment time can be shortened by either increasing the excitation fluence rates (for instance by employing a pulsed excitation source) or by increasing the QY of the UCNPs. However, it is quite clear that it is unrealistic to increase either of these factors by several orders of magnitudes directly, especially since the excitation power is already chosen to be very high. It may be possible to use a pulsed light source to keep the average power down, while using the peak power to excite the UCNPs. Pulsed light will allow higher fluence rates in the tissue without causing tissue heating. Ideally one would like to work with fluence rates well above the saturation of the UCNPs, meaning that the QY ideally would be in a region where it is not power dependent. For tissue regions with such high fluence rates, the PDT efficiency will not decrease with depth as quickly, and would have a depth profile more similar to the case of direct excitation of a photosensitizer. However, this approach most probably cannot fully close the gap between direct excitation and UCNP-mediated excitation, as the highest reported QY (obtained under very high intensities) for UCNPs are still on the order of a few percents [50, 151]. Thus, the treatment time while using UCNPs will still be longer than direct excitation for most practical cases.

The efficiency with depth depends on two things, attenuation of the excitation light (in favor for long excitation wavelengths) and the fact that the excitation is a two-photon process for UCNPs and a linear process for conventional PDT drugs (in favor for the linear excitation process). Our simulations clearly indicate that the non-linear excitation process hampers the excitation efficiency more than the gain in better light penetration. This is a very similar observation as for molecular two-photon PDT sensitizers. The calculations above are performed under extremely simplified conditions. Clearly, they are not meant to serve as an accurate representation of the reality, but rather to highlight the trends and needs in order to make UCNP-mediated PDT feasible. The quality and efficiency of UCNPs have been increasing in a very rapid fashion over the last years. Even though the results above may indicate that it is difficult to perform PDT with UCNPs directly, with the ever-increasing knowledge of the UCNPs, and the use of properly pulsed light sources, UCNP-mediated PDT may still be feasible within the foreseeable future.

### 6.6. Multimodality imaging

Multimodality imaging is a research field that has been explored extensively in the last few decades. Until recently, efforts have mainly been invested into the modalities such as X-ray computed tomography (CT), magnetic resonance imaging (MRI), single-photon emission computed tomography (SPECT), positron emission tomography (PET), and ultrasonography [293–296], mainly aiming for molecular imaging. In recent years, the availability of a large numbers of photoluminescent molecules has catalyzed a growing

 

REVIEW ARTICLE

Laser Photonics Rev. **7,** No. 5 (2013) 

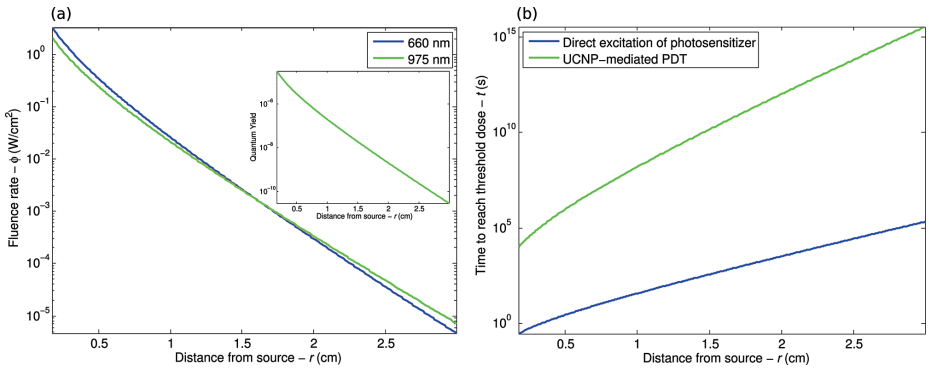


**Figure 26** (online color at: www.lpr-journal.org) (a) Calculated fluence rates within human prostate tissue under excitation by 660 nm and 975 nm, respectively, based on the assumptions given in the text. The inset shows the corresponding QY for the UCNPs (the QY for the photosensitizer at 660 nm is constant) as a function of depth. (b) The treatment time needed to reach the light threshold dose of 1 J/cm$^2$.

interest of enabling optical molecular imaging for multimodal contrast agents [297,298]. The high sensitivity, compactness and speed of optical imaging systems have made luminescence molecular imaging extremely attractive as a compliment to the more established modalities. However, luminescent contrast agents that are optically bright and stable are difficult to find. Thus the luminescent probes on the multimodal contrast agents tend to degrade and bleach, making it difficult to perform truly longitudinal studies in parallel with other modalities. UCNPs, on the other hand, are extremely stable and do not in general suffer from bleaching and aging effects. In addition, since UCNPs are based upon crystal hosts, multimodality imaging can, in some cases, be enabled by modifying the crystal host.

Diffuse optical imaging is often associated with poor spatial resolution, although the use of UCNPs can significantly improve this characteristic [151]. The spatial resolution of CT and MRI are in general higher, however, the information obtained is quite different. While CT and MRI can provide detailed anatomical information, for molecular imaging, luminescent optical contrast agents usually have a much higher sensitivity, comparable with PET. However, while PET can provide detailed pre-operative data, they are not practical for acquiring intra-operative data due to both complexity and the relatively short half lives of the radioactive tracers. In this section, the current state-of-the-art multimodality imaging agents which are based on UCNPs will be discussed.

### 6.6.1. Magnetic-optical imaging

UCNPs have been demonstrated for both $T_1$-and $T_2$-weighted MRI. For $T_1$ imaging, the UCNP crystal can be modified to provide contrast in an MR system directly. For MRI, gadolinium (Gd) has been an extensively used relaxation agent. Indeed Kumar et al. [299] co-doped $Gd^{3+}$ ions into the $NaYF_4$ crystal host of UCNPs, while Park et al. [72] used the $NaGdF_4$ crystal host, with both approaches showing magnetic properties under $T_1$-weighted MRI ($r_1 = 0.14$ s$^{-1}$ mM$^{-1}$ for the co-doping approach and $r_1 = 1.4$ s$^{-1}$ mM$^{-1}$ for the $NaGdF_4$ crystal host approach). The QY of $NaGdF_4$ UCNPs is expected to be comparable to that of $NaYF_4$ UCNPs, however, absolute numbers are seldom reported, which makes it difficult to draw final conclusions on the effects upon the optical efficiency.

Another strategy that can be employed is to use a core–shell structure. For example, Li et al. [300] used $NaYF_4$ cores coated with Si-DTTA-$Gd^{3+}$ shells to generate multifunctional UCNPs for multimodal imaging. This design was motivated as it should yield the most UC efficient core, while high $Gd^{3+}$ payload is achieved on the surface which is suitable for functionalization. Using this approach they report $r_1 = 20.1$ s$^{-1}$ mM$^{-1}$ and $r_2 = 55$ s$^{-1}$ mM$^{-1}$. However, the lack of reports upon the QY makes it once again difficult to obtain absolute numbers in terms of the efficiency.

For *in-vivo* studies, Zhou et al. [183] have shown that $NaGdF_4$:$Yb^{3+}$,$Er^{3+}$,$Tm^{3+}$ UCNPs can be accurately imaged, using both MRI and optical imaging, inside white Kunming mice following an intravenous injection. As expected, the UCNPs were found to accumulate mainly inside the spleen and liver of the animal.

### 6.6.2. Nuclear-optical imaging

Nuclear imaing is extensively used within the field of biology and medicine. PET imaging, for example, can achieve sensitivities down to picomolar range. Recently, the use of multimodal UCNPs for PET imaging was demonstrated [206, 301], thereby the commonly used $^{18}$F isotope was

LASER & PHOTONICS REVIEWS



chosen as the PET agent and very promising *in vivo* experiments were conducted. In addition, Zhou et al. used a gadolinium-based crystal host, thus simultaneously enabling tri-modal imaging (further discussed below). Such multimodal agents may prove to be very useful in future clinical development. However, due to the limited half-lives of the radioactive tracers, it is important to develop reaction processes with high yield. Another aspect that is worth to consider is information orthogonality. It is obvious that the largest gain from a certain contrast agent can be obtained if each modality provides independent information as compared with the other modalities. For the case of PET and UC emission, although the information space may overlap, the time window for acquiring PET data is much more limited as compared with UC emission, however, PET may be able to provide more detailed data.

#### 6.6.3. CT- and trimodal imaging

The high-atomic number associated with the RE elements in the host crystal of UCNPs can lead to effective attenuation of X-rays. Thus, very recently several groups have proposed the use of UCNPs for X-ray CT imaging [302–306]. Ytterbium (Yb) and lutetium (Lu) have received most attention due to their high atomic numbers that match the operating conditions found in CT systems. For the case of Yb, the host material $NaYbF_4$ has been demonstrated to provide contrast superior to iobitridol [302, 304]. Due to the nature of the electron structure within the RE elements, Lu in a similar fashion provides an enhanced CT contrast [304, 306].

Since the attenuation of X-rays is an inherent property of the most efficient crystal hosts, the application of tri-modal imaging (CT/MRI/optical) is often discussed and proposed. Similar to the discussion in section 6.6.1, this can be accomplished either by co-doping the host crystals with Gd or by using a core-shell structure that provides the MRI contrast, such as a Gd shell or an iron shell [303, 305, 306].

It is well known that optical systems are generally compact, fast, inexpensive and easy to operate. Thus, the possibility to perform imaging in multiple modalities can provide new opportunities in the understanding of biological systems. Perhaps even more importantly, the fast screening process enabled by optical imaging systems can lead to a more rapid development of new contrast agents as well as new drugs.

## 7. Challenges and Outlook

As clearly illustrated in this review article, UCNPs have many potential advantages and are extremely interesting for microscopy and *in vivo* applications of diffuse light imaging. Consequently, the use of UCNPs as improved contrast agents for optical bioimaging has grown enormously in just a few years. A main remaining challenge is obviously to make these particles compatible with currently used labeling and imaging technology and to be employed in important biomedical studies. This will require reproducible and commercially available nanoparticles in user-friendly kits and in large quantities. Also corresponding imaging systems must be developed for such applications. Apart from these obvious technical aspects, a few research challenges remain to be solved in order to fully explore the potential of these very promising particles as contrast agents. These challenges as well as ideas about how these could be addressed will be discussed below.

One challenge – despite the strong and rapid development of the particles – is their still relatively low QYs. We believe that this can be partly overcome by utilizing pulsed excitation with pulse lengths that match the relatively long lifetimes of UCNPs, as indicated in our discussion about QY in section 3. A similar case is the use of femtosecond pulsed excitation in two-photon fluorescence microscopy. Since it is known that the QY is power density dependent – as clearly illustrated in Fig. 5 – consequently, a high QY could be achieved by increasing the fluence rate of the excitation light. In order to limit the heating of the tissue to acceptable levels, strictly speaking, the only possibility is to utilize pulsed excitation with an acceptable average power. A difference from the two-photon fluorescence microscopy is that the excitation of UCNPs relies on long-lived intermediate states, which mean that pulses shorter than a few milliseconds do not improve the QY substantially. By utilizing pulsed excitation we foresee that improved sensitivity of deep tissue targets could be accomplished without much side-effects in terms of heating. This is a simple improvement which could be realized with off-the-shelf diode lasers, thereby drastically increasing the applicability of UCNPs for diffuse imaging.

For PDT applications, the potential of using UCNPs would also be drastically improved by pulsed excitation. The presented UCNP-PDT approaches seem to be severely limited by the relatively low efficiency in generating cytotoxic agents in the PDT process. The low efficiency in the excitation process using UCNP is here a limiting factor. The possibility to produce a sufficient PDT effect could probably be drastically improved by utilizing millisecond pulsed excitation. We suggest to further study this approach and to investigate its potential for improved efficiency. It seems more feasible to reach the threshold dose with improved QY of the production of cytotoxic agents in the PDT process *via* pulsed excitation.

The commonly used UCNPs employ $Yb^{3+}$ ions as sensitizers, which have a strong absorption band at 975 nm. However, this absorption band coincides with that of water which causes light attenuation and heating. To improve the penetration depth and reduce the heating of tissue in imaging applications, it is possible to shift the excitation wavelength to the 920-nm absorption band of $Yb^{3+}$. Although this absorption band is significantly weaker than the 975-nm band, excitation at this wavelength has been demonstrated to be very feasible and motivated for *in vitro* cell imaging, and imaging of very deeply embedded targets within tissues. The conditions determining which

 

REVIEW ARTICLE



excitation wavelength to use is not immediately trivial and relates to the optical properties of the studied tissue and the imaging depth of interest, and thus consideration must be taken based on the experimental conditions.

Development of protocols for improved synthesis of UCNPs with optimized properties for bioimaging would be highly desirable. Several aspects relate to this issue. A main issue is to develop reproducible and scalable production procedures – here the microfluidic approach may be a possibility. The use of other sensitizer ions, with an excitation wavelength better suitable for bioimaging applications would also provide a great advancement. In this respect, it would be more optimal with a slightly shorter or slightly longer excitation wavelength to decrease the attenuation caused by water absorption. This would provide a better penetration depth in tissue and at the same time avoid some of the side-effect of heating the tissue.

Another future challenge for diffuse optical imaging is to characterize the particles well enough to allow for direct comparison of results between different studies. In particular an absolute value of the efficiency of UCNPs needs to be provided, so that data can be directly inter-compared, thereby promoting the development in the field. A recommendation would be to measure the QY for a number of power densities, and also for different pulse lengths, at least if pulsed excitation is considered.

A further aspect of vital importance for the future utilization of UCNPs is to fully understand the health issues connected to these particles, in particular considering possible clinical applications that may develop. For cell or small animal studies, the toxicity may be slightly more relaxed, as the long-term effect may not be of critical importance.

Finally, multimodality approaches could become important in some clinical specialities of UCNP-based diagnostics. This could in particular be of interest as various modalities could provide different diagnostic information as well as employment in different clinical situations. Multimodality approaches have been explored a lot to gain complementary diagnostic information. The various tools could also be used in different conditions – for instance, one technique could be utilized in the initial diagnostic preparation phase and another technique could be used later as a bedside tool during a therapeutic procedure or as a monitoring device. For the latter cases simple optical techniques could present obvious benefits.

## Appendix

**List of abbreviations**

| | |
|---|---|
| AFM | atomic force microscopy |
| CR | cross relaxation |
| CS | cooperative sensitization |
| CT | computed tomography |
| CTAB | cetyltrimethylammonium bromide |
| CTX | chlorotoxin |
| DOI | diffuse optical imaging |
| ED | electric dipole |
| EDC | ethyl dimethylaminopropyl carbodiimide |
| EDTA | ethylenediamine tetraacetic acid |
| ESA | excited state absorption |
| ETU | energy transfer upconversion |
| FA | folic acid |
| FDOT | fluorescence diffuse optical tomography |
| FRET | Förster resonance energy transfer |
| FTIR | fourier transform infrared |
| GFP | green fluorescent protein |
| GSA | ground state absorption |
| IR | infrared |
| LDOT | luminescence diffuse optical tomography |
| LRET | luminescence resonance energy transfer |
| LSS | liquid-solid-solution |
| MD | magnetic dipole |
| MPR | multiphonon relaxation |
| MRI | magnetic resonance imaging |
| MTT | methylthiazol tetrazolium |
| NADH | nicotinamide adenine dinucleotide |
| NHS | N-hydroxysulfosuccinimide |
| OA | oleic acid |
| ODE | octadecene |
| OM | oleylamine |
| PA | photon avalance |
| PAA | polyacrylic acid |
| PAH | polyallylamine hydrochloride |
| PBS | phosphate buffer solution |
| PCI | photochemical internalization |
| PDT | photodynamic therapy |
| PEG | polyethylene glycol |
| PEI | polyethylenimine |
| PET | positron emission tomography |
| QD | quantum dot |
| QY | quantum yield |
| RE | rare-earth |
| RET | resonance energy transfer |
| RGD | argininеglycineaspartic acid |
| SNR | signal-to-noise ratio |
| SPECT | single-photon emission computed tomography |
| TEOS | tetraethyl orthosilicate |
| TOP | trioctyphosphine |
| TOPO | trioctylphosphine oxide |
| TSC | trisodium citrate |
| UC | upconversion |
| UCL | upconversion luminescence |
| UCNP | upconverting nanoparticles |
| UV | ultraviolet |

**Acknowledgements.** The authors would like to thank any collaborator in this field for nice and fruitful collaboration, including Pontus Svenmarker, Johan Axelsson, Dan Wang, Fuhong Cai, Ola Jakobsson, Thomas Laurell, Maria Messing, Reine Wallenberg, Björn Thomasson, Gökhan Dumlupinar and the dedicated scientists at Genovis AB. This work was supported by the Linneaus grant for Lund Laser Centre, the Swedish Research Council (grant No. 621-2011-4265), the National Nature Science Foundation of China (grant No. 60978063), the Science and Technology Department of Zhejiang Province (grant No. 2010R50007)

LASER & PHOTONICS REVIEWS



and Guangdong Innovative Research Team Program (grant no. 201001D0104799318).

**Received:** 2 July 2012, **Revised:** 18 October 2012, **Accepted:** 2 November 2012

**Published online:** 15 January 2013

**Key words:** Upconversion, quantum yield, photodynamic therapy, pulsed excitation.

**Can T. Xu** received his M.Sc. degree in Engineering Physics from Lund University, Lund, Sweden, in 2008. He is currently working towards the Ph.D. degree at the Atomic Physics division, Lund Laser Centre, Department of Physics, Lund University. His research interests include diffuse optical imaging and tomography of turbid materials for the use of *in-vivo* applications as well as fundamental research involving high-resolution spectroscopy of gases confined within nanoporous materials.

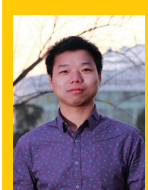

**Qiuqiang Zhan** was born in Nanchang, China. He received the B. Eng. degree in optical information science and technology from Shandong University, Ji'nan, China, in 2007 and the Ph.D. degree from the Department of Optical Engineering, Zhejiang University, Hangzhou, China, in 2012. He is currently a young faculty member at the ZJU-SCNU Joint Research Center of Photonics, South China Normal University, Guangzhou, China. His current research interests include nanoparticle-assisted bionanophotonics and nonlinear optical biomedical imaging.

**Haichun Liu** received his M.Sc. degree in Optics from Harbin Institute of Technology, Harbin, China, in 2008. Since then he has been working as a Ph.D. candidate under the supervision of Prof. Stefan Andersson-Engels at the Lund Laser Centre, Department of Physics, Lund University. His current research interest focuses on the bioapplications of upconverting nanoparticles based on their nonlinear photoluminescence property.

**Gabriel Somesfalean** received the Ph.D. degree in Engineering Physics from Lund University, Sweden, in 2005. Thereafter he worked with optical environmental monitoring and biophotonics at Harbin Institute of Technology, Lund University and Zhejiang University, where he became an Associate Professor in 2007. Currently, he is the Vice Director of the Joint Research Center of Photonics between the Royal Institute of Technology, Zhejiang University and Lund University. His current research interests include applied spectroscopy towards environmental sensing, biophotonics, and the study of gases in scattering media.

**Jun Qian** was born in Zhejiang, China, in 1981. He received the B. Eng. and the Ph.D. degrees from the Department of Optical Engineering, Zhejiang University, Hangzhou, China, in 2004 and 2009, respectively. During 2009–2011. He was a Postdoctoral Fellow at the Center for Optical and Electromagnetic Research, Zhejiang University. He is currently an Associate Professor at the Department of Optical Engineering, Zhejiang University. His main research activities are focused on nano-bio-photonics, including nanoparticle-assisted bioimaging and biotherapy.

**Sailing He** received the Licentiate of Technology and the Ph.D. degrees from the Royal Institute of Technology, Sweden, in 1991 and 1992, respectively. Since then he has worked at the Royal Institute of Technology as an Assistant Professor, an Associate Professor, and a Full Professor. He is currently the Director for Joint Research Center of Photonics of the Royal Institute of Technology (Sweden), Lund University (Sweden) and Zhejiang University, China. He is a Fellow of OSA and SPIE, and a Topical Editor for Optics Letters.

**Stefan Andersson-Engels** received his M.Sc. and Ph.D. degrees from Lund University in Engineering Physics 1985 and Physics 1990, respectively. He was a postdoc at McMasters University in Canada 1990–1991. He has since been at Lund University, and became a full professor in 1999. He is presently the director of the Lund University Medical Laser Centre and the deputy head of Atomic Physics Division at Lund University. He is also a topical editor for J. Biomed. Optics and an editorial board member for J. Biophotonics. His reseach interest include tissue optics as well as applications of light in biomedical diagnostics and treatments.

## References

[1] F. Auzel and D. Pecile, Journal of Luminescence **8**(1), 32–43 (1973).
[2] F. Auzel and D. Pecile, Journal of Luminescence **11**(5–6), 321–330 (1976).
[3] N. Bloembergen, Phys. Rev. Lett. **2**(Feb), 84–85 (1959).
[4] F. Auzel, Chemical Reviews **104**(1), 139–173 (2004).
[5] C. Reinhard, H. U. Gu, and C. Bern, Inorganic Chemistry **41**(5), 1048–1055 (2002).
[6] G. W. Faris, W. H. Wright, S. Pati, L. V. Schneider, and D. A. Zarling, Upconverting reporters for biomedical diagnostics: Applications in antibody and dna detection, in: Biomedical

 

REVIEW ARTICLE



Optical Spectroscopy and Diagnostics, (Optical Society of America, 1996), p. DR2.
[7] G. W. Faris, W. H. Wright, M. P. Hall, Y. Chen, Y. M. M. Yao, N. A. Mufti, and D. E. Cooper, Upconverting phosphors as reporters for immunoassay, in: Biomedical Optical Spectroscopy and Diagnostics / Therapeutic Laser Applications, (Optical Society of America, 1998), p. BTuB4.
[8] H. J. M. A. A. Zijlmans, J. Bonnet, J. Burton, K. Kardos, T. Vail, R. S. Niedbala, and H. J. Tanke, Analytical Biochemistry **267**(1), 30–36 (1999).
[9] J. Hampl, M. Hall, N. A. Mufti, Y. m. M. Yao, D. B. MacQueen, W. H. Wright, and D. E. Cooper, Analytical Biochemistry **288**(2), 176–187 (2001).
[10] F. Auzel, Comptes Rendus Hebdomadaires Des Seances De L Academie Des Sciences Serie B **262**(15), 1016 (1966).
[11] F. Auzel, Comptes Rendus Hebdomadaires Des Seances De L Academie Des Sciences Serie B **263**(14), 819 (1966).
[12] D. Gamelin and H. Gudel, Upconversion processes in transition metal and rare earth metal systems, in: Transition Metal and Rare Earth Compounds, edited by H. Yersin, Topics in Current Chemistry Vol. 214 (Springer Berlin/ Heidelberg, 2001), pp. 1–56.
[13] F. Wang, D. K. Chatterjee, Z. Li, Y. Zhang, X. Fan, and M. Wang, Nanotechnology **17**(23), 5786 (2006).
[14] J. Shan, X. Qin, N. Yao, and Y. Ju, Nanotechnology **18**(44), 445607 (2007).
[15] G. S. Yi and G. M. Chow, Chemistry Of Materials **19**(3), 341–343 (2007).
[16] G. Y. Chen, H. C. Liu, G. Somesfalean, Y. Q. Sheng, H. J. Liang, Z. G. Zhang, Q. Sun, and F. P. Wang, Applied Physics Letters **92**(11), 113114 (2008).
[17] J. F. Suyver, A. Aebischer, S. García-Revilla, P. Gerner, and H. U. Güdel, Phys. Rev. B **71**(Mar), 125123 (2005).
[18] M. Pollnau, D. R. Gamelin, S. R. Lüthi, H. U. Güdel, and M. P. Hehlen, Phys. Rev. B **61**(Feb), 3337–3346 (2000).
[19] C. T. Xu, N. Svensson, J. Axelsson, P. Svenmarker, G. Somesfalean, G. Chen, H. Liang, H. Liu, Z. Zhang, and S. Andersson-Engels, Applied Physics Letters **93**(17), 171103 (2008).
[20] J. C. G. Bunzli, Chemical Reviews **110**(5), 2729–2755 (2010).
[21] S. V. Eliseeva and J. C. G. Bunzli, Chemical Society Reviews **39**(1), 189–227 (2010).
[22] M. Haase and H. Schafer, Angewandte Chemie-international Edition **50**(26), 5808–5829 (2011).
[23] J. Zhou, Z. Liu, and F. Li, Chem. Soc. Rev. **41**(3), 1323 (2012).
[24] C. Jiang and W. Xu, J. Display Technol. **5**(8), 312–318 (2009).
[25] F. Wang, D. Banerjee, Y. Liu, X. Chen, and X. Liu, Analyst **135**(8), 1839–1854 (2010).
[26] F. Gu, S. F. Wang, M. K. Lu, G. J. Zhou, D. Xu, and D. R. Yuan, Langmuir **20**(9), 3528–3531 (2004).
[27] J. C. Boyer, J. Gagnon, L. A. Cuccia, and J. A. Capobianco, Chemistry of Materials **19**(14), 3358–3360 (2007).
[28] X. Liang, X. Wang, J. Zhuang, Q. Peng, and Y. Li, Inorganic Chemistry **46**(15), 6050–6055 (2007).
[29] P. Ptacek, H. Schäfer, K. Kämpe, and M. Haase, Advanced Functional Materials **17**(18), 3843–3848 (2007).
[30] R. Qin, H. Song, G. Pan, L. Hu, H. Yu, S. Li, X. Bai, L. Fan, Q. Dai, X. Ren, H. Zhao, and T. Wang, Materials Research Bulletin **43**(8-9), 2130–2136 (2008).
[31] G. Jia, H. You, Y. Song, J. Jia, Y. Zheng, L. Zhang, K. Liu, and H. Zhang, Inorganic Chemistry **48**(21), 10193–10201 (2009).
[32] R. Martín-Rodríguez, R. Valiente, S. Polizzi, M. Bettinelli, A. Speghini, and F. Piccinelli, The Journal of Physical Chemistry C **113**(28), 12195–12200 (2009).
[33] V. K. Tikhomirov, G. Adamo, A. E. Nikolaenko, V. D. Rodriguez, P. Gredin, M. Mortier, N. I. Zheludev, and V. V. Moshchalkov, Opt. Express **18**(9), 8836–8846 (2010).
[34] H. T. Wong, H. L. W. Chan, and J. Hao, Opt Express **18**(6), 6123–6130 (2010).
[35] Z. Xu, P. Ma, C. Li, Z. Hou, X. Zhai, S. Huang, and J. Lin, Biomaterials **32**(17), 4161–4173 (2011).
[36] E. L. Cates, A. P. Wilkinson, and J. H. Kim, The Journal of Physical Chemistry C **116**(23), 12772–12778 (2012).
[37] J. Suyver, A. Aebischer, D. Biner, P. Gerner, J. Grimm, S. Heer, K. Krämer, C. Reinhard, and H. Güdel, Optical Materials **27**(6), 1111–1130 (2005).
[38] F. Wang and X. G. Liu, Chemical Society Reviews **38**(4), 976–989 (2009).
[39] B. R. Judd, Physical Review **127**(3), 750 (1962).
[40] G. S. Ofelt, Journal of Chemical Physics **37**(3), 511 (1962).
[41] Q. Lv, A. Li, F. Guo, L. Sun, and L. Zhao, Nanotechnology **19**(14), 145701 (2008).
[42] F. Wang, J. Wang, and X. Liu, Angew Chem Int Ed Engl **49**(41), 7456–7460 (2010).
[43] K. W. Kramer, D. Biner, G. Frei, H. U. Güdel, M. P. Hehlen, and S. R. Lüthi, Chemistry of Materials **16**(7), 1244–1251 (2004).
[44] S. Heer, K. Kämpe, H. U. Güdel, and M. Haase, Advanced Materials **16**(23-24), 2102–2105 (2004).
[45] Z. Xu, C. Li, P. Yang, C. Zhang, S. Huang, and J. Lin, Crystal Growth & Design **9**(11), 4752–4758 (2009).
[46] C. Liu, H. Wang, X. Zhang, and D. Chen, Journal of Materials Chemistry **19**(4), 489–496 (2009).
[47] D. Chen, P. Huang, Y. Yu, F. Huang, A. Yang, and Y. Wang, Chem Commun (Camb) **47**(20), 5801–5803 (2011).
[48] R. E. Thoma, G. M. Hebert, H. Insley, and C. F. Weaver, Inorganic Chemistry **2**(5), 1005–1012 (1963).
[49] R. E. Thoma, H. Insley, and G. M. Hebert, Inorganic Chemistry **5**(7), 1222–1229 (1966).
[50] J. C. Boyer and F. C. J. M. van Veggel, Nanoscale **2**(8), 1417–1419 (2010).
[51] E. M. Chan, C. Xu, A. W. Mao, G. Han, J. S. Owen, B. E. Cohen, and D. J. Milliron, Nano Lett **10**(5), 1874–1885 (2010).
[52] S. F. Lim, R. Riehn, W. S. Ryu, N. Khanarian, C. K. Tung, D. Tank, and R. H. Austin, Nano Letters **6**(2), 169–174 (2006).
[53] S. Singh, K. Kumar, and S. Rai, Applied Physics B: Lasers and Optics **94**, 165–173 (2009).
[54] F. van de Rijke, H. Zijlmans, S. Li, T. Vail, A. K. Raap, R. S. Niedbala, and H. J. Tanke, Nat Biotech **19**(3), 273–276 (2001).

LASER & PHOTONICS REVIEWS




[55] Y. W. Zhang, X. Sun, R. Si, L. P. You, and C. H. Yan, Journal of the American Chemical Society **127**(10), 3260–3261 (2005).
[56] G. De, W. Qin, J. Zhang, D. Zhao, and J. Zhang, Chemistry Letters **34**(7), 914–915 (2005).
[57] C. Liu and D. Chen, J. Mater. Chem. **17**(37), 3875–3880 (2007).
[58] G. Yi, H. Lu, S. Zhao, Y. Ge, W. Yang, D. Chen, and L. H. Guo, Nano Letters **4**(11), 2191–2196 (2004).
[59] J. H. Zeng, J. Su, Z. H. Li, R. X. Yan, and Y. D. Li, Advanced Materials **17**(17), 2119–2123 (2005).
[60] Z. Li and Y. Zhang, Angewandte Chemie International Edition **45**(46), 7732–7735 (2006).
[61] H. X. Mai, Y. W. Zhang, R. Si, Z. G. Yan, L. d. Sun, L. P. You, and C. H. Yan, Journal of the American Chemical Society **128**(19), 6426–6436 (2006).
[62] J. C. Boyer, F. Vetrone, L. A. Cuccia, and J. A. Capobianco, J Am Chem Soc **128**(23), 7444–7445 (2006).
[63] G. Yi and G. Chow, Adv. Funct. Mater. **16**(18), 2324–2329 (2006).
[64] J. N. Shan and Y. G. Ju, Applied Physics Letters **91**(12), 123103 (2007).
[65] L. Wang and Y. Li, Chemistry of materials : a publication of the American Chemical Society **19**(4), 727–734 (2007).
[66] F. Zhang, Y. Wan, T. Yu, F. Zhang, Y. Shi, S. Xie, Y. Li, L. Xu, B. Tu, and D. Zhao, Angewandte Chemie International Edition **46**(42), 7976–7979 (2007).
[67] Y. Wei, F. Lu, X. Zhang, and D. Chen, Journal of Alloys and Compounds **427**(1-2), 333–340 (2007).
[68] Z. Li, Y. Zhang, and S. Jiang, Advanced Materials **20**(24), 4765–4769 (2008).
[69] A. Aebischer, S. Heer, D. Biner, K. Krämer, M. Haase, and H. U. Güdel, Chemical Physics Letters **407**(1–3), 124–128 (2005).
[70] F. Wang, X. P. Fan, M. Q. Wang, and Y. Zhang, Nanotechnology **18**(2), 025701 (2007).
[71] R. Naccache, F. Vetrone, V. Mahalingam, L. A. Cuccia, and J. A. Capobianco, Chemistry of Materials **21**(4), 717–723 (2009).
[72] Y. I. Park, J. H. Kim, K. T. Lee, K. S. Jeon, H. B. Na, J. H. Yu, H. M. Kim, N. Lee, S. H. Choi, S. I. Baik, H. Kim, S. P. Park, B. J. Park, Y. W. Kim, S. H. Lee, S. Y. Yoon, I. C. Song, W. K. Moon, Y. D. Suh, and T. Hyeon, Advanced Materials **21**(44), 4467–4471 (2009).
[73] G. Wang, Q. Peng, and Y. Li, Journal of the American Chemical Society **131**(40), 14200–14201 (2009).
[74] Y. P. Du, X. Sun, Y. W. Zhang, Z. G. Yan, L. D. Sun, and C. H. Yan, Crystal Growth & Design **9**(4), 2013–2019 (2009).
[75] M. Pedroni, F. Piccinelli, T. Passuello, M. Giarola, G. Mariotto, S. Polizzi, M. Bettinelli, and A. Speghini, Nanoscale **3**(4), 1456–1460 (2011).
[76] N. N. Dong, M. Pedroni, F. Piccinelli, G. Conti, A. Sbarbati, J. E. Ramírez-Hernández, L. M. Maestro, M. C. Iglesias de la Cruz, F. Sanz-Rodriguez, A. Juarranz, F. Chen, F. Vetrone, J. A. Capobianco, J. G. Solé, M. Bettinelli, D. Jaque, and A. Speghini, ACS Nano **5**(11), 8665–8671 (2011).
[77] Q. Liu, Y. Sun, T. Yang, W. Feng, C. Li, and F. Li, Journal of the American Chemical Society **133**(43), 17122–17125 (2011).
[78] T. Yang, Y. Sun, Q. Liu, W. Feng, P. Yang, and F. Li, Biomaterials **33**(14), 3733–3742 (2012).
[79] X. Teng, Y. Zhu, W. Wei, S. Wang, J. Huang, R. Naccache, W. Hu, A. I. Y. Tok, Y. Han, Q. Zhang, Q. Fan, W. Huang, J. A. Capobianco, and L. Huang, Journal of the American Chemical Society **134**(20), 8340–8343 (2012).
[80] J. C. Boyer, L. A. Cuccia, and J. A. Capobianco, Nano Lett **7**(3), 847–852 (2007).
[81] G. Chen, H. Liu, G. Somesfalean, H. Liang, and Z. Zhang, Nanotechnology **20**(38), 385704 (2009).
[82] M. Nyk, R. Kumar, T. Y. Ohulchanskyy, E. J. Bergey, and P. N. Prasad, Nano Letters **8**(11), 3834–3838 (2008).
[83] F. Wang, R. Deng, J. Wang, Q. Wang, Y. Han, H. Zhu, X. Chen, and X. Liu, Nat Mater, advance online publication (October),–(2011).
[84] G. Chen, G. Somesfalean, Y. Liu, Z. Zhang, Q. Sun, and F. Wang, Phys. Rev. B **75**(19), 195204 (2007).
[85] N. Rakov, G. S. Maciel, M. L. Sundheimer, L. de S. Menezes, A. S. L. Gomes, Y. Messaddeq, F. C. Cassanjes, G. Poirier, and S. J. L. Ribeiro, Journal of Applied Physics **92**(10), 6337–6339 (2002).
[86] L. Wang, W. Qin, Z. Liu, D. Zhao, G. Qin, W. Di, and C. He, Opt. Express **20**(7), 7602–7607 (2012).
[87] G. Chen, H. Liang, H. Liu, G. Somesfalean, and Z. Zhang, Opt. Express **17**(19), 16366–16371 (2009).
[88] C. Liu, J. Sun, H. Wang, and D. Chen, Scripta Materialia **58**(2), 89–92 (2008).
[89] C. Liu, H. Wang, X. Li, and D. Chen, J. Mater. Chem. **19**(21), 3546–3553 (2009).
[90] M. Wang, J. L. Liu, Y. X. Zhang, W. Hou, X. L. Wu, and S. K. Xu, Materials Letters **63**(2), 325–327 (2009).
[91] F. Zhang and D. Zhao, ACS Nano **3**(1), 159–164 (2009).
[92] X. Liu, J. Zhao, Y. Sun, K. Song, Y. Yu, C. Du, X. Kong, and H. Zhang, Chem. Commun. (43), 6628–6630 (2009).
[93] C. Zhang and J. Chen, Chem. Commun. **46**(4), 592–594 (2010).
[94] C. Chen, L. D. Sun, Z. X. Li, L. L. Li, J. Zhang, Y. W. Zhang, and C. H. Yan, Langmuir **26**(11), 8797–8803 (2010).
[95] C. Li and J. Lin, J. Mater. Chem. **20**(33), 6831–6847 (2010).
[96] D. K. Chatterjee, M. K. Gnanasammandhan, and Y. Zhang, Small **6**(24), 2781–2795 (2010).
[97] C. Zhang, L. SUN, Y. Zhang, and C. Yan, Journal of Rare Earths **28**(6), 807–819 (2010).
[98] H. X. Mai, Y. W. Zhang, L. D. Sun, and C. H. Yan, The Journal of Physical Chemistry C **111**(37), 13730–13739 (2007).
[99] Y. Wei, F. Lu, X. Zhang, and D. Chen, Chemistry of Materials **18**(24), 5733–5737 (2006).
[100] G. S. Yi, W. B. Lee, and G. M. Chow, Journal of Nanoscience and Nanotechnology **7**(8), 2790–2794 (2007).
[101] Y. P. Du, Y. W. Zhang, L. D. Sun, and C. H. Yan, Dalton Trans. (40), 8574–8581 (2009).
[102] V. Mahalingam, F. Vetrone, R. Naccache, A. Speghini, and J. A. Capobianco, Adv. Mater. **21**(40), 4025–4028 (2009).
[103] G. Chen, T. Y. Ohulchanskyy, A. Kachynski, H. Ågren, and P. N. Prasad, ACS Nano **5**, 4981–4986 (2011).
[104] V. Mahalingam, F. Vetrone, R. Naccache, A. Speghini, and J. A. Capobianco, Journal of Materials Chemistry **19**(20), 3149–3152 (2009).


 

REVIEW ARTICLE




[105] F. Vetrone, V. Mahalingam, and J. A. Capobianco, Chemistry of Materials **21**(9), 1847–1851 (2009).
[106] X. Wang, J. Zhuang, Q. Peng, and Y. D. Li, Nature **437**(7055), 121–124 (2005).
[107] J. H. Zeng, Z. H. Li, J. Su, L. Wang, R. Yan, and Y. Li, Nanotechnology **17**(14), 3549 (2006).
[108] L. Wang and Y. Li, Nano Letters **6**(8), 1645–1649 (2006).
[109] F. Zhang, J. Li, J. Shan, L. Xu, and D. Zhao, Chemistry A European Journal **15**(41), 11010–11019 (2009).
[110] Z. Li and Y. Zhang, Nanotechnology **19**(34), 345606 (2008).
[111] H. S. Qian and Y. Zhang, Langmuir **24**(21), 12123–12125 (2008).
[112] N. M. Idris, Z. Q. Li, L. Ye, E. K. W. Sim, R. Mahendran, P. C. L. Ho, and Y. Zhang, Biomaterials **30**(28), 5104–5113 (2009).
[113] J. C. Boyer, C. J. Carling, B. D. Gates, and N. R. Branda, J Am Chem Soc **132**(44), 15766–15772 (2010).
[114] F. Wang, Y. Han, C. S. Lim, Y. Lu, J. Wang, J. Xu, H. Chen, C. Zhang, M. Hong, and X. Liu, Nature **463**(7284), 1061–1065 (2010).
[115] Z. Li, L. Wang, Z. Wang, X. Liu, and Y. Xiong, The Journal of Physical Chemistry C **115**(8), 3291–3296 (2011).
[116] H. Q. Wang and T. Nann, ACS Nano **3**(11), 3804–3808 (2009).
[117] C. Chen, L. D. Sun, Z. X. Li, L. L. Li, J. Zhang, Y. W. Zhang, and C. H. Yan, Langmuir **26**(11), 8797–8803 (2010).
[118] C. Mi, Z. Tian, C. Cao, Z. Wang, C. Mao, and S. Xu, Langmuir **27**(23), 14632–14637 (2011).
[119] D. Wang, L. Ren, X. Zhou, X. Z. Wang, J. Zhou, Y. Han, and N. Kang, Nanotechnology **23**(22), 225705 (2012).
[120] J. B. Edel, R. Fortt, J. C. deMello, and A. J. deMello, Chem. Commun. (10), 1136–1137 (2002).
[121] E. M. Chan, A. P. Alivisatos, and R. A. Mathies, Journal of the American Chemical Society. **127**(40), 13854–13861 (2005).
[122] X. Z. Lin, A. D. Terepka, and H. Yang, Nano letters **4**(11), 2227–2232 (2004).
[123] J. Wagner and J. M. Kohler, Nano letters **5**(4), 685–691 (2005).
[124] Y. Song, J. Hormes, and C. S. S. R. Kumar, Small **4**(6), 698–711 (2008).
[125] H. C. Liu, O. Jakobsson, C. T. Xu, H. Y. Xie, T. Laurell, and S. Andersson-Engels, Colloidal Quantum Dots/nanocrystals For Biomedical Applications Vi **7909**, 790917 (2011).
[126] A. D. Ostrowski, E. M. Chan, D. J. Gargas, E. M. Katz, G. Han, P. J. Schuck, D. J. Milliron, and B. E. Cohen, ACS Nano **6**(3), 2686–2692 (2012).
[127] G. S. Yi and G. M. Chow, J. Mater. Chem. **15**(41), 4460–4464 (2005).
[128] J. Shan and Y. Ju, Nanotechnology **20**(27), 275603 (2009).
[129] P. Ghosh and A. Patra, The Journal of Physical Chemistry C **112**(9), 3223–3231 (2008).
[130] Z. Wang, F. Tao, L. Yao, W. Cai, and X. Li, Journal of Crystal Growth **290**(1), 296–300 (2006).
[131] X. Yu, M. Li, M. Xie, L. Chen, Y. Li, and Q. Wang, Nano Research **3**, 51–60 (2010), 10.1007/s12274-010-1008-2.
[132] G. Tian, Z. Gu, L. Zhou, W. Yin, X. Liu, L. Yan, S. Jin, W. Ren, G. Xing, S. Li, and Y. Zhao, Advanced Materials **24**(9), 1226–1231 (2012).
[133] H. Kobayashi, M. Ogawa, R. Alford, P. L. Choyke, and Y. Urano, Chem Rev **110**(5), 2620–2640 (2010).
[134] Y. Okuhata, Advanced Drug Delivery Reviews **37** 121–137 (1999).
[135] H. Soo Choi, W. Liu, P. Misra, E. Tanaka, J. P. Zimmer, B. Itty Ipe, M. G. Bawendi, and J. V. Frangioni, Nat Biotech **25**(10), 1165–1170 (2007).
[136] A. R. Lowe, J. J. Siegel, P. Kalab, M. Siu, K. Weis, and J. T. Liphardt, Nature **467**(7315), 600–603 (2010).
[137] G. Chen, T. Y. Ohulchanskyy, R. Kumar, H. Agren, and P. N. Prasad, ACS Nano **4**(6), 3163–3168 (2010).
[138] F. Wang and X. Liu, Journal of the American Chemical Society **130**(17), 5642–5643 (2008).
[139] Q. Zhan, J. Qian, H. Liang, G. Somesfalean, D. Wang, S. He, Z. Zhang, and S. Andersson-Engels, ACS Nano **5**(5), 3744–3757 (2011).
[140] H. U. G. Daniel R. Gamelin, Acc. Chem. Res. **33**, 235–242 (2000).
[141] Y. Mita, Journal of Applied Physics **43**(4), 1772–1778 (1972).
[142] E. M. Chan, G. Han, J. D. Goldberg, D. J. Gargas, A. D. Ostrowski, P. J. Schuck, B. E. Cohen, and D. J. Milliron, Nano Letters **12**(7), 3839–3845 (2012).
[143] E. M. Chan, D. J. Gargas, P. J. Schuck, and D. J. Milliron, The Journal of Physical Chemistry B **116**(35), 10561–10570 (2012).
[144] B. M. Walsh, N. P. Barnes, and B. Di Bartolo, Journal of Applied Physics **83**(5), 2772–2787 (1998).
[145] J. M. F. Vandijk and M. F. H. Schuurmans, Journal of Chemical Physics **78**(9), 5317–5323 (1983).
[146] S. Taccheo, G. Sorbello, S. Longhi, and P. Laporta, Optical and Quantum Electronics **31**(3), 249–262 (1999).
[147] X. P. Jiang, Z. M. Yang, T. Liu, and S. H. Xu, Journal of Applied Physics **105**(10), 103113 (2009).
[148] A. F. H. Librantz, L. Gomes, L. C. Courrol, I. M. Ranieri, and S. L. Baldochi, Journal of Applied Physics **105**(11), 113503 (2009).
[149] J. Shan, M. Uddi, R. Wei, N. Yao, and Y. Ju, The Journal of Physical Chemistry C **114**(6), 2452–2461 (2010).
[150] R. Page, K. Schaffers, P. Waide, J. Tassano, S. Payne, W. Krupke, and W. Bischel, Journal of the Optical Society of America B-Optical Physics **15**(3), 996–1008 (1998).
[151] C. T. Xu, P. Svenmarker, H. Liu, X. Wu, M. E. Messing, L. R. Wallenberg, and S. Andersson-Engels, ACS Nano **6**(6), 4788–4795 (2012).
[152] J. Suyver, J. Grimm, M. van Veen, D. Biner, K. Kramer, and H. Gudel, Journal of Luminescence **117**(1), 1–12 (2006).
[153] G. Chen, H. Liu, H. Liang, G. Somesfalean, and Z. Zhang, The Journal of Physical Chemistry C **112**(31), 12030–12036 (2008).
[154] Y. Bai, Y. Wang, K. Yang, X. Zhang, Y. Song, and C. Wang, Optics Communications **281**(21), 5448–5452 (2008).
[155] Y. Bai, Y. Wang, K. Yang, X. Zhang, G. Peng, Y. Song, Z. Pan, and C. H. Wang, The Journal of Physical Chemistry C **112**(32), 12259–12263 (2008).
[156] Y. Bai, K. Yang, Y. Wang, X. Zhang, and Y. Song, Optics Communications **281**(10), 2930–2932 (2008).

LASER & PHOTONICS REVIEWS



[157] Q. Cheng, J. Sui, and W. Cai, Nanoscale **4**(3), 779–784 (2012).
[158] D. Yang, C. Li, G. Li, M. Shang, X. Kang, and J. Lin, Journal of Materials Chemistry **21**(16), 5923–5927 (2011).
[159] F. Vetrone, R. Naccache, V. Mahalingam, C. G. Morgan, and J. A. Capobianco, Advanced Functional Materials **19**(18), 2924–2929 (2009).
[160] H. S. Qian and Y. Zhang, Langmuir **24**(21), 12123–12125 (2008).
[161] P. P. Pompa, L. Martiradonna, A. D. Torre, F. D. Sala, L. Manna, M. De Vittorio, F. Calabi, R. Cingolani, and R. Rinaldi, Nat Nano **1**(2), 126–130 (2006).
[162] R. Bardhan, N. K. Grady, J. R. Cole, A. Joshi, and N. J. Halas, ACS Nano **3**(3), 744–752 (2009).
[163] R. Esteban, M. Laroche, and J. J. Greffet, Journal of Applied Physics **105**(3), 033107–10 (2009).
[164] H. Mertens and A. Polman, Applied Physics Letters **89**(21), 211107–3 (2006).
[165] H. Zhang, Y. Li, I. Ivanov, Y. Qu, Y. Huang, and X. Duan, Angewandte Chemie **122**(16), 2927–2930 (2010).
[166] L. Sudheendra, V. Ortalan, S. Dey, N. D. Browning, and I. M. Kennedy, Chemistry of Materials **23**(11), 2987–2993 (2011).
[167] H. P. Paudel, L. Zhong, K. Bayat, M. F. Baroughi, S. Smith, C. Lin, C. Jiang, M. T. Berry, and P. S. May, The Journal of Physical Chemistry C **115**(39), 19028–19036 (2011).
[168] S. Schietinger, T. Aichele, H. Q. Wang, T. Nann, and O. Benson, Nano Letters **10**(1), 134–138 (2009).
[169] O. Kulakovich, N. Strekal, A. Yaroshevich, S. Maskevich, S. Gaponenko, I. Nabiev, U. Woggon, and M. Artemyev, Nano Letters **2**(12), 1449–1452 (2002).
[170] H. Zhang, D. Xu, Y. Huang, and X. Duan, Chemical Communications **47**(3), 979–981 (2011).
[171] S. Fischer, F. Hallermann, T. Eichelkraut, G. von Plessen, K. W. Kraemer, D. Biner, H. Steinkemper, M. Hermle, and J. C. Goldschmidt, OPTICS EXPRESS **20**(1), 271–282 (2012).
[172] J. Goldschmidt, S. Fischer, H. Steinkemper, F. Hallermann, G. von Plessen, K. Kraämer, D. Biner, and M. Hermle, Photovoltaics, IEEE Journal of **2**(2), 134–140 (2012).
[173] Y. Wei, F. Lu, X. Zhang, and D. Chen, Journal of Alloys and Compounds **455**(1–2), 376–384 (2008).
[174] R. Qin, H. Song, G. Pan, X. Bai, B. Dong, S. Xie, L. Liu, Q. Dai, X. Qu, X. Ren, and H. Zhao, Crystal Growth & Design **9**(4), 1750–1756 (2009).
[175] F. Wang, D. Chatterjee, Z. Li, Y. Zhang, X. Fan, and M. Wang, Nanotechnology **17**(23), 5786 (2006).
[176] Z. Jing Hui, L. Zhi Hua, S. Ji, W. Leyu, Y. Ruoxue, and L. Yadong, Nanotechnology **17**(14), 3549 (2006).
[177] L. Q. Xiong, Z. G. Chen, M. X. Yu, F. Y. Li, C. Liu, and C. H. Huang, Biomaterials **30**(29), 5592–5600 (2009).
[178] T. Zhang, H. Guo, and Y. Qiao, Journal of Luminescence **129**(8), 861–866 (2009).
[179] J. C. Boyer, M. P. Manseau, J. I. Murray, and F. C. J. M. van Veggel, Langmuir **26**(2), 1157–1164 (2009).
[180] S. A. Hilderbrand, F. Shao, C. Salthouse, U. Mahmood, and R. Weissleder, Chemical Communications (28), 4188–4190 (2009).
[181] J. Jin, Y. J. Gu, C. W. Y. Man, J. Cheng, Z. Xu, Y. Zhang, H. Wang, V. H. Y. Lee, S. H. Cheng, and W. T. Wong, ACS Nano **5**(10), 7838–7847 (2011).
[182] L. Wang, R. Yan, Z. Huo, L. Wang, J. Zeng, J. Bao, X. Wang, Q. Peng, and Y. Li, Angewandte Chemie International Edition **44**(37), 6054–6057 (2005).
[183] J. Zhou, Y. Sun, X. X. Du, L. Q. Xiong, H. Hu, and F. Y. Li, Biomaterials **31**(12), 3287–3295 (2010).
[184] H. P. Zhou, C. H. Xu, W. Sun, and C. H. Yan, Advanced Functional Materials **19**(24), 3892–3900 (2009).
[185] Q. Zhan, J. Qian, X. Li, and S. He, Nanotechnology **21**, 055704 (2010).
[186] R. A. Jalil and Y. Zhang, Biomaterials **29**(30), 4122–4128 (2008).
[187] D. K. Chatterjee and Z. Yong, Nanomedicine (London, England) **3**(1), 73–82 (2008).
[188] H. S. Qian, H. C. Guo, P. C. L. Ho, R. Mahendran, and Y. Zhang, Small **5**(20), 2285–2290 (2009).
[189] M. Wang, C. Mi, Y. Zhang, J. Liu, F. Li, C. Mao, and S. Xu, The Journal of Physical Chemistry C **113**(44), 19021–19027 (2009).
[190] O. Ehlert, R. Thomann, M. Darbandi, and T. Nann, ACS Nano **2**(1), 120–124 (2008).
[191] S. Gai, P. Yang, C. Li, W. Wang, Y. Dai, N. Niu, and J. Lin, Advanced Functional Materials **20**(7), 1166–1172 (2010).
[192] M. Darbandi, R. Thomann, and T. Nann, Chemistry of Materials **17**(23), 5720–5725 (2005).
[193] X. Li, F. J. Kao, C. C. Chuang, and S. He, Opt. Express **18**(11), 11335–11346 (2010).
[194] P. Zhang, W. Steelant, M. Kumar, and M. Scholfield, Journal of the American Chemical Society **129**(15), 4526–+ (2007).
[195] N. Bogdan, F. Vetrone, G. A. Ozin, and J. A. Capobianco, Nano Letters **11**(2), 835–840 (2011).
[196] G. S. Yi and G. M. Chow, Chemistry of Materials **19**(3), 341–343 (2006).
[197] Z. Li, H. Guo, H. Qian, and Y. Hu, Nanotechnology **21**(31), 315105 (2010).
[198] M. Wang, C. C. Mi, W. X. Wang, C. H. Liu, Y. F. Wu, Z. R. Xu, C. B. Mao, and S. K. Xu, ACS Nano **3**(6), 1580–1586 (2009).
[199] L. Q. Xiong, Z. G. Chen, Q. W. Tian, T. Y. Cao, C. J. Xu, and F. Y. Li, Analytical Chemistry **81**(21), 8687–8694 (2009).
[200] K. Kuningas, T. Rantanen, T. Ukonaho, T. Lvgren, and T. Soukka, Analytical Chemistry **77**(22), 7348–7355 (2005).
[201] Z. G. Chen, H. L. Chen, H. Hu, M. X. Yu, F. Y. Li, Q. Zhang, Z. G. Zhou, T. Yi, and C. H. Huang, Journal of the American Chemical Society **130**(10), 3023–3029 (2008).
[202] X. F. Yu, Z. B. Sun, M. Li, Y. Xiang, Q. Q. Wang, F. F. Tang, Y. L. Wu, Z. J. Cao, and W. X. Li, Biomaterials **31**(33), 8724–8731 (2010).
[203] D. K. Chatteriee, A. J. Rufalhah, and Y. Zhang, Biomaterials **29**(7), 937–943 (2008).
[204] J. N. Shan, J. B. Chen, J. Meng, J. Collins, W. Soboyejo, J. S. Friedberg, and Y. G. Ju, Journal of Applied Physics **104**(9), 094308 (2008).
[205] L. Q. Xiong, T. S. Yang, Y. Yang, C. J. Xu, and F. Y. Li, Biomaterials **31**(27), 7078–7085 (2010).

 

REVIEW ARTICLE




[206] Q. Liu, M. Chen, Y. Sun, G. Y. Chen, T. S. Yang, Y. Gao, X. Z. Zhang, and F. Y. Li, Biomaterials **32**(32), 8243–8253 (2011).
[207] J. C. Zhou, Z. L. Yang, W. Dong, R. J. Tang, L. D. Sun, and C. H. Yan, Biomaterials **32**(34), 9059–9067 (2011).
[208] L. Yu, Y. Lu, N. Man, S. H. Yu, and L. P. Wen, Small **5**(24), 2784–2787 (2009).
[209] P. Corstjens, M. Zuiderwijk, A. Brink, S. Li, H. Feindt, R. S. Niedbala, and H. Tanke, Clinical Chemistry **47**, 1885–1893 (2001).
[210] P. L. A. M. Corstjens, M. Zuiderwijk, M. Nilsson, H. Feindt, R. Sam Niedbala, and H. J. Tanke, Analytical Biochemistry **312**(2), 191–200 (2003).
[211] Y. Wang, P. Shen, C. Li, Y. Wang, and Z. Liu, Analytical Chemistry **84**(3), 1466–1473 (2012).
[212] K. Kuningas, T. Ukonaho, H. Päkkilä, T. Rantanen, J. Rosenberg, T. Lövgren, and T. Soukka, Analytical Chemistry **78**(13), 4690–4696 (2006).
[213] T. Rantanen, H. Pakkila, L. Jamsen, K. Kuningas, T. Ukonaho, T. Lovgren, and T. Soukka, Analytical Chemistry **79**(16), 6312–6318 (2007).
[214] T. Rantanen, M. L. Jarvenpaa, J. Vuojola, K. Kuningas, and T. Soukka, Angewandte Chemie International Edition **47**(20), 3811–3813 (2008).
[215] T. Rantanen, M. L. Jarvenpaa, J. Vuojola, R. Arppe, K. Kuningas, and T. Soukka, Analyst **134**(8), 1713–1716 (2009).
[216] P. Zhang, S. Rogelj, K. Nguyen, and D. Wheeler, Journal of the American Chemical Society **128**(38), 12410–12411 (2006).
[217] F. Vetrone, R. Naccache, A. Zamarrn, A. J. de la Fuente, F. Sanz-Rodríguez, L. M. Maestro, E. M. Rodriguez, D. Jaque, J. G. Solé, and J. A. Capobianco, ACS Nano **4**(6), 3254–3258 (2010).
[218] L. H. Fischer, G. S. Harms, and O. S. Wolfbeis, Angewandte Chemie International Edition **50**(20), 4546–4551 (2011).
[219] P. V. dos Santos, M. T. de Araujo, A. S. Gouveia-Neto, J. A. M. Neto, and A. S. B. Sombra, Applied Physics Letters **73**(5), 578–580 (1998).
[220] M. A. R. C. Alencar, G. S. Maciel, C. B. de Araujo, and A. Patra, Applied Physics Letters **84**(23), 4753–4755 (2004).
[221] B. Dong, D. P. Liu, X. J. Wang, T. Yang, S. M. Miao, and C. R. Li, Applied Physics Letters **90**(18), 181117 (2007).
[222] S. K. Singh, K. Kumar, and S. Rai, Sensors and Actuators A: Physical **149**(1), 16–20 (2009).
[223] K. Y. Wu, J. B. Cui, X. X. Kong, and Y. J. Wang, Journal of Applied Physics **110**(5), 053510 (2011).
[224] B. Dong, B. Cao, Y. He, Z. Liu, Z. Li, and Z. Feng, Advanced Materials **24**(15), 1987–1993 (2012).
[225] D. A. Rothamer and J. Jordan, Applied Physics B-lasers and Optics **106**(2), 435–444 (2012).
[226] A. K. Singh and S. B. Rai, Applied Physics B-lasers and Optics **86**(4), 661–666 (2007).
[227] L. Liu, Y. Wang, X. Zhang, K. Yang, Y. Bai, C. Huang, and Y. Song, Optics Communications **284**(7), 1876–1879 (2011).
[228] D. Li, Y. Wang, X. Zhang, K. Yang, L. Liu, and Y. Song, Optics Communications **285**(7), 1925–1928 (2012).
[229] A. Sedlmeier, D. E. Achatz, L. H. Fischer, H. H. Gorris, and O. S. Wolfbeis, Nanoscale **4**(22), 7090–7096 (2012).
[230] M. Yu, F. Li, Z. Chen, H. Hu, C. Zhan, H. Yang, and C. Huang, Analytical Chemistry **81**(3), 930–935 (2009).
[231] S. W. Wu, G. Han, D. J. Millirona, A. Shaul, A. Virginia, V. T. Dmitri, E. C. Bruce, and P. J. Schucka, Proceedings of the National Academy of Sciences of the United States of America **106**(27), 10917–10921 (2009).
[232] S. Manley, J. M. Gillette, G. H. Patterson, H. Shroff, H. F. Hess, E. Betzig, and J. Lippincott-Schwartz, Nature Methods **5**(2), 155–157 (2008).
[233] X. W. Zhuang, Nature Photonics **3**(7), 365–367 (2009).
[234] K. I. Willig, S. O. Rizzoli, V. Westphal, R. Jahn, and S. W. Hell, Nature **440**(7086), 935–939 (2006).
[235] M. G. L. Gustafsson, Journal of Microscopy-Oxford **198**, 82–87 (2000).
[236] L. A. Cheng, K. Yang, S. A. Zhang, M. W. Shao, S. T. Lee, and Z. A. Liu, Nano Research **3**(10), 722–732 (2010).
[237] T. Zako, H. Nagata, N. Terada, A. Utsumi, M. Sakono, M. Yohda, H. Ueda, K. Soga, and M. Maeda, Biochemical and Biophysical Research Communications **381**(1), 54–58 (2009).
[238] J. Shan, Z. Yong, L. Kian Meng, K. W. S. Eugene, and Y. Lei, Nanotechnology **20**(15), 155101 (2009).
[239] S. Jiang and Y. Zhang, Langmuir **26**(9), 6689–6694 (2010).
[240] J. Pichaandi, J. C. Boyer, K. R. Delaney, and F. C. J. M. van Veggel, The Journal of Physical Chemistry C **115**(39), 19054–19064 (2011).
[241] T. Durduran, R. Choe, W. B. Baker, and A. G. Yodh, Reports on Progress in Physics **73**(7), 076701 (2010).
[242] A. H. Hielscher, Current Opinion in Biotechnology **16**(1), 79–88 (2005).
[243] V. Ntziachristos, Nature Methods **7**(8), 603–614 (2010).
[244] V. Ntziachristos, J. Ripoll, L. H. V. Wang, and R. Weissleder, Nature Biotechnology **23**(3), 313–320 (2005).
[245] G. Alexandrakis, F. R. Rannou, and A. F. Chatziioannou, Physics In Medicine And Biology **50**(17), 4225–4241 (2005).
[246] D. Hyde, R. de Kleine, S. A. MacLaurin, E. Miller, D. H. Brooks, T. Krucker, and V. Ntziachristos, Neuroimage **44**(4), 1304–1311 (2009).
[247] J. P. Culver, T. Durduran, T. Furuya, C. Cheung, J. H. Greenberg, and A. G. Yodh, Journal of Cerebral Blood Flow and Metabolism **23**(8), 911–924 (2003).
[248] V. Ntziachristos, C. H. Tung, C. Bremer, and R. Weissleder, Nature Medicine **8**(7), 757–760 (2002).
[249] V. Ntziachristos, E. Schellenberger, J. Ripoll, D. Yessayan, E. Graves, A. Bogdanov, L. Josephson, and R. Weissleder, Proceedings of the National Academy of Sciences of the United States of America **101**, 12294–12299 (2004).
[250] R. Choe, A. Corlu, K. Lee, T. Durduran, S. D. Konecky, M. Grosicka-Koptyra, S. R. Arridge, B. J. Czerniecki, D. L. Fraker, A. DeMichele, B. Chance, M. A. Rosen, and A. G. Yodh, Medical Physics **32**(4), 1128–1139 (2005).
[251] A. Corlu, R. Choe, T. Durduran, M. A. Rosen, M. Schweiger, S. R. Arridge, M. D. Schnall, and A. G. Yodh, Optics Express **15**(11), 6696–6716 (2007).
[252] A. P. Gibson, J. C. Hebden, and S. R. Arridge, Physics In Medicine And Biology **50**(4), R1–R43 (2005).
[253] D. R. Leff, O. J. Warren, L. C. Enfield, A. Gibson, T. Athanasiou, D. K. Patten, J. Hebden, G. Z. Yang, and A.

LASER & PHOTONICS REVIEWS



Darzi, Breast Cancer Research and Treatment **108**(1), 9–22 (2008).
[254] A. Li, E. L. Miller, M. E. Kilmer, T. J. Brukilacchio, T. Chaves, J. Stott, Q. Zhang, T. Wu, M. Chorlton, R. H. Moore, D. B. Kopans, and D. A. Boas, Applied Optics **42**(25), 5181–5190 (2003).
[255] M. A. Franceschini and D. A. Boas, Neuroimage **21**(1), 372–386 (2004).
[256] W. M. S. Georges A. Wagnires and B. C. Wilson, Photochemistry and Photobiology **68**(5), 603–632 (1998).
[257] M. m. Monici, Biotechnology Annual Review **11**, 227–256 (2005).
[258] S. AnderssonEngels, C. afKlinteberg, K. Svanberg, and S. Svanberg, Physics In Medicine And Biology **42**(5), 815–824 (1997).
[259] P. Diagaradjane, M. A. Yaseen, J. Yu, M. S. Wong, and B. Anvari, Lasers in Surgery and Medicine **37**(5), 382–395 (2005).
[260] S. Moestue, P. Nunez, A. Healey, R. Bjerke, B. Indrevoll, T. Skotland, and S. O. Hustvedt, Contrast Media & Molecular Imaging **4**(2), 73–80 (2009).
[261] G. Y. Panasyuk, Z. M. Wang, J. C. Schotland, and V. A. Markel, Optics Letters **33**(15), 1744–1746 (2008).
[262] A. Soubret and V. Ntziachristos, Physics In Medicine And Biology **51**(16), 3983–4001 (2006).
[263] A. T. N. Kumar, E. Chung, S. B. Raymond, J. A. J. M. van de Water, K. Shah, D. Fukumura, R. K. Jain, B. J. Bacskai, and D. A. Boas, Optics Letters **34**(13), 2066–2068 (2009).
[264] H. Xu and B. W. Rice, Journal of Biomedical Optics **14**(6), 064011 (2009).
[265] M. R. Brown, H. D. Summers, P. Rees, S. C. Chappell, O. F. Silvestre, I. A. Khan, P. J. Smith, and R. J. Errington, Cytometry Part A **77A**(10), 925–932 (2010).
[266] G. Zacharakis, H. Shih, J. Ripoll, R. Weissleder, and V. Ntziachristos, Molecular Imaging **5**(3), 153–159 (2006).
[267] Q. A. Ma and X. G. Su, Analyst **135**(8), 1867–1877 (2010).
[268] S. R. Arridge and J. C. Schotland, Inverse Problems **25**(12), 123010 (2009).
[269] C. T. Xu, J. Axelsson, and S. Andersson-Engels, Applied Physics Letters **94**(25), 251107 (2009).
[270] P. Svenmarker, C. T. Xu, and S. Andersson-Engels, Optics Letters **35**(16), 2789–2791 (2010).
[271] H. C. Liu, C. T. Xu, and S. Andersson-Engels, Optics Letters **35**(5), 718–720 (2010).
[272] D. K. Chatterjee, A. J. Rufaihah, and Y. Zhang, Biomaterials **29**(7), 937–943 (2008).
[273] C. Salthouse, S. Hildebrand, R. Weissleder, and U. Mahmood, Optics Express **16**(26), 21731–21737 (2008).
[274] T. Y. Cao, Y. Yang, Y. A. Gao, J. Zhou, Z. Q. Li, and F. Y. Li, Biomaterials **32**(11), 2959–2968 (2011).
[275] H. Kobayashi, N. Kosaka, M. Ogawa, N. Y. Morgan, P. D. Smith, C. B. Murray, X. C. Ye, J. Collins, G. A. Kumar, H. Bell, and P. L. Choyke, Journal of Materials Chemistry **19**(36), 6481–6484 (2009).
[276] L. R. Braathen, R. M. Szeimies, N. Basset-Seguin, R. Bissonnette, P. Foley, D. Pariser, R. Roelandts, A. M. Wennberg, and C. A. Morton, Journal of the American Academy of Dermatology **56**(1), 125–143 (2007).
[277] A. Johansson and S. Andersson-Engels, in: Laser Imaging and Manipulation in Cell Biology, edited by F. Pavone (Wiley-VCH Verlag, Weinheim, Germany, 2010), chap. Photodynamic Therapy - the Quest for Imprved Dosimety in the Management of Solid Tumors, pp. 167–202.
[278] K. Svanberg, N. Bendsoe, J. Axelsson, S. Andersson-Engels, and S. Svanberg, Journal of Biomedical Optics **15**(4), 041502 (2010).
[279] D. M. Adolfo Vera, M. H. Haynes, A. R. Ball, T. Dai, C. Astrakas, M. J. Kelso, M. R. Hamblin, and G. P. Tegos, Photochemistry and Photobiology **88**(3), 499–511 (2012).
[280] P. Calzavara-Pinton, M. T. Rossi, R. Sala, and M. Venturini, Photochemistry and Photobiology **88**(3), 512–522 (2012).
[281] K. Berg, M. Folini, L. Prasmickaite, P. K. Selbo, A. Bonsted, B. Engesaeter, N. Zaffaroni, A. Weyergang, A. Dietze, G. M. Maelandsmo, E. Wagner, O. J. Norum, and A. Hgset, Curr Pharm Biotechnol **8**(6), 362–372 (2007).
[282] K. Berg, P. Kristian Selbo, L. Prasmickaite, T. E. Tjelle, K. Sandvig, J. Moan, G. Gaudernack Fodstad, S. Kjlsrud, H. Anholt, G. H. Rodal, S. K. Rodal, and A. Hgset, Cancer Research **59**(6), 1180–1183 (1999).
[283] D. Gao, R. R. Agayan, H. Xu, M. A. Philbert, and R. Kopelman, Nano Letters **6**(11), 2383–2386 (2006).
[284] D. K. Chatterjee, L. S. Fong, and Y. Zhang, Advanced Drug Delivery Reviews **60**(15), 1627–1637 (2008).
[285] J. N. Shan, S. J. Budijono, G. H. Hu, N. Yao, Y. B. Kang, Y. G. Ju, and R. K. Prud'homme, Advanced Functional Materials **21**(13), 2488–2495 (2011).
[286] B. Ungun, R. K. Prud'homme, S. J. Budijon, J. Shan, S. F. Lim, Y. Ju, and R. Austin, Opt. Express **17**(1), 80–86 (2009).
[287] C. Wang, H. Q. Tao, L. Cheng, and Z. Liu, Biomaterials **32**(26), 6145–6154 (2011).
[288] T. J. Dougherty, C. J. Gomer, B. W. Henderson, G. Jori, D. Kessel, M. Korbelik, J. Moan, and Q. Peng, Journal of the National Cancer Institute **90**(12), 889–905 (1998).
[289] B. W. Pogue and M. S. Patterson, Journal of Biomedical Optics **11**(4), 041102 (2006).
[290] B. C. Wilson and M. S. Patterson, Physics In Medicine and Biology **53**(9), R61–R109 (2008).
[291] S. L. Jacques and B. W. Pogue, Journal of Biomedical Optics **13**(4), 041302 (2008).
[292] T. Svensson, S. Andersson-Engels, M. Einarsdottir, and K. Svanberg, Journal of Biomedical Optics **12**(1), 014022 (2007).
[293] J. Ashburner and K. Friston, Neuroimage **6**(3), 209–217 (1997).
[294] W. B. Cai and X. Y. Chen, Journal of Nuclear Medicine **49**(June), 113S–128S (2008).
[295] F. Maes, A. Collignon, D. Vandermeulen, G. Marchal, and P. Suetens, Ieee Transactions On Medical Imaging **16**(2), 187–198 (1997).
[296] T. Peters, B. Davey, P. Munger, R. Comeau, A. Evans, and A. Olivier, Ieee Transactions On Medical Imaging **15**(2), 121–128 (1996).
[297] B. J. Tromberg, B. W. Pogue, K. D. Paulsen, A. G. Yodh, D. A. Boas, and A. E. Cerussi, Medical Physics **35**(6), 2443–2451 (2008).
[298] Q. Zhang, T. J. Brukilacchio, A. Li, J. J. Stott, T. Chaves, E. Hillman, T. Wu, M. Chorlton, E. Rafferty, R. H. Moore, D. B. Kopans, and D. A. Boas, Journal of Biomedical Optics **10**(2), 024033 (2005).

 

REVIEW ARTICLE



[299] R. Kumar, M. Nyk, T. Y. Ohulchanskyy, C. A. Flask, and P. N. Prasad, Advanced Functional Materials **19**(6), 853–859 (2009).
[300] Z. Q. Li, Y. Zhang, B. Shuter, and N. M. Idris, Langmuir **25**(20), 12015–12018 (2009).
[301] J. Zhou, M. X. Yu, Y. Sun, X. Z. Zhang, X. J. Zhu, Z. H. Wu, D. M. Wu, and F. Y. Li, Biomaterials **32**(4), 1148–1156 (2011).
[302] Y. L. Liu, K. L. Ai, J. H. Liu, Q. H. Yuan, Y. Y. He, and L. H. Lu, Angewandte Chemie-international Edition **51**(6), 1437–1442 (2012).
[303] A. Xia, M. Chen, Y. Gao, D. Wu, W. Feng, and F. Li, Biomaterials **33**(21), 5394–5405 (2012).
[304] H. Xing, W. Bu, Q. Ren, X. Zheng, M. Li, S. Zhang, H. Qu, Z. Wang, Y. Hua, K. Zhao, L. Zhou, W. Peng, and J. Shi, Biomaterials **33**(21), 5384–5393 (2012).
[305] H. Y. Xing, W. B. Bu, S. J. Zhang, X. P. Zheng, M. Li, F. Chen, Q. J. He, L. P. Zhou, W. J. Peng, Y. Q. Hua, and J. L. Shi, Biomaterials **33**(4), 1079–1089 (2012).
[306] X. J. Zhu, J. Zhou, M. Chen, M. Shi, W. Feng, and F. Y. Li, Biomaterials **33**(18), 4618–4627 (2012).

# Paper IV

**Balancing power density based quantum yield characterization of upconverting nanoparticles for arbitrary excitation intensities**

H. Liu, C. T. Xu, D. Lindgren, H. Xie, D. Thomas, C. Gundlach, S. Andersson-Engels.

*Nanoscale* **5**, 4770-4775 (2013).

Nanoscale

RSC Publishing

PAPER

View Article Online
View Journal | View Issue

# Balancing power density based quantum yield characterization of upconverting nanoparticles for arbitrary excitation intensities†

Cite this: *Nanoscale*, 2013, **5**, 4770

Haichun Liu,*[a] Can T. Xu,[a] David Lindgren,[b] Haiyan Xie,[a] Diana Thomas,[c] Carsten Gundlach‡[c] and Stefan Andersson-Engels[a]

Received 26th January 2013
Accepted 15th March 2013

DOI: 10.1039/c3nr00469d

www.rsc.org/nanoscale

Upconverting nanoparticles (UCNPs) have recently shown great potential as contrast agents in biological applications. In developing different UCNPs, the characterization of their quantum yield (QY) is a crucial issue, as the typically drastic decrease in QY for low excitation power densities can either impose a severe limitation or provide an opportunity in many applications. The power density dependence of the QY is governed by the competition between the energy transfer upconversion (ETU) rate and the linear decay rate in the depopulation of the intermediate state of the involved activator in the upconversion process. Here we show that the QYs of $Yb^{3+}$ sensitized two-photon upconversion emissions can be well characterized by the balancing power density, at which the ETU rate and the linear decay rate have equal contributions, and its corresponding QY. The results in this paper provide a method to fully describe the QY of upconverting nanoparticles for arbitrary excitation power densities, and is a fast and simple approach for assessing the applicability of UCNPs from the perspective of energy conversion.

## 1 Introduction

Upconverting nanoparticles (UCNPs) doped with rare-earth ions have been rapidly developing during the last decade,[1–5] and their unique properties together with very promising results suggest that they have the potential to become a major class of contrast agents in the field of biophotonics.[6–10] This is mainly due to their ability to convert low energy excitation photons into emission photons with higher energy,[11] even under broadband excitation.[12] This upconversion (UC) ability provides advantages including autofluorescence rejection,[13] better light penetration and improved spatial image resolution.[7,14,15] So far, UCNPs have been successfully used in diverse biological applications such as photodynamic therapy (PDT),[8] microscopy,[9,10] bioanalytical assays,[16,17] diffuse optical imaging,[7,15,18,19] and multimodality imaging.[20] Although UCNPs have many beneficial properties for biological applications, a major challenge of their use is the power density dependent and relatively low QYs at the low excitation intensities required for these applications.[21] It has been reported that UCNPs could have QYs on the order of a few percent at high excitation intensities where the UCNPs are saturated,[14] while the QYs could decline by many orders of magnitude when they are used at low excitation intensities.[14] Obviously, such power density dependent QYs need to be properly evaluated in order to assess the applicability of UCNPs in specific biomedical areas. In spite of the interest, this crucial issue has not been addressed in any satisfactory manner, neither theoretically nor experimentally.[22] To date, the reports on the QYs of UCNPs are surprisingly scarce in the literature,[14,23–26] and even in the few publications available, the QY data are usually provided at a specific excitation intensity, ignoring their power density dependency.[23–26] Although full QY information can be obtained by extensive measurements at all excitation intensities, obviously this approach is not ideal because of the accompanying burden of such measurements. In addition, large errors would be also introduced in the measurements at high excitation intensities due to saturation effects of the optical equipment, such as the attenuator and the power meter typically needed for such measurements. This will ruin the accuracy of the QY data. Hence, a better understanding of the power density dependency of the QY for a particular design of UCNPs and thus characterizing this in a convenient way is highly desirable, and will be of major importance for the future development and applications of UCNPs in general. This is addressed in this paper.

The power density dependence of the QY is governed by the competition between the two major relaxation mechanisms involved at the intermediate energy state in the UC process, *i.e.*,

[a]*Division of Atomic Physics, Department of Physics, Lund University, P. O. Box 118, S-221 00 Lund, Sweden. E-mail: haichun.liu@fysik.lth.se; Fax: +46 46 222 4250; Tel: +46 46 222 7471*

[b]*Division of Solid State Physics, Department of Physics, Lund University, P. O. Box 118, S-221 00 Lund, Sweden*

[c]*MAX IV Laboratory, Lund University, P. O. Box 118, S-221 00 Lund, Sweden*

† Electronic supplementary information (ESI) available. See DOI: 10.1039/c3nr00469d

‡ Present address: Department of Physics, Technical University of Denmark, 2800 Kgs. Lyngby, Denmark.

the energy transfer upconversion (ETU) and the linear decay.[27,28] In this paper, the dependence of the QY of $Yb^{3+}$ sensitized two-photon UC emission on the excitation intensity is modeled using steady-state rate equation analysis, with the activator described by a quasi-three-level structure (including the ground, intermediate and emitting states). It is found that the power density dependent QY can be well characterized by the balancing power density, at which the ETU rate and the linear decay rate equally contribute to the depopulation of the intermediate state of the activator, and the QY at this balancing point. This is experimentally exemplified using near infrared (NIR) emitting $Yb^{3+}/Tm^{3+}$ codoped $NaYF_4$ UCNPs. Thus, the determination of the balancing power density and its corresponding QY is suggested as a fast approach for characterizing the power density dependent QYs of UCNPs, for the sake of assessing the applicability of UCNPs in biological applications from the perspective of energy conversion.

## 2 Experimental

### 2.1 Synthesis of the UCNPs

All the chemicals were purchased from Sigma-Aldrich and used without further purification. The core nanoparticles were synthesized through a recently reported approach.[29] In a typical synthesis procedure, 0.75 mmol $YCl_3$, 0.25 mmol $YbCl_3$ and 0.003 mmol $TmCl_3$ were mixed with 6 mL oleic acid and 17 mL octadecene in a 250 mL flask and heated to 160 °C for 30 min to form a clear solution. After cooling down to room temperature, 10 mL of a methanol solution containing 4 mmol $NH_4F$ (0.1482 g) and 2.5 mmol NaOH (0.1 g) was added, followed by a stirring of the mixture for 30 min at 50 °C. By slowly heating the solution, the methanol was removed and the resulting solution was heated to 300 °C for 1.5 h under an argon atmosphere, and then cooled to room temperature. The nanoparticles were precipitated with ethanol and washed with an ethanol–water mixture for three times, and then collected after centrifugation and redispersed in a nonpolar solvent. The core–shell nanoparticles were produced by slightly modifying the above procedure through incorporating the prepared core nanoparticles as the seeds in the synthesis.[30] 1 mmol $YCl_3$ was solely used to provide rare-earth ions for the coating layer. Due to the presence of the capping ligand, both the core and core–shell nanoparticles could be well dispersed in commonly used nonpolar solvents, such as hexane, cyclohexane, chloroform, and toluene, and are colloidally stable for months without visible agglomeration.

### 2.2 Characterization of the UCNPs

Transmission electron microscopy (TEM) images were recorded on a JEOL model 3000F microscope. X-ray diffraction (XRD) measurements of UCNP hexane suspensions were performed on the crystallography beamline I711 at the synchrotron facility MAXlab, Lund, Sweden.[31] A wavelength of 1.01 Å was employed in the measurements. The samples were placed in glass capillaries with a diameter of 0.5 mm which rotated during data acquisition. The data were recorded using a Titan CCD camera placed 70 mm from the sample. For the photoluminescence (PL) measurements, a Thorlabs L975P1WJ laser diode at 975 nm was utilized as the excitation source driven by a Thorlabs benchtop laser diode current controller LDC220C, with the temperature stabilized at 25 °C. The downconversion infrared luminescence was collected by a 20× objective lens with an NA of 0.45 and further directed through two pieces of Spectrogon LP-1000 nm long-pass filters in order to minimize any influence of reflected laser light. The luminescence light was then diffracted in a monochromator by a 150 gr $mm^{-1}$ grating blazed at 1200 nm and finally detected by a liquid $N_2$-cooled NIR HgCdTe camera. The UC luminescence spectra were measured on a sensitive spectrofluorometer setup using the same 975 nm laser diode as the excitation source.[14] The emissions were recorded using a grating spectrometer Ocean Optics QE65000 with a slit width of 50 μm. The excitation power was measured using an Ophir Nova II laser power meter equipped with a photodiode sensor (PD300), while the spot size of the excitation beam was measured using a Hamamatsu ORCA-ER C4742-80 camera. For QY measurements, the system utilized standard fluorophores as a reference, calibrated using the integrating-sphere based Hamamatsu C9920 QY measurement system. The principle of the QY measurement was described in detail in our previously published work.[14] All optical measurements were carried out at room temperature.

## 3 Results and discussion

### 3.1 Quantitative analysis using rate equations

The mechanism of $Yb^{3+}$ sensitized two-photon UC emission is simplified and schematically depicted in Fig. 1. Here the activator is described by a quasi-three-level model: the ground state 0, the intermediate state 1, and the emitting state 2. States 1 and 2 may represent coupled energy levels rather than a single level for specific two-photon UC emissions. As shown, the activator ion at the ground state is first excited to state 1 through a phonon-assisted energy transfer from an excited $Yb^{3+}$ ion (ETU1), and further excited to state 2 through a second energy transfer process (ETU2). Subsequently, the UC emission is generated by the transition 2 → 0.

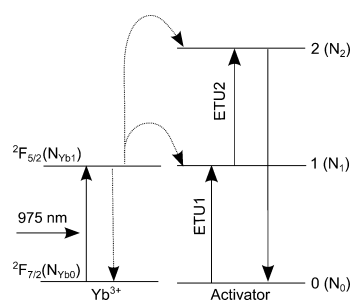


**Fig. 1** Schematic energy level diagrams of the $Yb^{3+}$ and activator ions and the proposed UC mechanism following laser diode excitation at 975 nm. The variables used in the text for the population densities of different levels are indicated within the parentheses.

The power density dependent behavior of the UC emission intensity under continuous wave (CW) excitation can be described by the following steady-state rate equations:

$$\frac{dN_{Yb1}}{dt} = \sigma\rho N_{Yb0} - \frac{N_{Yb1}}{\tau_{Yb1}} = 0, \quad (1a)$$

$$\frac{dN_1}{dt} = C_0 N_0 N_{Yb1} - C_1 N_1 N_{Yb1} - \frac{N_1}{\tau_1} = 0, \quad (1b)$$

$$\frac{dN_2}{dt} = C_1 N_1 N_{Yb1} - \frac{N_2}{\tau_2} = 0, \quad (1c)$$

where $\sigma$ is the absorption cross-section of $Yb^{3+}$ ions; $\rho$ is the excitation photon flux, which is linearly related to power density; $\tau_1$ and $\tau_2$ are the lifetimes of activator ions at states 1 and 2, respectively, including both the contributions of radiative and non-radiative relaxation mechanisms, while $\tau_{Yb1}$ is the lifetime of $Yb^{3+}$ ions at $^2F_{5/2}$ state; $C_0$ and $C_1$ are the rate constants for the energy transfer processes ETU1 and ETU2, respectively. In this model, the depletion of the population of $^2F_{5/2}$ ($Yb^{3+}$) state due to ETU processes is omitted because the ETU rates at $^2F_{5/2}$ ($Yb^{3+}$) state are much lower than its linear decay rates.[32,33] For the same reason, the contribution to the depletion of state 2 due to ETU to even higher states is not considered either. Under these assumptions, an expression for the population density of $^2F_{5/2}$ ($Yb^{3+}$) state can be obtained

$$N_{Yb1} = \tau_{Yb1}\sigma N_{Yb0}\rho, \quad (2)$$

and the power density dependence of the UC steady-state emission from state 2 can be derived as by rearranging eqn (1a–c)

$$I = \frac{N_2}{\tau_2^{rad}}h\nu = \frac{C_0 C_1 \tau_{Yb1}{}^2\left(\tau_2/\tau_2^{rad}\right)N_0 h\nu\sigma^2 N_{Yb0}{}^2\rho^2}{\frac{1}{\tau_1} + C_1\tau_{Yb1}\sigma N_{Yb0}\rho}, \quad (3)$$

where $\tau_2^{rad}$ is the radiative lifetime of state 2, $h$ is the Planck's constant and $\nu$ is the frequency of the UC emission light. The slope efficiency of the UC PL intensity with respect to the excitation intensity can be extracted by a linear fit of the data in a double-logarithmic scale, and indicates the multi-photon excitation nature of the UC emission.[27,28] Mathematically, this slope efficiency is described by the derivative of log $I$ over log $\rho$, *i.e.*,

$$k \equiv \frac{d\log I}{d\log \rho} = 1 + \frac{1}{1 + \tau_1 \cdot C_1\tau_{Yb1}\sigma N_{Yb0}\rho}. \quad (4)$$

The details of the derivation of the above equation are described in Section S4 in the ESI.† According to eqn (4), the excitation intensity will determine the shape of the power density dependence curve. Under low excitation intensities, where the linear decay rate is dominating over the ETU rate, *i.e.*, $\frac{1}{\tau_1} \gg C_1\tau_{Yb1}\sigma N_{Yb0}\rho$, the power density dependence curve will appear with a slope of 2.0, indicating a quadratic dependence on the excitation intensity; while under high excitation intensities, where the ETU rate plays a significantly more important role, the curve will appear with a slope of 1.0, *i.e.*, exhibiting a linear dependence on the excitation intensity. In the intermediate range, the slope efficiency changes gradually from 2.0 to 1.0 as the excitation intensity is increased. It is noteworthy to point out that, at the balancing point

$$\rho_b = \frac{1}{\tau_1 \cdot C_1\tau_{Yb1}\sigma N_{Yb0}}, \quad (5)$$

where the ETU rate and linear decay rate equally contribute to the depopulation of state 1, *i.e.*, $\frac{1}{\tau_1} = C_1\tau_{Yb1}\sigma N_{Yb0}\rho_b$, the power density dependence curve has a slope efficiency of 1.5.

Based on eqn (3), the QY, $\eta$, of the two-photon UC emission at any power density can be defined by

$$\eta \equiv \frac{I}{\sigma N_{Yb0}\rho h\nu} = \frac{C_0 C_1 \tau_{Yb1}{}^2\left(\tau_2/\tau_2^{rad}\right)N_0\sigma N_{Yb0}\rho}{\frac{1}{\tau_1} + C_1\tau_{Yb1}\sigma N_{Yb0}\rho}. \quad (6)$$

The maximum, $\eta_s$, is reached when the pump power density is at the saturation level so that the contribution of the term $1/\tau_1$ can be neglected,

$$\eta_s = C_0 N_0 \tau_{Yb1}\tau_2/\tau_2^{rad}. \quad (7)$$

By inserting eqn (5) and (7) into eqn (6), we obtain

$$\eta = \frac{\eta_s \cdot \frac{\rho}{\rho_b}}{1 + \frac{\rho}{\rho_b}}. \quad (8)$$

Particularly, when the excitation intensity is at the balancing power density, $\rho_b$, the QY is the half of the maximum QY, $\eta_s$, *i.e.*,

$$\eta_b = \eta(\rho = \rho_b) = \frac{\eta_s}{2}. \quad (9)$$

Thus, full QY information can be obtained by determining the balancing power density, $\rho_b$, and the corresponding QY, $\eta_b$, because $\rho_b$ characterizes the power density dependence of the QY while twofold $\eta_b$ determines the maximum attainable QY.

The UC mechanisms of most $Yb^{3+}$ sensitized two-photon UC emissions of major activators ($Er^{3+}$, $Ho^{3+}$ and $Tm^{3+}$) of UCNPs, including the green emissions of $Er^{3+}$ ions ($^2H_{11/2}/^4S_{3/2} \rightarrow {}^4I_{15/2}$) and $Ho^{3+}$ ions ($^5S_2/^5F_4 \rightarrow {}^5I_8$), and the NIR emission of $Tm^{3+}$ ions ($^3H_4 \rightarrow {}^3H_6$), have been well determined in the literature.[11,34,35] The simplified model and the corresponding conclusions above are valid for all these two-photon UC emissions, as verified by the detailed rate equation analysis based on more reliable and sophisticated models in Sections S1–S3 in the ESI.† When describing the green UC emission of $Er^{3+}$ ions, state 2 corresponds to the coupled levels $^4F_{7/2}/^2H_{11/2}/^4S_{3/2}$, achieved by fast non-radiative decay from state $^4F_{7/2}$ to states $^2H_{11/2}/^4S_{3/2}$, while for the NIR UC emission of $Tm^{3+}$ ions, the states 1 and 2 correspond to the coupled levels $^3H_5/^3F_4$ and $^3F_{2,3}/^3H_4$, respectively. It is notable that in some special cases the UC emissions mentioned above exhibit cubic power density dependence, *e.g.*, the green UC emission of $Er^{3+}$ ions.[36] In such cases, the proposed approach needs to be modified. In addition, the simplified model does not cover the red UC emissions of $Er^{3+}$ and $Ho^{3+}$ ions, where a more sophisticated model is required due to their slightly different mechanisms.

 

### 3.2 Morphology, crystalline structure and UC luminescence property of UCNPs

The validity of this approach for QY characterization was tested by investigating the NIR UC emission of two different $Yb^{3+}/Tm^{3+}$ codoped samples: core ($NaYF_4$:$Yb^{3+}$,$Tm^{3+}$) and core–shell ($NaYF_4$:$Yb^{3+}$,$Tm^{3+}$@$NaYF_4$) nanoparticles, synthesized through recently reported approaches.[29,30] Fig. 2a and b show the TEM images of the synthesized UCNPs. As is seen, the core and core–shell nanoparticles appear monodisperse and nearly spherical in shape, and have average diameters of approximately 33 and 43 nm, respectively. The thickness of the shell in core–shell nanoparticles is thus estimated to be 5 nm. The growth of a $NaYF_4$ layer did not change the morphological uniformity. In addition, the phase of the nanoparticles also remained unchanged. Both the core and core–shell nanoparticles have the same phase, verified by the XRD results shown in Fig. 2c. All the peaks can be well indexed in accordance with the data reported in JCPDS standard card (28-1192), indicating the pure hexagonal phase of the nanoparticles.

The PL result of the core nanoparticles under excitation of a CW 975 nm laser diode, shown in Fig. 3, confirms that this NIR UC emission can be treated with the proposed model. As is seen, the emission peaks resulting from states $^3F_{2,3}$ and $^3H_5$ at 696 nm ($^3F_{2,3} \rightarrow {}^3H_6$), 1170 nm ($^3F_{2,3} \rightarrow {}^3F_4$), 1650 nm ($^3F_{2,3} \rightarrow {}^3H_5$) and 1220 nm ($^3H_5 \rightarrow {}^3H_6$) are absent or significantly weaker compared with those originating from states $^3H_4$ and $^3F_4$ at 800 nm ($^3H_4 \rightarrow {}^3H_6$), 1470 nm ($^3H_4 \rightarrow {}^3F_4$) and 1850 nm ($^3F_4 \rightarrow {}^3H_6$),[37,38] indicating fast non-radiative decays, $^3F_{2,3} \rightsquigarrow {}^3H_4$ and $^3H_5 \rightsquigarrow {}^3F_4$.[38,39] The strong emission peak centered at 1035 nm in Fig. 3b originates from the transition of

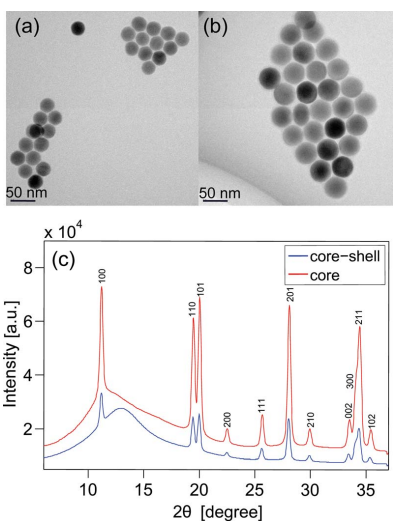


**Fig. 2** TEM images of (a) the core $NaYF_4$:$Yb^{3+}$,$Tm^{3+}$ nanoparticles and (b) the core–shell $NaYF_4$:$Yb^{3+}$,$Tm^{3+}$@$NaYF_4$ nanoparticles. (c) XRD patterns of the synthesized core and core–shell UCNPs.

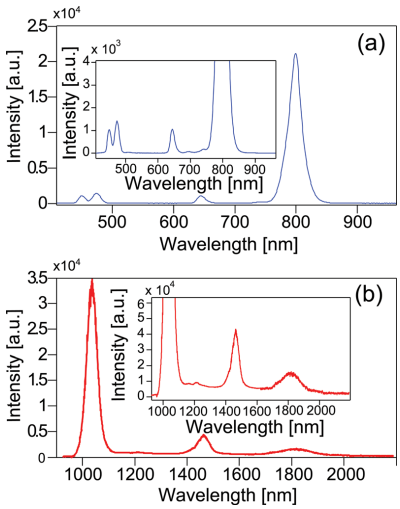


**Fig. 3** (a) The upconversion and (b) the infrared PL spectra of the core $NaYF_4$:$Yb^{3+}$,$Tm^{3+}$ nanoparticles. The insets in (a) and (b) present the zoomed-in spectra in order to visualize the emission peaks around 700 nm and 1200 nm, respectively. Both spectra were recorded at a power density of 125 W $cm^{-2}$ under excitation of a CW 975 nm laser diode.

$Yb^{3+}$: $^2F_{5/2} \rightarrow {}^2F_{7/2}$,[40–42] while the emissions in Fig. 3a at 450 nm, 474 nm and 646 nm are generated by the transitions of $Tm^{3+}$: $^1D_2 \rightarrow {}^3F_4$, $^1G_4 \rightarrow {}^3H_6$ and $^1G_4 \rightarrow {}^3F_4$, respectively. The core–shell nanoparticles have very similar PL spectra, thus not shown. It should be noted that the UC emissions in the blue and red spectral regions originating from the states $^1D_2$ and $^1G_4$ are much weaker than the NIR UC emission, even at an excitation power density as high as 125 W $cm^{-2}$. This supports the treatment of omitting the ETU rate from state 2 to higher energy levels in the theoretical model.

### 3.3 Power density dependence and quantum yield characterization of UCNPs

In order to determine the balancing power density, the power dependence curves for the core and core–shell nanoparticles were measured in a power density span of 0.027–130 W $cm^{-2}$, as shown in Fig. 4. At the lowest power densities (below 0.05 W $cm^{-2}$), both the samples appear with a slope of 2.0, indicating two-photon excitation processes. When the excitation power density is increased, the power dependence curves start to deviate, with the curve for core–shell nanoparticles deviating earlier than that for core nanoparticles. By fitting the power dependence data with eqn (3) followed by the calculation of the power density giving a slope of 1.5 using eqn (4), the balancing power densities were determined to be approximately 3.8 W $cm^{-2}$ and 1.3 W $cm^{-2}$ for the core and core–shell nanoparticles, respectively. As no obvious phase change is found in the XRD patterns of these two samples as shown in Fig. 2c, the smaller value for core–shell nanoparticles could be explained by the

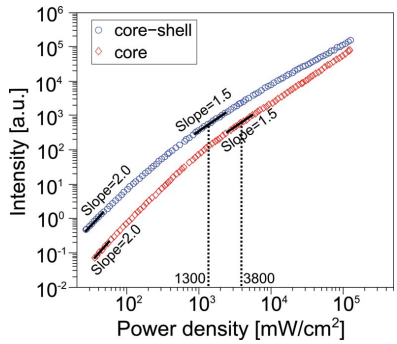


**Fig. 4** The power density dependencies of the NIR UC emission band at 800 nm of the core $NaYF_4$:$Yb^{3+}$,$Tm^{3+}$ nanoparticles (red diamonds) and the core–shell $NaYF_4$:$Yb^{3+}$,$Tm^{3+}$@$NaYF_4$ nanoparticles (blue circles). The black solid lines represent the tangents of the power density dependence curves.

longer lifetimes $\tau_1$ and $\tau_{Yb1}$, caused by the protection of the shielding layer epitaxially grown on the core nanoparticles.[38,43]

The QYs of the synthesized UCNPs were measured in a power density range of 0.027–20 W $cm^{-2}$ on a spectrofluorometer-based setup reported in our previous work,[14] as shown in Fig. 5. At the balancing power density, the core and core–shell nanoparticles have QYs of approximately 0.45% and 1.2%, respectively. The fittings of the QY data with eqn (8) were subsequently implemented with the parameter $\rho_b$ locked to the experimentally obtained values. As is seen, the QY data can be well fitted both for the core and core–shell nanoparticles, with the fitted maximum attainable QY of 0.91% for the core and 2.6% for core–shell nanoparticles, which can be well estimated by the twofold QY at the balancing power density.

One main advantage of the proposed approach for QY characterization by providing ($\rho_b$, $2\eta_b$) is that the number of quantitative QY measurements can be dramatically reduced. Especially, measurements under harsh pump conditions (in a saturating range) can be avoided because the balancing power density is significantly lower than the saturation power density. Noticing that the QY starts to decline dramatically when the excitation intensity decreases to below the balancing point according to eqn (8), a low balancing power density implies that a considerable QY can be achieved under mild pump conditions. In this sense, the determination of the balancing power density can be used as a fast and simple approach to evaluate the applicability of UCNPs in applications where low excitation intensities are required, such as deep tissue imaging in biological applications. The merit by doing so is that no absolute measurements on luminescence intensities need to be performed, since the balancing power density depends on the trend of the luminescence intensity change instead of absolute intensities.

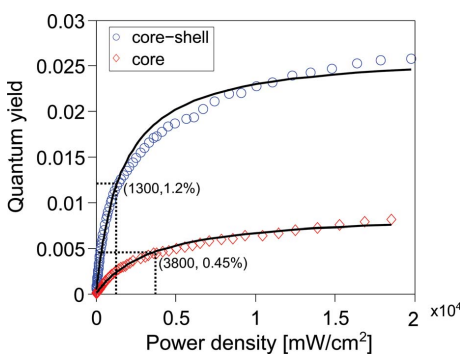


**Fig. 5** The quantum yields of the NIR UC emission band at 800 nm of the core $NaYF_4$:$Yb^{3+}$,$Tm^{3+}$ nanoparticles (red diamonds) and the core–shell $NaYF_4$:$Yb^{3+}$,$Tm^{3+}$@$NaYF_4$ nanoparticles (blue circles) at various excitation power densities. The black solid lines stand for the fitted data.

## 4 Conclusions

To conclude, the QY of $Yb^{3+}$ sensitized two-photon UC emission is theoretically investigated based on a simplified steady-state rate equation model. It is found that the QY can be well characterized by the balancing power density and its corresponding QY. The former describes the power density dependent behavior of the QY, while the latter determines the maximum attainable QY. This is exemplified by experimental measurements on the QYs of core and core–shell $Yb^{3+}$/$Tm^{3+}$ codoped $NaYF_4$ UCNPs prepared in our lab. Currently, no simple approach exists to characterize the power density dependent QY of UCNPs and thus to assess their applicability in biological applications from the perspective of energy conversion. The determination of the balancing power density and its corresponding QY of the proposed method can be used as a fast and simple approach for such purposes.

## Acknowledgements

M. E. Messing and L. R. Wallenberg are gratefully acknowledged for the help with the TEM measurements. J. Larsson is acknowledged for the help with the XRD measurements. D. Hessman is acknowledged for the help with infrared PL measurements. We thank S. Fredriksson, F. Olsson, A. Gisselsson, G. Dumlupinar and X. Wu for the help with the synthesis of the nanoparticles. This work was supported by a grant from the Swedish Research Council (grant no. 621-2011-4265) and a Linneaus grant to the Lund Laser Centre.

## References

1 X. Wang, J. Zhuang, Q. Peng and Y. D. Li, *Nature*, 2005, **437**, 121–124.
2 H.-X. Mai, Y.-W. Zhang, R. Si, Z.-G. Yan, L.-D. Sun, L.-P. You and C.-H. Yan, *J. Am. Chem. Soc.*, 2006, **128**, 6426–6436.
3 J.-C. Boyer, L. A. Cuccia and J. A. Capobianco, *Nano Lett.*, 2007, **7**, 847–852.

 

4 F. Wang, Y. Han, C. S. Lim, Y. Lu, J. Wang, J. Xu, H. Chen, C. Zhang, M. Hong and X. Liu, *Nature*, 2010, **463**, 1061–1065.
5 F. Wang, R. Deng, J. Wang, Q. Wang, Y. Han, H. Zhu, X. Chen and X. Liu, *Nat. Mater.*, 2011, **10**, 968–973.
6 D. K. Chatterjee, A. J. Rufaihah and Y. Zhang, *Biomaterials*, 2008, **29**, 937–943.
7 M. Nyk, R. Kumar, T. Y. Ohulchanskyy, E. J. Bergey and P. N. Prasad, *Nano Lett.*, 2008, **8**, 3834–3838.
8 N. M. Idris, M. K. Gnanasammandhan, J. Zhang, P. C. Ho, R. Mahendran and Y. Zhang, *Nat. Med.*, 2012, **18**, 1580–1585.
9 S. Wu, G. Han, D. J. Milliron, S. Aloni, V. Altoe, D. V. Talapin, B. E. Cohen and P. J. Schuck, *Proc. Natl. Acad. Sci. U. S. A.*, 2009, **106**, 10917–10921.
10 J. Pichaandi, J.-C. Boyer, K. R. Delaney and F. C. J. M. van Veggel, *J. Phys. Chem. C*, 2011, **115**, 19054–19064.
11 F. Auzel, *Chem. Rev.*, 2004, **104**, 139–173.
12 W. Zou, C. Visser, J. A. Maduro, M. S. Pshenichnikov and J. C. Hummelen, *Nat. Photonics*, 2012, **6**, 560–564.
13 C. T. Xu, N. Svensson, J. Axelsson, P. Svenmarker, G. Somesfalean, G. Chen, H. Liang, H. Liu, Z. Zhang and S. Andersson-Engels, *Appl. Phys. Lett.*, 2008, **93**, 171103.
14 C. T. Xu, P. Svenmarker, H. Liu, X. Wu, M. E. Messing, L. R. Wallenberg and S. Andersson-Engels, *ACS Nano*, 2012, **6**, 4788–4795.
15 P. Svenmarker, C. T. Xu and S. Andersson-Engels, *Opt. Lett.*, 2010, **35**, 2789–2791.
16 M. Ylihärsilä, T. Valta, M. Karp, L. Hattara, E. Harju, J. Hölsä, P. Saviranta, M. Waris and T. Soukka, *Anal. Chem.*, 2011, **83**, 1456–1461.
17 H. Päkkilä, M. Ylihärsilä, S. Lahtinen, L. Hattara, N. Salminen, R. Arppe, M. Lastusaari, P. Saviranta and T. Soukka, *Anal. Chem.*, 2012, **84**, 8628–8634.
18 C. T. Xu, J. Axelsson and S. Andersson-Engels, *Appl. Phys. Lett.*, 2009, **94**, 251107.
19 H. Liu, C. T. Xu and S. Andersson-Engels, *Opt. Lett.*, 2010, **35**, 718–720.
20 J. Zhou, M. Yu, Y. Sun, X. Zhang, X. Zhu, Z. Wu, D. Wu and F. Li, *Biomaterials*, 2011, **32**, 1148–1156.
21 C. T. Xu, Q. Zhan, H. Liu, G. Somesfalean, J. Qian, S. He and S. Andersson-Engels, *Laser Photonics Rev.*, 2013, DOI: 10.1002/lpor201200052.
22 D. O. Faulkner, S. Petrov, D. D. Perovic, N. P. Kherani and G. A. Ozin, *J. Mater. Chem.*, 2012, **22**, 24330–24334.
23 J.-C. Boyer and F. C. J. M. van Veggel, *Nanoscale*, 2010, **2**, 1417–1419.
24 Q. Liu, Y. Sun, T. Yang, W. Feng, C. Li and F. Li, *J. Am. Chem. Soc.*, 2011, **133**, 17122–17125.
25 A. D. Ostrowski, E. M. Chan, D. J. Gargas, E. M. Katz, G. Han, P. J. Schuck, D. J. Milliron and B. E. Cohen, *ACS Nano*, 2012, **6**, 2686–2692.
26 G. Chen, J. Shen, T. Y. Ohulchanskyy, N. J. Patel, A. Kutikov, Z. Li, J. Song, R. K. Pandey, H. Ågren, P. N. Prasad and G. Han, *ACS Nano*, 2012, **6**, 8280–8287.
27 M. Pollnau, D. R. Gamelin, S. R. Lüthi, H. U. Güdel and M. P. Hehlen, *Phys. Rev. B: Condens. Matter Mater. Phys.*, 2000, **61**, 3337–3346.
28 J. F. Suyver, A. Aebischer, S. García-Revilla, P. Gerner and H. U. Güdel, *Phys. Rev. B: Condens. Matter Mater. Phys.*, 2005, **71**, 125123.
29 Z. Li and Y. Zhang, *Nanotechnology*, 2008, **19**, 345606.
30 H. Qian and Y. Zhang, *Langmuir*, 2008, **24**, 12123–12125.
31 Y. Cerenius, K. Ståhl, L. A. Svensson, T. Ursby, Å. Oskarsson, J. Albertsson and A. Liljas, *J. Synchrotron Radiat.*, 2000, **7**, 203–208.
32 A. M. Pires, O. A. Serra, S. Heer and H. U. Güdel, *J. Appl. Phys.*, 2005, **98**, 063529.
33 G. Chen, H. Liu, H. Liang, G. Somesfalean and Z. Zhang, *J. Phys. Chem. C*, 2008, **112**, 12030–12036.
34 J. Wright, *Top. Appl. Phys.*, 1976, **15**, 239.
35 G. Chen, H. Liu, G. Somesfalean, H. Liang and Z. Zhang, *Nanotechnology*, 2009, **20**, 385704.
36 F. Song, G. Zhang, M. Shang, H. Tan, J. Yang and F. Meng, *Appl. Phys. Lett.*, 2001, **79**, 1748–1750.
37 T. Schweizer, B. N. Samson, J. R. Hector, W. S. Brocklesby, D. W. Hewak and D. N. Payne, *J. Opt. Soc. Am. B*, 1999, **16**, 308–316.
38 F. Wang, J. Wang and X. Liu, *Angew. Chem., Int. Ed.*, 2010, **49**, 7456–7460.
39 G. Chen, T. Y. Ohulchanskyy, R. Kumar, H. Ågren and P. N. Prasad, *ACS Nano*, 2010, **4**, 3163–3168.
40 F. Güell, J. Massons, J. Gavaldà, M. C. Pujol, M. Aguiló and F. Díaz, *J. Appl. Phys.*, 2007, **101**, 033108.
41 L. Huang, S. Shen and A. Jha, *J. Non-Cryst. Solids*, 2004, **345–346**, 349–353.
42 D. Chen, Y. Yu, F. Huang, H. Lin, P. Huang, A. Yang, Z. Wang and Y. Wang, *J. Mater. Chem.*, 2012, **22**, 2632–2640.
43 Y. Wang, K. Liu, X. Liu, K. Dohnalová, T. Gregorkiewicz, X. Kong, M. C. G. Aalders, W. J. Buma and H. Zhang, *J. Phys. Chem. Lett.*, 2011, **2**, 2083–2088.

# Paper V

**Deep tissue optical imaging of upconverting nanoparticles enabled by exploiting higher intrinsic quantum yield through use of millisecond single pulse excitation with high peak power**

H. Liu, C. T. Xu, G. Dumlupinar, O. B. Jensen, P. E. Andersen, S. Andersson-Engels.

*Nanoscale* **5**, 10034-10040 (2013).

Nanoscale

RSC Publishing

PAPER

View Article Online
View Journal | View Issue

Cite this: *Nanoscale*, 2013, **5**, 10034

# Deep tissue optical imaging of upconverting nanoparticles enabled by exploiting higher intrinsic quantum yield through use of millisecond single pulse excitation with high peak power†

Haichun Liu,*[a] Can T. Xu,[a] Gökhan Dumlupinar,[a] Ole B. Jensen,[b] Peter E. Andersen[b] and Stefan Andersson-Engels[a]

Received 17th April 2013
Accepted 22nd July 2013

DOI: 10.1039/c3nr01917a

www.rsc.org/nanoscale

We have accomplished deep tissue optical imaging of upconverting nanoparticles at 800 nm, using millisecond single pulse excitation with high peak power. This is achieved by carefully choosing the pulse parameters, derived from time-resolved rate-equation analysis, which result in higher intrinsic quantum yield that is utilized by upconverting nanoparticles for generating this near infrared upconversion emission. The pulsed excitation approach thus promises previously unreachable imaging depths and shorter data acquisition times compared with continuous wave excitation, while simultaneously keeping the possible thermal side-effects of the excitation light moderate. These key results facilitate means to break through the general shallow depth limit of upconverting-nanoparticle-based fluorescence techniques, necessary for a range of biomedical applications, including diffuse optical imaging, photodynamic therapy and remote activation of biomolecules in deep tissues.

## 1 Introduction

During the last decade, upconverting nanoparticles (UCNPs) have developed rapidly,[1–6] and show great promise as contrast agents in biological applications.[7–11] Despite tremendous improvements of UCNPs, their limited quantum yield (QY), especially at a low excitation light level, is still a major concern for most potential biological applications.[12] Two interesting and powerful techniques under development are deep tissue optical imaging[13] and photodynamic therapy (PDT),[14] both of which require high QY. The present low QY thus hinders the potential of these techniques to be unleashed due to prolonged data acquisition and treatment times, and shallow applicable depths.[12,15] Although low QY to some extent can be overcome by increasing the excitation light level, such improvements are fundamentally restricted for continuous wave (CW) excitation due to risks of tissue damage, regulated by the ANSI standards.[16]

Instead, the opportunity to break through the low power density limit of upconversion (UC) emission while limiting thermal effects of the excitation light is proposed here by employing pulsed excitation.[12,17,18] In addition, we realize that the applicability of UCNPs could be further boosted by utilizing single-shot excitation schemes, *i.e.*, short single pulse excitation with high peak power. Similar to multiphoton microscopy, pulsed excitation would provide high photon density during the pulse, while keeping the average power (*i.e.*, the deposited energy responsible for the heating) moderate. Due to the non-linear power density dependence of UC emission, pulsed excitation would be highly beneficial. However, two important differences exist between the UC emission and direct two-photon fluorescence. Firstly, the QY is much higher for UCNPs at low photon density rates, which constitutes one main reason for the interest in them and removes the reliance of and restriction to focal volume excitation, thus broadening their field of application.[19,20] Secondly, the excitation for UC emission relies on intermediate energy levels,[21] complicating the process. This has led to some less successful attempts to utilize pulsed excitation for UCNPs in the past.[22,23] It is thus necessary to carefully consider the excitation dynamics of UC emissions under pulsed excitation in order to utilize higher intrinsic QY of UCNPs.

In this paper, through investigation of the excitation dynamics of UC emission, we prove through simulations and experiments that significant QY increase can be achieved by using pulsed excitation with wisely selected pulse characteristics, *i.e.*, with sufficiently long pulse width and non-saturated energy transfer transitions. Our proposed scheme renders pulsed excitation an ideal excitation approach for UCNPs, especially for deeply located tissue volumes. In fact, the net QY

[a]*Department of Physics, Lund University, P.O. Box 118, S-221 00 Lund, Sweden. E-mail: haichun.liu@fysik.lth.se; Fax: +46 46 222 4250; Tel: +46 46 222 7471*

[b]*Department of Photonics Engineering, Technical University of Denmark, Frederiksborgvej 399, DK-4000 Roskilde, Denmark*

† Electronic supplementary information (ESI) available. See DOI: 10.1039/c3nr01917a

increase enables us to implement single-shot imaging of UCNPs, shortening data acquisition time by orders of magnitude while simultaneously improving imaging depth as compared to CW excitation. These results have the potential to fundamentally broaden the applicability of UCNPs in deep tissue regions relying on diffuse light excitation, breaking the shallow-depth limitation in UCNP-based imaging.

## 2 Experimental

### 2.1 Synthesis of UCNPs

Core–shell $NaYF_4$:$Yb^{3+}$,$Tm^{3+}$@$NaYF_4$ nanoparticles, synthesized through a recently reported protocol,[24] are used as a representative of UCNPs in this work.

All the chemicals were purchased from Sigma-Aldrich and used without further purification. The core nanoparticles $NaYF_4$:$Yb^{3+}$,$Tm^{3+}$ were first synthesized using the protocol reported in ref. 25. In a typical synthesis, anhydrous powders of $YCl_3$ (0.75 mmol), $YbCl_3$ (0.25 mmol) and $TmCl_3$ (0.003 mmol) were dissolved in 6 mL oleic acid and 17 mL octadecene in a 250 mL flask at 160 °C for 30 min. After the clear solution cooled down to room temperature, 10 mL of a methanol solution containing 4 mmol $NH_4F$ and 2.5 mmol NaOH was added, and the mixture was stirred for 30 min at 50 °C. The methanol was removed from the system by slowly heating it, and the resulting solution was heated to 300 °C for 1.5 h under argon atmosphere. After the mixture cooled to room temperature, the nanoparticles were precipitated with ethanol and washed with an ethanol–water mixture several times, and then redispersed in hexane to form a nanoparticle suspension. The core–shell nanoparticles were subsequently produced by slightly modifying the above procedure through incorporation of the prepared core nanoparticles as the seeds in the synthesis.[24] 1 mmol $YCl_3$ was solely used to provide rare-earth ions for the shielding layer. Other steps were kept the same as the synthesis of core nanoparticles.

### 2.2 Characterization and photoluminescence measurements on the UCNP suspension

The as-prepared core–shell UCNPs were dispersed in hexane and used as the sample. Transmission electron microscopy (TEM) images and the density of the UCNPs were measured on a JEOL 3000F microscope equipped with an X-ray energy dispersive spectroscopy (XEDS) facility. The molar concentrations of rare earth ions were measured on a PerkinElmer Optima 8300 inductively coupled plasma optical emission spectrometer (ICP-OES). The photoluminescence measurements were performed on a sensitive spectrometer setup. A CW laser diode at 975 nm (Thorlabs L975P1WJ) was employed as the excitation source driven by a benchtop laser diode current controller (Thorlabs LDC220C), with the temperature stabilized at 25 °C. Pulsed laser light output was achieved by modulating the current controller using a function generator (Philips PM5139). The excitation power was measured using an Ophir Nova II laser power meter equipped with a photodiode sensor (Ophir PD300), while the spot size of the excitation beam was measured using a laser beam profiler (DataRay Inc. WinCamD-UCD23). The emission light was detected using a grating spectrometer (Ocean Optics QE65000) with a slit width of 50 μm. The rise profile of the 800 nm emission was recorded by an oscilloscope (Tektronix TDS520A) coupled to the output of a photomultiplier tube (Hamamatsu R928), using excitation at 975 nm from a laser diode operating in the pulsed mode. All measurements were carried out at room temperature.

### 2.3 Diffuse optical imaging using UCNPs

Diffuse optical imaging of UCNPs in a liquid tissue phantom was performed either in *trans*-illumination or in *epi*-illumination mode. A capillary tube with an inner diameter of 2 mm, filled with a UCNP suspension, was immersed within the tissue phantom to simulate the luminescent target. Excitation of the UCNPs was accomplished either by a Thorlabs L975P1WJ laser diode running in the CW mode, or by a broad area laser (Eagleyard Photonics, EYP-BAL-0980-10000-4020-CDL02-0000) operating in the pulsed mode driven by a laser diode driver (LIMO LDD50). The excitation power was measured using an Ophir Nova II laser power meter equipped with a medium power thermal laser sensor [Ophir L40(150)A-SH-V2]. A charge-coupled device (CCD) camera (Andor iXon) was used to acquire fluorescence images.

## 3 Results and discussion

### 3.1 Numerical simulations on the QY increase by the pulsed excitation

The feasibility of increasing the QY of UCNPs using pulsed excitation is first investigated through numerical simulations. The $Yb^{3+}$/$Tm^{3+}$ codoped nanoparticles are used as a representative of UCNPs in this work. The UC dynamics of their major UC emission band, *i.e.*, the NIR UC emission band at around 800 nm, is modeled using the following time-resolved rate equations based on its well verified UC pathway under excitation of 975 nm light,[21,29] as shown in Fig. 1,

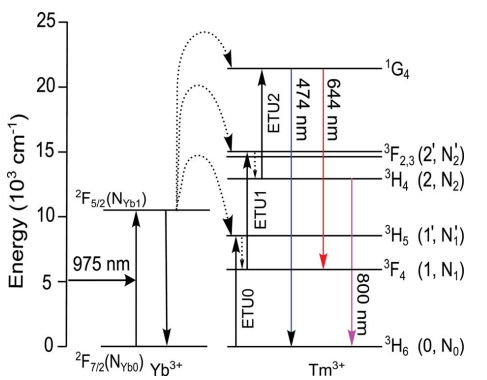


**Fig. 1** Schematic energy level diagrams of $Yb^{3+}$ and $Tm^{3+}$ ions and the proposed UC mechanism following the excitation at 975 nm. The variables used in the text for the population densities of different levels are indicated within the parentheses.

$$\frac{dN_{Yb1}}{dt} = \frac{\sigma\rho}{h\nu}N_{Yb0} - (C_0N_0 + C_1N_1 + C_2N_2)\,N_{Yb1} - \frac{N_{Yb1}}{\tau_{Yb1}}, \quad (1a)$$

$$\frac{dN_1'}{dt} = C_0N_0N_{Yb1} - \beta_1'N_1', \quad (1b)$$

$$\frac{dN_1}{dt} = \beta_1'N_1' - C_1N_1N_{Yb1} - \frac{N_1}{\tau_1}, \quad (1c)$$

$$\frac{dN_2'}{dt} = C_1N_1N_{Yb1} - \beta_2'N_2', \quad (1d)$$

$$\frac{dN_2}{dt} = \beta_2'N_2' - C_2N_2N_{Yb1} - \frac{N_2}{\tau_2}, \quad (1e)$$

where $\sigma$ is the absorption cross-section of $Yb^{3+}$ ions; $\rho$ is the excitation power density; $h$ is Planck's constant; $\nu$ is the frequency of the excitation light; $C_0$, $C_1$ and $C_2$ are the energy transfer upconversion (ETU) rates from excited $Yb^{3+}$ ions to the $Tm^{3+}$ ions in states 0, 1 and 2, respectively; $\tau_1$ and $\tau_2$ are the radiative lifetimes of $Tm^{3+}$ ions in states 1 and 2 (non-radiative de-excitation neglected for these levels), while $\tau_{Yb1}$ is the lifetime of $Yb^{3+}$ ions in the $^2F_{5/2}$ state; $\beta_1'$ and $\beta_2'$ represent the non-radiative decay rates for $1' \rightsquigarrow 1$ and $2' \rightsquigarrow 2$, respectively. A power density dependent and temporally cumulative QY for the NIR UC emission in the time interval $[0, t]$, $\eta(\rho,t)$, is defined as

$$\eta(\rho, t) \equiv \frac{\int_0^t N_2(t)/\tau_2 dt}{\int_0^t \sigma N_{Yb0}\rho/h\nu dt}, \quad (2)$$

which can be calculated by numerically solving eqn (1a–e). The QY in the steady state following CW excitation is given by $\eta(\rho, \infty)$.

In the modeling, we used parameter values which were measured or calculated for the UCNPs used in the experimental work. The ion concentrations were calculated based on the TEM, ICP-OES and XEDS measurements on the UCNPs (see the ESI† for the calculation of ion concentrations), and the lifetimes $\tau_{Yb1}$ and $\tau_2$ were measured experimentally. $\sigma$, $\tau_1$, $\beta_1'$ and $\beta_2'$ were taken from the literature. The power density dependent steady-state QY of the used UCNPs has been measured and reported recently in our previous work.[30] The ETU rates were thus selected based on the principle of giving the best fitting of the simulated power density dependency of steady-state QY with the measured results (see the ESI† for the selection of the ETU rates). Table 1 summarizes the parameter values used in the simulations. Fig. 2a shows the simulated QY under steady-state conditions following CW excitation of different power densities. As seen, the QY increases with the excitation power density in a complex manner with a constant steady-state level (saturation level) at high power densities, which is consistent with experimental observations reported in the literature.[31,32]

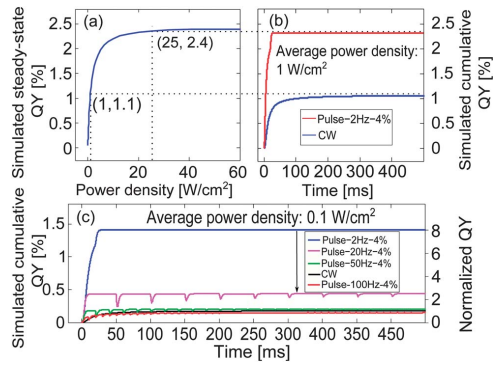


**Fig. 2** (a) Simulated power density dependence of the QY of the NIR UC emission in the steady state under CW excitation. (b) The temporally cumulative QYs under CW excitation and under pulsed excitation in the first pulse period. The pulsed excitation had a duty cycle of 4% and a repetition rate of 2 Hz. Both the CW and pulsed excitation approaches provided an average power density of 1 W $cm^{-2}$. (c) The temporally cumulative QYs under CW excitation and under pulsed excitation in multiple periods. The pulsed excitation had a fixed duty cycle of 4% and various repetition rates. All the excitation approaches provided the same average power density of 0.1 W $cm^{-2}$.

Fig. 2b presents the simulated time dependent QY under CW excitation and under pulsed excitation in the first pulse period. The CW excitation has a constant power density of 1 W $cm^{-2}$. The pulsed excitation, having a 2 Hz repetition rate and a 4% duty cycle, has power densities of 25 W $cm^{-2}$ and 0 W $cm^{-2}$ in the "on" and "off" states, respectively, thus resulting in the same average power density as that of CW excitation. As shown in Fig. 2b, under CW excitation, the UC emission has a constant $QY_{CW}$ except that at the very early stage when the energy levels start to be populated due to the effect of the excitation. This constant $QY_{CW}$ is associated with the steady state of the UC system, and is given by the QY at the power density of 1 W $cm^{-2}$ in Fig. 2a. Under pulsed excitation, the $QY_{pulsed}$ is very small at the start of the laser pulse, and then increases with time. If the length of the pulse duration allows, the $QY_{pulsed}$ will surpass the $QY_{CW}$, and asymptotically approach a maximum. This maximum is restricted to the steady-state QY at the power density of 25 W $cm^{-2}$ in Fig. 2a. Clearly, the advantage of using pulsed excitation to replace the equivalent CW excitation is that the late excitation photons can be potentially used with higher energy conversion efficiency, while the disadvantage is that the

**Table 1** Summary of general parameter values used in the simulations

| $\sigma$ ($cm^2$) | $N_0$ ($cm^{-3}$) | $N_{Yb0}$ ($cm^{-3}$) | $\tau_{Yb1}$ (ms) | $\tau_1$ (ms) | $\tau_2$ (ms) | $C_0$ ($cm^3\ s^{-1}$) | $C_1$ ($cm^3\ s^{-1}$) | $C_2$ ($cm^3\ s^{-1}$) | $\beta_1'$ ($s^{-1}$) | $\beta_2'$ ($s^{-1}$) |
|---|---|---|---|---|---|---|---|---|---|---|
| $1.69 \times 10^{-20}$[a] | $1.25 \times 10^{19}$[b] | $1.52 \times 10^{21}$[b] | 1.32[c] | 7.43[d] | 1.49[c] | $1.6 \times 10^{-18}$[e] | $6.2 \times 10^{-16}$[e] | $1.6 \times 10^{-18}$[e] | $1.7 \times 10^{4}$[d] | $1 \times 10^{5}$[d] |

[a] From Jiang *et al.*[26] [b] Calculated (see the ESI† for the calculation of ion concentrations). [c] From measurement (see Fig. S2†). [d] From Ivanova *et al.*[27] [e] Estimated from Braud *et al.*[28] and Ivanova *et al.*[27] (see the ESI† for the selection of the ETU rates).

early excitation photons in each pulse period are used with lower efficiency than those in the CW excitation. Through balancing the increased power density and decreased excitation duration under the same amount of energy, an overall UC signal gain (defined as the ratio of the $QY_{pulsed}/QY_{CW}$) can be expected.

Cumulative QY in multiple periods under pulsed excitation was investigated in order to estimate the influence of the pulse width on the signal gain, compared to the equivalent CW excitation. The average power density was kept at 0.1 W $cm^{-2}$ in the simulations. The pulsed excitation used throughout this study had the same duty cycle of 4% unless otherwise specified, and its repetition rate was adjusted in order to achieve different pulse widths. As illustrated in Fig. 2c, a significant UC signal gain is obtained by using pulsed excitation when the repetition rate is well below 50 Hz. For example, the signal gain by the 2 Hz square wave in the time interval of [0, 500] ms is approximately 8. The signal gain decreases with the repetition rate, *i.e.*, increases with pulse width as expected. When the repetition rate is even higher, *e.g.*, up to 100 Hz, the signal generated by the pulsed excitation becomes slightly smaller than that generated by equivalent CW excitation. In addition, it should be noted that the signal gain decreases with the applied power density. When the average power density is increased to 1 W $cm^{-2}$, the signal gain decreases to 2, as shown in Fig. S3.† This can be ascribed to the gradual saturation property of UC emission, indicated in Fig. 2a.

Although the parameter values were carefully calculated or modified in the simulations so that they gave the best fitting between the measured and simulated steady-state QY power density dependency, the modeling is not an accurate description of the real UC system. Due to the lack of accuracy and precision data for such values, it is difficult to evaluate the uncertainty of the simulated results. However, the influence of the variation of parameter values on the simulated signal gain was investigated, with the results for the change of ETU rates shown in Fig. S4.† In each comparison, one ETU rate among others was adjusted across the two orders of magnitude around the value listed in Table 1, while two other ETU rates remained unchanged. All simulated results confirm that the UC emission enhancement effect can be achieved by using pulsed excitation with a considerably long pulse duration when the energy transfer transitions are not saturated by the applied power density, as long as the emission originates from a multi-stepwise photon upconversion process. The only difference exists in the extent of the signal gain. It is worth mentioning that the simulated signal gain has a strong dependence on the change of the ETU rate $C_1$ rather than $C_0$ and $C_2$, as shown in Fig. S4.† This can be explained by the fact that the balancing power density of UCNPs is highly dependent on $C_1$.[30] Above this power density, the UCNPs would behave more linearly in emitting upconverted photons upon NIR excitation,[30] leading to decreased signal gain by using pulsed excitation.

### 3.2 Quantum yield increase by pulsed excitation in the UCNP suspension

In order to experimentally validate the gain in the UC signal due to the pulsed excitation predicted by the simulations in Section 3.1, experiments were carried out on colloidal stable UCNPs.

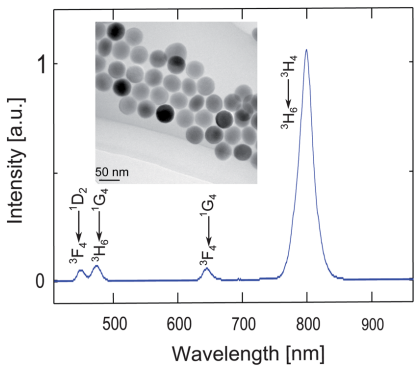


**Fig. 3** The upconversion spectrum of core–shell $NaYF_4$:$Yb^{3+}$,$Tm^{3+}$@$NaYF_4$ nanoparticles under excitation of a CW 975 nm laser diode, measured at a power density of 125 W $cm^{-2}$. The inset shows the TEM image of the prepared core–shell UCNPs.

Core–shell $NaYF_4$:$Yb^{3+}$,$Tm^{3+}$@$NaYF_4$ UCNPs were dispersed in hexane and used as the sample. The prepared UCNPs emit the major UC emission bands at around 800 nm under excitation of 975 nm light, as shown in Fig. 3, assigned to the transition $^3H_4 \rightarrow {}^3H_6$ of $Tm^{3+}$ ions.[29] Other weaker UC emission bands at around 450 nm, 474 nm and 644 nm originate from the transitions of $Tm^{3+}$ ions: $^1D_2 \rightarrow {}^3F_4$, $^1G_4 \rightarrow {}^3H_6$ and $^1G_4 \rightarrow {}^3F_4$, respectively.[29] The inset of Fig. 3 shows the TEM image of the prepared core–shell UCNPs. The nanoparticles were spherical in shape with an average diameter of 42 nm. The core nanoparticles prior to coating had an average diameter of 32 nm (see Fig. S1 in the ESI†).

The intensities of the NIR UC emission under CW excitation and pulsed excitation (square wave) were measured. The pulsed excitation had a fixed duty cycle of 4% and different pulse widths. The average power density of the excitation light was kept at 0.12 W $cm^{-2}$. As shown in Fig. 4a, a signal gain, monotonically increasing with pulse width, was obtained by using the pulsed excitation even with a pulse duration as short as 0.8 ms. When the pulse width reaches 20 ms, the gain is as high as 8.7. It is noteworthy to point out that the required pulse width for the UC signal gain in the present case (~0.8 ms) is much shorter than the rise time of the UC emission (*i.e.*, approximately 10 ms, as shown in the inset of Fig. 4a), dominated by the lifetime of the intermediate level $^3F_4$ of $Tm^{3+}$ ions. This is different from previous predictions reported in the literature,[12,18] and makes the pulsed excitation approach even more flexible to use due to a broader pulse width window for QY increase.

The dependence of the gain in the UC signal on the applied power density was also investigated using a square-wave excitation with a 20 ms pulse width and 2 Hz repetition rate. Fig. 4b shows the UC signal gain by the pulsed excitation at various average excitation power densities, where a decreasing trend with increasing excitation power densities is clearly seen. At the minimum power density investigated (~0.12 W $cm^{-2}$), the

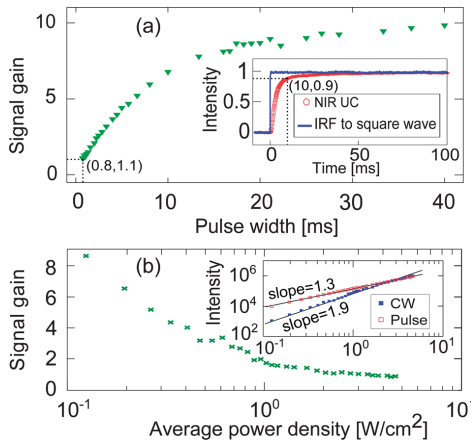


**Fig. 4** (a) The NIR UC signal gain by the pulsed excitation with different pulse widths. The data were measured with an average excitation power density of 0.12 W $cm^{-2}$. Inset: the response of the NIR UC emission to a square-wave excitation with IRF denoting the instrument response function. (b) The dependence of the NIR UC signal gain by the pulsed excitation on the average power density. The pulsed excitation was set to have a 20 ms pulse width and 2 Hz repetition rate. Inset: the average power density dependence of the NIR UC emission intensity under CW and pulsed excitations.

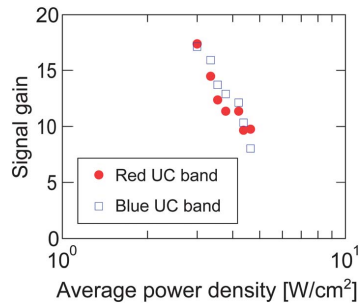


**Fig. 5** The dependency of the blue (at 474 nm) and red (at 644 nm) UC signal gains by the pulsed excitation on the average power density. The pulsed excitation was set to have a pulse width of 20 ms and a repetition rate of 2 Hz.

signal gain is approximately 8.7, while at the maximum power density (~4.65 W $cm^{-2}$), the UC signal generated by the pulsed excitation is slightly weaker than that generated by the CW excitation. The UC emission intensity dependence on the excitation power density under pulsed excitation exhibits a smaller slope than that under the CW excitation, as shown in the inset of Fig. 4b, which could explain the signal-gain trend above.

The amplification effect of increasing the excitation power density here essentially originates from the non-linear power density dependence of the UC emission. Thus, a higher-order power density dependence would result in a larger UC signal gain. This is confirmed by the measurements on the blue (at 474 nm) and red (at 644 nm) UC emissions, both generated through a three-photon excitation process. They exhibit significantly larger signal gains than the NIR UC emission at any given average power density, as shown in Fig. 5. In view of this, we foresee that pulsed excitation can be employed to increase the applicability of recently implemented migration-mediated UC emissions from ions such as $Eu^{3+}$ and $Tb^{3+}$ in biological applications, due to their high-order multi-stepwise excitation nature *via* excited $Tm^{3+}$ ions.[33] At present, their applications in such areas are challenged due to their low QYs.

It is worth mentioning that the usefulness of pulsed excitation for increasing the QY of UC emissions is not merely limited to $Yb^{3+}/Tm^{3+}$ codoped UCNPs. Instead, it is a general scheme for enhancing UC emissions and would work in diverse UCNPs with different dopants if the characteristic of the pulsed excitation light is wisely tailored. In addition, as different UCNPs exhibit different optical characteristics, proper characterization will make it possible to accurately predict the performance of UCNPs in general under pulsed excitation.

### 3.3 Single-shot imaging of UCNPs

When UCNPs are used as contrast agents in diffuse optical imaging, the imaging depth is usually shallow due to the very low QY of UC emissions at the low fluence rates found in deep tissues.[12] The pulsed excitation constitutes an ideal approach for exciting deeply located UCNPs, since the UC emissions can be enhanced without consuming more excitation energy than an equivalent CW source, thus not increasing the thermal side-effects of the excitation light. This would in turn lead to higher image quality and larger imaging depth.

The merit of using pulsed excitation light to image deeply located UCNPs was subsequently tested in a liquid tissue phantom. The phantom, made of water, intralipid and ink, was characterized by photon time-of-flight spectroscopy (pTOFS)[34] and determined to have reduced scattering coefficient $\mu_s' = 10.1\ cm^{-1}$ and absorption coefficient $\mu_a = 0.52\ cm^{-1}$ at 975 nm, hence mimicking skin tissue properties. Its thickness was 17 mm. A glass tube with an inner diameter of 2 mm, containing the colloidal core–shell UCNPs ($c = 1$ wt%), was inserted into the phantom as the luminescent inclusion to mimic a UCNP-labeled target, *e.g.*, a tumor inside real tissue. CW excitation and pulsed excitation, having 20 ms pulse duration and 2 Hz repetition rate, at 975 nm were applied, respectively. The average power density impinging on the surface of the tissue phantom was 1.2 W $cm^{-2}$ for both excitation approaches. The excitation source and the detector were positioned in a *trans*-illumination geometry. A more detailed description of the experimental setup is found in ref. 32. When buried at a depth of 10 mm from the source, the luminescent inclusion was barely detectable under CW excitation even with an exposure time of 10 s, as shown in Fig. 6a. However, by using pulsed excitation, the signal-to-background ratio was significantly increased by a factor of approximately 7 under the same detection conditions, as illustrated in Fig. 6b. An obvious implication is that the data acquisition time can be drastically reduced whilst maintaining the signal quality equivalent to CW excitation. Moreover, it is

 

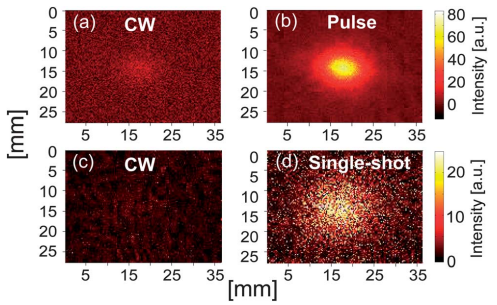


**Fig. 6** The NIR UC emission images taken for a luminescent inclusion located at a depth of 10 mm under the (a) CW and (b) pulsed excitation, detected in a *trans*-illumination geometry. The average power density was 1.2 W $cm^{-2}$, and the exposure time was 10 s for both excitation approaches. The NIR UC emission images taken for a luminescent inclusion located at a depth of 13 mm under the (c) CW and (d) 50 ms single pulse excitation, detected in an *epi*-illumination geometry. Both excitation sources provided the maximum permissible power density allowed by the ANSI standard for exposure to human skin. The exposure time was 10 s for the CW excitation and 1 s for the single pulse excitation.

notable that the maximum imaging depth can be increased to 15 mm for pulsed excitation (data not shown).

The QY of UC emission can be further optimized by using single pulse excitation, through which even higher power density can be achieved. For instance, the maximum permissible power density for exposure to human skin at 975 nm is 17.4 W $cm^{-2}$ for a repetitive pulse excitation with a pulse width of 20 ms and a repetition rate of 2 Hz, while the number for a 50 ms single pulse is as high as 36.9 W $cm^{-2}$,[16] referring to Section 8 in the ESI.† Such a strong single pulse with a pulse width longer than the rise time of the UC emission enables the UCNPs to be used in a very efficient way in terms of energy conversion. This excitation approach would improve the imaging ability of using UCNPs without violating the ANSI standard, which is a fundamental limit for bio-imaging.

The feasibility of single-shot imaging was experimentally investigated. A 50 ms single pulse providing an excitation power density of 36.9 W $cm^{-2}$ was used. When the luminescent inclusion was placed at a depth of 13 mm into the phantom, it could be relatively well detected using the single pulse excitation with a detector integration time of 1 s, even using an *epi*-illumination imaging setup described in ref. 17, as shown in Fig. 6d. Nevertheless, when the CW laser was used for excitation, also outputting the maximum permissible power density by the ANSI standard on the same illumination area, *i.e.*, 709.6 mW $cm^{-2}$, referring to Section 8 in the ESI,† the inclusion was not detectable at all even with a much longer integration time of 10 s, as shown in Fig. 6c. Obviously, the integration time for the single pulse excitation can be shortened to 50 ms still without loss in the UC signal quality, as long as the excitation source and the detector are synchronized. The results demonstrated here, although preliminary, show great potential of single-shot excitation in UCNP-guided deep tissue optical imaging.

## 4 Conclusions

In conclusion, significant QY increase in UCNPs is achieved by using pulsed excitation. This is supported theoretically by the study of the UC dynamics based on time resolved rate equations. Such QY increase enables us to implement single-shot imaging of UCNPs in deep tissues. Pulsed excitation thus constitutes an ideal excitation approach for UCNPs, as the shallow imaging limit can be overcome and data acquisition time can be drastically shortened by applying this excitation scheme. The pulsed excitation approach will greatly increase the applicability of UCNPs not only in diffuse optical imaging but also in many other biomedical applications, such as photodynamic therapy and remote activation of biomolecules in deep tissues.[35,36] It is worth mentioning that metallic nanostructures are reported to be effective in enhancing UC emissions owing to their local field enhancement effect by surface plasmonic coupling.[37] We envisage that the combination of the pulsed excitation approach and metallic nanostructures could become a major scheme of using UCNPs in the diffuse light regime, due to the synergistic effect in increasing the excitation power density. In addition, this study provides a general method for promoting the applications of nonlinear fluorophores (including UCNPs and triplet–triplet annihilation based upconverters[38]) under low light conditions by increasing the excitation fluence rate through a limited illumination area.

## Acknowledgements

S. Fredriksson, F. Olsson, A. Gisselsson, and P. Kjellman are gratefully acknowledged for the help with the synthesis of the UCNPs and ICP-OES measurement. M. E. Messing and L. R. Wallenberg are acknowledged for the help with the TEM and XEDS measurements. B. Thomasson is acknowledged for the help in the single-shot imaging experiment. S. Johansson and A. Shaharin are acknowledged for the help with the pTOFS measurements. We thank D. Kroon and D. Guenot for the assistance in the laser power measurement, and J. Axelsson and P. Svenmarker for their helpful discussions. This work was supported by a grant from the Swedish Research Council (grant no. 621-2011-4265) and a Linneaus grant to the Lund Laser Centre.

## References

1 X. Wang, J. Zhuang, Q. Peng and Y. D. Li, *Nature*, 2005, **437**, 121–124.
2 H.-X. Mai, Y.-W. Zhang, R. Si, Z.-G. Yan, L.-D. Sun, L.-P. You and C.-H. Yan, *J. Am. Chem. Soc.*, 2006, **128**, 6426–6436.
3 J.-C. Boyer, L. A. Cuccia and J. A. Capobianco, *Nano Lett.*, 2007, **7**, 847–852.
4 E. M. Chan, C. Xu, A. W. Mao, G. Han, J. S. Owen, B. E. Cohen and D. J. Milliron, *Nano Lett.*, 2010, **10**, 1874–1885.
5 F. Wang, Y. Han, C. S. Lim, Y. Lu, J. Wang, J. Xu, H. Chen, C. Zhang, M. Hong and X. Liu, *Nature*, 2010, **463**, 1061–1065.
6 F. Zhang, G. B. Braun, A. Pallaoro, Y. Zhang, Y. Shi, D. Cui, M. Moskovits, D. Zhao and G. D. Stucky, *Nano Lett.*, 2012, **12**, 61–67.

7 L. Wang, R. Yan, Z. Huo, L. Wang, J. Zeng, J. Bao, X. Wang, Q. Peng and Y. Li, *Angew. Chem., Int. Ed.*, 2005, **44**, 6054–6057.
8 S. F. Lim, R. Riehn, W. S. Ryu, N. Khanarian, C. K. Tung, D. Tank and R. H. Austin, *Nano Lett.*, 2006, **6**, 169–174.
9 M. Nyk, R. Kumar, T. Y. Ohulchanskyy, E. J. Bergey and P. N. Prasad, *Nano Lett.*, 2008, **8**, 3834–3838.
10 H. Päkkilä, M. Ylihärsilä, S. Lahtinen, L. Hattara, N. Salminen, R. Arppe, M. Lastusaari, P. Saviranta and T. Soukka, *Anal. Chem.*, 2012, **84**, 8628–8634.
11 M. Yu, F. Li, Z. Chen, H. Hu, C. Zhan, H. Yang and C. Huang, *Anal. Chem.*, 2009, **81**, 930–935.
12 C. T. Xu, Q. Zhan, H. Liu, G. Somesfalean, J. Qian, S. He and S. Andersson-Engels, *Laser Photonics Rev.*, 2012, DOI: 10.1002/lpor201200052.
13 J. Zhou, Z. Liu and F. Li, *Chem. Soc. Rev.*, 2012, **41**, 1323–1349.
14 N. M. Idris, M. K. Gnanasammandhan, J. Zhang, P. C. Ho, R. Mahendran and Y. Zhang, *Nat. Med.*, 2012, **18**, 1580–1585.
15 F. C. J. M. van Veggel, C. Dong, N. J. J. Johnson and J. Pichaandi, *Nanoscale*, 2012, **4**, 7309–7321.
16 Laser Institute of America, *Americal National Standard for Safe Use of Lasers; in ANSI Z136.1-2000*, Laser Institute of America, Orlando, Florida, 2000.
17 C. T. Xu, N. Svensson, J. Axelsson, P. Svenmarker, G. Somesfalean, G. Chen, H. Liang, H. Liu, Z. Zhang and S. Andersson-Engels, *Appl. Phys. Lett.*, 2008, **93**, 171103.
18 Q. Zhan, S. He, J. Qian, H. Cheng and F. Cai, *Theranostics*, 2013, **3**, 303–316.
19 H. Liu, C. T. Xu and S. Andersson-Engels, *Opt. Lett.*, 2010, **35**, 718–720.
20 P. Svenmarker, C. T. Xu and S. Andersson-Engels, *Opt. Lett.*, 2010, **35**, 2789–2791.
21 F. Auzel, *Chem. Rev.*, 2004, **104**, 139–173.
22 L. M. Maestro, E. M. Rodriguez, F. Vetrone, R. Naccache, H. L. Ramirez, D. Jaque, J. A. Capobianco and J. G. Solé, *Opt. Express*, 2010, **18**, 23544–23553.
23 C. F. Gainer, G. S. Joshua, C. R. De Silva and M. Romanowski, *J. Mater. Chem.*, 2011, **21**, 18530–18533.
24 H.-S. Qian and Y. Zhang, *Langmuir*, 2008, **24**, 12123–12125.
25 Z. Li and Y. Zhang, *Nanotechnology*, 2008, **19**, 345606.
26 X. P. Jiang, Z. M. Yang, T. Liu and S. H. Xu, *J. Appl. Phys.*, 2009, **105**, 103113.
27 S. E. Ivanova, A. M. Tkachuk, A. Mirzaeva and F. Pelle, *Opt. Spectrosc.*, 2008, **105**, 228–241.
28 A. Braud, S. Girard, J. L. Doualan, M. Thuau, R. Moncorg'e and A. M. Tkachuk, *Phys. Rev. B: Condens. Matter Mater. Phys.*, 2000, **61**, 5280–5292.
29 G. Chen, T. Y. Ohulchanskyy, R. Kumar, H. Ågren and P. N. Prasad, *ACS Nano*, 2010, **4**, 3163–3168.
30 H. Liu, C. T. Xu, D. Lindgren, H. Xie, D. Thomas, C. Gundlach and S. Andersson-Engels, *Nanoscale*, 2013, **5**, 4770–4775.
31 R. Page, K. Schaffers, P. Waide, J. Tassano, S. Payne, W. Krupke and W. Bischel, *J. Opt. Soc. Am. B*, 1998, **15**, 996–1008.
32 C. T. Xu, P. Svenmarker, H. Liu, X. Wu, M. E. Messing, L. R. Wallenberg and S. Andersson-Engels, *ACS Nano*, 2012, **6**, 4788–4795.
33 F. Wang, R. Deng, J. Wang, Q. Wang, Y. Han, H. Zhu, X. Chen and X. Liu, *Nat. Mater.*, 2011, **10**, 968–973.
34 T. Svensson, E. Alerstam, D. Khoptyar, J. Johansson, S. Folestad and S. Andersson-Engels, *Rev. Sci. Instrum.*, 2009, **80**, 063105.
35 C. J. Carling, F. Nourmohammadian, J. C. Boyer and N. R. Branda, *Angew. Chem., Int. Ed.*, 2010, **49**, 3782–3785.
36 M. K. G. Jayakumar, N. M. Idris and Y. Zhang, *Proc. Natl. Acad. Sci. U. S. A.*, 2012, DOI: 10.1073/pnas.1114551109.
37 S. Schietinger, T. Aichele, H.-Q. Wang, T. Nann and O. Benson, *Nano Lett.*, 2010, **10**, 134–139.
38 S. Baluschev, T. Miteva, V. Yakutkin, G. Nelles, A. Yasuda and G. Wegner, *Phys. Rev. Lett.*, 2006, **97**, 143903.


 

# Paper VI

**Autofluorescence insensitive imaging using upconverting nanoparticles in scattering media**

C. T. Xu, N. Svensson, J. Axelsson, P. Svenmarker, G. Somesfalean, G. Chen, H. Liang, H. Liu, Z. Zhang, S. Andersson-Engels.

*Applied Physics Letters* **93(17)**, 171103-1 - 171103-3 (2008).

APPLIED PHYSICS LETTERS **93**, 171103 (2008)

# Autofluorescence insensitive imaging using upconverting nanocrystals in scattering media

Can T. Xu,[1,a)] Niclas Svensson,[1] Johan Axelsson,[1] Pontus Svenmarker,[1] Gabriel Somesfalean,[1] Guanying Chen,[2] Huijuan Liang,[2] Haichun Liu,[2] Zhiguo Zhang,[2] and Stefan Andersson-Engels[1]
[1]*Department of Physics, Lund University, P.O. Box 118, S-221 00 Lund, Sweden*
[2]*Department of Physics, Harbin Institute of Technology, P.O. Box 3025, Harbin 150080, People's Republic of China*

(Received 27 August 2008; accepted 1 October 2008; published online 27 October 2008)

Autofluorescence is a nuisance in the field of fluorescence imaging and tomography of exogenous molecular markers in tissue, degrading the quality of the collected data. In this letter, we report autofluorescence insensitive imaging using highly efficient upconverting nanocrystals ($NaYF_4:Yb^{3+}/Tm^{3+}$) in a tissue phantom illuminated with near-infrared radiation of 85 $mW/cm^2$. It was found that imaging with such nanocrystals leads to an exceptionally high contrast compared to traditional downconverting fluorophores due to the absence of autofluorescence. Upconverting nanocrystals may be envisaged as important biological markers for tissue imaging purposes. © *2008 American Institute of Physics*. [DOI: 10.1063/1.3005588]

In recent years, the interest for fluorescence diffuse optical imaging and tomography has grown tremendously.[1–3] Much of the work has been focused on developing inexpensive and compact systems for macroscopic imaging of fluorophores embedded in small animals. The systems could, for example, be used to monitor the effects from drugs on cancer tumors over a period of time, without sacrificing the animals. Extensive research has been performed both on the practical and the theoretical side in this area. Currently, mainly traditional dyes are used as fluorophores. These dyes emit Stoke shifted light upon excitation, and can be very effective with quantum efficiencies close to unity. However, since tissue itself autofluoresces due to several endogenous fluorophores mainly in the skin, a background fluorescence from the bulk tissue will always exist.[4,5] In the presence of tissue autofluorescence, different spectral unmixing algorithms can also be used to extract the signal. These algorithms utilize the spectral characteristics of the fluorophores and the autofluorescence.[6] However, the measurement procedure can be quite complex since one needs to acquire the emission at multiple wavelengths. To suppress the effects of autofluorescence, several approaches have been suggested. The two most promising ones are based on quantum dots and upconverting markers.

Quantum dots have been used as fluorophores in a great number of studies.[7–9] Their large Stoke shift and narrow emission spectra allow the emission to be detected in a spectral band with low tissue autofluorescence. Quantum dots are very bright fluorophores due to their high absorption, mainly in the UV region. Their emission wavelength is dependent on the core size and can be selected over a wide range while the same excitation wavelength can be used.[7] The main drawback at this stage for these fluorophores is their toxicity, together with the fact that penetration of the UV light is low in tissue. Typical quantum dots are based on CdSe due to the well established fabrication technology.[10] Recent studies have shown that these quantum dots are potentially harmful to organisms.[11,10] The quantum dots tend to destabilize when exposed to biological environments. Adding the fact that they can easily penetrate into cells, the damage can be quite substantial. Research, however, is underway to produce less harmful quantum dots, as well as enhancing their biocompatibility.[12]

Upconverting nanoparticles have been proposed as a fluorophore in biomedical imaging applications due to their unique property to efficiently emit anti-Stoke shifted light upon near-infrared excitation.[13,14] The main challenge has been to develop upconverting markers with high-quantum yield in the wavelength region above 650 nm where tissue is relatively transparent.

In this letter, we demonstrate autofluorescence insensitive imaging with novel high-quantum yield upconverting nanoparticles emitting at 800 nm. The study is performed in a controlled environment within tissue phantoms in which autofluorescence is simulated, and comparison with ordinary Stoke shifted fluorophores emitting at the same wavelength is made.

Efficient upconverting phosphors of nanometer size have been fabricated.[14] The particles are doped with $Yb^{3+}$, which acts as sensitizer, and another rare earth ion, which acts as activator.[15] By using different activators, various emission wavelengths can be accomplished with the same excitation wavelength. It has been shown that $NaYF_4$ is the most efficient host known for upconverting phosphorous crystals.[16] In this study, highly efficient $NaYF_4$ crystals doped with $Yb^{3+}$ and $Tm^{3+}$ were used, which were prepared according to the procedure described in detail in Ref. 17. The particles absorb light at 980 nm and emit upconverted light at 800 nm. The process involves absorption of two or more photons with an intermediate metastable state.[15] Figure 1 shows the emission spectrum for the nanoparticles, the blue emission line at 477 nm is only visible for higher pump intensities. The pump-power dependence of the 800 nm line was measured to be quadratic (slope=2.0) using low intensities, as seen in the inset of Fig. 1, suggesting a two-photon process.

[a)]Electronic mail: can.xu@fysik.lth.se.

 

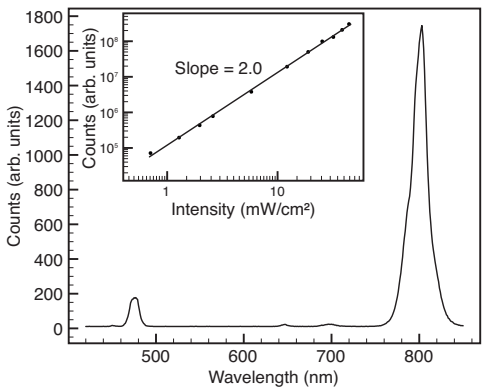


FIG. 1. Emission spectrum recorded for the nanoparticles under 980 nm excitation with an intensity of 6 W/cm$^2$. The inset shows the pump-power dependence of the interesting 800 nm line measured under low intensities.

A tissue phantom consisting of water, intralipid, and ink was prepared. The optical properties of the tissue phantom were measured with a time-of-flight spectroscopy system,[18] and determined to have a reduced scattering coefficient $\mu_s'$ =6.5 cm$^{-1}$ and an absorption coefficient $\mu_a$=0.44 cm$^{-1}$ for $\lambda$=660 nm. The parameters were chosen to have a good correspondence to real tissue in small animals.[19] Two capillary tubes with inner diameters of 2.4 mm were used as containers for the fluorophores.

The imaging system is schematically shown in Fig. 2. The tubes were submerged into the tissue phantom to a depth of 5.0 mm, where the depth was taken as the distance from the front surface of the tubes to the surface of the phantom. Fiber-coupled lasers were used to illuminate the phantom with a slightly divergent beam. The spot sizes of the lasers on the phantom were approximately 1 cm$^2$. An air cooled charge coupled device (CCD) camera captured the images through a set of dielectric bandpass filters centered at 800 nm.

The first tube was filled with a solution of the nanocrystals dissolved in dimethyl sulfoxide (DMSO) with a concentration of 1 wt %. To excite the nanoparticles, a 978 nm laser diode was used, with a power of approximately 85 mW on

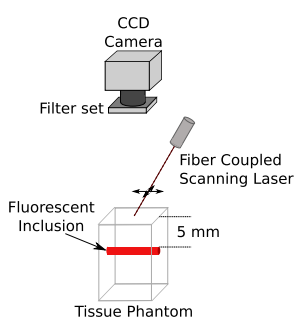


FIG. 2. (Color online) Schematic of the imaging setup. Light from a fiber-coupled laser is scanned in an array on the surface of the phantom. An air cooled CCD camera is used to capture an image for every scanned position.

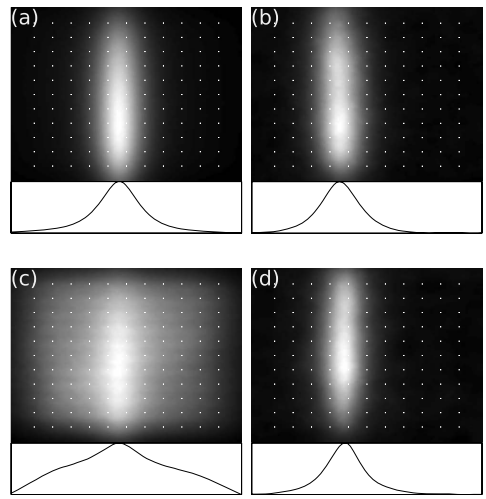


FIG. 3. Images comparing the DY-781 dye and the nanoparticles with and without autofluorescence, along with plots showing the sums in the vertical directions. The white dots have been added artificially and represent the positions used for the excitation light. The left column shows the results using DY-781, and the right column shows the results using upconverting nanoparticles. (a) and (b) are taken without any added autofluorophores. (c) and (d) are taken with a background autofluorophore concentration of 40 nM.

the surface of the tissue phantom. The second tube was filled with a solution of ordinary fluorophores (DY-781, Dyomics GmbH) dissolved in ethanol with a concentration of 1 $\mu$M. The fluorophores were excited with a 780 nm laser diode with a power of 40 mW on the surface of the phantom. The concentration of the nanoparticles is reasonably consistent with studies performed using quantum dots *in vivo*. In those studies, approximately 1 nmol of CdSe quantum dots were injected into a mouse ($\sim$18 g), giving an approximate concentration of 0.01 wt % if distributed homogeneously.[8,9] With functionalized quantum dots, selective accumulation in tumors can be achieved. Taking this into consideration and the fact that the nanoparticles have molar mass of the same order of magnitude as the quantum dots, the concentration of 1 wt % used in this study seems acceptable.

The lasers were raster scanned in a 4.4$\times$4.4 cm$^2$ array consisting of 121 positions, and an image was acquired for every laser position. In order to minimize the effects of random bright pixels, a median filter with a mask of 3 $\times$3 pixels was applied to all images. The individual images were then summed, and a representation of the photon distribution on the surface was obtained. Even if this does not accurately reflect the fluorophore distribution, it enables detection of fluorescent inclusions. To mimic tissue autofluorescence, a small amount of DY-781 was also added into the phantom.

Figure 3 shows images taken with and without autofluorescence. As expected, the autofluorescence effectively hides the signal from the inclusion with the ordinary fluorophores [Fig. 3(c)], while no background appears on the images using the upconversion scheme [Fig. 3(d)]. It is worth to notice that using traditional fluorophores, even without any artificial

autofluorophores added, the autofluorescence introduced by the intralipid within the phantom is visible, see the cross section profile in Fig. 3(a).

As seen in Fig. 3, the signal-to-background contrast is superior for upconverting nanoparticles emitting in a wavelength region where no Stoke shifted tissue autofluorescence is present. Higher excitation power can increase the signal-to-noise ratio, without sacrificing the high contrast. Increasing the signal-to-noise ratio, however, will not boost the image quality using traditional fluorophores since they are limited by a lower signal-to-background contrast due to the ubiquitous autofluorescence. Even with the lower quantum efficiency of the nanoparticles compared to traditional fluorophores the image quality is therefore expected to be better.

Background caused by autofluorescence is very prominent when working with an epifluorescence imaging setup in comparison to a fluorescence transmission imaging setup. In the latter setup, it is possible to suppress the autofluorescence signal fairly effectively.[20] However, such a system can be very ineffective when used to detect and image a superficial signal.

The particles used for this study were still in the development stage. For example, they were in bulk state without any kind of coating, and thus not soluble in water and therefore not biocompatible. However, improved fabrication methods can make them water soluble.[21,22] In addition, there are also reports suggesting that coating the particles with an undoped layer reduces the nonradiative losses at the surface, thus effectively enhancing their upconversion efficiency.[22,23] Using a pulsed light source with a higher peak power should further increase the signal tremendously, due to the quadratic pump-power dependence of the upconverting process. Such a light source should still be harmless in terms of tissue heating and damaging, since the mean power can still be kept low.

Future work will involve the use of nanocrystals for diffuse optical tomography. With their unique features in emitting a signal that is insensitive to the downconverting autofluorescence, they have the potential to become an important biological marker. In a longer perspective we hope to functionalize the particles with tumor seeking properties. Early studies by other groups have already been performed, and the prospects are very promising.[24]

We gratefully acknowledge Erik Alerstam and Tomas Svensson for their assistance with the time-of-flight measurements. This work was supported by the EC integrated projects Molecular Imaging LSHG-CT-2003-503259 and Brighter 1ST-2005–035266, as well as by VR-SIDA 348-2007-6939.

[1]V. Ntziachristos, Annu. Rev. Biomed. Eng. **8**, 1 (2006).
[2]V. Ntziachristos, J. Ripoll, L. Wang, and R. Weissleder, Nat. Biotechnol. **23**, 313 (2005).
[3]L. Sampath, W. Wang, and E. M. Sevick-Muraca, J. Biomed. Opt. **13**, 041312 (2008).
[4]G. Wagnieres, W. Star, and B. Wilson, Photochem. Photobiol. **68**, 603 (1998).
[5]S. Andersson-Engels and B. Wilson, J. Cell Pharmacol **3**, 48 (1992).
[6]D. Farkas, C. Du, G. Fisher, C. Lau, W. Niu, E. Wachman, and R. Levenson, Comput. Med. Imaging Graph. **22**, 89 (1998).
[7]M. Bruchez, M. Moronne, P. Gin, S. Weiss, and A. Alivisatos, Science **281**, 2013 (1998).
[8]X. Gao, Y. Cui, R. M. Levenson, L. W. K. Chung, and S. Nie, Nat. Biotechnol. **22**, 969 (2004).
[9]B. Ballou, B. Lagerholm, L. Ernst, M. Bruchez, and A. Waggoner, Bioconjugate Chem. **15**, 79 (2004).
[10]V. Karabanovas, E. Zakarevicius, A. Sukackaite, G. Streckyte, and R. Rotomskis, Photochem. Photobiol. Sci. **7**, 725 (2008).
[11]A. O. Choi, S. E. Brown, M. Szyf, and D. Maysinger, J. Mol. Med. **86**, 291 (2008).
[12]W. B. Cai, A. R. Hsu, Z. B. Li, and X. Y. Chen, Nanoscale Res. Lett. **2**, 265 (2007).
[13]J. Shan and Y. Ju, Appl. Phys. Lett. **91**, 123103 (2007).
[14]S. Heer, K. Kompe, H. Güdel, and M. Haase, Adv. Mater. (Weinheim, Ger.) **16**, 2102 (2004).
[15]F. Auzel, Chem. Rev. (Washington, D.C.) **104**, 139 (2004).
[16]K. Kramer, D. Biner, G. Frei, H. Güdel, M. Hehlen, and S. Luthi, Nano Lett. **16**, 1244 (2004).
[17]G. Yi, H. Lu, S. Zhao, Y. Ge, W. Yang, D. Chen, and L.-H. Guo, Nano Lett. **4**, 2191 (2004).
[18]E. Alerstam, S. Andersson-Engels, and T. Svensson, J. Biomed. Opt. **13**, 041304 (2008).
[19]V. Ntziachristos, E. Schellenberger, J. Ripoll, D. Yessayan, E. Graves, A. Bogdanov, L. Josephson, and R. Weissleder, Proc. Natl. Acad. Sci. U.S.A. **101**, 12294 (2004).
[20]G. Zacharakis, H. Shih, J. Ripoll, R. Weissleder, and V. Ntziachristos, Mol. Imaging **5**, 153 (2006).
[21]F. Wang, D. K. Chatterjee, Z. Li, Y. Zhang, X. Fan, and M. Wang, Nanotechnology **17**, 5786 (2006).
[22]G.-S. Yi and G.-M. Chow, Chem. Mater. **19**, 341 (2007).
[23]J. Suyver, A. Aebischer, D. Biner, P. Gerner, J. Grimm, S. Heer, K. Kramer, C. Reinhard, and H. Güdel, Opt. Mater. (Amsterdam, Neth.) **27**, 1111 (2005).
[24]Q. Lü, F. Guo, L. Sun, A. Li, and L. Zhao, J. Phys. Chem. C **112**, 2836 (2008).

# Paper VII

**High-resolution fluorescence diffuse optical tomography developed with nonlinear upconverting nanoparticles**

C. T. Xu, P. Svenmarker, H. Liu, X. Wu, M. E. Messing, L. R. Wallenberg, S. Andersson-Engels.

*ACS Nano* **6(6)**, 4788-4795 (2012).

ARTICLE

# High-Resolution Fluorescence Diffuse Optical Tomography Developed with Nonlinear Upconverting Nanoparticles

**Can T. Xu,[†,*] Pontus Svenmarker,[†] Haichun Liu,[†] Xia Wu,[†] Maria E. Messing,[‡] L. Reine Wallenberg,[§] and Stefan Andersson-Engels[†]**

[†]Department of Physics, Lund University, Box 118, S-221 00 Lund, Sweden, [‡]Division of Solid State Physics, Lund University, Box 118, S-221 00 Lund, Sweden, and [§]Polymer and Materials Chemistry/nCHREM, Lund University, Box 124, S-221 00 Lund, Sweden

**ABSTRACT**

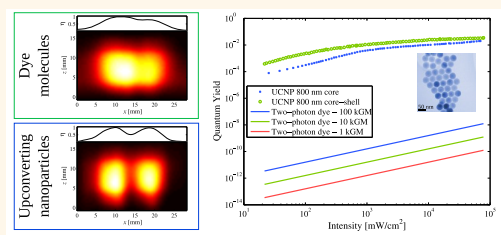


Fluorescence diffuse optical tomography (FDOT) is an emerging biomedical imaging technique that can be used to localize and quantify deeply situated fluorescent molecules within tissues. However, the potential of this technique is currently limited by its poor spatial resolution. In this work, we demonstrate that the current resolution limit of FDOT can be breached by exploiting the nonlinear power-dependent optical emission property of upconverting nanoparticles doped with rare-earth elements. The rare-earth-doped core–shell nanoparticles, $NaYF_4$:$Yb^{3+}$/$Tm^{3+}$@$NaYF_4$ of hexagonal phase, are synthesized through a stoichiometric method, and optical characterization shows that the upconverting emission of the nanoparticles in tissues depends quadratically on the power of excitation. In addition, quantum-yield measurements of the emission from the synthesized nanoparticles are performed over a large range of excitation intensities, for both core and core–shell particles. The measurements show that the quantum yield of the 800 nm emission band of core–shell upconverting nanoparticles is 3.5% under an excitation intensity of 78 W/cm$^2$. The FDOT reconstruction experiments are carried out in a controlled environment using liquid tissue phantoms. The experiments show that the spatial resolution of the FDOT reconstruction images can be significantly improved by the use of the synthesized upconverting nanoparticles and break the current spatial resolution limits of FDOT images obtained from using conventional linear fluorophores as contrast agents.

**KEYWORDS:** upconversion nanoparticles · bioimaging · quantum yield · resolution · diffuse imaging

Nanostructure contrast agents have become very important and versatile assets for optical imaging of biomedical systems. Nanostructures, such as quantum dots, carbon nanotubes, nanodiamonds, gold nanoparticles, and rare-earth-doped nanoparticles, have, for example, been explored for cancer targeting and treatment,[1,2] deep-tissue anatomical imaging of mice,[3] and background-free deep-tissue imaging of small animals.[4−7] For *in vivo* optical imaging of deeply situated fluorescent agents in biomedical systems, an emerging method of fluorescence diffuse optical tomography (FDOT) has recently been employed with an increasing interest.[8−12] FDOT is a compact, fast, and highly sensitive technique for three-dimensional deep-tissue imaging of fluorescent targets. These properties and the noninvasive nature of FDOT have made it very attractive for longitudinal studies of small animals, where it has been applied to follow the development in time of, for example, cancer tumors,[13] proteases,[10] Alzheimer's disease,[14] and different drug effects.[12]

Traditionally, the contrast agents used in FDOT are based on different types of Stokes-shifting fluorophores, such as molecular dyes or quantum dots. The linear power-density dependence of the emission from these fluorophores results in poor spatial resolution in the reconstructed images, as sharp spatial features are inevitably smeared out during diffuse light propagation. Several approaches have been employed to increase the spatial resolution, including multispectral methods,[15] the use of *a priori* information,[16,17] and structured illumination methods.[18] Although these approaches all have positive effects on the spatial resolution of the reconstructed images, ultimately they cannot circumvent the resolution-limiting factor originating from the use of linear fluorophores in diffusive tissues. In this work, we report on the exploration of rare-earth-doped core–shell nanoparticles with upconverting optical properties as contrast agents for FDOT and demonstrate that the spatial resolution of FDOT can be significantly improved by exploiting their nonlinear power-dependent optical properties. The experiments were

* Address correspondence to can.xu@fysik.lth.se.

Received for review December 19, 2011 and accepted May 7, 2012.

**Published online May 08, 2012**
10.1021/nn3015807

performed in a well-controlled environment using liquid tissue phantoms. Comparisons with FDOT reconstruction images obtained from an optically similar system employing linear fluorophores show that the spatial resolution of the reconstruction images obtained using the upconverting nanoparticles can go much beyond the current limits of conventional FDOT images. Using simulations, the mechanism behind the improved spatial resolution is described through a theoretical model. Furthermore, through careful optical characterization, we report, for the first time, the quantum yield of the 800 nm emission band and compare the quantum yield of core and core−shell particles. In addition to being a highly relevant material parameter, knowledge of the quantum yield enables the possibility to perform quantitative imaging of deeply situated targets within tissues.

Upconverting materials in bulk form have existed for decades.[19] However, only recently has it been possible to synthesize upconverting nanoparticles with quantum efficiencies high enough to be used as biological markers for microscopy and deep-tissue diffuse imaging.[4,20−30] Upconverting nanoparticles possess the unique property of being able to emit anti-Stokes-shifted light. This is accomplished by doping a host crystal with a sensitizer, typically $Yb^{3+}$, and an activator, for example, $Tm^{3+}$, $Er^{3+}$, or $Ho^{3+}$. The sensitizer can, through mainly energy transfer upconversion, excite an activator in a stepwise manner, leading to the emission of anti-Stokes-shifted light.[23,31,32] This unique property has made upconverting nanoparticles very attractive for imaging and labeling of biological samples, yielding images that are virtually background free since the endogenous tissue autofluorescence is Stokes-shifted.[4−6,28] Furthermore, these particles are not susceptible to photobleaching and aging effects, in contrast to the commonly used dye molecules,[27] have a very low toxicity,[33,34] and can be used for multimodality imaging by carefully designing the synthesization process.[35,36] Recently, it has also been demonstrated that unwanted emission bands can be suppressed, which can be used for simplifying the instrumentation and enhancing the contrast.[37]

## RESULTS AND DISCUSSION

Core−shell $NaYF_4$:$Yb^{3+}$/$Tm^{3+}$@$NaYF_4$ nanoparticles were utilized as contrast agents in this study. The core $NaYF_4$:$Yb^{3+}$/$Tm^{3+}$ nanoparticles were synthesized through an efficient stoichiometric method,[38] and nonradiative losses caused by surface effects were reduced by coating the nanoparticles with an undoped layer of $NaYF_4$.[28,39−41] Due to the presence of the capping ligand (oleate), the $NaYF_4$:$Yb^{3+}$/$Tm^{3+}$@$NaYF_4$ nanoparticles could be dispersed in nonpolar solvents and were colloidally stable for months without visible agglomeration. Figure 1a and b show transmission electron microscope (TEM) images of the synthesized

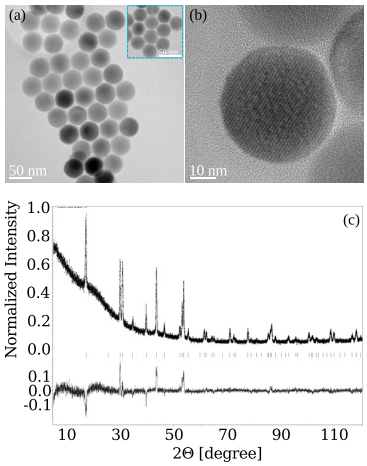


**Figure 1. (a) TEM image of the monodisperse core−shell $NaYF_4$:$Yb^{3+}$/$Tm^{3+}$@$NaYF_4$ nanoparticles. The inset shows the core $NaYF_4$:$Yb^{3+}$/$Tm^{3+}$ nanoparticles prior to coating with the undoped $NaYF_4$ layer. The mean diameters of the core−shell nanoparticles and the core nanoparticles were determined to be 43 and 31 nm, respectively. (b) High-resolution TEM image of the core−shell $NaYF_4$:$Yb^{3+}$/$Tm^{3+}$@$NaYF_4$ nanoparticles. (c) XRD pattern of the synthesized core−shell $NaYF_4$:$Yb^{3+}$/$Tm^{3+}$@$NaYF_4$ nanoparticles (top panel) and residual of fit for the hexagonal crystal phase (bottom panel).**

core−shell $NaYF_4$:$Yb^{3+}$/$Tm^{3+}$@$NaYF_4$ upconverting nanoparticles. The nanoparticles were spherical in shape with a mean diameter of 42 nm and had a dominant lattice spacing of 0.52 nm. The inset in Figure 1a shows the core nanoparticles, which through a comparison with the core−shell nanoparticles show that the thickness of the undoped $NaYF_4$ shell was 6 nm. The X-ray diffraction (XRD) pattern of the synthesized core−shell $NaYF_4$:$Yb^{3+}$/$Tm^{3+}$@$NaYF_4$ nanoparticles is shown in the top panel of Figure 1c with the residual of fit for the hexagonal crystal phase[42] shown in the bottom panel. The cell parameters of $a$ = 5.976 nm, $b$ = 0.599 nm, and $c$ = 0.350 nm are consistent with the pure hexagonal $NaYF_4$ crystal in the JCPDS 16-0334 data.

Optical characterization of the synthesized core−shell nanoparticles was carried out using a spectrofluorometer setup under excitation by a laser diode at 975 nm. As shown in Figure 2, the excitation generated one strong emission band at 800 nm and two weak ones around 470 and 650 nm. These emission bands can be assigned to the transitions of $Tm^{3+}$.[43] The effective attenuation spectrum of a typical murine muscle tissue[44] is also presented in Figure 2, where it can be seen that light in the near-infrared region has considerably lower attenuation than light in the visible region. Thus, the emissions at the shorter wavelengths (470 and 650 nm) were filtered out and only the

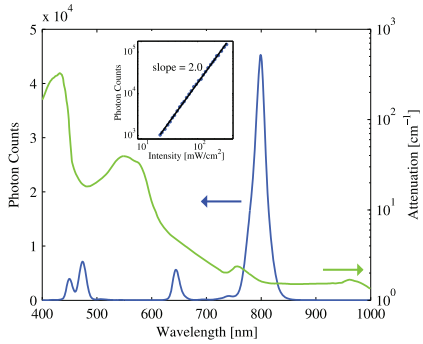


**Figure 2. Emission spectrum (blue solid line) for the synthesized $NaYF_4$:$Yb^{3+}$/$Tm^{3+}$@$NaYF_4$ nanoparticles of hexagonal phase under excitation at 975 nm and attenuation spectrum (green solid line) of typical murine muscle tissue. The excitation intensity was 1 W/cm$^2$, leading to a strong emission band at 800 nm. The weak emission bands around 470 and 650 nm are less suitable for use within tissues, since the attenuation at those wavelengths is significantly higher, as shown. The inset shows the power dependence of the emission band at 800 nm, demonstrating that the emission originates from a two-photon process.**

emission at 800 nm was used for the experimental study in this work. The excitation at 975 nm and the emission at 800 nm are both highly suitable wavelengths residing around the optimal regions in the tissue optical window,[44] *i.e.*, a region where tissue is relatively translucent and light penetration depths of several centimeters can be achieved. The inset in Figure 2 shows the power dependence of the 800 nm emission band of the nanoparticles. Since the fluence rate within scattering materials is in general small, the power dependence of the emission band was measured using weak excitation intensities, well below saturation limits.[20] From the slope of the linear fit (log−log scale), it can be seen that in contrast to the traditionally used fluorophores, which have a linear power dependence, the emission from the upconverting nanoparticles has a quadratic power dependence, consistent with the fact that the upconversion is a two-photon process.

The results from the quantum-yield measurements of both the synthesized core−shell and the core upconverting nanoparticles are shown in Figure 3. As seen, the synthesis produced efficient hexagonal core−shell $NaYF_4$:$Yb^{3+}$/$Tm^{3+}$@$NaYF_4$ upconverting nanoparticles with a quantum yield of 3.5% under an excitation intensity of 78 W/cm$^2$. At the lower excitation intensity of 21.7 mW/cm$^2$, the quantum yield was determined to be $3.8 \times 10^{-4}$. Evidently, in this power-density regime, core−shell nanoparticles are, due to their protective shell layer, about 6 times brighter than unshielded particles.[45] Under low excitation intensities, the slope of the quantum yield is close to 1, consistent with the expected behavior for quadratic fluorophores. As the excitation intensity is increased, the power dependence factor of the upconverting nanoparticles will begin to decrease due to saturation of the energy levels in the rare-earth ions,[20] resulting in a quantum yield that approaches a constant for large excitation intensities. For comparison, the quantum yields for the most efficient two-photon dyes were simulated under identical experimental conditions and are also shown in Figure 3. It can be seen that even for the very efficient dyes,[46−48] such as those based on fluorene derivatives,[49,50] the required excitation intensity is clearly too high to be used in scattering tissues. The reason is that these dyes require simultaneous absorption of two photons *via* a virtual state, in contrast to upconverting nanoparticles, which possess real long-lived intermediate states.

Reports on the absolute quantum yield of $NaYF_4$ upconverting nanoparticles in the literature are very scarce.[51−53] For bulk $NaYF_4$:$Yb^{3+}$/$Tm^{3+}$ material, Page *et al.*[51] have determined the power conversion factor of the blue emission band to be $2 \times 10^{-4}$, for the most efficient material studied at an excitation intensity of 1 W/cm$^2$. The corresponding power conversion factor for the synthesized core−shell $NaYF_4$:$Yb^{3+}$/$Tm^{3+}$@$NaYF_4$ upconverting nanoparticles in this work was determined to be $5.8 \times 10^{-5}$. However, it is important to point out that since bulk material was used, direct comparisons with our results is nontrivial, without considering size-dependent effects. The size-dependent effects of $NaYF_4$:$Yb^{3+}$/$Er^{3+}$ crystals have, however, been examined by Boyer *et al.*,[53] where a 10 times lower quantum yield of core−shell nanoparticles (30 nm) as compared with bulk material under an excitation intensity of 150 W/cm$^2$ was found. Accounting for the size dependency, a more realistic power efficiency conversion factor that can be expected from the material used by Page *et al.*[51] should be $2 \times 10^{-5}$, which is in reasonable agreement with the results obtained in this work. However, as this is an indirect comparison, the results should be interpreted with caution and further studies of the efficiency of upconverting nanoparticles are certainly needed.

To evaluate the spatial resolution of FDOT with the use of the quadratically power-dependent upconverting nanoparticles and linearly power-dependent fluorophores as contrast agents, two 17 mm thick liquid phantoms consisting of water, intralipid, and ink were prepared. The concentrations of intralipid and ink were chosen to provide optical properties typically found in small animals.[44] Since the upconverting nanoparticles emit at 800 nm, DY-781 (Dyomics GmbH) dye molecules were chosen as the linear fluorophores, as they also emit at 800 nm. To further ensure a proper comparison between the FDOT images obtained using the linear fluorophores and the upconverting nanoparticles, the two phantoms were prepared to have identical optical properties at their respective excitation wavelengths of 785 and 975 nm. The phantom for

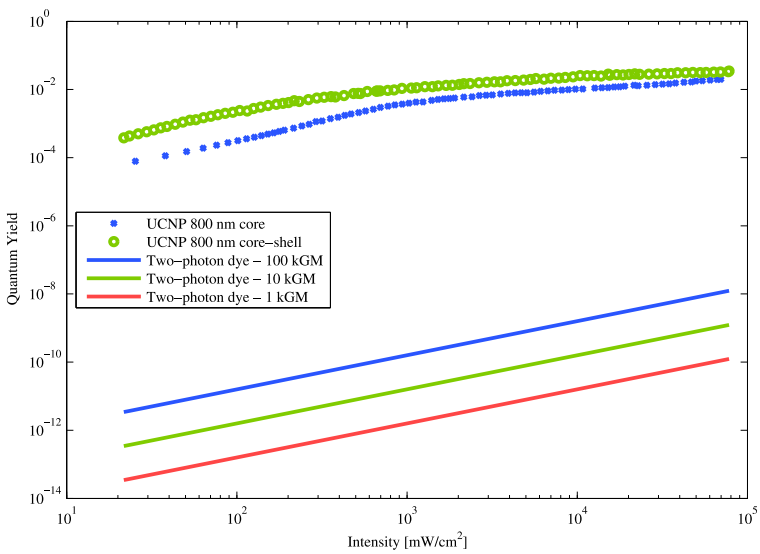


**Figure 3. Quantum yield of the 800 nm emission band for the synthesized hexagonal core–shell $NaYF_4$:$Yb^{3+}$/$Tm^{3+}$@$NaYF_4$ nanoparticles and hexagonal core $NaYF_4$:$Yb^{3+}$/$Tm^{3+}$ nanoparticles. It can be seen that the quantum yield increases linearly (slope of 1) with the excitation intensity until a saturation point, from which the quantum yield approaches a constant value, which is the expected behavior for a linear fluorophore. Solid lines show simulated corresponding quantum yields for highly efficient two-photon dyes under identical experimental conditions, which in contrast to upconverting nanoparticles require two photons to be simultaneously absorbed. Compared with upconverting nanoparticles, even two-photon dyes with cross sections on the order of 100 kGM will be $10^8$ times less bright.**

the linear fluorophores had a reduced scattering coefficient of $\mu'_s$(785 nm) = 10.1 $cm^{-1}$ and an absorption coefficient of $\mu_a$(785 nm) = 0.51 $cm^{-1}$, while the phantom for the upconverting nanoparticles had a reduced scattering coefficient of $\mu'_s$(975 nm) = 10.1 $cm^{-1}$ and an absorption coefficient of $\mu_a$(975 nm) = 0.52 $cm^{-1}$, determined by a time-of-flight spectroscopy (TOFS) system.[54] The experimental setup is schematically illustrated in Figure 4, where two capillary tubes with inner diameters of 2.0 mm, filled with either the DY-781 fluorophores or the synthesized upconverting nanoparticles, were used to simulate fluorescent targets. By adjusting the center-to-center distance of the two fluorescent tubes and performing one tomographic reconstruction for each separation distance, the obtainable spatial resolution in the reconstruction images could be evaluated. It is important to note that autofluorescence can cause severe artifacts in the reconstructions for linear Stokes-shifting fluorophores.[5] Thus, a phantom material with low autofluorescence was selected, and any remaining autofluorescence effects or other background signals were removed by subtracting from each image its corresponding image obtained from a scan without any fluorescent targets.

Cross-sectional slices from the tomographic reconstructions for different center-to-center distances of the fluorescent tubes are shown in Figure 5. The reconstructions for the linearly power-dependent DY-781 fluorophores

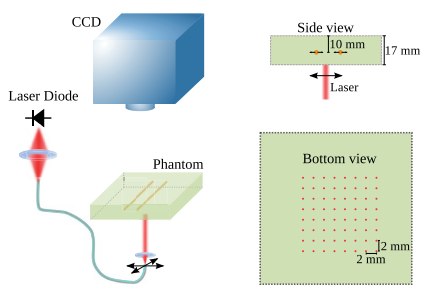


**Figure 4. Schematic of the transilluminating experimental setup used for FDOT. An excitation beam was scanned from below in an 8 × 8 grid pattern with each excitation spot separated from its neighbor spots by 2 mm (see the bottom view). A CCD camera was used to capture one image for each scanned position. Two fluorescent tubes, containing either the DY-781 fluorophores or the rare-earth-doped core–shell $NaYF_4$:$Yb^{3+}$/$Tm^{3+}$@$NaYF_4$ upconverting nanoparticles, were mounted on a stage within the liquid phantom 10 mm from the top surface (see the side view). The separation distance between the two tubes was varied in discrete steps of 1 mm, and an FDOT reconstruction was performed for each separation distance.**

are shown in Figure 5a to e, with decreasing tube separations from 10 mm in Figure 5a to 6 mm in Figure 5e. The corresponding reconstructions for the quadratically power-dependent $NaYF_4$:$Yb^{3+}$/$Tm^{3+}$@$NaYF_4$ upconverting nanoparticles are shown in Figure 5f to m, with

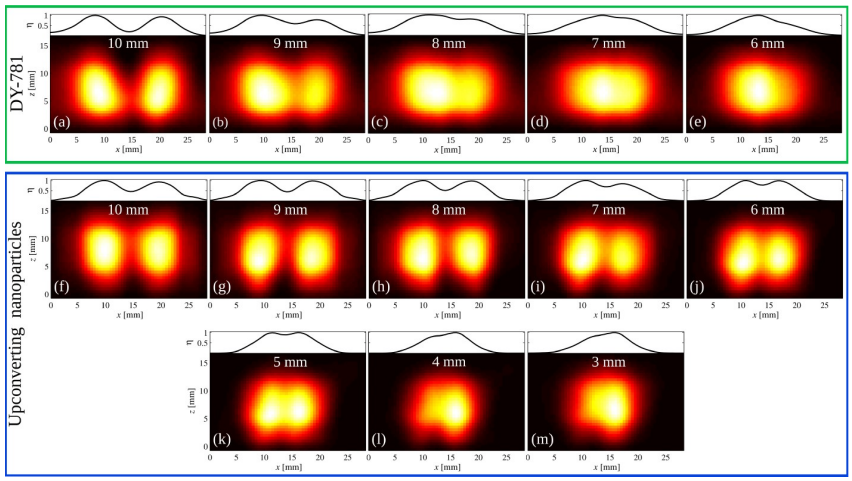


**Figure 5. Cross-sectional slices (two-dimensional plots) of the FDOT reconstructions with the linearly power-dependent DY-781 fluorophores and the quadratically power-dependent $NaYF_4$:$Yb^{3+}$/$Tm^{3+}$@$NaYF_4$ upconverting nanoparticles as contrast agents and their corresponding intensity profiles (line plots). The true depth was $z$ = 7 mm. The separation distance between the fluorescent tubes was varied from 10 to 6 mm (step sizes of 1 mm) for the case of the linear fluorophores, shown in (a)−(e). The use of quadratic upconverting nanoparticles clearly leads to reconstructions with higher spatial resolutions and qualities. Thus, the separation distance between the fluorescent tubes was varied from 10 to 3 mm (stepsizes of 1 mm), shown in (f)−(m). Using the linear fluorophores, already at a separation distance of 8 mm (c), the two fluorescent tubes can no longer be separated. However, in the images obtained with the use of the quadratic upconverting nanoparticles, besides the significantly higher qualities of the reconstructions, the two fluorescent tubes can still be separated at a separation distance of 5 mm (k).**

decreasing tube separations, from 10 mm (Figure 5f) to 3 mm (Figure 5m). As can be seen, in all cases, the depth of the fluorescent tubes ($z$ = 7 mm) can be correctly retrieved. However, the difference in spatial resolution between the images with the use of the DY-781 fluorophores and the upconverting nanoparticles, in particular along the lateral dimension ($x$-axis), is immense. In the images obtained with the use of the upconverting nanoparticles, the two tubes can be retrieved from the reconstructions for separation distances down to 5 mm (Figure 5k). However, in the images obtained with the DY-781 fluorophores, retrieval of the two tubes breaks down already at 8 mm (Figure 5c). A comparison of the reconstructions in Figure 5h and c shows that the obtainable reconstruction quality by using the upconverting nanoparticles is exceedingly superior to what one could obtain with the use of traditional linear fluorophores. Furthermore, it is important to point out that although the optical properties of the phantom at the excitation wavelengths (785 and 975 nm) were chosen to be identical to ensure proper comparisons, this, inevitably resulted in slightly differing optical properties at the emission wavelength of 800 nm. Using TOFS, the optical properties of the phantom for the linear DY-781 fluorophores were determined to be $\mu'_s$(800 nm) = 9.95 $cm^{-1}$ and $\mu_a$(800 nm) = 0.49 $cm^{-1}$, while the optical properties of the upconverting nanoparticles were $\mu'_s$(800 nm) = 11.5 $cm^{-1}$ and $\mu_a$(800 nm) = 0.041 $cm^{-1}$. Thus, the phantom for the upconverting nanoparticles, due to its higher scattering relative absorption ratio, is actually much more penalizing in terms of resolution as compared with the phantom for the DY-781 fluorophores.

The experimental results presented in this work clearly demonstrate that the spatial resolution of FDOT can be significantly improved by employing upconverting nanoparticles as contrast agents due to their nonlinear power-dependent optical properties. This improvement can be explained as follows by considering the effective light propagation profiles and the corresponding sensitivity profiles. For a given source−detector pair, the sensitivity profile describes the most probable origin of any detected emission light. Thus, a confined and sharp sensitivity profile results in a higher spatial resolution. Figure 6 shows simulated sensitivity profiles of traditionally used linear fluorophores and the quadratically power-dependent upconverting nanoparticles. The simulations were performed for three different source positions, with the detector position fixed. The circles within the slices indicate the positions of two fluorescent tubes separated by 5 mm. Comparing the sensitivity profiles of the linear fluorophores (Figure 6a−c) and the sensitivity profiles of the quadratically power-dependent upconverting nanoparticles (Figure 6d−f), it is evident that the gradient for the quadratic case, in particular close to the source, is much larger than

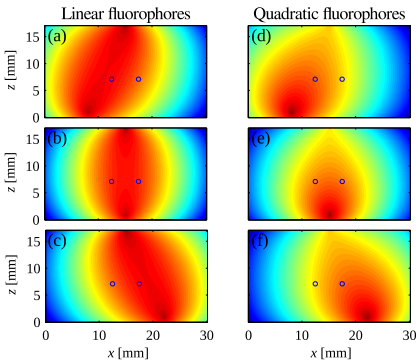


**Figure 6. Simulated sensitivity profiles of linearly power-dependent fluorophores and quadratically power-dependent upconverting nanoparticles for three source positions and a fixed detector position. The circles represent the experimental case of two fluorescent tubes with a center-to-center separation of 5 mm. (a–c) Sensitivity profiles of linear fluorophores. (d–f) Sensitivity profiles of the upconverting nanoparticles. From the figure, it is clear that the quadratic power dependence of the emission results in sensitivity profiles that are much more confined and sharply defined as compared with linear fluorophores. Thus, the two fluorescent targets can effectively be selectively excited if upconverting nanoparticles are employed as contrast agents.**

the gradient for the linear case. Therefore, here selective excitation of the individual fluorescent targets can be achieved if upconverting nanoparticles are employed. The large excitation volumes resulting from employing traditional linear fluorophores, on the other hand, severely limit the spatial selectivity.

The resolution in the lateral dimension was experimentally investigated in this study. However, since the resolution enhancement originates from the confinement of the sensitivity profile for the upconverting nanoparticles, it is clear that the axial resolution will certainly also exhibit a higher spatial resolution as compared with linear fluorophores. This intrinsic property of nonlinear upconverting nanoparticles that leads to selective excitation should be applicable to arbitrary geometries and will in all cases excel linear fluorophores in terms of spatial resolution. Furthermore, since the resolution enhancement can be attributed to an intrinsic property of the upconverting nanoparticles, it is possible and straightforward to implement the previously mentioned approaches, such as multispectral methods, incorporation of *a priori* information, and other mathematical formulations of the problem, to further improve the spatial resolution.

## CONCLUSIONS

In summary, core–shell $NaYF_4$:$Yb^{3+}$/$Tm^{3+}$@$NaYF_4$ upconverting nanoparticles of hexagonal phase have been synthesized and employed as contrast agents in the demonstration of FDOT with high spatial resolution. The optical characterization shows that the emission from the core–shell nanoparticles depends quadratically on the power of excitation in tissues and that the quantum yield of the synthesized upconverting nanoparticles is 3.5% under a more intense excitation intensity of 78 W/$cm^2$. It is demonstrated that the spatial resolution of FDOT can be significantly improved by exploiting the nonlinear optical emission properties of the upconverting core–shell nanoparticles as compared with the traditionally used fluorophores. In contrast to previously employed approaches to improve the spatial resolution of FDOT, which mainly aim to utilize and optimize the available data, our approach attacks the limiting factor directly by instead tailoring the shape of the sensitivity profiles. This fundamentally different approach, which exploits the unique nonlinear power-dependent emission property of upconverting nanoparticles, significantly improves the current spatial-resolution limit of FDOT, enabling deep-tissue optical imaging of targets in biomedical systems with unprecedented resolutions.

## EXPERIMENTAL METHODS

**Synthesis and Characterization of the Nanoparticles.** In the synthesis of the core $NaYF_4$:$Yb^{3+}$/$Tm^{3+}$ nanoparticles, stoichiometric amounts of $YCl_3$ (0.75 mmol), $YbCl_3$ (0.25 mmol), and $TmCl_3$ (0.003 mmol) were mixed with 6 mL of oleic acid (OA) and 17 mL of octadecene (ODE) in a 250 mL flask. The mixture was heated to 160 °C for 30 min, forming a clear solution. Then, 4 mmol of $NH_4F$ (0.1482 g) and 2.5 mmol of NaOH (0.1 g) dissolved in 10 mL of methanol was aspirated into a syringe and added into the solution by a syringe pump using a flow rate of 200 L/min. The obtained solution was first slowly heated to evaporate the methanol and degassed at 100 °C for 10 min, followed by a second step of heating to 300 °C for 1.5 h under an argon atmosphere. After the solution had cooled to room temperature, the nanoparticles were precipitated and washed with 100 mL of ethanol/water mixture (1:1 v/v) three times and centrifuged at 5100 rpm for 10 min before being collected and redispersed in 6 mL of *n*-hexane. In order to reduce the nonradiative losses caused by surface effects, the nanoparticles were further coated with an undoped layer of $NaYF_4$ through a similar procedure to that above. A clear solution containing 1.00 mmol of $Y^{3+}$ was first obtained by dissolving $YCl_3$ in 6 mL of oleic acid and 17 mL of ODE in a 200 mL flask. $NaYF_4$:$Yb^{3+}$/$Tm^{3+}$ nanoparticles (1 mmol) in 6 mL of hexane was then added to the solution. Using a syringe pump, with the above-mentioned flow rate, 4 mmol of $NH_4F$ (0.1482 g) and 2.5 mmol of NaOH (0.1 g) in 10 mL of methanol was added. The following steps, including degassing, reaction, precipitation, washing, centrifugation, and collection, were identical to the synthesis of the core nanoparticles. TEM images were obtained using a JEOL 3000F analytical transmission electron microscope.

Optical characterization of the core–shell nanoparticles was performed using a sensitive spectrofluorometer setup. Excitation of the synthesized core–shell nanoparticles was performed using the Thorlabs L975P1WJ laser diode with the temperature stabilized at 25 °C. The emission was measured using a grating spectrometer with a slit width of 50 m (Ocean Optics QE65000). For the quantum-yield measurements, the system employed

standard fluorophores calibrated using the integrating-sphere-based Hamamatsu C9920 quantum yield measurement system. The resulting quantum yield of the upconverting nanoparticles was thus given by

$$\Phi_{NP} = \frac{A_s}{A_{NP}} \frac{F_{NP}}{F_s} \Phi_s \quad (1)$$

where $A$ denotes the fraction of absorbed photons, $\Phi$ is the quantum yield, $F$ is the collected photons, and the subscripts s and NP denote the standard and the upconverting nanoparticles, respectively.

**FDOT Imaging System.** Imaging of the phantom was performed in a transmission mode. Four capillary tubes with inner diameters of 2.0 mm were used to simulate fluorescent targets. The first two tubes were filled with a solution of DY-781 ($c = 1\ \mu$M), and the last two tubes were filled with a solution of the $NaYF_4$: $Yb^{3+}/Tm^{3+}$@$NaYF_4$ nanoparticles ($c = 1$ wt %). For each type of fluorophores, two tubes were mounted in parallel (in the lateral direction) on a 7 mm tall stage immersed within the tissue phantom. The center-to-center distance of the two tubes had an initial value of 10 mm and was gradually decreased with a step size of 1 mm. A tomographic reconstruction was performed for each separation distance. Excitation of the fluorophores was accomplished using a laser diode at 785 nm for the linear fluorophores and at 975 nm for the upconverting nanoparticles, illuminating the phantom from below with spot sizes of 1 mm. The excitation intensities at the surface of the phantoms were moderate (95 mW/cm$^2$ for the 785 nm laser and 800 mW/cm$^2$ for the 975 nm laser), well below the thresholds for tissue damage. For each reconstruction, the excitation beam was scanned over an area of 14 × 14 mm$^2$ in an 8 × 8 grid using two computer-controlled translation stages. A charge-coupled device (CCD) camera (Andor iXon) was used to acquire one image for every scanned position. After background and autofluorescence subtraction, the signal-to-noise ratios of the resulting images for the DY-781 fluorophores and the upconverting nanoparticles were very similar and were determined to be 52:1 for the DY-781 fluorophores and 62:1 for the upconverting nanoparticles.

**FDOT Model.** The FDOT technique is a model-based inverse approach that aims to find the fluorophore or the nanoparticle number density, $\eta(\mathbf{r})$, within a scattering material. Using a set of fluence measurements on the surface of the media and a forward model, the problem was formulated as an optimization problem where $\eta$ is optimized to minimize the residual between a predicted set of measurement data, $\Theta_f^c(\eta)$, and a set of experimentally retrieved measurement data, $\Theta_f^m$. In this study, the excitation field, $\Phi_e(\mathbf{r})$, and the emission field, $\Phi_f(\mathbf{r})$, were modeled using two coupled diffusion equations,

$$(\mu_a^e - \kappa_e(\mathbf{r})\nabla^2)\Phi_e(\mathbf{r}) = S(\mathbf{r}) \quad (2)$$

$$(\mu_a^f - \kappa_f(\mathbf{r})\nabla^2)\Phi_f(\mathbf{r}) = \xi\eta(\mathbf{r})\,\Phi_e^\gamma(\mathbf{r}) \quad (3)$$

where $\xi$ is a constant denoting the efficiency of a fluorophore and $\gamma$ describes the power dependence of a fluorophore, *i.e.*, $\gamma = 1$ for a linear fluorophore and $\gamma = 2$ for a quadratic fluorophore such as the upconverting nanoparticles employed in this study; $\mu_a^{e,f}$ and $\kappa_{e,f}$ denote the absorption and diffusion coefficient at the excitation and fluorescence wavelengths, respectively. The diffusion equations were solved using the finite-element method, and Robin boundary conditions were used to account for the refractive index mismatch between the phantom material and the surrounding air. Since the problem is highly ill-posed, Tikhonov regularization was used in the optimization process to obtain a stable solution, and the regularization parameter was derived by gradually decreasing an initially large value, until a plateau in the residual was reached.[5]

*Conflict of Interest:* The authors declare no competing financial interest.

*Acknowledgment.* E. Alerstam is gratefully acknowledged for the help with the TOFS measurements. S. Lidin and C. Müller are acknowledged for the help with the XRD measurements. S. Fredriksson and F. Olsson are acknowledged for the help with synthesizing the nanoparticles. This work was supported by grants from the Swedish Research Council, the Crafoord Foundation, a Linnaeus grant to the Lund Laser Centre, and a Linnaeus grant for Nanoscience and Quantum Engineering.

## REFERENCES AND NOTES

1. Gao, X.; Cui, Y.; Levenson, R. M.; Chung, L. W. K.; Nie, S. *In Vivo* Cancer Targeting and Imaging with Semiconductor Quantum Dots. *Nat. Biotechnol.* **2004**, *22*, 969–976.
2. Huang, X. H.; Neretina, S.; El-Sayed, M. A. Gold Nanorods: From Synthesis and Properties to Biological and Biomedical Applications. *Adv. Mater.* **2009**, *21*, 4880–4910.
3. Welsher, K.; Sherlock, S. P.; Dai, H. J. Deep-Tissue Anatomical Imaging of Mice Using Carbon Nanotube Fluorophores in the Second Near-Infrared Window. *Proc. Natl. Acad. Sci. U. S. A.* **2011**, *108*, 8943–8948.
4. Chatterjee, D. K.; Rufalhah, A. J.; Zhang, Y. Upconversion Fluorescence Imaging of Cells and Small Animals Using Lanthanide Doped Nanocrystals. *Biomaterials* **2008**, *29*, 937–943.
5. Xu, C. T.; Axelsson, J.; Andersson-Engels, S. Fluorescence Diffuse Optical Tomography Using Upconverting Nanoparticles. *Appl. Phys. Lett.* **2009**, *94*, 251107.
6. Xu, C. T.; Svensson, N.; Axelsson, J.; Svenmarker, P.; Somesfalean, G.; Chen, G.; Liang, H.; Liu, H.; Zhang, Z.; Andersson-Engels, S. Autofluorescence Insensitive Imaging Using Upconverting Nanocrystals in Scattering Media. *Appl. Phys. Lett.* **2008**, *93*, 171103.
7. Zhan, Q.; Qian, J.; Liang, H.; Somesfalean, G.; Wang, D.; He, S.; Zhang, Z.; Andersson-Engels, S. Using 915 nm Laser Excited $Tm^{3+}/Er^{3+}/Ho^{3+}$-Doped $NaYbF_4$ Upconversion Nanoparticles for *in Vitro* and Deeper *in Vivo* Bioimaging without Overheating Irradiation. *ACS Nano* **2011**, *5*, 3744–3757.
8. Ntziachristos, V.; Ripoll, J.; Wang, L. H. V.; Weissleder, R. Looking and Listening to Light: The Evolution of Whole-Body Photonic Imaging. *Nat. Biotechnol.* **2005**, *23*, 313–320.
9. Hielscher, A. H. Optical Tomographic Imaging of Small Animals. *Curr. Opin. Biotechnol.* **2005**, *16*, 79–88.
10. Ntziachristos, V.; Tung, C.-H.; Bremer, C.; Weissleder, R. Fluorescence Molecular Tomography Resolves Protease Activity *in Vivo*. *Nat. Med. (N. Y., NY, U. S.)* **2002**, *8*, 757–760.
11. Ntziachristos, V. Going Deeper than Microscopy: The Optical Imaging Frontier in Biology. *Nat. Methods* **2010**, *7*, 603–614.
12. Ntziachristos, V.; Schellenberger, E.; Ripoll, J.; Yessayan, D.; Graves, E.; Bogdanov, A.; Josephson, L.; Weissleder, R. Visualization of Antitumor Treatment by Means of Fluorescence Molecular Tomography with an Annexin V-Cy5.5 Conjugate. *Proc. Natl. Acad. Sci. U. S. A.* **2004**, *101*, 12294–12299.
13. Corlu, A.; Choe, R.; Durduran, T.; Rosen, M. A.; Schweiger, M.; Arridge, S. R.; Schnall, M. D.; Yodh, A. G. Three-Dimensional *in Vivo* Fluorescence Diffuse Optical Tomography of Breast Cancer in Humans. *Opt. Express* **2007**, *15*, 6696–6716.
14. Hyde, D.; de Kleine, R.; MacLaurin, S. A.; Miller, E.; Brooks, D. H.; Krucker, T.; Ntziachristos, V. Hybrid FMT-CT Imaging of Amyloid-Beta Plaques in a Murine Alzheimer's Disease Model. *Neuroimage* **2009**, *44*, 1304–1311.
15. Chaudhari, A. J.; Ahn, S.; Levenson, R.; Badawi, R. D.; Cherry, S. R.; Leahy, R. M. Excitation Spectroscopy in Multispectral Optical Fluorescence Tomography: Methodology, Feasibility and Computer Simulation Studies. *Phys. Med. Biol.* **2009**, *54*, 4687–4704.
16. Lin, Y. T.; Yan, H.; Nalcioglu, O.; Gulsen, G. Quantitative Fluorescence Tomography with Functional and Structural a Priori Information. *Appl. Opt.* **2009**, *48*, 1328–1336.
17. Panagiotou, C.; Somayajula, S.; Gibson, A. P.; Schweiger, M.; Leahy, R. M.; Arridge, S. R. Information Theoretic Regularization in Diffuse Optical Tomography. *J. Opt. Soc. Am. A* **2009**, *26*, 1277–1290.

18. Mazhar, A.; Cuccia, D. J.; Gioux, S.; Durkin, A. J.; Frangioni, J. V.; Tromberg, B. J. Structured Illumination Enhances Resolution and Contrast in Thick Tissue Fluorescence Imaging. *J. Biomed. Opt.* **2010**, *15*, 010506.
19. Menyuk, N.; Pierce, J.; Dwight, K. $NaYF_4$:Yb,Er - Efficient Upconversion Phosphor. *Appl. Phys. Lett.* **1972**, *21*, 159–161.
20. Haase, M.; Schafer, H. Upconverting Nanoparticles. *Angew. Chem., Int. Ed.* **2011**, *50*, 5808–5829.
21. Mader, H. S.; Kele, P.; Saleh, S. M.; Wolfbeis, O. S. Upconverting Luminescent Nanoparticles for Use in Bioconjugation and Bioimaging. *Curr. Opin. Chem. Biol.* **2010**, *14*, 582–596.
22. Ong, L. C.; Gnanasammandhan, M. K.; Nagarajan, S.; Zhang, Y. Upconversion: Road to El Dorado of the Fluorescence World. *Luminescence* **2010**, *25*, 290–293.
23. Wang, F.; Banerjee, D.; Liu, Y. S.; Chen, X. Y.; Liu, X. G. Upconversion Nanoparticles in Biological Labeling, Imaging, and Therapy. *Analyst (Cambridge, U. K.)* **2010**, *135*, 1839–1854.
24. Liu, H. C.; Xu, C. T.; Andersson-Engels, S. Multibeam Fluorescence Diffuse Optical Tomography Using Upconverting Nanoparticles. *Opt. Lett.* **2010**, *35*, 718–720.
25. Svenmarker, P.; Xu, C. T.; Andersson-Engels, S. Use of Nonlinear Upconverting Nanoparticles Provides Increased Spatial Resolution in Fluorescence Diffuse Imaging. *Opt. Lett.* **2010**, *35*, 2789–2791.
26. Nyk, M.; Kumar, R.; Ohulchanskyy, T. Y.; Bergey, E. J.; Prasad, P. N. High Contrast *in Vitro* and *in Vivo* Photoluminescence Bioimaging Using Near Infrared to Near Infrared Up-Conversion in $Tm^{3+}$ and $Yb^{3+}$ Doped Fluoride Nanophosphors. *Nano Lett* **2008**, *8*, 3834–3838.
27. Bouzigues, C.; Gacoin, T.; Alexandrou, A. Biological Applications of Rare-Earth Based Nanoparticles. *ACS Nano* **2011**, *5*, 8488–8505.
28. Wang, F.; Deng, R. R.; Wang, J.; Wang, Q. X.; Han, Y.; Zhu, H. M.; Chen, X. Y.; Liu, X. G. Tuning Upconversion through Energy Migration in Core-Shell Nanoparticles. *Nat. Mater.* **2011**, *10*, 968–973.
29. Cao, T. Y.; Yang, Y.; Gao, Y. A.; Zhou, J.; Li, Z. Q.; Li, F. Y. High-Quality Water-Soluble and Surface-Functionalized Upconversion Nanocrystals as Luminescent Probes for Bioimaging. *Biomaterials* **2011**, *32*, 2959–2968.
30. Bunzli, J. C. G. Lanthanide Luminescence for Biomedical Analyses and Imaging. *Chem. Rev. (Washington, DC, U. S.)* **2010**, *110*, 2729–2755.
31. Auzel, F. Upconversion and Anti-Stokes Processes with f and d Ions in Solids. *Chem. Rev. (Washington, DC, U. S.)* **2004**, *104*, 139–173.
32. Yi, G.; Lu, H.; Zhao, S.; Yue, G.; Yang, W.; Chen, D.; Guo, L. Synthesis, Characterization, and Biological Application of Size-Controlled Nanocrystalline $NaYF_4$:Yb,Er Infrared-to-Visible Up-Conversion Phosphors. *Nano Lett.* **2004**, *4*, 2191–2196.
33. Lim, S. F.; Riehn, R.; Tung, C. K.; Ryu, W. S.; Zhuo, R.; Dalland, J.; Austin, R. H. Upconverting Nanophosphors for Bioimaging. *Nanotechnology* **2009**, *20*, 405701.
34. Nam, S. H.; Bae, Y. M.; Il Park, Y.; Kim, J. H.; Kim, H. M.; Choi, J. S.; Lee, K. T.; Hyeon, T.; Suh, Y. D. Long-Term Real-Time Tracking of Lanthanide Ion Doped Upconverting Nanoparticles in Living Cells. *Angew. Chem., Int. Ed.* **2011**, *50*, 6093–6097.
35. Zhou, J.; Yu, M. X.; Sun, Y.; Zhang, X. Z.; Zhu, X. J.; Wu, Z. H.; Wu, D. M.; Li, F. Y. Fluorine-18-Labeled $Gd^{3+}/Yb^{3+}/Er^{3+}$ Co-Doped $NaYF_4$ Nanophosphors for Multimodality PET/MR/UCL Imaging. *Biomaterials* **2011**, *32*, 1148–1156.
36. Liu, Q.; Chen, M.; Sun, Y.; Chen, G. Y.; Yang, T. S.; Gao, Y.; Zhang, X. Z.; Li, F. Y. Multifunctional Rare-Earth Self-Assembled Nanosystem for Tri-Modal Upconversion Luminescence/Fluorescence/Positron Emission Tomography Imaging. *Biomaterials* **2011**, *32*, 8243–8253.
37. Wang, J.; Wang, F.; Wang, C.; Liu, Z.; Liu, X. G. Single-Band Upconversion Emission in Lanthanide-Doped $KMnF_3$ Nanocrystals. *Angew. Chem., Int. Ed.* **2011**, *50*, 10369–10372.
38. Li, Z. Q.; Zhang, Y. An Efficient and User-Friendly Method for the Synthesis of Hexagonal-Phase $NaYF_4$:Yb, Er/Tm Nanocrystals with Controllable Shape and Upconversion Fluorescence. *Nanotechnology* **2008**, *19*, 345606.
39. Boyer, J.; Vetrone, F.; Cuccia, L.; Capobianco, J. Synthesis of Colloidal Upconverting $NaYF_4$ Nanocrystals Doped with $Er^{3+}$, $Yb^{3+}$ and $Tm^{3+}$, $Yb^{3+}$ *via* Thermal Decomposition of Lanthanide Trifluoroacetate Precursors. *J. Am. Chem. Soc.* **2006**, *128*, 7444–7445.
40. Qian, H. S.; Zhang, Y. Synthesis of Hexagonal-Phase Core-Shell $NaYF_4$ Nanocrystals with Tunable Upconversion Fluorescence. *Langmuir* **2008**, *24*, 12123–12125.
41. Ow, H.; Larson, D. R.; Srivastava, M.; Baird, B. A.; Webb, W. W.; Wiesner, U. Bright and Stable Core-Shell Fluorescent Silica Nanoparticles. *Nano Lett.* **2005**, *5*, 113–117.
42. Wang, Z. J.; Tao, F.; Yao, L. Z.; Cai, W. L.; Li, X. G. Selected Synthesis of Cubic and Hexagonal $NaYF_4$ Crystals *via* a Complex-Assisted Hydrothermal Route. *J. Cryst. Growth* **2006**, *290*, 296–300.
43. Wei, Y.; Lu, F. Q.; Zhang, X. R.; Chen, D. P. Synthesis and Characterization of Efficient Near-Infrared Upconversion Yb and Tm Codoped $NaYF_4$ Nanocrystal Reporter. *J. Alloys Compd.* **2007**, *427*, 333–340.
44. Alexandrakis, G.; Rannou, F. R.; Chatziioannou, A. F. Tomographic Bioluminescence Imaging by Use of a Combined Optical-PET (OPET) System: A Computer Simulation Feasibility Study. *Phys. Med. Biol.* **2005**, *50*, 4225–4241.
45. Wang, F.; Wang, J. A.; Liu, X. G. Direct Evidence of a Surface Quenching Effect on Size-Dependent Luminescence of Upconversion Nanoparticles. *Angew. Chem., Int. Ed.* **2010**, *49*, 7456–7460.
46. He, G. S.; Bhawalkar, J. D.; Zhao, C. F.; Prasad, P. N. Optical Limiting Effect In a 2-photon Absorption Dye-Doped Solid-mMatrix. *Appl. Phys. Lett.* **1995**, *67*, 2433–2435.
47. Pawlicki, M.; Collins, H. A.; Denning, R. G.; Anderson, H. L. Two-Photon Absorption and the Design of Two-Photon Dyes. *Angew. Chem., Int. Ed.* **2009**, *48*, 3244–3266.
48. Drobizhev, M.; Makarov, N. S.; Tillo, S. E.; Hughes, T. E.; Rebane, A. Two-Photon Absorption Properties of Fluorescent Proteins. *Nat. Methods* **2011**, *8*, 393–399.
49. Belfield, K. D.; Morales, A. R.; Kang, B. S.; Hales, J. M.; Hagan, D. J.; Van Stryland, E. W.; Chapela, V. M.; Percino, J. Synthesis, Characterization, and Optical Properties of New Two-Photon-Absorbing Fluorene Derivatives. *Chem. Mater.* **2004**, *16*, 4634–4641.
50. Reinhardt, B. A.; Brott, L. L.; Clarson, S. J.; Dillard, A. G.; Bhatt, J. C.; Kannan, R.; Yuan, L.; He, G. S.; Prasad, P. N. Highly Active Two-Photon Dyes: Design, Synthesis, and Characterization toward Application. *Chem. Mater.* **1998**, *10*, 1863–1874.
51. Page, R. H.; Schaffers, K. I.; Waide, P. A.; Tassano, J. B.; Payne, S. A.; Krupke, W. F.; Bischel, W. K. Upconversion-Pumped Luminescence Efficiency of Rare-Earth-Doped Hosts Sensitized with Trivalent Ytterbium. *J. Opt. Soc. Am. B* **1998**, *15*, 996–1008.
52. Suyver, J.; Grimm, J.; van Veen, M.; Biner, D.; Kramer, K.; Gudel, H. Upconversion Spectroscopy and Properties of $NaYF_4$ Doped with $Er^{3+}$, $Tm^{3+}$ and/or $Yb^3$. *J. Lumin.* **2006**, *117*, 1–12.
53. Boyer, J. C.; van Veggel, F. C. J. M. Absolute Quantum Yield Measurements of Colloidal $NaYF_4$:$Er^{3+}$, $Yb^{3+}$ Upconverting Nanoparticles. *Nanoscale* **2010**, *2*, 1417–1419.
54. Svensson, T.; Alerstam, E.; Khoptyar, D.; Johansson, J.; Folestad, S.; Andersson-Engels, S. Near-Infrared Photon Time-of-Flight Spectroscopy of Turbid Materials up to 1400 nm. *Rev. Sci. Instrum.* **2009**, *80*, 063105.

# Paper VIII

**Multibeam fluorescence diffuse optical tomography using upconverting nanoparticles**

H. Liu, C. T. Xu, S. Andersson-Engels.

*Optics Letters* **35(5)**, 718-720 (2010).

718 OPTICS LETTERS / Vol. 35, No. 5 / March 1, 2010

# Multibeam fluorescence diffuse optical tomography using upconverting nanoparticles

**Haichun Liu,* Can T. Xu, and Stefan Andersson-Engels**

*Department of Physics, Lund University, P.O. Box 118, S-221 00 Lund, Sweden*
**Corresponding author: haichun.liu@fysik.lth.se*

Received November 2, 2009; revised December 18, 2009; accepted January 11, 2010;
posted January 12, 2010 (Doc. ID 119223); published February 25, 2010

Fluorescence diffuse optical tomography (FDOT) is a biomedical imaging modality that can be used for localization and quantification of fluorescent molecules inside turbid media. In this ill-posed problem, the reconstruction quality is directly determined by the amount and quality of the information obtained from the boundary measurements. Regularly, more information can be obtained by increasing the number of excitation positions in an FDOT system. However, the maximum number of excitation positions is limited by the finite size of the excitation beam. In the present work, we demonstrate a method in FDOT to exploit the unique nonlinear power dependence of upconverting nanoparticles to further increase the amount of information in a raster-scanning setup by including excitation with two beams simultaneously. We show that the additional information can be used to obtain more accurate reconstructions. © 2010 Optical Society of America

*OCIS codes:* 170.3880, 170.6960, 170.7050, 100.3190.

Fluorescence diffuse optical tomography (FDOT) is a relatively new modality that seeks to reconstruct the spatial distribution of fluorescent probes inside turbid materials [1]. As an imaging tool, it has good prospects in biomedical studies to image, for example, tumors [2], proteases [3], and drug effects [4].

FDOT is a numerically very ill-posed problem. In this problem, the quality of the reconstructions for the fluorescent target is directly determined by the amount and quality of fluorescence information obtained from boundary measurements [5]. Instrumental noise and tissue autofluorescence are the main perturbations of the measurements, resulting in poor signal quality, and can cause severe artifacts in the reconstructed results [6]. To overcome this, one could, for example, employ low-noise equipment, use background subtraction [7], or use spectral unmixing [8]. However, such methods cannot resolve all problems, since they essentially are only utilizing the present information in a better way rather than adding new constraints for the reconstructions, i.e., adding new independent information, which is critical to improve the quality of the reconstructions.

In a noncontact CCD-based FDOT system, one preferred way to gain more information is by increasing the number of excitation positions [9]. However, in order to keep the intensity of the excitation beam within reasonable levels, there is a limit on the minimum size of the excitation beam. This implies a practical upper limit to the highest excitation-position density, since distinct, i.e., nonoverlapping, excitation positions are desired in the reconstructions. It is also possible to employ an anatomical imaging modality such as magnetic-resonance imaging to provide *a priori* structural information [10]. However, this is at the cost of significantly increased complexity and reduced flexibility of the system.

Upconverting nanoparticles have been proposed as fluorophores in biomedical imaging [11,12] as well as in FDOT [13]. These nanoparticles can emit anti-Stokes shifted light when excited at 980 nm [14], which enables the signal to be detected in an autofluorescence-free environment [15]. This leads to a significant reduction of artifacts in the reconstructions. In addition, owing to the quadratic power dependence of the nanoparticles, the reconstructions are more sharply defined compared with the reconstructions of a linear fluorophore [13].

In this Letter, we present an approach to exploit the quadratic power dependence of upconverting nanoparticles to gain additional information by utilizing two beams simultaneously for excitation in FDOT. The effect of the images taken with dual-beam excitation (named type-D images) on the reconstructions of the nanoparticle number density distribution, $n$, is demonstrated. In addition, comparisons of reconstructed results between the linear rhodamine 6G and the quadratic upconverting nanoparticles are made.

The excitation and emission fields can be modeled by two coupled diffusion equations [13]. For quadratic fluorophores, the fluorescence signal detected at a fixed detector position under excitation of the $k$th beam, $\Gamma_k$, can be described by the forward model

$$\Gamma_k = \sum_{i=1}^{N} U_f^*(\mathbf{r}_d, \mathbf{r}_i) n(\mathbf{r}_i) [U_e(\mathbf{r}_{s_k}, \mathbf{r}_i)]^2 \Delta V_i, \qquad (1)$$

where $N$ denotes the number of voxels; $\mathbf{r}_{s,d,i}$ denotes the coordinates for source, detector, and voxel, respectively; and $\Delta V_i$ is the volume of voxel $i$. The forward solution of the excitation light is represented by $[U_e(\mathbf{r}_{s_k}, \mathbf{r}_i)]^2$, while the adjoint solution to the forward fluorescence problem is represented by $U_f^*(\mathbf{r}_d, \mathbf{r}_i)$. When exciting the medium using two beams simultaneously, the detected signal is given by

0146-9592/10/050718-3/$15.00 

$$\Gamma_{k\&j} = \sum_{i=1}^{N} U_{\mathrm{f}}^{*}(\mathbf{r}_{\mathrm{d}},\mathbf{r}_i)n(\mathbf{r}_i)[U_{\mathrm{e}}(\mathbf{r}_{\mathrm{s}_k},\mathbf{r}_i) + U_{\mathrm{e}}(\mathbf{r}_{\mathrm{s}_j},\mathbf{r}_i)]^2\Delta V_i$$
$$= 2\sum_{i=1}^{N} U_{\mathrm{f}}^{*}(\mathbf{r}_{\mathrm{d}},\mathbf{r}_i)n(\mathbf{r}_i)U_{\mathrm{e}}(\mathbf{r}_{\mathrm{s}_k},\mathbf{r}_i)U_{\mathrm{e}}(\mathbf{r}_{\mathrm{s}_j},\mathbf{r}_i)\Delta V_i + \Gamma_k + \Gamma_j, \quad (2)$$

which reveals the involvement of cross terms. In a raster-scanning setup, if two images are taken sequentially with one excitation beam scanning over two positions (named type-S images), and a third image is taken with dual-beam excitation (type-D) above the previous two positions, the involvement of cross terms implies that the type-D image cannot be obtained by any mathematical manipulation from the existing type-S images, indicating that it is independent and contains additional information. However, for linear fluorophores, e.g., rhodamine 6G, the type-D image is only a linear combination of the existing type-S images and will not add more constraints for the inverse problem. For nonlinear fluorophores, it is obvious that Eq. (2) can be generalized to include more simultaneous excitation beams.

The significance of the measurements with dual-beam excitation in the reconstructions was confirmed by the singular-value analysis of the weight matrix, $W$, whose elements are given by [13]

$$W_{(\mathrm{s,d}),i} = U_{\mathrm{f}}^{*}(\mathbf{r}_{\mathrm{d}},\mathbf{r}_i)[U_{\mathrm{e}}(\mathbf{r}_{\mathrm{s}},\mathbf{r}_i)]^{\gamma}\Delta V_i, \quad (3)$$

with $\gamma=1$ for linear fluorophores and $\gamma=2$ for quadratic fluorophores. Calculations were performed using the NIRFAST package implementing the finite-element method [16]. $W$ was factorized according to

$$W = U\Sigma V^{*}, \quad (4)$$

where $U$ and $V$ are unitary matrices containing the left and right singular vectors of $W$, respectively, and $\Sigma$ is a diagonal matrix containing the singular values of $W$. The column space of $V$ is spanned by the image-space modes, while the column space of $U$ is spanned by the detection-space modes. The singular values of $W$ denote how effectively a given image-space mode can be detected by an experimental setup [17].

Figure 1 shows the normalized singular-value distribution of $W$. For clarity, only every second singular value is shown. The circle and plus signs represent the linear fluorophore, the former for the single-beam excitation, while the latter for the combined single-beam excitation and dual-beam excitation. As seen, the normalized intensities of the additional singular values due to dual-beam excitation have dropped to machine precision, which indicates that the measurements with dual-beam excitation will not alleviate the ill-posedness of FDOT. In other words, the type-D images cannot provide more information than the existing type-S images. Hence, it will not improve the quality of the reconstructions. However, for the quadratic fluorophore (denoted by asterisk and dot signs in Fig. 1), the intensities of the additional singular values are still significant. This implies that type-D images will contribute to the quality of the reconstructions.

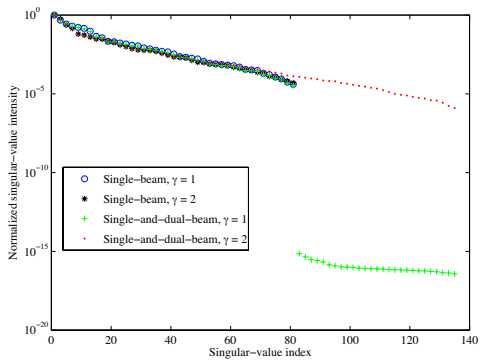


Fig. 1. (Color online) Singular-value distribution of $W$.

The experiments were carried out in a gelatin phantom with optical properties of $\mu_{\mathrm{a}}=0.29$ cm$^{-1}$ and $\mu_{\mathrm{s}}'=10.0$ cm$^{-1}$ at 660 nm, measured with a time-of-flight spectroscopy system [18]. Two glass tubes with inner diameters of 2.4 mm, filled with aqueous solutions of rhodamine 6G ($c=0.1$ $\mu$M) and ultrasound-agitated dimethyl sulfoxide colloidal of $NaYF_4$:$Yb^{3+}$/$Tm^{3+}$ nanoparticles ($c=1$ wt%), respectively, were used to simulate the fluorescent lesions. The spot sizes of the lasers were 2.6 mm in diameter, which gave optical power densities of 480 mW/cm$^2$ for the 980 nm laser and 85 mW/cm$^2$ for the 532 nm laser, well below the damage thresholds of continuous human-skin exposure. The experimental setup and corresponding running parameters were similar with those used in our previous work [13]. Owing to the limited area of the phantom under investigation, only nine excitation positions ($3\times3$ grid) were used in the present work. The separation of two nearest-neighboring positions was 3.5 mm. During the experiments, a single excitation beam was first used to scan over the $3\times3$ grid, and one image was captured for each scanned position by a CCD camera. In the next step, two excitation beams, located at two nearest-neighboring sites of the same grid, were simultaneously employed to illuminate the phantom, giving six extra type-D images.

Figure 2 shows the three-dimensional rendering of the reconstructed upconverting nanoparticles. The cylinders in the subfigures are identical and represent the true fluorescent lesions. In the reconstruction of Fig. 2(a), only type-S images were used. As can be seen, the shape of the fluorescent lesion is overestimated. This overestimation may be explained by the ill-posedness of the inverse problem. When adding type-D images, the reconstruction of the fluorescent lesion shape is improved remarkably, as shown in Fig. 2(b). In order to emphasize the difference between the two reconstructions, cross-sectional slices of the reconstructed relative fluorophore distribution are shown in Fig. 3. Although the depth is relatively

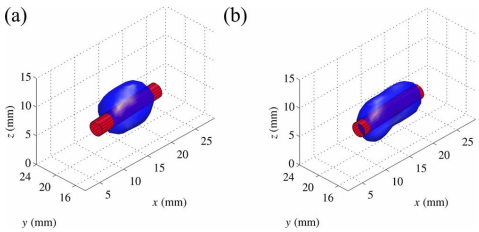


Fig. 2. (Color online) Three-dimensional reconstruction of upconverting nanoparticles. (a) Reconstruction using only type-S images. (b) Reconstruction using the combined data from type-S and type-D images.

well reconstructed at the center of the fluorescent lesion (represented by the circles) for both reconstructions, the reconstructed fluorescent lesion is more confined for the case of using both type-S and type-D images. This result confirms that the images of type D indeed contribute to the inverse problem and lead to better reconstructions for the quadratic upconverting nanoparticles. The corresponding reconstructions for the linear rhodamine 6G were also carried out, whose cross-sectional slices are presented in Fig. 4. Compared with the results for the nanoparticles, the reconstructions for rhodamine 6G do not benefit from adding the type-D images, which is in agreement with the theory. The true depth of the fluorescent lesion is also poorly reconstructed.

In summary, based on previous work regarding the employment of upconverting nanoparticles in FDOT, we propose and demonstrate an additional unique advantage of the nonlinear power dependence of upconverting nanoparticles. This advantage enables the possibility to obtain additional information for the inverse problem by using images taken with two or more excitation beams simultaneously. We found that this resulted in improved reconstructions. The same advantage could not be found when using linear fluorophores, e.g., rhodamine 6G.

This work was supported by a Swedish Research Council grant (VR 2007-4214) and a Linnaeus grant for the Lund Laser Centre. The authors thank Prof. Zhiguo Zhang and his group from the Harbin Institute of Technology and Dr. Gabriel Somesfalean for their collaboration work.

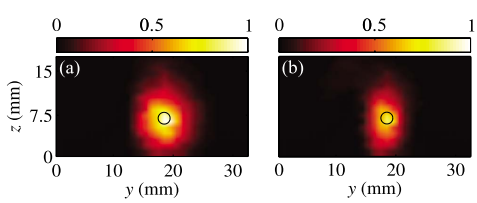


Fig. 3. (Color online) Cross-sectional slices of the reconstructed relative nanoparticle distribution at $x = 17$ mm. (a) Reconstruction with only type-S images. (b) Reconstruction with both type-S and type-D images.

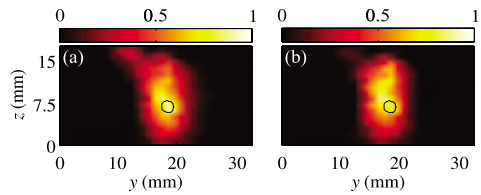


Fig. 4. (Color online) Cross-sectional slices of the reconstructed relative rhodamine 6G distribution at $x = 17$ mm. (a) Reconstruction with only type-S images. (b) Reconstruction with both type-S and type-D images.

## References

1. A. Hielscher, Curr. Opin. Biotechnol. **16**, 79 (2005).
2. A. Corlu, R. Choe, T. Durduran, M. A. Rosen, M. Schweiger, S. R. Arridge, M. D. Schnall, and A. G. Yodh, Opt. Express **15**, 6696 (2007).
3. V. Ntziachristos, C.-H. Tung, C. Bremer, and R. Weissleder, Nat. Med. **8**, 757 (2002).
4. V. Ntziachristos, E. A. Schellenberger, J. Ripoll, D. Yessayan, E. Graves, A. Bogdanov, L. Josephson, and R. Weissleder, Proc. Natl. Acad. Sci. USA **101**, 12294 (2004).
5. S. R. Arridge, Inverse Probl. **15**, R41 (1999).
6. A. Soubret and V. Ntziachristos, Phys. Med. Biol. **51**, 3983 (2006).
7. D. C. Comsa, T. J. Farrell, and M. S. Patterson, Phys. Med. Biol. **53**, 5797 (2008).
8. J. R. Mansfield, K. W. Gossage, C. C. Hoyt, and R. M. Levenson, J. Biomed. Opt. **10**, 041207 (2005).
9. G. Y. Panasyuk, Z.-M. Wang, J. C. Schotland, and V. A. Markel, Opt. Lett. **33**, 1744 (2008).
10. S. C. Davis, B. W. Pogue, R. Springett, C. Leussler, P. Mazurkewitz, S. B. Tuttle, S. L. Gibbs-Strauss, S. S. Jiang, H. Dehghani, and K. D. Paulsen, Rev. Sci. Instrum. **79**, 064302 (2008).
11. S. F. Lim, R. Riehn, W. S. Ryu, N. Khanarian, C.-K. Tung, D. Tank, and R. H. Austin, Nano Lett. **6**, 169 (2006).
12. C. Vinegoni, D. Razansky, S. A. Hilderbrand, F. Shao, V. Ntziachristos, and R. Weissleder, Opt. Lett. **34**, 2566 (2009).
13. C. T. Xu, J. Axelsson, and S. Andersson-Engels, Appl. Phys. Lett. **94**, 251107 (2009).
14. H. J. Liang, G. Y. Chen, L. Li, Y. Liu, F. Qin, and Z. G. Zhang, Opt. Commun. **282**, 3028 (2009).
15. C. T. Xu, N. Svensson, J. Axelsson, P. Svenmarker, G. Somesfalean, G. Y. Chen, H. J. Liang, H. C. Liu, Z. G. Zhang, and S. Andersson-Engels, Appl. Phys. Lett. **93**, 171103 (2008).
16. H. Dehghani, M. E. Eames, P. K. Yalavarthy, S. C. Davis, S. Srinivasan, C. M. Carpenter, B. W. Pogue, and K. D. Paulsen, Commun. Numer. Methods Eng. **25**, 711 (2009).
17. J. P. Culver, V. Ntziachristos, M. J. Holboke, and A. G. Yodh, Opt. Lett. **26**, 701 (2001).
18. E. Alerstam, S. Andersson-Engels, and T. Svensson, J. Biomed. Opt. **13**, 041304 (2008).

# Paper IX

**Multispectral guided fluorescence diffuse optical tomography using upconverting nanoparticles**

P. Svenmarker, C. T. Xu, H. Liu, X. Wu, S. Andersson-Engels.

(2013) *Accepted for publication by Applied Physics Letters.*

## Multispectral Guided Fluorescence Diffuse Optical Tomography using Upconverting Nanoparticles

Pontus Svenmarker,[1,2,3,a] Can T. Xu,[1] Haichun Liu,[1] Xia Wu,[1] and Stefan Andersson-Engels[1]
[1] *Department of Physics, Lund University, P.O. Box 118, SE-221 00 Lund, Sweden*
[2] *Department of Physics, Umeå University, SE-901 87 Umeå Sweden*
[3] *Centre for Mircobial Research (UCMR), Umeå University, SE-901 87 Umeå Sweden*

(Dated: 7 October 2013)

We report improved image detectability for fluorescence diffuse optical tomography using upconverting nanoparticles doped with rare-earth elements. Core-shell $NaYF_4:Yb^{3+}/Er^{3+}@NaYF_4$ upconverting nanoparticels were synthesized through a stoichiometric method. The $Yb^{3+}/Er^{3+}$ sensitizer-activator pair yielded two anti-Stokes shifted fluorescence emission bands at 540 nm and 660 nm, here used to *a priori* estimate the fluorescence source depth with sub-millimeter precision. A spatially varying regularization incorporated the *a priori* fluorescence source depth estimation into the tomography reconstruction scheme. Numerically it is fast, simple and direct to implement. Tissue phantom experiments showed both an improved resolution and contrast in the reconstructed images as compared to not using any *a priori* information.

During the last decade, *in vivo* fluorescence imaging has grown to become the most commonly used pre-clinical imaging modality.[1] Alongside the instrument and algorithm development, a rich flora of fluorescent contrast agents has emerged.[2] One contrast agent class with unique properties is upconverting nanoparticles.[3] Upon near-infrared (NIR) excitation, they are able to emit anti-Stokes shifted fluorescence, thereby allowing for autofluorescence insensitive detection.[4,5] Further, they have a non-linear excitation power-dependence, due to successive absorption of two or more photons, which can be exploited to increase the resolution in diffuse fluorescence imaging and tomography.[6–8] Upconverting nanoparticles are photo-stable even under intense irradiation, hence facilitating prolonged experiments. Additionally, the availability of narrow multi-color emission bands with large anti-Stokes shifts is a key feature, which will be exploited in this letter.[9]

In fluorescence diffuse optical tomography (fDOT), a fair amount of attention has been directed towards multispectral approaches.[10–13] It is well understood that spectra provides information on source depth, and that such spectral encoded source depth information can be accessed through reading multiple emission or excitation wavelengths, or a combination of the two.[10,14–17] The key lay in covering a spectral region with large tissue attenuation differences, which for biological samples is typically manifested at the blue end of the tissue-optical-window. To access the necessary spectral coverage requires a fluorophore that either has a wide emission or excitation band, and at the same time, spectrally overlap with a large tissue attenuation difference. Available fluorescent dyes emit and absorb photons across the whole visible and part of the NIR spectrum, but exhibit a limited emission and excitation band width (∼100 nm) and only small Stokes shifts (∼30 nm). Still they are used for source depth estimation.[10,14–16] Quantum dots have been proposed as an alternative.[13] They offer a wider excitation band, which may extend over a few hundreds of nanometers, while being accompanied by large Stokes shifted narrow band emission. Quantum dots, however, typically suffers from limited imaging depth, since their excitation band in the ultra-violet to the blue part of the spectrum coincides with strong tissue attenuation. Upconverting nanoparticles, on the other hand, enable deep tissue imaging due to a combination of NIR excitation and large anti-Stokes shifted NIR and visible emission bands.[18]

In this letter, we report improved image detectability for fDOT using core-shell $NaYF_4:Yb^{3+}/Er^{3+}@NaYF_4$ upconverting nanoparticles. By the use of the $Yb^{3+}/Er^{3+}$ sensitizer-activator pair, two anti-Stokes shifted emission bands (540 nm and 660 nm) upon 980 nm excitation, were available for fluorescence source depth estimation. An advantageous approach of incorporating the *a priori* fluorescence source depth information into the fDOT image reconstruction is through a spatially varying regularization.[15] To evaluate the performance gained, a comparison between a multispectral guided spatially varying regularization and a non-spatially varying Tikhonov regularization were made in a well controlled tissue phantom experiment.

The method used for reconstructing the fluorescence distribution follows the procedure undertaken by Zacharopoulos *et al.*.[12] In brief, it involves modeling the photon migration as a set of diffusion equations expressed as

$$-\nabla \cdot \mathrm{D}^{\mathrm{x}}(\mathbf{r})\nabla\Phi^{\mathrm{x}}(\mathbf{r}) + \mu_{\mathrm{a}}^{\mathrm{x}}\Phi^{\mathrm{x}}(\mathbf{r}) = \mathrm{q}(\mathbf{r}_{\mathrm{q}}) \quad (1)$$

$$-\nabla \cdot \mathrm{D}^{\mathrm{f}}(\mathbf{r})\nabla\Phi^{\mathrm{f}}(\mathbf{r},\lambda) + \mu_{\mathrm{a}}^{\mathrm{f}}\Phi^{\mathrm{f}}(\mathbf{r},\lambda) = \eta(\mathbf{r})[\Phi^{\mathrm{x}}(\mathbf{r})]^{\beta} \quad (2)$$

where $\mathrm{D}^{\mathrm{x/f}}$ is the diffusion coefficient, $\mu_{\mathrm{a}}^{\mathrm{x/f}}$ is the absorption coefficient at the excitation/fluorescence wavelength, respectively; $\mathrm{q}(\mathbf{r}_{\mathrm{q}})$ is the excitation source at position $\mathbf{r}_{\mathrm{q}}$ and $\beta$ is the power-dependence exponent ($\beta = 2$ for the upconverting nanoparticles used in this work ). A Robin

[a] Electronic mail: pontus.svenmarker@physics.umu.se

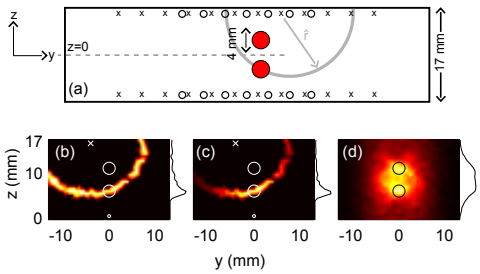


FIG. 1. (a) A cross-sectional view of the imaging geometry with two fluorescent inclusions on axis (4 mm in diameter). Open circles indicate source positions and crosses detector positions. The gray arc describes the estimated distance, as given by the fluorescence ratio, between one particular detector and the emitting fluorescent inclusion. (b) A visualization of the three-step process involved for calculating the spatially varying multispectral guided regularization. The estimated distance, as given by the fluorescent ratio, for a single detector located at the position indicated by the cross. (c) Each voxel is thereafter weighted by the intensity recorded by its closest detector, for a given source, here exemplified by a source at the position of the circle. This will act as a triangulation. (d) Repeating this procedure for every source and detector, and summing the contributions yields the multispectral guided regularization.

boundary condition is used to account for reflection and refraction at the tissue surface. The sought parameter is the fluorescence yield $\eta(\mathbf{r}) = \mu_{\mathrm{a}}^{\mathrm{np}}\gamma(\lambda)$, which can be written as the product of the nanoparticle absorption coefficient $\mu_{\mathrm{a}}^{\mathrm{np}}$ and its slope efficiency $\gamma(\lambda)$ at wavelength $\lambda$. In the reconstruction, the difference between the measured and calculated projections is minimized with respect to the fluorescence yield distribution in a least-square manner.

$$\|\mathrm{J}\eta(\mathbf{r}) - \mathbf{b}\|^2 + \alpha \|\mathrm{L}\eta(\mathbf{r})\|^2 \qquad (3)$$

Here the elements in the Jacobian $\mathrm{J} = [\Phi_{\mathrm{q}}^{\mathrm{x}}(\mathbf{r})]^{\beta}\ \Phi_{\mathrm{m}}^{\mathrm{f}}(\mathbf{r},\lambda)$ equal the product of the excitation fluence rate and the emission fluence rate and $\mathbf{b} = [\Gamma_{\mathrm{q_1,m_1}}(\lambda_1)\ldots\Gamma_{\mathrm{q_1,m_1}}(\lambda_2)\ldots]$ contains the measured projections. A regularization term L is added for stabilizing minimization and thus making it possible to find an estimated solution to an otherwise ill-conditioned inverse problem. In the simplest case, L is chosen as the identity matrix, which gives the Tikhonov regularization. In practice, it will add an offset, with its strength determined by the regularization hyper-parameter $\alpha$, giving rise to the effect of smoothing the resulting image towards the shape of the regularization matrix - a featureless flat image. Since we can estimate the fluorescence yield distribution by the fluorescence emission ratio, it can be used to calculate a spatially varying regularization matrix, and thereby allow for a more sophisticated smoothing.

The procedure for calculating the multispectral regularization was inspired by the work of Axelsson *et al.*.[15] By taking advantage of that the fluorescence photons at different wavelengths will encounter a wavelength-dependent attenuation while escaping the imaging volume, the relative loss between different emission bands can be used to calculate the distance between the position where the fluorescence emission takes place and where it is detected.[14] An estimation of this distance, $\hat{\mathbf{r}}$, can be found by solving the following expression,

$$\left|\frac{\Gamma_{\mathrm{q,m}}(\lambda_1)}{\Gamma_{\mathrm{q,m}}(\lambda_2)} - \frac{\Phi_{\mathrm{m}}^{\mathrm{f}}(\mathbf{r},\lambda_1)}{\Phi_{\mathrm{m}}^{\mathrm{f}}(\mathbf{r},\lambda_2)}\right| < \epsilon. \qquad (4)$$

In two dimensions, $\hat{\mathbf{r}}$ describes an arc (see Fig. 1b), and in three dimensions a spherical surface with its origin at the detector position. The precision of the estimated distance is controlled by a user defined threshold $\epsilon$. To further pinpoint the location of the fluorophore, each voxel is weighted by the fluorescence intensity of its closest detector. This will act as a weighted triangulation, where $\hat{\mathbf{r}}$ provides the depth position and the boundary fluorescence emission profile gives the lateral positioning (see Fig. 1c). To receive the final regularization (see Fig. 1d), a weighted triangulation is performed for every projection and the collective response is summed to give the diagonal elements of the spatially varying multispectral regularization matrix. The implementation was straightforward, only requiring direct calculations for solving Eq.4 and performing the weighted sum.

Core-shell $NaYF_4{:}Yb^{3+}/Er^{3+}@NaYF_4$ upconverting nanoparticles were synthesized through a stoichiometric method and dispersed in a non-polar solution to a concentration of 1 wt% to act as the fluorescent inclusions.[7] Figure 2a shows the size distribution measured with dynamic light scattering (DLS) together with a transmission electron microscopy (TEM) image confirming the size of the particles. The average particle size measured with DLS including the coating was 28 nm in diameter. The fluorescence spectrum of the particles following excitation at 975 nm is displayed in Fig. 2b showing two emission bands at 540 nm and 660 nm, respectively. Figure 1a depicts the layout of the measurement geometry with two fluorescent inclusions on axis. Two glass tubes (2 mm inner diameter) filled with the suspension were submerged in a tissue phantom with a thickness of 17 mm consisting of water, intralipid and bovine blood. The phantom was characterized with photon time-of-flight spectroscopy (TOFS)[19] and steady-state spectroscopy to determine its optical properties. Fig. 2b presents the effective attenuation coefficient $\mu_{\mathrm{eff}}$ as a function of wavelength measured with steady-state spectroscopy, together with the reduced scattering coefficient $\mu_{\mathrm{s}}'$ values obtained from TOFS. By extrapolating the reduced scattering coefficient on the form $\mu_{\mathrm{s}}' = a\lambda^{-b}$, the absorption coefficient

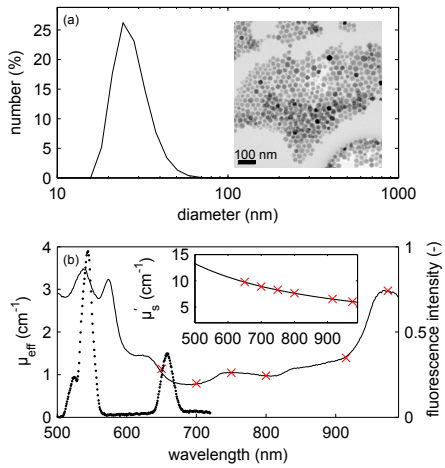


FIG. 2. Characterization of the core-shell $NaYF_4:Yb^{3+}/Er^{3+}@NaYF_4$ nanoparticles and optical properties of the tissue phantom. (a) Nanoparticle size distribution measured with DLS (diameter average equals 28 nm) together with an inset containing a corresponding TEM image with a median particle diameter of 22 nm. (b) A Fluorescence emission spectrum of the nanoparticles upon 975 nm excitation is given by the dotted line. The solid line indicates the effective attenuation of the liquid phantom measured with steady-state spectroscopy and the red crosses give the same quantity measured by TOFS. The inset show the reduced scattering coefficient obtained by TOFS together with an extrapolation.

and the reduced scattering coefficient for all wavelengths of interest could be determined. Transillumination imaging was performed for a set of $7 \times 7$ source positions spaced 2 mm apart. Excitation was performed by a diode laser emitting at 975 nm and delivering an intensity of 1 W/cm$^2$. An image was acquired for each source position using an EMCCD camera equipped with a 30 mm/0.95 lens. A combination of two filters, a short-pass cut-off filter at 900 nm together with either a 660 nm or 540 nm interference filter, were used to block the excitation light and extract the desired emission band. Each image was cropped and binned to give $8 \times 12$ detectors.

To evaluate the performance of the spatially varying multispectral regularization, a series of fDOT reconstructions with varying tube center-center distances were performed. Each step in the series displaced the tubes 1 mm further apart while preserving the axial symmetry, starting at a center-center distance of 4 mm and ending at 8 mm. The axial positions of each fluorescent inclusion were independently controlled within an accuracy of 125 $\mu$m through the use of micrometer translation stages. By enforcing symmetry, only one side of the phantom needed to be measured and the conjugate view (symmetrically mirror the phantom at $z = 0$ mm, see Fig. 1a) could be obtained by duplicating the data.

The first row in Fig. 3 displays the reconstructed images when using the multispectral regularization to guide the reconstruction process. Each image shows an x-z slice at $y = 0$ mm together with a cross-sectional plot. For comparison, reconstructed images using Tikhonov regularization are presented in the second row. Both the resolution and the contrast were higher when using the multispectral regularization compared to the use of Tikhonov regularization, leading to an increased detectability for the multispectral regularization guided reconstructions. The rods spaced 4 mm apart could be resolved by the multispectral regularization guided reconstructions, while the Tikhonov regularization guided reconstructions could only resolve the rods at an 8 mm center-center distance. A comparison of the image contrast, defined as $I_C = (I_{max} - I_{min})/I_{max}$, for the case when the rods were placed at an 8 mm center-center distance gave 0.46 compared to 0.24, for the multispectral regularization and the Tikhonov regularization, respectively.

For creation of a successful multispectral regularization, accurate and a large difference in optical properties between the two wavelengths detected are crucial. In a simplistic analysis, assuming an infinite homogeneous geometry, the fluorescence ratio depth dependence can be written as; $\log(\Gamma^1/\Gamma^2) = \log(D^2/D^1) - r(\mu^1_{eff} - \mu^2_{eff})$. From this expression, it is clear that the difference in effective attenuation coefficients between wavelengths 1 and 2 sets the depth sensitivity. A large difference, typically achieved by utilizing the sharp absorption profile of haemoglobin, gives a high sensitivity and hence facilitates precise depth localization. An error in the deduced optical properties will naturally lead to an inaccurate estimated depth.[17] Any autofluorescence present will further misguide the depth localization.

In conclusion, we reported improved image detectability for fDOT using core-shell $NaYF_4:Yb^{3+}/Er^{3+}@NaYF_4$ upconverting nanoparticles, while guiding the reconstruction procedure with *a priori* fluorescence source depth estimations, here implemented through a spatially varying regularization. Numerically it was fast, simple and direct to implement. The use of $NaYF_4:Yb^{3+}/Er^{3+}@NaYF_4$ upconverting nanoparticles as contrast agent, with two emission bands experiencing drastically different tissue attenuation, yielded a multispectral regularization with precise depth localization. Careful characterization of the tissue attenuation by time-of-flight and steady-state spectroscopy resulted in an accurate depth localization. Autofluorescence insensitive measurements achieved through the use of upconverting nanoparticles ensured contamination free data, which otherwise may misguide the source depth estimation and also the fDOT reconstruction.

The authors would like to acknowledge Erik Alerstam for assisting with the TOFS measurements.

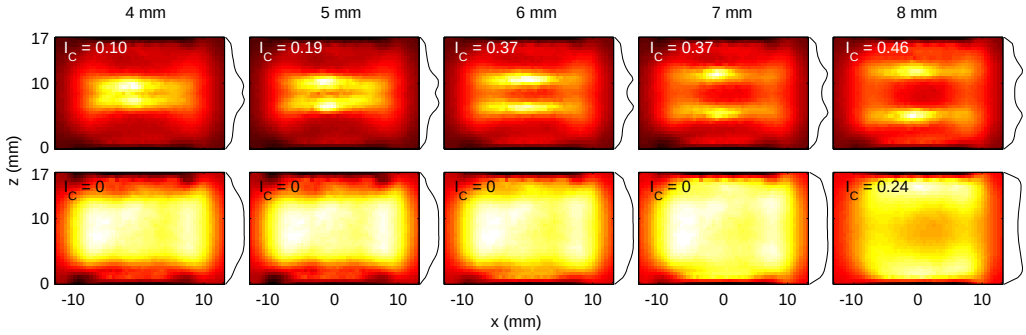


FIG. 3. Reconstructed fluorescence diffuse optical tomography images for different center-center distances of the fluorescent contrast agent. All images show a x-z slice at y=0 mm together with a cross-section plot along the z-direction. The first row displays multispectral regularization guided reconstructions and the second row Tikhonov regularization guided reconstructions.

## REFERENCES


[1]Frederic Leblond, Scott C. Davis, Pablo A. Valdes, and Brian W. Pogue. Pre-clinical whole-body fluorescence imaging: Review of instruments, methods and applications. *Journal of Photochemistry and Photobiology B - Biology*, 98(1):77–94, JAN 21 2010.

[2]Hisataka Kobayashi, Mikako Ogawa, Raphael Alford, Peter L. Choyke, and Yasuteru Urano. New strategies for fluorescent probe design in medical diagnostic imaging. *Chemical Reviews*, 110(5):2620–2640, MAY 2010.

[3]F. Wang and X. G. Liu. Recent advances in the chemistry of lanthanide-doped upconversion nanocrystals. *Chemical Society Reviews*, 38(4):976–989, 2009.

[4]Can T. Xu, Niclas Svensson, Johan Axelsson, Pontus Svenmarker, Gabriel Somesfalean, Guanying Chen, Huijuan Liang, Haichun Liu, Zhiguo Zhang, and Stefan Andersson-Engels. Autofluorescence insensitive imaging using upconverting nanocrystals in scattering media. *Applied Physics Letters*, 93(17), OCT 27 2008.

[5]Can T. Xu, Johan Axelsson, and Stefan Andersson-Engels. Fluorescence diffuse optical tomography using upconverting nanoparticles. *Applied Physics Letters*, 94(25), JUN 22 2009.

[6]Pontus Svenmarker, Can T. Xu, and Stefan Andersson-Engels. Use of nonlinear upconverting nanoparticles provides increased spatial resolution in fluorescence diffuse imaging. *Optics Letters*, 35(16):2789–2791, 2010.

[7]C. T. Xu, P. Svenmarker, H. C. Liu, X. Wu, M. E. Messing, L. R. Wallenberg, and S. Andersson-Engels. High-resolution fluorescence diffuse optical tomography developed with nonlinear upconverting nanoparticles. *Acs Nano*, 6(6):4788–4795, June 2012.

[8]Haichun Liu, Can T. Xu, and Stefan Andersson-Engels. Multibeam fluorescence diffuse optical tomography using upconverting nanoparticles. *Optics Letters*, 35(5):718–720, MAR 1 2010.

[9]Z. Q. Li, Y. Zhang, and S. Jiang. Multicolor core/shell-structured upconversion fluorescent nanoparticles. *Advanced Materials*, 20(24):4765–+, December 2008.

[10]G Zavattini, S Vecchi, G Mitchell, U Weisser, RM Leahy, BJ Pichler, DJ Smith, and SR Cherry. A hyperspectral fluorescence system for 3d in vivo optical imaging. *Physics in Medicine and Biology*, 51(8):2029–2043, APR 21 2006.

[11]Abhijit J. Chaudhari, Sangtae Ahn, Richard Levenson, Ramsey D. Badawi, Simon R. Cherry, and Richard M. Leahy. Excitation spectroscopy in multispectral optical fluorescence tomography: methodology, feasibility and computer simulation studies. *Physics in Medicine and Biology*, 54(15):4687–4704, AUG 7 2009.

[12]Athanasios D. Zacharopoulos, Pontus Svenmarker, Johan Axelsson, Martin Schweiger, Simon R. Arridge, and Stefan Andersson-Engels. A matrix-free algorithm for multiple wavelength fluorescence tomography. *Optics Express*, 17(5):3025–3035, MAR 2 2009.

[13]A. D. Klose. Hyperspectral excitation-resolved fluorescence tomography of quantum dots. *Optics Letters*, 34(16):2477–2479, August 2009.

[14]J Swartling, J Svensson, D Bengtsson, K Terike, and S Andersson-Engels. Fluorescence spectra provide information on the depth of fluorescent lesions in tissue. *Applied Optics*, 44(10):1934–1941, APR 1 2005.

[15]Johan Axelsson, Jenny Svensson, and Stefan Andersson-Engels. Spatially varying regularization based on spectrally resolved fluorescence emission in fluorescence molecular tomography. *Optics Express*, 15(21):13574–13584, OCT 17 2007.

[16]F Leblond, Z Ovanesyan, S C Davis, P A Valds, A Kim, A Hartov, B C Wilson, B W Pogue, K D Paulsen, and D W Roberts. Analytic expression of fluorescence ratio detection correlates with depth in multi-spectral

sub-surface imaging. *Physics in Medicine and Biology*, 56(21):6823, 2011.

[17] J. Svensson and S. Andersson-Engels. Modeling of spectral changes for depth localization of fluorescent inclusion. *Optics Express*, 13(11):4263–4274, May 2005.

[18] Qiuqiang Zhan, Jun Qian, Huijuan Liang, Gabriel Somesfalean, Dan Wang, Sailing He, Zhiguo Zhang, and Stefan Andersson-Engels. Using 915 nm laser excited $Tm^{3+}/Er^{3+}/Ho^{3+}$-doped $NaYbF_4$ upconversion nanoparticles for in vitro and deeper in vivo bioimaging without overheating irradiation. *Acs Nano*, 5(5):3744–3757, MAY 2011.

[19] Tomas Svensson, Erik Alerstam, Dmitry Khoptyar, Jonas Johansson, Staffan Folestad, and Stefan Andersson-Engels. Near-infrared photon time-of-flight spectroscopy of turbid materials up to 1400 nm. *Review of Scientific Instruments*, 80(6):063105, JUN 2009.